

The Catalysis of Uniform Metal Nanoparticles Deposited onto Oxide Supports:  
The Components of a Catalyst that Control Activity and Selectivity

By  
Nathan Musselwhite

A dissertation submitted in partial satisfaction of the  
requirements for the degree of  
Doctor of Philosophy  
in  
Chemistry  
in the  
Graduate Division  
of the  
University of California, Berkeley

Committee in charge:  
Professor Gabor A. Somorjai, Chair  
Professor Stephen Leone  
Professor Enrique Iglesia

Summer 2015



## Abstract

### The Catalysis of Uniform Metal Nanoparticles Deposited onto Oxide Supports: The Components of a Catalyst that Control Activity and Selectivity By

Nathan Musselwhite

Doctor of Philosophy in Chemistry

University of California, Berkeley

Professor Gabor A. Somorjai, Chair

Model materials consisting of metal nanoparticles loaded onto oxide supports were synthesized, characterized, and investigated in a number of catalytic chemical reactions. By varying the size, shape, and composition of nanoparticle, as well as the material used to support the nanoparticles, it was found that small changes to the catalyst can have enormous changes to the reaction activity and selectivity. Investigation of these carefully synthesized catalysts via in situ characterization, and reaction studies, leads to a deeper understanding of the molecular level parameters that govern catalysis.

Through study of the properties of the nanoparticles it was discovered that nanoparticle size and shape have a dominant role in the chemoselective catalysis of furfural over platinum nanoparticles. When vapor phase furfural and hydrogen gas were passed over Pt nanoparticles ranging in size from 1.5 to 7.1 nm, the catalytic selectivity was found to be dominated by the size of the nanoparticle. Large nanoparticles promoted hydrogenation of furfural to furfuryl alcohol, while smaller nanoparticles favored decarbonylation to furan.

The same size specific selectivity was found in the hydrogenative reforming (the transformation of hydrocarbons to branched isomers) of C<sub>6</sub> hydrocarbons, in which Pt nanoparticle size controls isomerization selectivity. Methylcyclopentane was found to be extremely size dependent at lower temperatures (553 K). It was found that smaller sized nanoparticles favored isomer formation, while larger sizes catalyzed the aromatization reaction more efficiently. n-hexane was found to be much less dependent on particle size, but still showed an increase in isomerization with small particles over larger sized Pt nanoparticles.

The composition of Pt<sub>x</sub>Rh<sub>1-x</sub> bimetallic nanoparticles was also studied. These catalysts were characterized under hexane reforming conditions with Ambient Pressure X-ray Photoelectron Spectroscopy (AP-XPS), in order to find the actual surface atomic composition under real catalytic working conditions. By using AP-XPS and catalytic data in tandem, it was found that an optimum Rh loading occurred when the surface ensemble statistically favored one Rh atom surrounded by Pt atoms.

By utilizing different oxide materials for catalytic supports the flow of charge can play a role in the reaction at the surface or interface in a phenomenon known as the strong metal-support interaction (SMSI). When Pt nanoparticles were loaded onto mesoporous supports made of Co<sub>3</sub>O<sub>4</sub>, NiO, MnO<sub>2</sub>, Fe<sub>2</sub>O<sub>3</sub>, and CeO<sub>2</sub> it was found that their activity for carbon monoxide oxidation was greatly enhanced relative to the support alone or Pt loaded onto inert mesoporous silica. This finding demonstrates that the interface of the metallic Pt nanoparticle and the oxide

support is able to produce turnovers that are orders of magnitude higher than the two materials separately.

When the same type of experiments were investigated with n-hexane as the reactant and macroporous  $\text{Al}_2\text{O}_3$ ,  $\text{TiO}_2$ ,  $\text{Nb}_2\text{O}_5$ ,  $\text{Ta}_2\text{O}_5$ , and  $\text{ZrO}_2$  were utilized as supports, it was found that the reaction selectivity was greatly altered depending on the catalytic support material.  $\text{TiO}_2$ ,  $\text{Nb}_2\text{O}_5$ , and  $\text{Ta}_2\text{O}_5$  (all of which are strong Lewis acids) were found to be much more selective for isomer production than the standard  $\text{SiO}_2$  mesoporous silica supported Pt nanoparticle catalyst.

Finally, an acidified mesoporous silica material was utilized as the support. This material was synthesized by using  $\text{AlCl}_3$  to modify the surface of mesoporous silica. This support was found to have no activity for hexane isomerization alone. However, when Pt nanoparticles were supported on the material, the activity and isomer selectivity in hexane reforming was increased several orders of magnitude as compared to the same nanoparticles supported on unmodified mesoporous silica.

This dissertation builds on the existing knowledge of known concepts in catalysis science such as structure sensitive reactions, the metal-support interaction, and acid-base chemistry. The results show how small changes in the active sites of a catalyst can create large changes in the catalytic chemistry. This research demonstrates how careful material control, characterization and reaction study can help to elucidate the molecular level components necessary to design efficient catalysts.

# Table of Contents

<b>Acknowledgements .....</b>	<b>iii</b>
<b>Chapter 1 Introduction.....</b>	<b>1</b>
1.1 Background and Motivation .....	2
1.2 The Need for Model Catalytic Systems .....	3
1.3 Covalent Metal Catalysis .....	4
1.4 Catalysis from Charge Flow .....	6
1.5 Summary of Dissertation .....	11
1.6 References .....	11
<b>Chapter 2 Experimental Methods .....</b>	<b>19</b>
2.1 Introduction.....	20
2.2 Synthetic Techniques .....	20
2.3 Characterization .....	27
2.4 Catalytic Measurements .....	30
2.5 References .....	33
<b>Chapter 3 High Structure Sensitivity of Vapor-phase Furfural Decarbonylation/Hydrogenation Reaction Network as a Function of Size and Shape of Pt Nanoparticles .....</b>	<b>34</b>
3.1 Introduction.....	35
3.2 Experimental.....	35
3.3 Results and Discussion .....	41
3.4 Conclusions .....	48
3.5 References .....	49
<b>Chapter 4 Reforming C6 Hydrocarbons over Model Pt Nanoparticle Catalysts .....</b>	<b>51</b>
4.1 Introduction.....	52
4.2 Experimental.....	52
4.3 Results .....	53
4.4 Discussion .....	61
4.5 Conclusions .....	63
4.6 References .....	63
<b>Chapter 5 Isomerization of n-Hexane Catalyzed by Supported Monodisperse PtRh Bimetallic Nanoparticles .....</b>	<b>66</b>
5.1 Introduction.....	67
5.2 Experimental.....	67
5.3 Results and Discussion .....	68
5.4 Conclusions .....	76
5.5 References .....	77
<b>Chapter 6 Enhanced CO Oxidation Rates at the Interface of Mesoporous Oxides and Pt Nanoparticles.....</b>	<b>78</b>
6.1 Introduction.....	79
6.2 Experimental.....	79
6.3 Results and Discussion .....	81
6.4 Conclusions .....	92
6.5 References .....	93

<b>Chapter 7 Designed Catalysts from Pt Nanoparticles Supported on Macroporous Oxides for Selective Isomerization of n-Hexane .....</b>	<b>97</b>
7.1 Introduction .....	98
7.2 Experimental .....	98
7.3 Results and Discussion .....	101
7.4 Conclusions .....	107
7.5 References .....	107
<b>Chapter 8 The Pathway to Total Isomer Selectivity: n-Hexane Conversion (Reforming) on Platinum Nanoparticles Supported on Aluminum Modified Mesoporous Silica (MCF-17) .....</b>	<b>111</b>
8.1 Introduction .....	112
8.2 Experimental .....	113
8.3 Results and Discussion .....	114
8.4 Conclusions .....	121
8.5 References .....	121
<b>Chapter 9 Summary and Outlook .....</b>	<b>124</b>
8.1 Summary of Dissertation .....	125
8.2 Future Research Directions .....	125
8.1 References .....	126

# Acknowledgements

This research was supported by the U.S. Department of Energy, Office of Basic Energy Sciences, under Contract No. DE-AC02-05CH11231. I would also like to express my gratitude to the Department of Chemistry, University of California, Berkeley; the Chemical Sciences Division, Lawrence Berkeley National Laboratory; and the Chevron Energy Corporation for funding.

I am sincerely appreciative to the many individuals who I have met and have contributed to my education in my four years at UC Berkeley. First, I would like to thank Professor Somorjai. I remember my first time speaking to him on the phone in May 2011. He asked me if there was any way I could finish my undergraduate studies early, because he had an exciting new reactor he wanted me to begin work on immediately. His passion for scientific discovery is always apparent and extremely contagious. I immediately knew he was the type of scientist I wanted to work with and learn from. Not only has he provided me with a strong foundational education from which to continue my scientific career, he has also been a constant advisor and mentor outside of the laboratory. Professor Somorjai sincerely cares about every one of his students. I will be forever grateful for his constant kindness, guidance and support. I also wish to thank Inger Coble for her immense support, and continuous assistance in handling nearly every problem that arises within the Somorjai group.

Working in the Somorjai group has been one of the most incredible and rewarding experiences of my life. I have been extremely fortunate to work with a group of people who are not only exceedingly talented and intelligent, but whom I consider my very close friends. I would like to thank Chris Thompson, Walter Ralston, G r me Melaet, Griffin Kennedy, Andras "Bandi" Sapi, Selim Alayoglu, Zhongwei Zhou, Kwangjin An, Vladimir Pushkarev, Robert Baker, Fudong Liu, Tyler Hurlburt, Rong "Rocky" Ye, Antoine Hervier, Wenchi Liu, FeiFei Shi, and Yonatan Horowitz, for all being the best group of friends and coworkers I have ever had. I would like to extend an additional thank you to Selim Alayoglu and G r me Melaet. These two have not only been very close friends, but have provided constant scientific mentorship. If not for them, I would not be the scientist I am today. I would also like to extend an additional thank you to Walter Ralston and G r me for keeping graduate school fun. I will never forget our Friday and Saturday night "Catalysis Group" meetings.

Finally, I would like to thank my family. My mother and father have provided endless support for me, not only during my time at Berkeley, but throughout my entire life. Ever since I could talk I knew I wanted to be a chemist. My parents supported me through 21 years of school and pushed me to always do my best, even when I didn't want to, and for that I will be forever grateful. I wish to thank my girlfriend Kiona Padilla, who has made my life exponentially more enjoyable. I have cherished the time I have spent with her, and I look forward to our future together. Lastly, I wish to thank my daughter Alexis. Pursuing a PhD in Chemistry at Berkeley, while being a single father 3,000 miles away from any family is not easy. However, together, we made it work. Alexis, you are the reason I pursued this degree, you are the reason I strive to be better, you are my inspiration. Thank you for everything.





# Chapter 1

## Introduction

### Abstract

This chapter will discuss the techniques utilized to accomplish the research undertaken in this dissertation. Techniques discussed will be divided into synthetic, characterization, and reaction studies. Synthetic techniques include nanoparticle and catalyst support material synthesis. Characterization includes various types of transmission electron microscopy (TEM) and ambient pressure x-ray photoelectron spectroscopy (AP-XPS). The reaction studies portion of this chapter will describe the home-built high pressure reactor system in depth, along with the standard experimental procedures and operating parameters.

\* This chapter includes material from Musselwhite, N.; Somorjai, G.A. *Top. Catal.* **2014**, 58, 184-189. — reproduced with permission, copyright 2014 Springer Science+Business Media, LLC.

## 1.1 Background and Motivation

One of the most challenging responsibilities for scientists today is how to provide clean, renewable energy for the world's ever-growing population. Current global energy consumption is at an all-time high, and is growing exponentially, as shown in Figure 1.<sup>1</sup> Heterogeneous catalysis provides a promising means to solve this energy crisis. Catalytic reactions are utilized in numerous applications ranging from cleaning automobile emissions (catalytic converters) to producing more efficient fuels (oil refining) to sustaining the world's agricultural supply through ammonia synthesis (Haber process).<sup>2</sup> The need to efficiently use resources is paramount to controlling the energy problem in our society. In this regard, catalysis must be accomplished with high activity (overall products formed) and selectivity (percentage of desired product in a multi-product reaction).

Catalysis science has a somewhat empirical history. Trial and error spawned advancements and when discoveries were made there was seldom investigation as to why things functioned more efficiently.<sup>2</sup> With the advent of modern surface science, molecular level studies were undertaken on the nature of the surfaces of catalytic metals. However, the information about these catalytic metals was determined in Ultra-High Vacuum (UHV) with single crystal metals, nowhere close to the conditions of a functioning industrial catalyst.<sup>2</sup> Through the bridging of catalysis science and surface science, the problems of real world catalysts can be systematically solved using the real working conditions of industrial catalysis. Garnering a fundamental understanding of the molecular level factors that control catalytic activity and selectivity, and elucidating what components are necessary for efficient catalysis have been the motivation of my Ph.D. research.

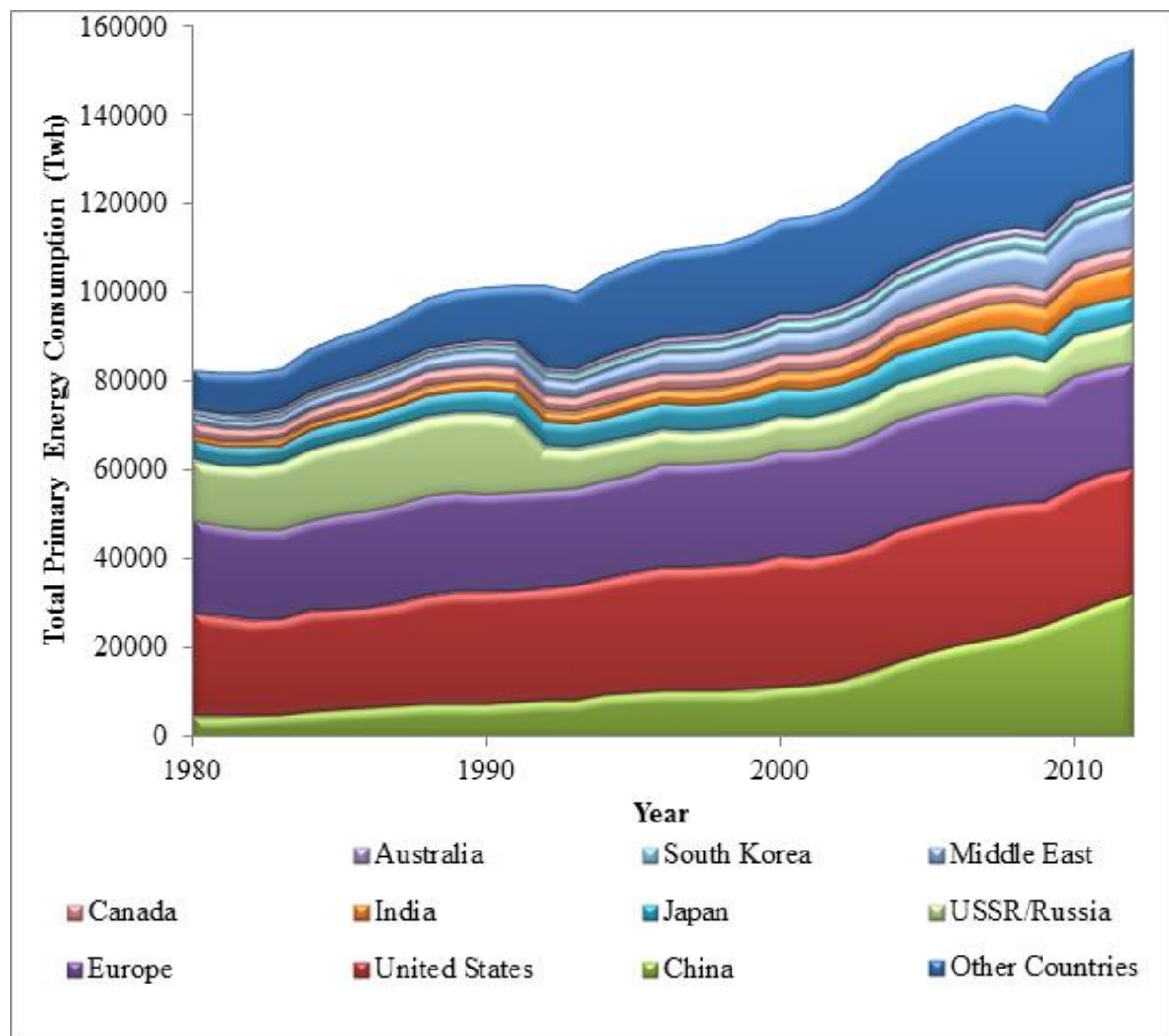


**Figure 1.** World total primary energy usage statistics for the last 35 years. <sup>1</sup>

## 1.2 The Need for Model Catalytic Systems

In order to maximize the performance of a catalyst, a molecular level understanding of the role of each individual component and also of the tandem chemistry of the different components in the reaction of interest is essential. In order to fully understand the science of catalysis, the entire sequence of the catalytic steps (i.e. adsorption, surface diffusion, molecular transformations, and finally desorption) must be thoroughly studied.<sup>3-7</sup> In recent years, the experimental techniques for studying catalysis and surface science have grown rapidly.<sup>8,9</sup> Tools, such as sum frequency generation (SFG) spectroscopy, ambient pressure X-ray photoelectron (AP-XPS), X-ray Absorption Spectroscopy (XAS) and a variety of other techniques, allow for in

situ molecular level studies of the fundamental processes which govern complex catalytic reactions.<sup>10,11</sup>

Industrial catalysts utilize a variety of constituent materials, which are carefully controlled to produce the highest possible selectivity and activity for the desired chemical transformation.<sup>2,12-14</sup> The components of these catalysts can be highly varied and complex: for example, bimetallic platinum/iridium loaded acidified gamma alumina, for hydrocarbon conversion to high octane fuels; and cobalt supported on zinc oxide with a potassium promoter, for fuel synthesis from CO and H<sub>2</sub> (Fischer–Tropsch synthesis).<sup>15-17</sup> Each component of the catalyst has a desired function for a specific reaction. Unfortunately, to quantitatively study these complex systems with the techniques listed above can be extremely difficult. Therefore, in order to determine the components of an effective catalyst, each variable must be controlled independently, without the influence of other catalytic components. This can be accomplished through the use of model catalysts, or catalysts that lack many components of their industrial counterparts, but allow for focus on one specific variable that is to be evaluated.

### 1.3 Covalent Metal Catalysis

There have been many studies aimed at understanding reactions catalyzed by metal surfaces at a molecular level. These studies range from UHV experiments with single crystals to experiments on model nanoparticle catalysts.<sup>18-22</sup> The different types of model catalyst systems used in studies of metal catalysis in surface science are summarized in Figure 2.

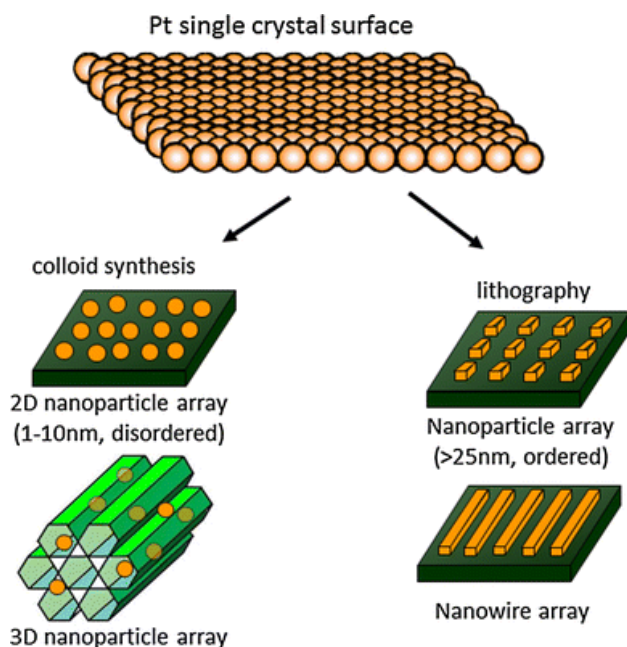


**Figure 2.** The types of model metal catalyst systems utilized in surface science. Single crystals are the most fundamental, with different types of model nanoparticle systems being one step closer to industrial catalysts.

---

Single crystal studies have given vast information about the fundamental chemical processes on metal surfaces for a great number of important reactions including: Fischer–Tropsch chemistry, ammonia synthesis, and the refining of hydrocarbons.<sup>23-28</sup> From single crystal studies, many important discoveries were made that aided in advancing the field of heterogeneous catalysis. In fact, these studies have greatly enhanced the knowledge of catalytic mechanisms in numerous important reactions.<sup>26,29-31</sup> Also, several surface phenomena have been discovered by UHV studies, for example the unique adsorption of the ethylidene species, the effect of surface atom ensemble, and many others.<sup>32-34</sup> Another important concept is the idea of surface structure sensitivity; while discovered with supported catalysts, it was unequivocally demonstrated with single crystals.<sup>35-40</sup> Structure sensitivity in heterogeneous catalysis suggests that specific surface sites are preferred for the catalysis of certain chemical reactions. For example, bond breaking exchange reactions of many diatomic molecules were found to be more efficient at step and kink sites, as represented in Figure 3.<sup>41-48</sup> Ambient pressure scanning tunneling microscopy (STM) has proven to be an invaluable tool in learning about metal surfaces under actual reaction conditions. One such example is the reversible restructuring of Pt stepped surfaces (557) under carbon monoxide or hydrogen oxidation reaction conditions.<sup>49,50</sup>

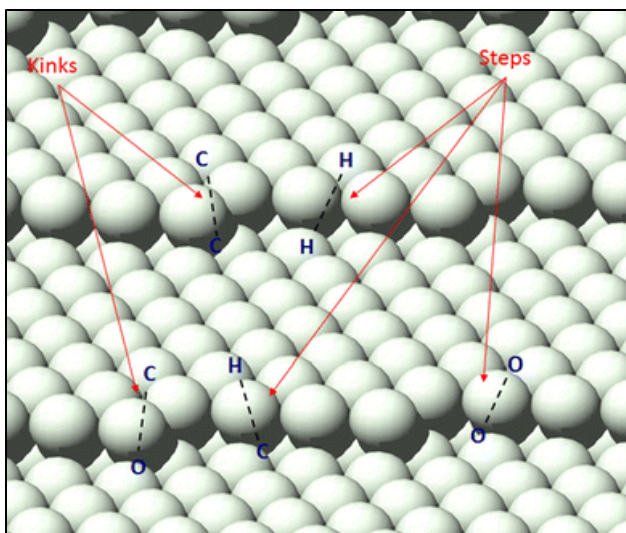


**Figure 3.** Representative image for bond scission at surface step and kink sites. Through the use of molecular beam surface scattering experiments it has been discovered that the dissociation of H–H, C–H, C–C, C=O, and O=O bonds occur preferentially at atomic steps and kinks, while the terrace sites are much less active.

Current studies in model systems to investigate the chemistry of metal catalysis lie in nanoparticles, which more closely resemble actual industrial catalysts. By using colloidal synthetic techniques, the size, shape, and metal composition of the nanoparticles can be precisely controlled. The understanding of how these variables affect the chemistry of the system is crucial to the science of catalysis. One such example is the effect of nanoparticle size on reaction activity and selectivity. It was found that the activity for both benzene and toluene hydrogenation

is dependent on the size of the nanoparticle.<sup>51</sup> The selectivity of reactions has also been found to be greatly affected by particle size. For example, the product selectivity in the platinum catalyzed hydrogenation of pyrrole can be altered by changing nanoparticle size.<sup>52</sup> The product selectivity versus Pt nanoparticle size and shape is plotted in Figure 4. Pyrrole reacting with hydrogen yields four major products, pyrrolidine, n-butylamine and butane and ammonia, via the scheme shown in Figure 4. By increasing the size of the platinum nanoparticle catalyst (from 1 to 5 nm), the selectivity of the reaction was shifted from producing pyrrolidine and n-butylamine to exclusively n-butylamine.

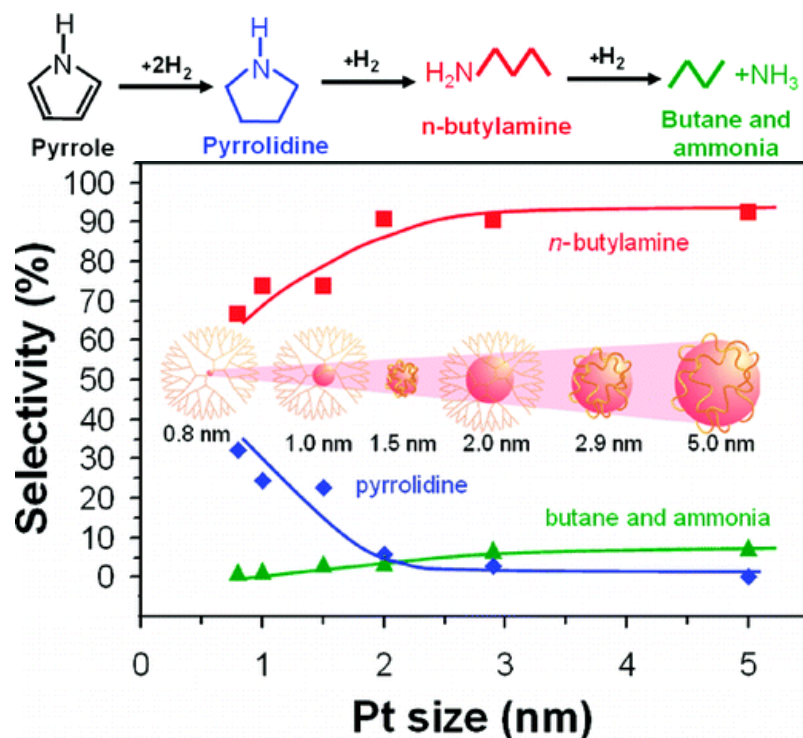


**Figure 4.** Pyrrole hydrogenation reaction selectivity as a function of nanoparticle size.

#### 1.4 Catalysis from Charge Flow

The first fundamental chemical studies of surface science in catalysis focused primarily on what was considered the “active” catalyst, or the metal component. However, industrial catalysts normally consist of a minimum of two primary components: the metal and the support. The support, which is usually an oxide, is necessary to provide thermal stability and help with dispersion of the catalyst. The idea that different support materials change reaction activity and selectivity has been known in catalysis science for decades, beginning with work done by Schwab in the late 1960s.<sup>53-57</sup> However, the effect was only quantified and understood chemically and molecularly for the first time with inverse catalysis studies.<sup>58-61</sup> In these studies sub-monolayer metal oxides were evaporated onto a Rh foil, and the rate of methane formation from the reaction between CO<sub>2</sub> and H<sub>2</sub> was measured. A summary of the collected data is shown in the plot in Figure 5. The plot in Figure 5a displays the activity of both ethylene and CO<sub>2</sub> hydrogenation versus the coverage of TiO<sub>2</sub>. Ethylene hydrogenation (which is active only on Rh

metal) is used as a means to quantify the surface area of Rh, which decreases linearly with the addition of TiO<sub>2</sub>. The CO<sub>2</sub> hydrogenation activity follows a volcano type behavior, reaching a maximum around 0.5 monolayers of TiO<sub>2</sub> coverage. This sharp increase in activity was attributed to the strong metal-support interaction (SMSI) between the rhodium metal and the TiO<sub>2</sub> metal oxide. The same type of experiment was run for several different metal oxides and a trend was found between the catalytic activity and the electronegativity (which is related to the Lewis acidity) of the oxide. This trend is plotted in Figure 5b.

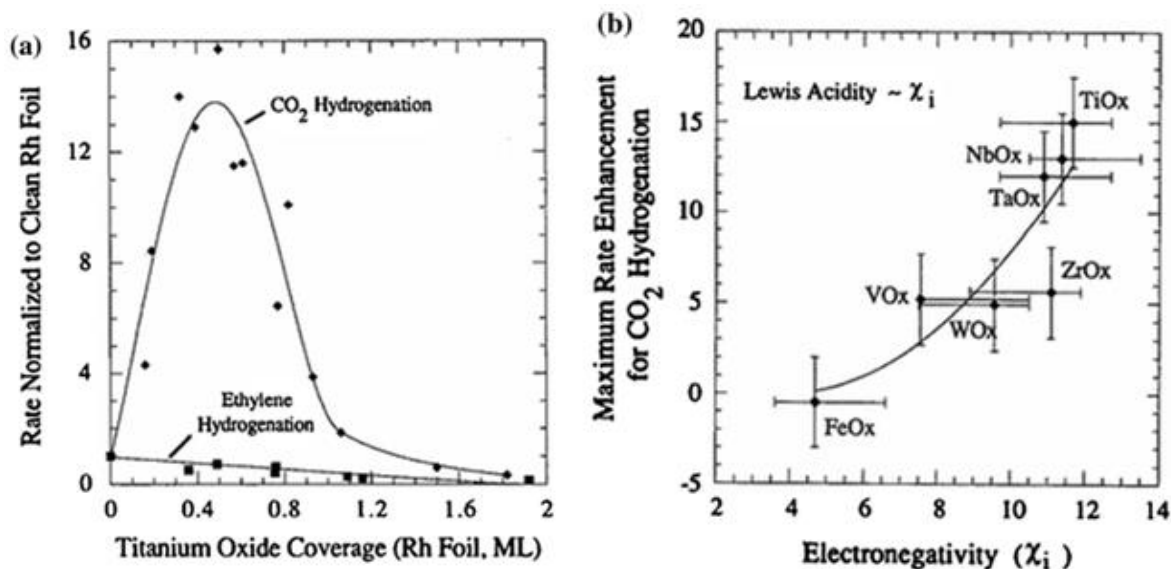


**Figure 5.** a) A plot displaying the methane formation activity for various TiO<sub>2</sub> coverages on Rh foil.<sup>58</sup> It can be seen by ethylene hydrogenation (which only occurs on Rh metal) that the Rh surface area is decreasing as TiO<sub>2</sub> coverage increases. However, the CO<sub>2</sub> hydrogenation follows a volcano type pattern, due to the strong metal-support interaction (SMSI), reaching a maximum at 0.5 monolayers of TiO<sub>2</sub> coverage. b) The trend between the maximum rate enhancement for CO<sub>2</sub> hydrogenation for different metal oxide species and the electronegativity (related to Lewis acidity) of that metal oxide.

The strong metal-support interaction has been studied extensively in catalysis science.<sup>62-</sup>  
<sup>64</sup> The movement of charged species (i.e. electrons, protons, etc.) from catalyst to reactant which then forms a product, is known as charge flow catalysis.<sup>65</sup> This process was quantified through the use of a Pt/TiO<sub>2</sub> Schottky diode to measure hot electron flow in catalytic reactions.<sup>65-68</sup> The construction of this nanodiode is accomplished by creating an interface of a catalytic metal and a semiconductor. This forms a Schottky barrier ( $E_{SB}$ ), which is equal to the difference between the work function of the metal and the semiconductor's electron affinity. An energy diagram of a catalytic metal-semiconductor diode is shown, as well as a depiction of a cross-section of the

Pt/TiO<sub>2</sub> diode, in Figure 6a. This experimental setup allows for collection of any electron with an energy higher than the Schottky barrier. Both hydrogen and carbon monoxide oxidation were tested catalytically on this system, and in both cases the activation energy of the reaction was found to correlate with the activation energy of the reaction extrapolated from the collected chemicurrent, shown in Figure 6b and 6c. This suggests that the catalysis in this system is strongly related to the flow of electrons.

Protons are also capable of producing charge flow, which can control catalytic chemistry. The most well-known example of this type of chemistry is in zeolites.<sup>69-72</sup> Through the use of acidic sites, zeolites are capable of stabilizing cationic intermediate species, which when used in tandem with covalent metal chemistry can create excellent catalysts for processes such as hydrocarbon reforming, fluid catalytic cracking, and other important industrial reactions.<sup>73,74</sup>

Charge flow catalytic chemistry and tandem catalysis have been shown to control catalytic activity as well as selectivity.<sup>75-77</sup> For example, the Pt catalyzed chemistry of furfural has been shown to change in selectivity when the support material is changed.<sup>78</sup> It was found that the charge transfer from the TiO<sub>2</sub> support on a Pt nanoparticle/TiO<sub>2</sub> catalyst controls the product selectivity of the reaction via an acid–base mechanism. When SiO<sub>2</sub> was used as a support for Pt nanoparticles the decarbonylation product, furan, showed the highest selectivity. However, when TiO<sub>2</sub> was used as a support for UV/ozone cleaned Pt nanoparticles, a 50-fold enhancement in furfuryl alcohol, the hydrogenation product, was obtained, as shown in Figure 7a. Through the use of SFG spectroscopy it was found that a charge-transfer reaction involving a surface intermediate species adsorbed onto a Ti cation adjacent to an oxygen vacancy was responsible for the high production of furfuryl alcohol. This intermediate species is shown in Figure 7b. The intermediate is formed on the support and then subsequently hydrogenated via atomic hydrogen, spilling over from the Pt surface, to form the alcohol product, shown in Figure 7c.



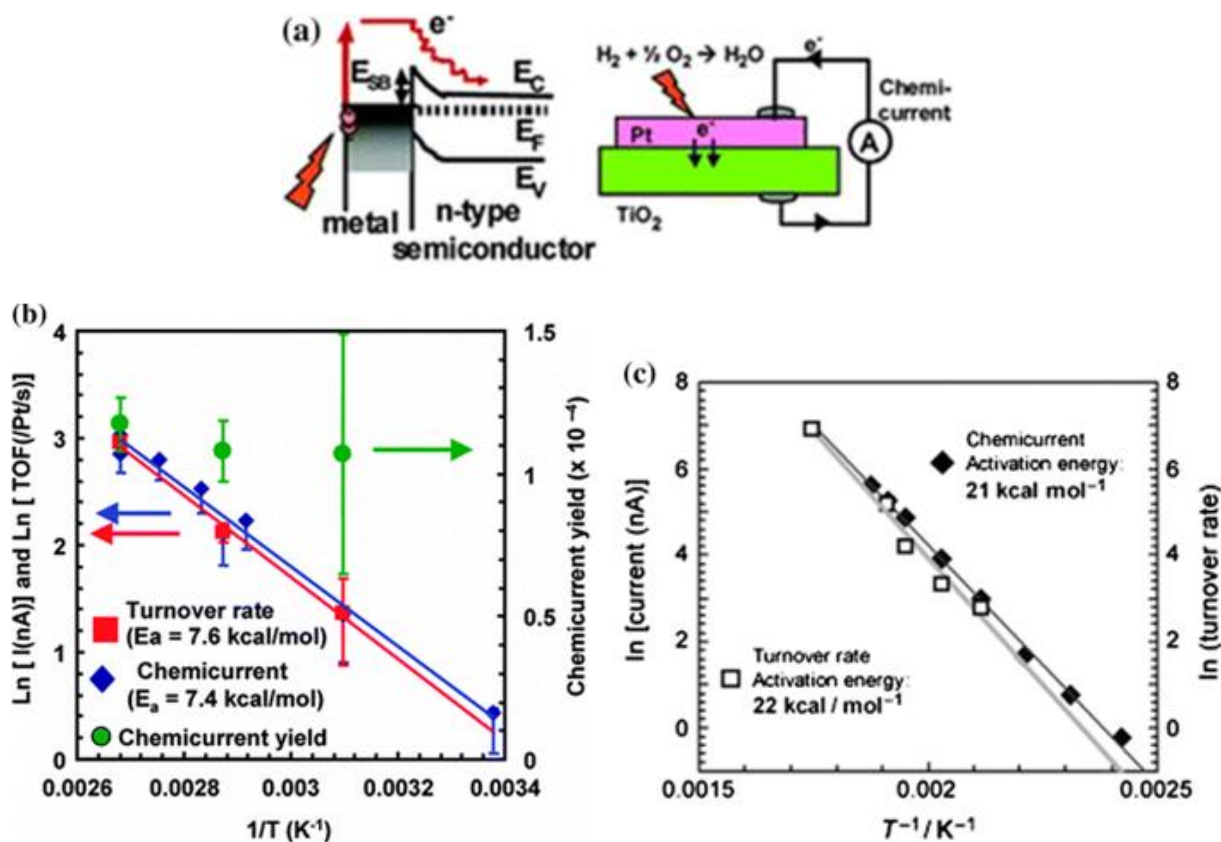


**Figure 6.** a) The energy diagram of a catalytic metal–semiconductor diode is shown, as well as a depiction of a cross-section of the Pt/TiO<sub>2</sub> diode. The interface of the metal and semiconductor creates a Schottky barrier ( $E_{SB}$ ), which is equal to the difference between the work function of the metal and the semiconductor’s electron affinity. b) A plot displaying the correlation between the chemi-current and the turnover measurements on a Pt/TiO<sub>2</sub> diode for the hydrogen oxidation reaction. Both processes give similar activation energies, which implies that hot electron generation under hydrogen oxidation is proportional to the catalytic turnover rate. c) A similar correlation plot for the oxidation of carbon monoxide.

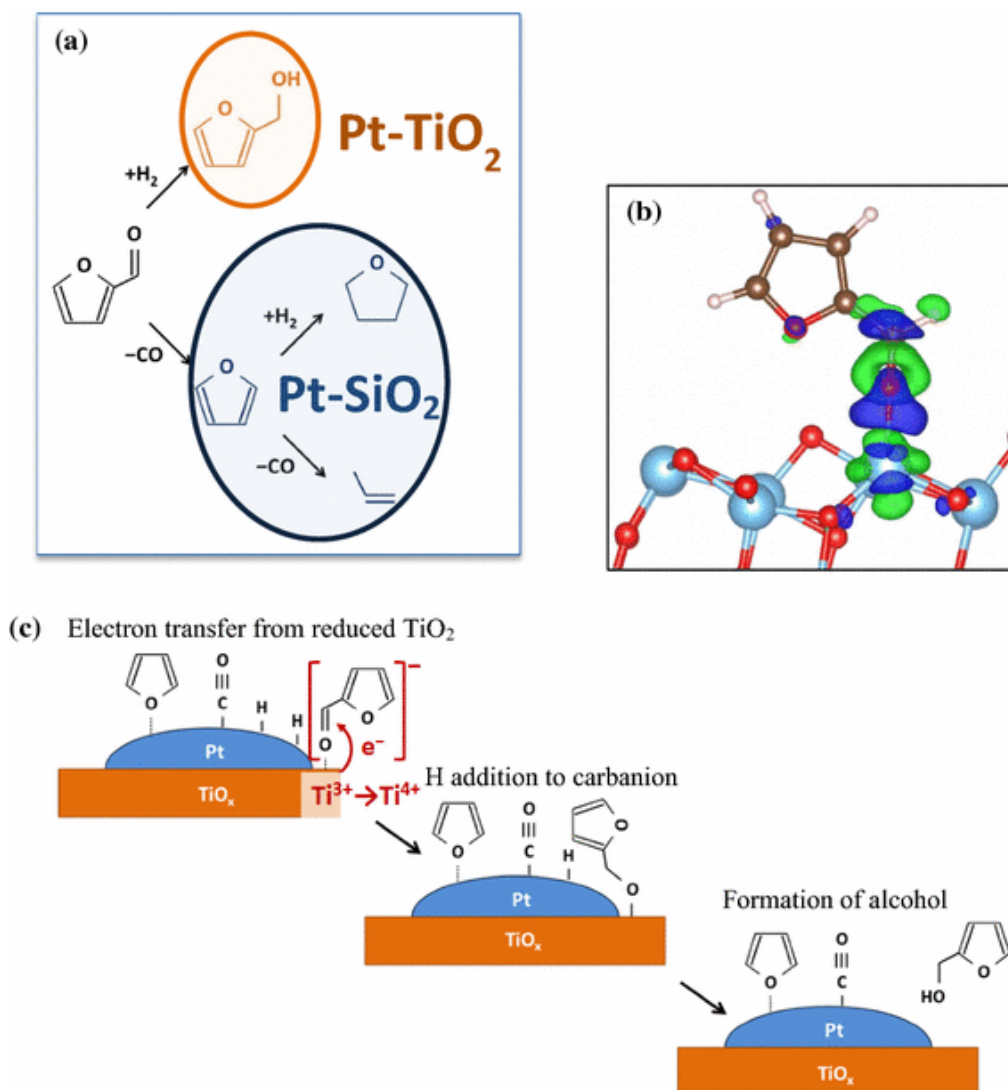


**Figure 7.** a) The product selectivity for Pt catalyzed furfural chemistry on two different oxide supports.  $\text{TiO}_2$  as a support was highly selective for the hydrogenation product, furfuryl alcohol.  $\text{SiO}_2$  as a support favored furan, the decarbonylation product. b) Diagram of furfural binding to a Ti cation near an O-vacancy site on anatase  $\text{TiO}_2$  (101), and the charge transfer induced by the surface binding interaction. The filled cyan, red, brown and white circles show the Ti, O, C and H atoms, respectively. The green contour shows the electron charge loss, and the blue contour shows the electron charge gain induced by the surface binding. c) The proposed mechanism for the formation of furfural alcohol at the  $\text{Pt/TiO}_2$  interface. The mechanism involves the electron transfer from reduced  $\text{TiO}_2$  into the surface adsorbed furfural species, followed by hydrogen addition to form the alcohol species.

## 1.5 Summary of Dissertation

### 1.5.1 Experimental Methods

The experimental methods utilized in this doctoral research are discussed in Chapter 2. The topics include: material synthesis, characterization, and catalytic measurements. Material synthesis will explain the procedures for synthesizing uniform metal nanoparticles, with a controlled size, shape, and composition. This section will also discuss synthesis of the mesoporous oxides used as catalyst support materials. The characterization portion of this chapter will discuss the techniques utilized to study the synthesized materials. Special focus will be given to Transmission Electron Microscopy (TEM) and Ambient Pressure X-ray Photoelectron Spectroscopy (AP-XPS), as they were most frequently utilized in this research. The section on catalytic measurement contains a description of the home-built high pressure – high temperature catalytic flow reactor system, as well as the common procedures for running catalytic evaluations of the model systems.

### 1.5.2 Effects of the Nanoparticle (Size and Composition)

Chapters 3, 4 and 5 describe how catalytic activity and selectivity can be altered by varying the properties of nanoparticle catalysts. In Chapter 3, the Pt catalyzed chemistry of vapor phase furfural was studied, and Pt nanoparticle size is shown to have a marked effect on product selectivity.<sup>79</sup> In Chapter 4, the size effect of Pt nanoparticles was studied with various C<sub>6</sub> hydrocarbons.<sup>80</sup> This chapter paves the way for the topic of n-hexane reforming, a reaction that I focused on heavily during my Ph.D. research. Chapter 5 investigates the effect of Rh composition in Pt<sub>x</sub>Rh<sub>1-x</sub> bimetallic nanoparticles, which is an analogue to the use of promoter metals to obtain higher activity in industrial hydrocarbon reforming catalysts.<sup>15</sup>

### 1.5.3 Effects of the Support (Strong Metal-Support Interaction and Acid-Base Catalysis)

In Chapters 6, 7 and 8, the effect of the catalytic support on reaction activity and selectivity was studied. In these experiments, nanoparticle size, shape and composition were held constant in order to study the effect of the mesoporous support material on the reaction. In Chapter 6, Pt nanoparticles were loaded onto several types of mesoporous oxides and their activity in CO oxidation was studied.<sup>81</sup> In Chapter 7, macroporous oxides were synthesized, loaded with Pt nanoparticles, and evaluated in n-hexane isomerization reactions.<sup>82</sup> Chapter 8 discusses hexane reforming over an aluminum modified mesoporous silica catalyst, which causes the isomer production of the catalyst to be greatly enhanced.<sup>83</sup> Chapter 9 summarizes the work in this thesis and gives a brief outlook to the future.

## 1.6 References

1. International Energy Statistics. *U. S. Energy Information Administration*. U.S. Department of Energy, Washington D.C. **2014**.
2. Somorjai, G. A.; Li, Y. *Introduction to Surface Chemistry and Catalysis*; Wiley: New York, **2010**.
3. Ertl, G.; Freund, H. J. Catalysis and Surface Science. *Phys. Today* **1999**, 52, 32-38.

4. Campbell, C. T. Ultrathin Metal Films and Particles on Oxide Surfaces: Structural, Electronic and Chemisorptive Properties. *Surf. Sci. Rep.* **1997**, 27, 1-111.
5. Somorjai, G. A.; Park, J. Y. Molecular Factors of Catalytic Selectivity. *Angew. Chem., Int. Ed.* **2008**, 47, 9212-9228.
6. Weckhuysen, B. M. Snapshots of a Working Catalyst: Possibilities and Limitations of in situ Spectroscopy in the Field of Heterogeneous Catalysis. *Chem. Commun.* **2002**, 97-101.
7. Tinnemans, S. J.; Mesu, G. J.; Kervinen, K.; Visser, T.; Nijhuis, T. A.; Beale, A. M.; Keller, D. E.; van der Eerden, A. M. J.; Weckhuysen, B. M. Combining Operando Techniques in One Spectroscopic-Reaction Cell: New Opportunities for Elucidating the Active Site and Related Reaction Mechanism in Catalysis. *Catal. Today* **2006**, 113, 3-15.
8. Alayoglu, S.; Krier, J. M.; Michalak, W. D.; Zhu, Z.; Gross, E.; Somorjai, G. A. In Situ Surface Reaction Probe Studies with Model Nanoparticle Catalysts. *ACS Catal.* **2012**, 2, 2250-2258.
9. Somorjai, G. A.; Aliaga, C. Molecular Studies of Model Surfaces of Metals from Single Crystals to Nanoparticles under Catalytic Reaction Conditions. Evolution from Prenatal and Postmortem Studies of Catalysts. *Langmuir* **2010**, 26, 16190-16203.
10. Su, X.; Cremer, P. S.; Shen, Y. R.; Somorjai, G. A. High Pressure CO Oxidation on Pt(111) Monitored with Infrared-Visible Sum Frequency Generation (SFG). *J. Am. Chem. Soc.* **1997**, 119, 3994-4000.
11. Somorjai, G. A.; McCrea, K. R. Sum Frequency Generation: Surface Vibrational Spectroscopy Studies of Catalytic Reactions on Metal Single-Crystal Surfaces. *Adv. Catal.* **2000**, 45, 385-438.
12. Ertl, G.; Knozinger, H.; Weitkamp, J. *Handbook of Heterogeneous Catalysis*; Wiley: New York, **2008**.
13. Somorjai, G. A. The Development of Molecular Surface Science and the Surface Science of Catalysis: The Berkeley Contribution. *J. Phys. Chem. B* **2000**, 104, 2969-2979.
14. Boudart, M. Turnover Rates in Heterogeneous Catalysis. *Chem. Rev.* **1995**, 95, 661-666.
15. Musselwhite, N.; Alayoglu, S.; Melaet, G.; Pushkarev, V. V.; Lindeman, A. E.; An, K.; Somorjai, G. A. Isomerization of *n*-Hexane Catalyzed by Supported Monodisperse PtRh Bimetallic Nanoparticles. *Catal. Lett.* **2013**, 143, 907-911.
16. Na, K.; Musselwhite, N.; Cai, X.; Alayoglu, S.; Somorjai, G. A. Promotional Effects of Mesoporous Zeolites with Pt Nanoparticle Catalysts During Reforming of Methylcyclopentane. *J Phys Chem A* **2014**, 118, 8446-8452.

17. Melae, G.; Ralston, W. T.; Li, C. S.; Alayoglu, S.; An, K.; Musselwhite, N.; Kalkan, B.; Somorjai, G. A. Evidence of Highly Active Cobalt Oxide Catalyst for the Fischer-Tropsch Synthesis and CO<sub>2</sub> Hydrogenation. *J. Am. Chem. Soc.* **2014**, *136*, 2260-2263.
18. Somorjai, G. A.; Frei, H.; Park, J. Y. Advancing the Frontiers in Nanocatalysis, Biointerfaces, and Renewable Energy Conversion by Innovations of Surface Techniques. *J. Am. Chem. Soc.* **2009**, *131*, 16589-16605.
19. Zhu, J.; Somorjai, G. A. Formation of Platinum Silicide on a Platinum Nanoparticle Array Model Catalyst Deposited on Silica during Chemical Reaction. *Nano Lett.* **2001**, *1*, 8-13.
20. Song, H.; Rioux, R. M.; Hoefelmeyer, J. D.; Komor, R.; Niesz, K.; Grass, M.; Yang, P.; Somorjai, G. A. Hydrothermal Growth of Mesoporous SBA-15 Silica in the Presence of PVP-Stabilized Pt Nanoparticles: Synthesis, Characterization, and Catalytic Properties. *J. Am. Chem. Soc.* **2006**, *128*, 3027-3037.
21. Konya, Z.; Puentes, V. F.; Kiricsi, I.; Zhu, J.; Alivisatos, A. P.; Somorjai, G. A. Nanocrystal Templating of Silica Mesopores with Tunable Pore Sizes. *Nano Lett.* **2002**, *2*, 907-910.
22. Rioux, R. M.; Song, H.; Hoefelmeyer, J. D.; Yang, P.; Somorjai, G. A. High-Surface-Area Catalyst Design: Synthesis, Characterization, and Reaction Studies of Platinum Nanoparticles in Mesoporous SBA-15 Silica. *J. Phys. Chem. B* **2005**, *109*, 2192-2202.
23. Asscher, M.; Somorjai, G. A. The Remarkable Surface Structure Sensitivity of the Ammonia Synthesis over Rhenium Single Crystals. *Surf. Sci.* **1984**, *143*, L389-L392.
24. Asscher, M.; Carrazza, J.; Khan, M. M.; Lewis, K. B.; Somorjai, G. A. The Ammonia Synthesis over Rhenium Single-Crystal Catalysts: Kinetics, Structure Sensitivity, and Effect of Potassium and Oxygen. *J. Catal.* **1986**, *98*, 277-287.
25. Geerlings, J. J. C.; Wilson, J. H.; Kramer, G. J.; Kuipers, H. P. C. E.; Hoek, A.; Huisman, H. M. Fischer-Tropsch Technology - From Active Site to Commercial Process. *Appl. Catal. A* **1999**, *186*, 27-40.
26. Oosterbeek, H. Bridging the Pressure and Material Gap in Heterogeneous Catalysis: Cobalt Fischer-Tropsch Catalysts from Surface Science to Industrial Application. *Phys. Chem. Chem. Phys.* **2007**, *9*, 3570-3576.
27. Davis, S. M.; Somorjai, G. A. In *Hydrocarbon Conversion over Metal Catalysts; The Chemical Physics of Solid Surfaces and Heterogeneous Catalysis: Fundamental Studies of Heterogeneous Catalysis*; Elsevier: Amsterdam, 1982; Vol. 4, .
28. Goodman, D. W. Ethane Hydrogenolysis over Single Crystals of Nickel: Direct Detection of Structure Sensitivity. *Surf. Sci.* **1982**, *123*, L679-L685.

29. Strongin, D. R.; Bare, S. R.; Somorjai, G. A. The Effects of Aluminium Oxide in Restructuring Iron Single Crystal Surfaces for Ammonia Synthesis. *J. Catal.* **1987**, *103*, 289-301.
30. Strongin, D. R.; Somorjai, G. A. In *A Surface Science and Catalytic Study of the Effects of Aluminum Oxide and Potassium on the Ammonia Synthesis over Iron Single-Crystal Surfaces*; Jennings, J. R., Ed.; Catalytic Ammonia Synthesis: Fundamentals and Practice; Plenum: New York, **1991**.
31. Goodman, D. W. Catalytic Studies with Metal Single Crystals. *Ann. Rev. Phys. Chem.* **1986**, *37*, 425-457.
32. Sachtler, J. W. A.; Somorjai, G. A. Influence of Ensemble Size on CO Chemisorption and Catalytic n-Hexane Conversion by Au-Pt(111) Bimetallic Single-Crystal Surfaces. *J. Catal.* **1983**, *81*, 77-94.
33. Stair, P. C.; Somorjai, G. A. The Adsorption of Hydrocarbons on Platinum Studied by Low-Energy Electron Diffraction Intensities. The Ordered (2x2) Overlayers of Acetylene and Ethylene on the (111) Crystal Face of Platinum. *J. Chem. Phys.* **1977**, *66*, 2036-2044.
34. Gland, J. L.; Somorjai, G. A. Low Energy Electron Diffraction and Work Function Studies of Benzene, Naphthalene and Pyridine Adsorbed on Pt(111) and Pt(100) Single Crystal Surfaces. *Surf. Sci.* **1973**, *38*, 157-186.
35. Boudart, M. In *Catalysis by Supported Metals*; Eley, D. D., Ed.; Advances in Catalysis and Related Subjects; Elsevier: New York, **1969**; Vol. 20, pp 153-166.
36. Boudart, M.; Djega-Mariadassou, G. *Kinetics of Heterogeneous Catalytic Reactions*; Princeton University Press: Princeton, **1984**.
37. Musselwhite, N.; Somorjai, G. A. Investigations of Structure Sensitivity in Heterogeneous Catalysis: From Single Crystals to Monodisperse Nanoparticles. *Top. Catal.* **2013**, *56*, 1277-1283.
38. Guthrie, W. L.; Sokol, J. D.; Somorjai, G. A. The Decomposition of Ammonia on the Flat (111) and Stepped (557) Platinum Single Crystal Surfaces. *Surf. Sci.* **1981**, *109*, 390-418.
39. Engstrom, J. R.; Goodman, D. W.; Weinberg, W. H. The Reaction of Cyclopropane, Methylcyclopropane and Propylene with Hydrogen over the (111) and (110)-(1x2) Surfaces of Iridium. *J. Phys. Chem. B* **1990**, *94*, 396-409.
40. Gillespie, W. D.; Herz, R. K.; Petersen, E. E.; Somorjai, G. A. The Structure Sensitivity of n-Heptane Dehydrocyclization and Hydrogenolysis Catalyzed by Platinum Single Crystals at Atmospheric Pressure. *J. Catal.* **1981**, *70*, 147-159.

41. Ferrer, S.; Rojo, J. M.; Salmeron, M.; Somorjai, G. A. The Role of Irregularities (Steps, Kinks) and Point Defects on the Chemical Reactivity of Solid Surfaces. *Philos. Mag. A* **1982**, *45*, 261-269.
42. Koel, B. E.; White, J. M.; Goodman, D. W. The Adsorption and Decomposition of Ethylene on Ni(100). *Chem. Phys. Lett.* **1982**, *88*, 236-242.
43. Lin, T. H.; Somorjai, G. A. Modulated Molecular Beam Scattering of CO and NO from Pt(111) and the Stepped Pt(557) Crystal Surfaces. *Surf. Sci.* **1981**, *107*, 573-585.
44. Lin, T. H.; Somorjai, G. A. Angular and Velocity Distributions of HD Molecules Produced by the H<sub>2</sub>-D<sub>2</sub> Exchange Reaction on the Stepped Pt(557) Surface. *J. Chem. Phys.* **1984**, *81*, 704-709.
45. Lin, T. H.; Somorjai, G. A. The Dynamics of Atomic Hydrogen and Deuterium Recombination on the Stepped Platinum(557) Crystal Face. *J. Phys. Chem.* **1985**, *89*, 135-139.
46. Somorjai, G. A.; Van Hove, M. A. Surface Restructuring as a Mechanism for Bond Breaking and Catalytic Reactions at Metal Surfaces. *Catal. Lett.* **1988**, *1*, 433-437.
47. Falicov, L. M.; Somorjai, G. A. Correlation Between Catalytic Activity and Bonding and Coordination Number of Atoms and Molecules on Transition Metal Surfaces: Theory and Experimental Evidence. *Proc. Natl. Acad. Sci. U. S. A.* **1985**, *82*, 2207-2211.
48. Somorjai, G. A. Progress in Our Understanding of Structure Bonding and Reactivity of Metal Surfaces and Adsorbed Monolayers at the Molecular Level: A 25 Year Perspective. *Prog. Surf. Sci.* **1995**, *50*, 3-29.
49. Tao, F.; Dag, S.; Wang, L. W.; Liu, Z.; Butcher, D. R.; Bluhm, H.; Salmeron, M.; Somorjai, G. A. Break-Up of Stepped Platinum Catalyst Surfaces by High CO Coverage. *Science* **2010**, *327*, 850-853.
50. Zhu, Z.; Melaet, G.; Axnanda, S.; Alayoglu, S.; Liu, Z.; Salmeron, M.; Somorjai, G. A. Structure and Chemical State of the Pt(557) Surface during Hydrogen Oxidation Reaction Studied by in Situ Scanning Tunneling Microscopy and X-ray Photoelectron Spectroscopy. *J. Am. Chem. Soc.* **2013**, *135*, 12560-12563.
51. Pushkarev, V. V.; An, K.; Alayoglu, S.; Beaumont, S. K.; Somorjai, G. A. Hydrogenation of Benzene and Toluene over Size Controlled Pt/SBA-15 Catalysts: Elucidation of the Pt Particle Size Effect on Reaction Kinetics. *J. Catal.* **2012**, *292*, 64-72.
52. Kuhn, J. N.; Huang, W.; Tsung, C. K.; Zhang, Y.; Somorjai, G. A. Structure Sensitivity of Carbon-Nitrogen Ring Opening: Impact of Platinum Particle Size From Below 1 to 5 nm Upon Pyrrole Hydrogenation Product Selectivity Over Monodisperse Platinum Nanoparticles Loaded onto Mesoporous Silica. *J. Am. Chem. Soc.* **2008**, *130*, 14026-14027.

53. Schwab, G. M.; Koller, K. Combined Action of Metal and Semiconductor Catalysts. *J. Am. Chem. Soc.* **1968**, *90*, 3078-3080.
54. Tauster, S. J.; Fung, S. C.; Garten, R. L. Strong Metal-Support Interactions. Group 8 Noble Metals Supported on Titanium Dioxide. *J. Am. Chem. Soc.* **1978**, *100*, 170-175.
55. Tauster, S. J.; Fung, S. C. Strong Metal-Support Interactions: Occurrence Among the Binary Oxides of Groups IIA-VB. *J. Catal.* **1978**, *55*, 29-35.
56. Tauster, S. J. Strong Metal-Support Interactions. *Acc. Chem. Res.* **1987**, *20*, 389-394.
57. Ko, E. I.; Garten, R. L. Ethane Hydrogenolysis Studies of TiO<sub>2</sub>-Supported Group VIII Metal-Catalysts. *J. Catal.* **1981**, *68*, 233-236.
58. Boffa, A. B.; Lin, C.; Bell, A. T.; Somorjai, G. A. Promotion of CO and CO<sub>2</sub> Hydrogenation over Rh by Metal Oxides: The Influence of Oxide Lewis Acidity and Reducibility. *J. Catal.* **1994**, *149*, 149-158.
59. Gunter, P. L. J.; Niemantsverdriet, J. W.; Ribiero, F. H.; Somorjai, G. A. Surface Science Approach to Modeling Supported Catalysts. *Catal. Rev.* **1997**, *39*, 77-168.
60. Storp, S.; Holm, R. ESCA Investigation of the Oxide Layers on Some Cr Containing Alloys. *Surf. Sci.* **1977**, *68*, 10-19.
61. Boffa, A. B.; Lin, C.; Bell, A. T.; Somorjai, G. A. Lewis Acidity as an Explanation for Oxide Promotion of Metals: Implications of its Importance and Limits for Catalytic Reactions. *Catal. Lett.* **1994**, *27*, 243-249.
62. Bernal, S.; Calvino, J. J.; Cauqui, J. M.; Larese, C.; Perez Omil, J. A.; Pintado, J. M. Some Recent Results on Metal/Support Interaction Effects in NM/CeO<sub>2</sub> (NM: Noble Metal) Catalysts. *Catal. Today* **1999**, *50*, 175-206.
63. Fu, Q.; Saltsburg, H.; Flytzani-Stephanopoulos, M. Active Nonmetallic Au and Pt Species on Ceria-Based Water-Gas Shift Catalysts. *Science* **2003**, *301*, 935-938.
64. Vannice, M. A.; Wang, S. Y.; Moon, S. H. The Effect of SMSI (Strong Metal-Support Interaction) Behaviour on CO Adsorption and Hydrogenation on Pd Catalysts: I. IR Spectra of Adsorbed CO Prior to and During Reaction Conditions. *J. Catal.* **1981**, *71*, 152-166.
65. Park, J. Y.; Somorjai, G. A. The Catalytic Nanodiode: Detecting Continuous Electron Flow at Oxide-Metal Interfaces Generated by a Gas-Phase Exothermic Reaction. *Chem. Phys. Chem.* **2006**, *7*, 1409-1413.
66. Park, J. Y.; Renzas, J. R.; Contreras, A. M.; Somorjai, G. A. The Genesis and Importance of Oxide-Metal Interface Controlled Heterogeneous Catalysis; The Catalytic Nanodiode. *Top. Catal.* **2007**, *46*, 217-222.



67. Hervier, A.; Renzas, J. R.; Park, J. Y.; Somorjai, G. A. Hydrogen Oxidation-Driven Hot Electron Flow Detected by Catalytic Nanodiodes. *Nano Lett.* **2009**, *9*, 3930-3933.
68. Baker, L. R.; Hervier, A.; Kennedy, G.; Somorjai, G. A. Solid-State Charge-Based Device for Control of Catalytic Carbon Monoxide Oxidation on Platinum Nanofilms Using External Bias and Light. *Nano Lett.* **2012**, *12*, 2554-2558.
69. Koningsberger, D. C.; de Graaf, J.; Mojet, B. L.; Ramaker, D. E.; Miller, J. T. The Metal-Support Interaction in Pt/Y Zeolite: Evidence for a Shift in Energy of Metal d-Valence Orbitals by Pt-H Shape Resonance and Atomic XAFS Spectroscopy. *Appl. Catal. A* **2000**, *191*, 205-220.
70. Holm, M. S.; Taarning, E.; Egeblad, K.; Christensen, C. H. Catalysis with Hierarchical Zeolites. *Catal. Today* **2011**, *168*, 3-16.
71. Tourinho, R.; de Oliveira, I. F.; Arroyo, P. A.; Mota, C. J. A. Acid Strength of Pt-Zeolite Catalysts: Evidence of Metal-Support Interaction from linear Free-Energy Relationship. *Catal. Lett.* **2011**, *141*, 1472-1475.
72. Smirniotis, P. G.; Ruckenstein, E. Platinum Impregnated Zeolite  $\beta$  as a Reforming Catalyst. *Catal. Lett.* **1993**, *17*, 341-347.
73. Karge, H. G.; Weitkamp, J. *Zeolites as Catalysts, Sorbents and Detergent Builders*; Studies in Surface Science and Catalysis; Elsevier: **1989**.
74. Prasada Rao, T. S. R.; Murali Dhar, G. *Recent Advances in Basic and Applied Aspects of Industrial Catalysis*; Elsevier: New York, **1998**.
75. Naito, S.; Aida, S.; Kasahara, T.; Miyao, T. Infrared Spectroscopic Study on the Reaction Mechanism of CO Hydrogenation over Pd/CeO<sub>2</sub>. *Res. Chem. Intermed.* **2006**, *32*, 279-290.
76. Yoon, K.; Yang, Y.; Lu, P.; Wan, D.; Peng, H. C.; Stamm Masias, K.; Fanson, P. T.; Campbell, C. T.; Xia, Y. A Highly Reactive and Sinter-Resistant Catalytic System Based on Platinum Nanoparticles Embedded in the Inner Surfaces of CeO<sub>2</sub> Hollow Fibers. *Angew. Chem., Int. Ed* **2012**, *51*, 9543-9546.
77. Kennedy, G.; Baker, L. R.; Somorjai, G. A. Selective Amplification of C=O Bond Hydrogenation on Pt/TiO<sub>2</sub>: Catalytic Reaction and Sum-Frequency Generation Vibrational Spectroscopy Studies of Crotonaldehyde Hydrogenation. *Angew. Chem.* **2014**, *126*, 3473-3476.
78. Baker, L. R.; Kennedy, G.; Van Spronsen, M.; Hervier, A.; Cai, X.; Chen, S.; Wang, L. W.; Somorjai, G. A. Furfuraldehyde Hydrogenation on Titanium Oxide-Supported Platinum Nanoparticles Studied by Sum Frequency Generation Vibrational Spectroscopy: Acid-Base Catalysis Explains the Molecular Origin of Strong Metal-Support Interactions. *J. Am. Chem. Soc.* **2012**, *134*, 14208-14216.

79. Pushkarev, V. V.; Musselwhite, N.; An, K.; Alayoglu, S.; Somorjai, G. A. High Structure Sensitivity of Vapor-Phase Furfural Decarbonylation/Hydrogenation Reaction Network as a Function of Size and Shape of Pt Nanoparticles. *Nano Lett.* **2012**, *12*, 5196-5201.
80. Alayoglu, S.; Pushkarev, V. V.; Musselwhite, N.; An, K.; Beaumont, S. K.; Somorjai, G. A. Reforming of C-6 Hydrocarbons Over Model Pt Nanoparticle Catalysts. *Top. Catal.* **2012**, *55*, 723-730.
81. An, K.; Alayoglu, S.; Musselwhite, N.; Plamthottam, S.; Melaet, G.; Lindeman, A. E.; Somorjai, G. A. Enhanced CO Oxidation Rates at the Interface of Mesoporous Oxides and Pt Nanoparticles. *J. Am. Chem. Soc.* **2013**, *135*, 16689-16696.
82. An, K.; Alayoglu, S.; Musselwhite, N.; Na, K.; Somorjai, G. A. Designed Catalysts from Pt Nanoparticles Supported on Macroporous Oxides for Selective Isomerization of n-Hexane. *J. Am. Chem. Soc.* **2014**, *136*, 6830.
83. Musselwhite, N.; Na, K.; Alayoglu, S.; Somorjai, G. A. The Pathway to Total Isomer Selectivity: n-Hexane Conversion (Reforming) on Platinum Nanoparticles Supported on Aluminum Modified Mesoporous Silica (MCF-17). *J. Am. Chem. Soc.* **2014**, *136*, 16661-16665.

## **Chapter 2**

# **Experimental Methods**

### **Abstract**

This chapter will discuss the techniques utilized to accomplish the research undertaken in this dissertation. Techniques discussed will be divided into synthetic, characterization, and reaction studies. Synthetic techniques include nanoparticle and catalyst support material synthesis. Characterization includes various types of transmission electron microscopy (TEM) and ambient pressure x-ray photoelectron spectroscopy (AP-XPS). The reaction studies will describe the home-built high pressure reactor system in depth, along with the standard experimental procedures and operating parameters.

## 2.1 Introduction

Molecular level factors that control both catalytic activity (amount of all products) and selectivity (ratio of desired products to undesired products) can be determined through careful study of model catalytic systems.<sup>1</sup> In order to elucidate which molecular level components are important for efficient catalysis, it is necessary to perform careful synthesis, characterization, and studies under relevant reaction conditions.<sup>1</sup> This chapter intends to explain the techniques used in this dissertation that grant insight into the workings of a catalytic system.

## 2.2 Synthetic Techniques

### 2.2.1 Pt Nanoparticle Synthesis

Polyvinylpyrrolidone (PVP) capped Pt NPs in the size range 1.5–7.1 nm were synthesized by colloidal alcohol reduction methods. The approach for synthesis of the 1.5, 2.6, 3.6, and 7.1 nm particle sizes is described in literature.<sup>2</sup> The methods for preparing 1.9 and 5.0 nm sizes were developed in house. For the 1.5 nm Pt/PVP NPs, NaOH was dissolved in ethylene glycol (12.5 mL, 0.5 M) and the resulting solution was added to an ethylene glycol solution (12.5 mL) containing (0.25 g, 0.48 mmol) of  $\text{H}_2\text{PtCl}_6 \cdot 6\text{H}_2\text{O}$  in a 50 ml three necked flask. Under an argon atmosphere the mixture was heated to 433 K and held at that temperature for 3 h. The resulting NPs were precipitated with 0.5 ml of 2.0 M HCl and re-dispersed in a 0.1 mM solution of PVP in ethanol. To synthesize 1.9 nm Pt NPs, 60 mg of  $\text{H}_2\text{PtCl}_6 \cdot 6\text{H}_2\text{O}$  (0.15 mmol) and 0.1 g of PVP were added to 7 ml of water and 14 ml of ethanol in a 100 ml three necked flask installed with a condenser. When the solution was refluxed at 373 K for 2.5 h, water and ethanol as solvents allow the Pt precursor in the solution to be reduced slowly due to their mild reducing properties. On the contrary, ethylene glycol and diethylene glycol are strong enough to reduce Pt precursors because the glycols have strong reduction ability and the reaction proceeds at high temperature (above 473 K). In order to make 2.6 nm Pt/PVP NPs, 60 mg of  $\text{H}_2\text{PtCl}_6 \cdot 6\text{H}_2\text{O}$  (0.15 mmol) and 0.1 g of PVP were added to 7 ml of water and 14 ml of ethanol in a 100 ml three necked flask installed with a condenser. The solution was refluxed at 373 K for 3 h under an argon gas atmosphere, 80 ml of acetone was then added to form a cloudy black suspension after the solution was cooled to room temperature. The black precipitate was separated by centrifugation at 3000 rpm for 10 min and then re-dispersed in 40 mL of ethanol. For 3.6 nm Pt particles, first Pt NPs with 2.9 size were prepared: PVP (133 mg) was dissolved in a mixture of 180 mL of methanol and 20 mL of aqueous  $\text{H}_2\text{PtCl}_6 \cdot 6\text{H}_2\text{O}$  (6.0 mM). Then, freshly synthesized colloidal 2.9 nm Pt particle solution (100 mL) was added to 90 ml methanol and 10 mL of aqueous  $\text{H}_2\text{PtCl}_6 \cdot 6\text{H}_2\text{O}$  (6.0 mM). The solution was refluxed for 3 h under constant stirring. To synthesize 5.0 nm Pt NPs, PVP (55 mg) and  $\text{H}_2\text{PtCl}_6 \cdot 6\text{H}_2\text{O}$  (26 mg) were dissolved in diethylene glycol (10 mL). The solution was then placed under vacuum at 353 K for 20 min, followed by Argon flow over the solution for 20 min. The solution was then heated to 508 K and held at this temperature for 5 min. Particles were precipitated by adding triple volume of acetone. For 7.1 nm Pt NPs, a 0.375 M PVP solution (3 mL) and a 0.0625 M  $\text{H}_2\text{PtCl}_6 \cdot 6\text{H}_2\text{O}$  (1.5 mL) were alternatively added to 2.5 mL of boiling ethylene glycol every 30 s over 16 min. The solution was then refluxed for an additional 5 min. Particles were precipitated by adding a triple volume of acetone. In a typical synthesis for 6.8 nm cubes, 15.4 mg  $\text{Pt}(\text{acac})_2$  and 28.0 mg PVP55k were dissolved in 10 mL triethylene glycol (TEG) under Ar atmosphere. 100 mL acetylacetone was added to the reaction solution and the reaction flask was placed in an oil bath preheated to 453 K. The solution turned dark at 453 K within 5 hours, and completely black and colloidal in 12 hours. The colloidal suspension was further aged at 453 K for 12 hours. As-synthesized colloids

are stable for about 1 year. The synthetic procedure for 6.3 nm octahedron is similar to that of 6.8 nm Pt cubes. Differently, the reaction solution was placed in an oil bath at 433 K, and the reaction was carried out for 96 hours. The final product was dark brown and stable in the colloidal suspension for about 1 year. TEM images and particle size data are shown in Figure 1. The shape of all Pt NPs used in the study (excluding cubic and octahedral nanoparticles) can be characterized as rounded (polyhedral) based on TEM characterization.

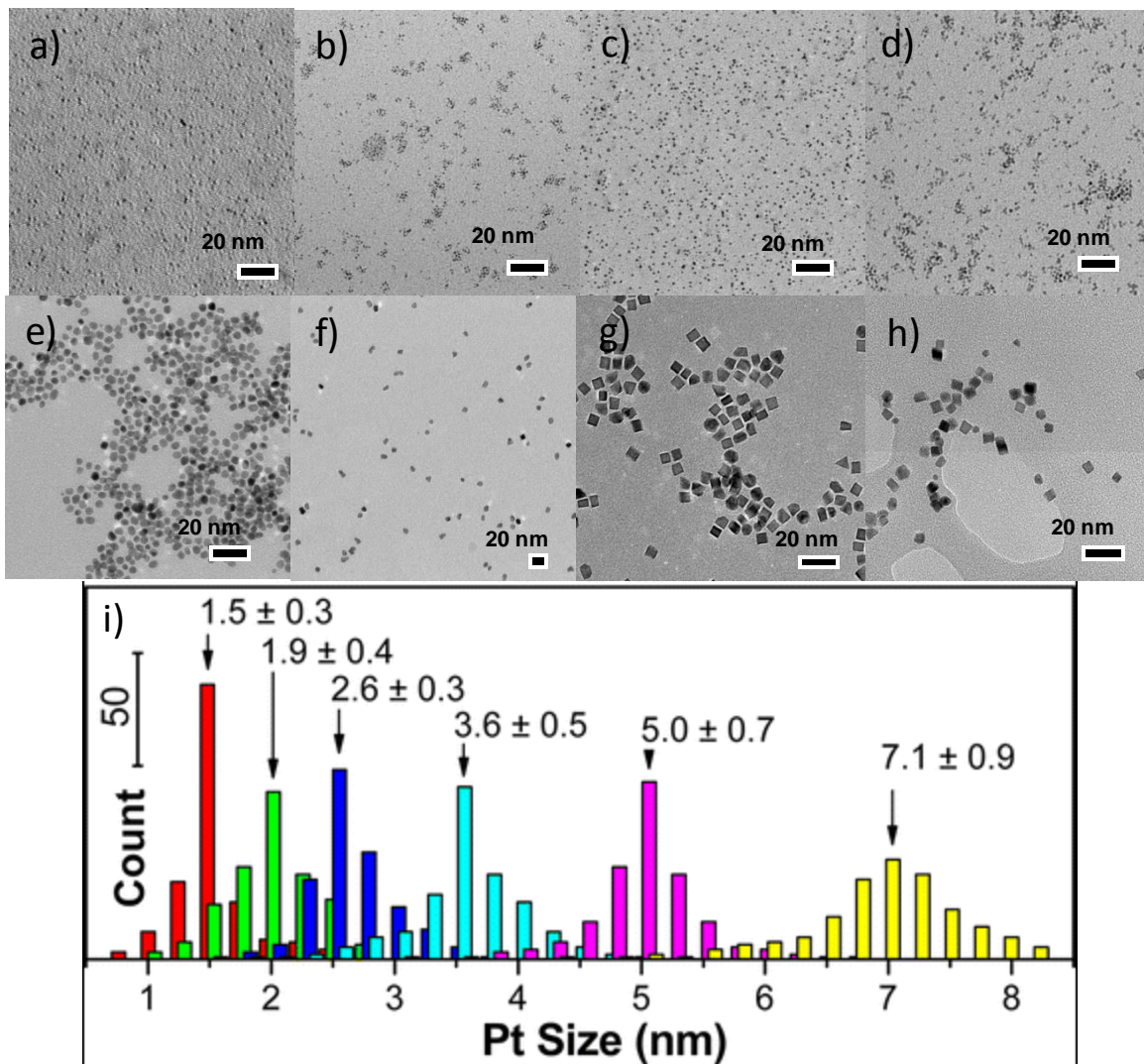


**Figure 1.** TEM Images of Pt NPs with average sizes of a) 1.5 nm b) 1.9 nm c) 2.6 nm d) 2.9 nm e) 5.0 nm f) 7.1 nm (different scale bar) g) 6.8 nm (cubes) h) 6.3 nm (octahedron) i) size distribution histogram for polyhedral particles.

### 2.2.2 $Pt_xRh_{1-x}$ Nanoparticle Synthesis

Platinum nanoparticles alloyed with rhodium were synthesized in various metal compositions through colloidal techniques. Briefly,  $H_2PtCl_6 \cdot 6H_2O$  (Sigma-Aldrich, 37.50 % Pt basis),  $Pt(acac)_2$  (Aldrich, 97 %), and  $Rh(acac)_3$  (Aldrich, 97 %) were used as metal sources in 6.5 nm particle synthesis. The ratio of Pt to Rh metals was varied, but the overall metal amount was kept at a constant  $1.0 \times 10^{-4}$  mol. The mole ratio of  $H_2PtCl_6 \cdot 6H_2O$  to  $Pt(acac)_2$  was also kept at a constant 4:1 for 6.5 nm. In a typical synthesis the metal salts were added to a round bottom flask, triethylene glycol (10 mL) and polyvinylpyrrolidone (28 mg, 55,000 g/mol) were added, and the solution was sonicated for 30 min to ensure dissolving of the solids. The flask was then placed under vacuum for 20 min and then repeatedly purged with argon and vacuum pumped before finally being filled with argon, to ensure an oxygen free environment. The flask was then placed in a molten salt bath held at a constant 503 K for 1 h. During this time the solution changed to dark black in color as nanoparticles were formed. Smaller sized bimetallic nanoparticles were synthesized by addition of  $NaNO_3$  ( $7 \times 10^{-5}$  mol) to a solution containing triethylene glycol, PVP and  $Pt(acac)_2$  and  $Rh(acac)_3$  ( $1.0 \times 10^{-4}$  mol total metal) and following a similar reduction procedure as reported above. After synthesis, the nanoparticles were precipitated from solution by addition of acetone and subsequent centrifugation ( $550 \times 9.8 \text{ m/s}^2$ , 20 min). STEM-EDS images of the two compositions of 6.5 nm  $Pt_xRh_{1-x}$  nanoparticles are shown in Figure 2.

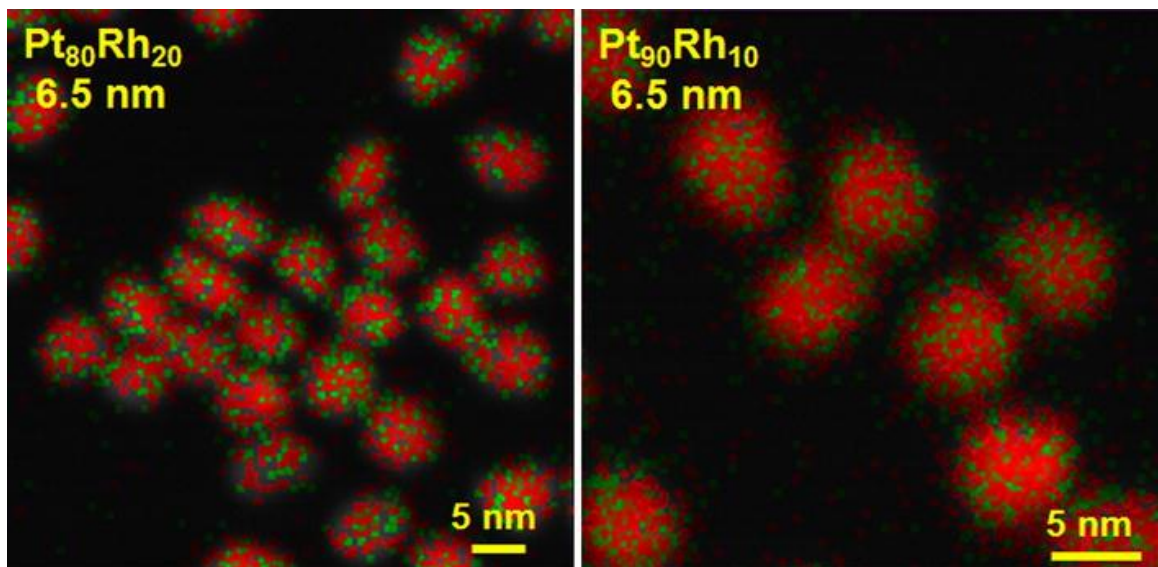


**Figure 2.** Scanning transmission electron microscopy/electron-dispersive spectrometry (STEM-EDS) images of bimetallic nanoparticles. The red points represent the Pt and the green points represent Rh.

### 2.2.3 Mesoporous Silica Support Synthesis

The synthesis of MCF-17 mesoporous silica with 25 nm average pore diameter, 500 m<sup>2</sup>/g BET surface area, and 2.5 cm<sup>3</sup>/g pore volume was accomplished by using literature methods.<sup>3,4</sup> Triblock copolymer Pluronic P123 (4 g), 1,3,5 Trimethylbenzene (4 g), and concentrated HCl (10 mL) were all added to a flask containing deionized water (75 mL). The resulting solution was stirred constantly for 2 h, while being heated at 313 K, tetraethoxysilane (9.2 mL) was then added, followed by an additional 5 min of stirring. The solution was then aged at 313 K, without stirring, for 20 h, followed by the addition of NH<sub>4</sub>F (46 mg). The solution was then hydrothermally aged in an autoclave for 24 h at 373 K. The precipitate was then filtered, washed with ethanol and water, and calcined at 873 K for 6 hours in air. The powdery white product was kept in a desiccator for further use.

The MCF-17 supported catalysts were prepared by mixing the mesoporous silica powder with colloidal solutions of Pt NPs in ethanol, then subjecting the mixture to sonication for 3 h at room temperature in a commercial ultrasonic cleaner (1510R-MT, 70 W, Branson). After immobilization of the NPs in the support, the resulting precipitate was separated by centrifugation ( $550 \times 9.8 \text{ m/s}^2$ , 20 min). The samples prepared using PVP were thoroughly washed with ethanol to ensure removal of excess polymer at this stage. The resulting catalysts were dried in air at 373 K overnight before use. TEM images of the final samples are shown in Figure 3.

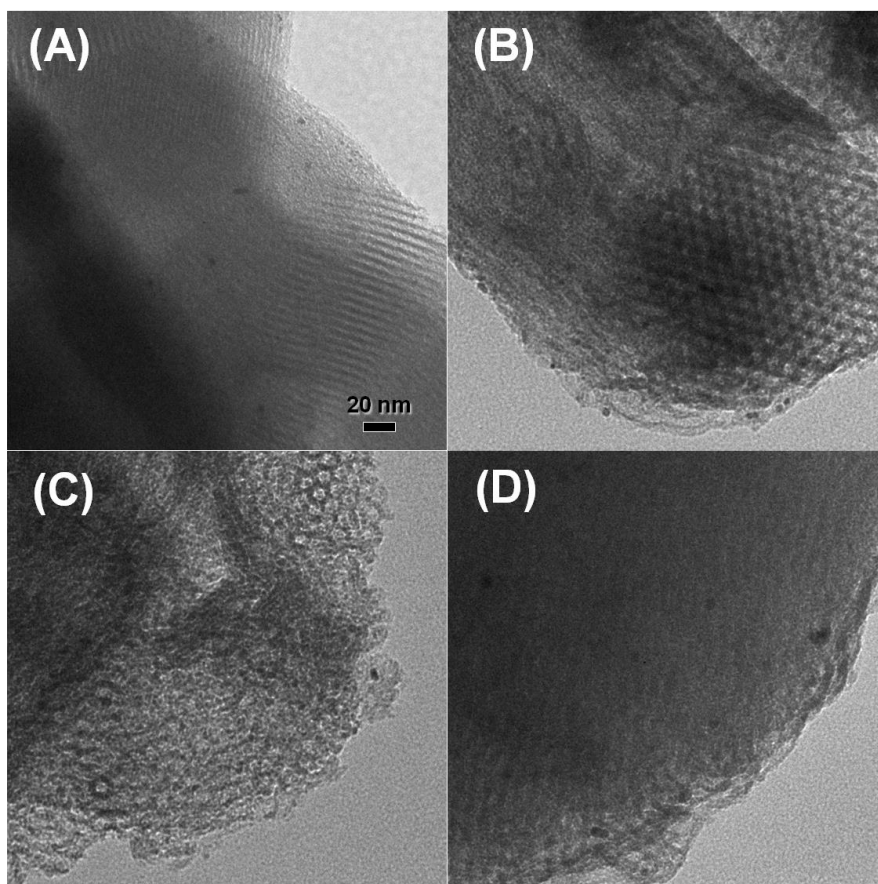


**Figure 3.** TEM images of Pt NPs loaded onto mesoporous silica. The average diameters of the Pt nanoparticles are (A) 1.9 nm, (B) 3.1 nm, (C) 4.0 nm, and (D) 5.2, respectively. The scale bar represents 20 nm.

---

### 3.2.3 Synthesis of other Mesoporous Materials

Throughout the course of this project, numerous techniques have been developed to synthesize novel mesoporous oxide materials, which have never before been studied catalytically. Mesoporous materials, with a highly ordered structure, were formed via two methods: 1) by a self-assembled supramolecular structure of a surfactant as a soft template and 2) the use of a hard-template (nano-casting) approach.<sup>5</sup> The soft template approach was utilized to synthesize the mesoporous materials of  $\text{Al}_2\text{O}_3$ ,  $\text{TiO}_2$ ,  $\text{Nb}_2\text{O}_5$ , and  $\text{Ta}_2\text{O}_5$ , which have hexagonally channeled pore structures. The resultant materials created via this method are shown in Figure 4. Pluronic P123 was used as a soft template to direct the pore structures.



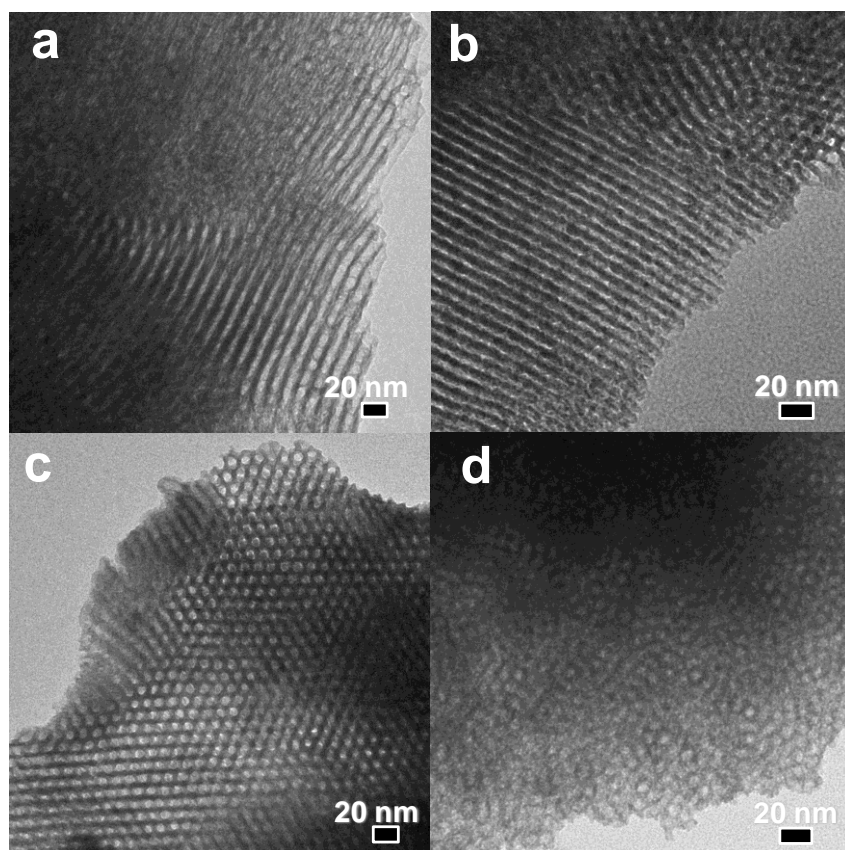
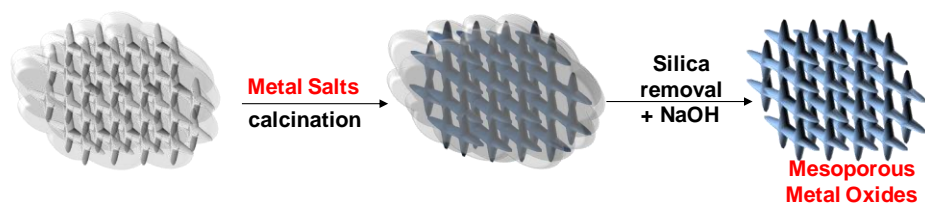


**Figure 4.** TEM images of mesoporous (a)  $\text{Al}_2\text{O}_3$ , (b)  $\text{TiO}_2$ , (c)  $\text{Nb}_2\text{O}_5$ , and (d)  $\text{Ta}_2\text{O}_5$ .

---

The second method, hard-templating, provides efficient and versatile ways to synthesize crystalline mesoporous materials with controlled pore structures. In the hard template approach, shown in Scheme 1, the templates determine the final structure of the material and make them stable during high-temperature crystallization. Many different types of mesoporous materials can be made with this method, including:  $\text{Co}_3\text{O}_4$ ,  $\text{NiO}$ ,  $\text{MnO}_2$ ,  $\text{Fe}_2\text{O}_3$ , (shown in Figure 5) along with many others.



**Scheme 1.** Schematic illustration of the hard-templating (nanocasting) approach for the preparation of mesoporous oxides.

---

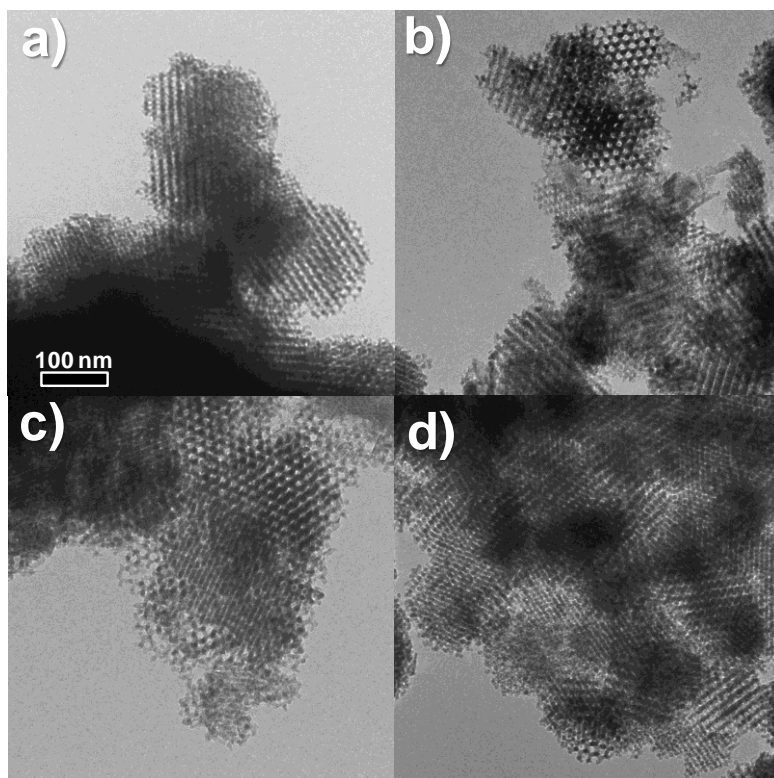


**Figure 5.** TEM images of mesoporous oxides of a)  $\text{Co}_3\text{O}_4$ , b)  $\text{NiO}$ , c)  $\text{MnO}_2$ , and d)  $\text{Fe}_2\text{O}_3$ , which were synthesized by using KIT-6 silica as a hard template.

---

## 2.3 Characterization

### 2.3.1 Transmission Electron Microscopy

Transmission electron microscopy (TEM) is utilized in several chapters of this dissertation. This technique allows for the imaging of synthesized nanoparticles. Briefly, a high energy (120 kV) electron is focused onto a target containing the nanoparticle sample. The transmitted electrons are captured with a CCD camera, giving an image correlated to the transmission efficiency of the electrons, which varies based on the thickness and atomic composition of the material being imaged.<sup>6</sup> Several processes occur simultaneously when the electron beams hit the sample target. These processes include: transmission, diffraction, auger electron emission, X-ray emission, visible light emission, and transmission with energy loss. Figure 6 shows an illustrative scheme of these processes.

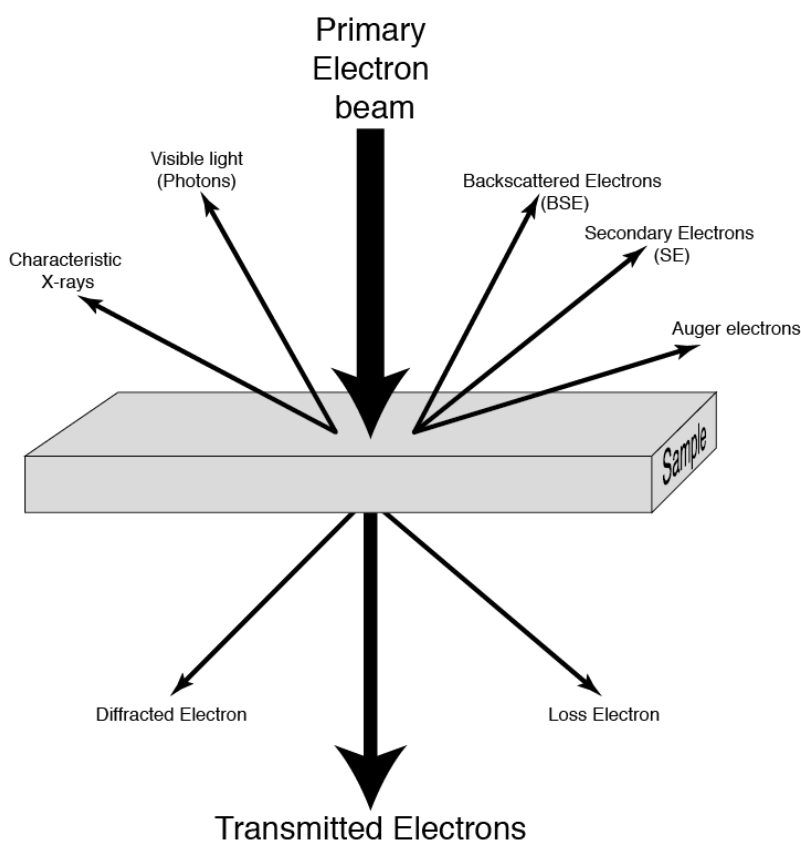


**Figure 6.** Scheme showing different processes of electron beam interacting with sample target. The processes include: transmission, diffraction, auger electron emission, X-ray emission, visible light emission, and transmission with energy loss.

---

Transmission of electrons, in order to determine nanoparticle size and shape is utilized in every chapter of this dissertation. In several chapters the X-rays are utilized through energy-dispersive X-ray spectroscopy (EDS). As electrons are ejected from core orbitals, holes are created and subsequently filled with electrons in higher level orbitals. This process releases energy in the form of X-ray photons. The energy of the emitted X-ray is equal to the energy difference of the two orbitals, therefore this technique allows for elemental analysis of the sample. The fundamental process required for EDS is depicted in Figure 7.

---

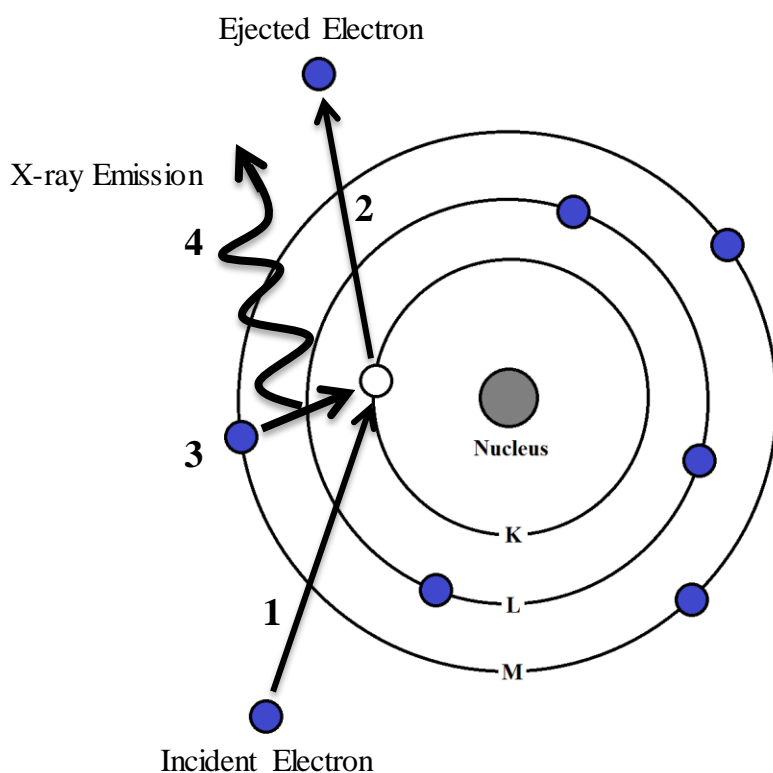


**Figure 7.** Scheme showing the fundamental process required for energy dispersive X-ray spectroscopy (EDS). (1) A high energy incident electron ejects a core electron (2) which generates a hole. (3) This hole is filled with a higher level electron, causing an (4) X-ray to be emitted with energy equal to the energy difference of the two

---

### 2.3.1 Ambient-Pressure X-ray Photoelectron Spectroscopy

X-ray photoelectron spectroscopy (XPS) works by utilizing the photoelectric effect, in which electrons are emitted from materials after absorption of photons with high enough incident energy. A schematic description of the photoemission process is shown in Figure 8.

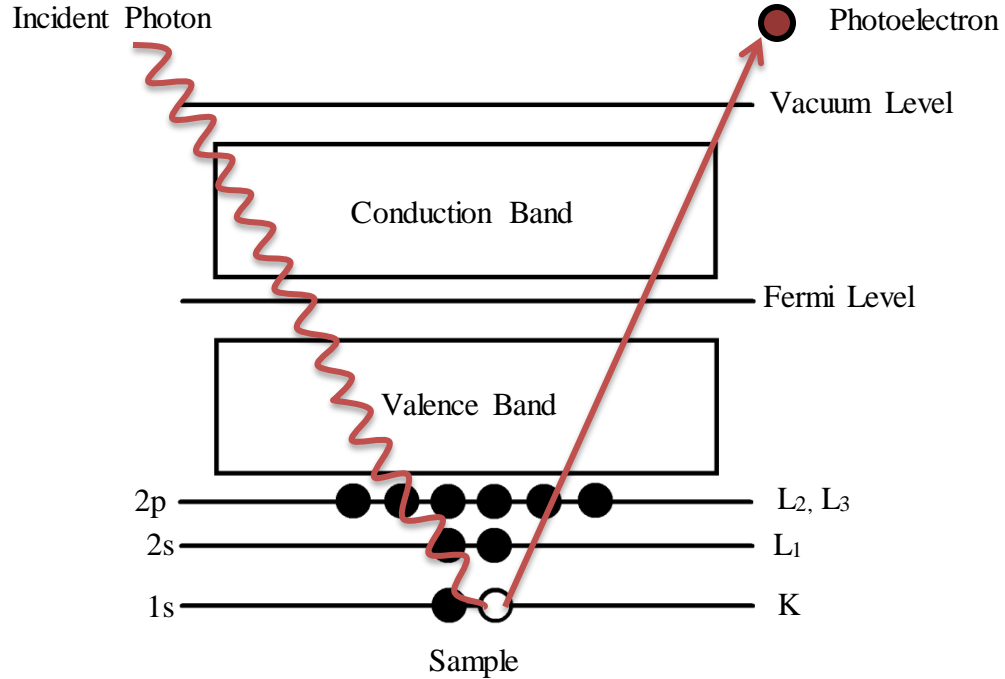


**Figure 8.** Schematic of the photoemission process. A high energy incident photon ejects a core level electron.

By measuring the kinetic energy of these emitted electrons it is possible to determine the binding energy ( $E_B$ ) of the electron through the following equation:

$$E_B = h\nu - E_k - \phi_a \quad \text{Eq. 1}$$

Where  $h$  is Planck's constant,  $\nu$  is the frequency incident photon,  $E_k$  is the kinetic energy of the ejected electron and  $\phi_a$  is the work function of the analyzer. This information can then be used to identify the elements present in the sample. In addition, through proper peak integration and deconvolution, the fractional content of all atoms in the sample can be determined along with the oxidation state of each atom. XPS is a technique that is normally restricted to ultra-high vacuum (UHV), due to the short mean free path of the ejected electrons. However, with Ambient Pressure X-ray Photoelectron Spectroscopy (AP-XPS) a differentially pumped cone is utilized to allow for pressures in the Torr regime in the sample chamber, while the analyzer chamber remains at very low pressures ( $\sim 10^{-8}$  Torr).<sup>7</sup> An illustration of the design of the AP-XPS utilized in Beamline 9.3.2 at the Advanced Light Source Synchrotron system is shown in Figure 9.

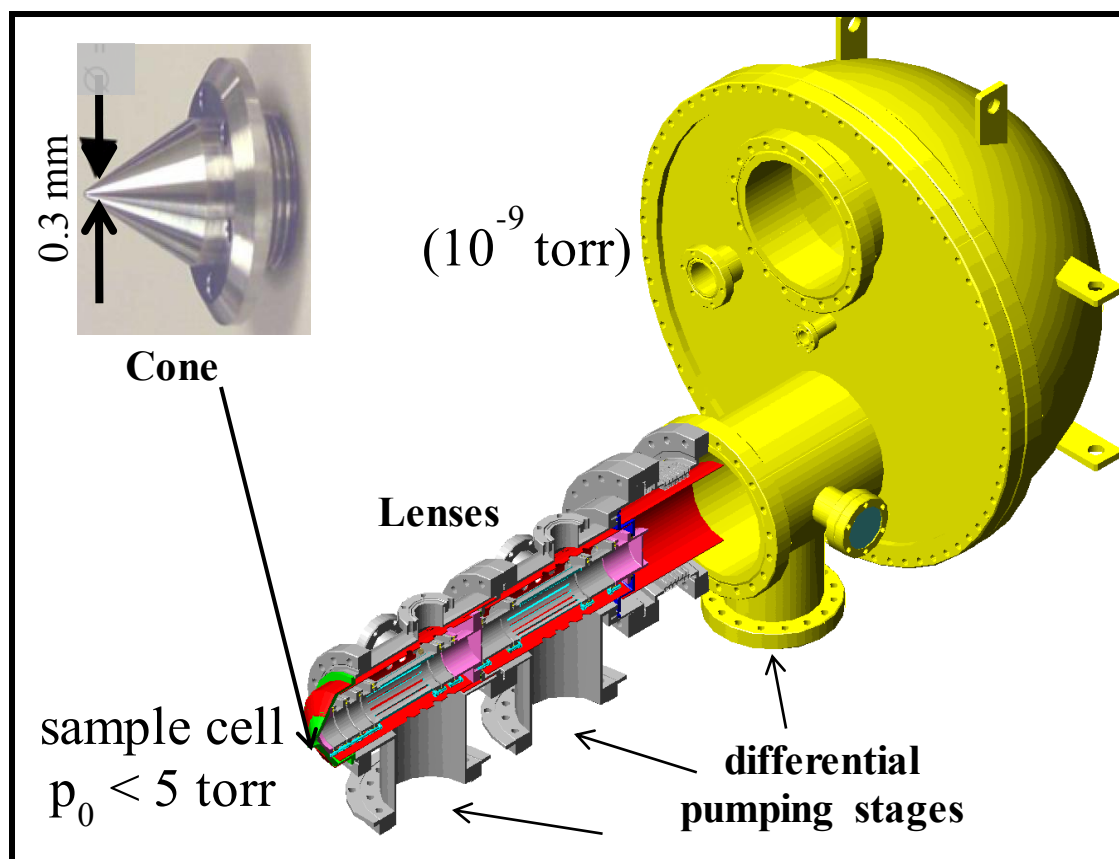


**Figure 9.** Schematic of the AP-XPS system found in Beamline 9.3.2 at the Advanced Light Source Synchrotron.

## 2.4 Catalytic Measurements

### 2.4.1 Reactor Description

Catalytic kinetic measurements of all reactions were conducted in the vapor phase in a plug-flow fixed catalyst bed micro-reactor test system, which was built around a single vertically mounted stainless steel tubular (55 cm long, 0.6 cm O.D., 0.45 cm I.D.) reactor. A schematic of the reactor design is shown in Figure 10, and a picture of the reactor system is shown in Figure 11. A stainless steel tube holding the catalyst to be evaluated was positioned inside of a tubular furnace (Model 3210, Applied Test Systems) capable of operating from 298-1043 K. The H<sub>2</sub> and N<sub>2</sub> gas flowrates were controlled with Brooks high pressure mass flow controllers (5850Etype) in the 2–100 sccm range for each gas, which gave the reactor the capability to be operated with pressures ranging from 1-120 bar. Reactor inlet pressure was monitored using a capacitance manometer transducer (Baratron 890B, MKS Instruments). The reactor outlet was connected to a pneumatic pressure control valve and then a hydrocarbon scrubber, which was connected to the vent. The quantitative analysis of reactants and reaction products was done chromatographically using a Hewlett–Packard (5890 Series II) gas chromatograph equipped with a 50 meter

dimethylpolysiloxane (HP-1, Hewlett–Packard) capillary column, a computer interface and Chemstation data acquisition and processing software (Agilent).

---

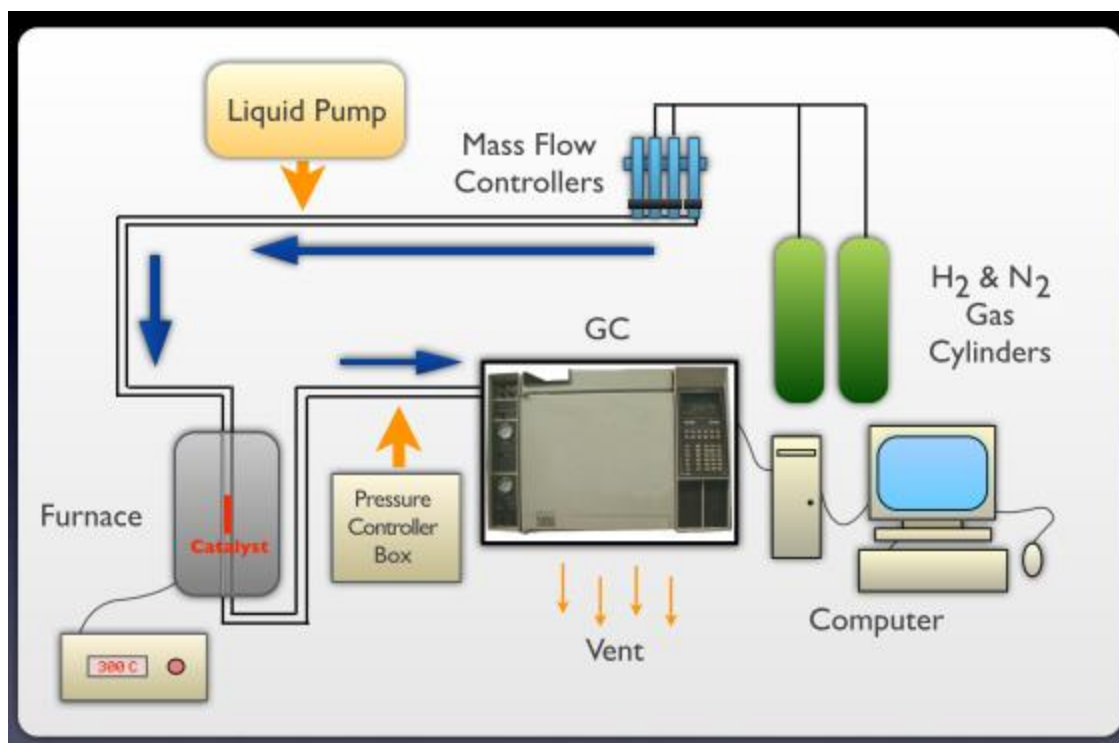


**Figure 10.** Schematic of the home-built high pressure high temperature stainless steel reactor system.

---



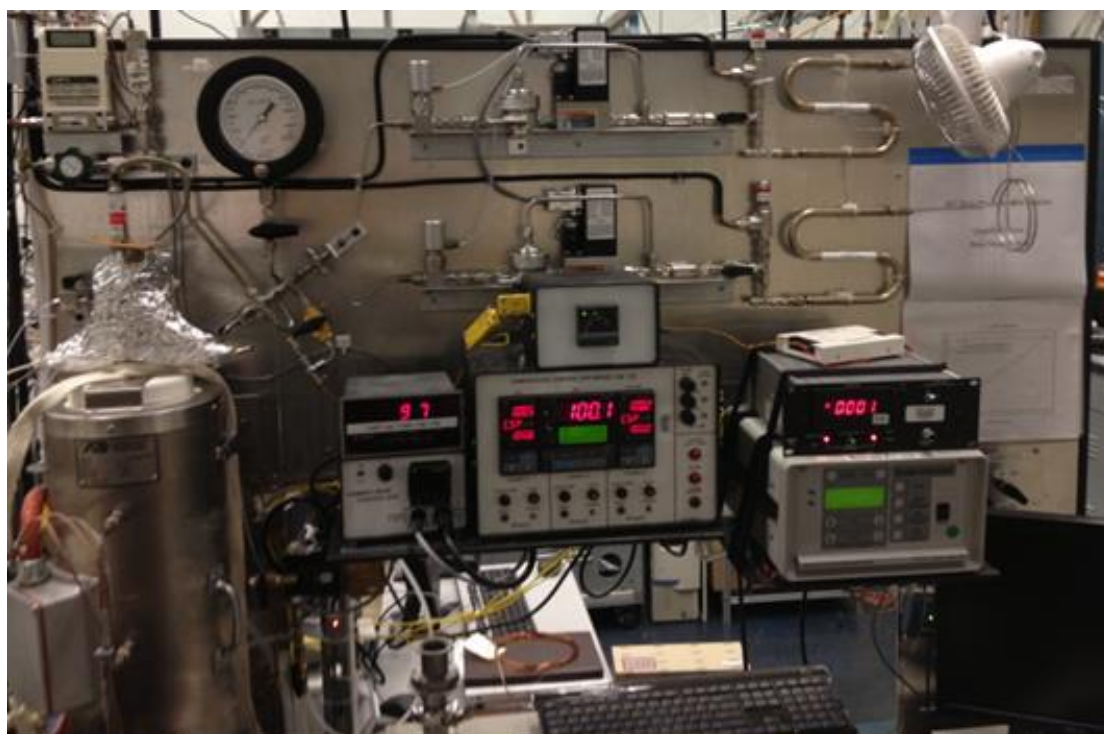


**Figure 11.** Photograph of the home-built high pressure high temperature stainless steel reactor system.

---

#### 2.4.1 Experimental Procedure

All synthesized catalysts were evaluated in a tubular fixed catalyst bed reactor. The 1/4" diameter stainless steel reactor was mounted vertically, which allowed for the downflow operation. A load of catalyst was placed in the middle of the reactor tube, delimited by a layer of purified glass wool and a layer of purified alundum granulate at each end. Prior to loading, the catalyst sample was pelletized to obtain 160–250  $\mu\text{m}$  size granulates, to prevent pressure drop. The amount of catalyst was varied from 0.050 to 0.500 g to achieve a similar conversion, which is required for selectivity comparison. The “freshly” loaded catalyst was pretreated under an ambient pressure flow of a  $\text{H}_2$  (10 sccm) and  $\text{N}_2$  (10 sccm) gas mixture at 633 K for 2 h. The heating/cooling rate during the pretreatment was limited to 2  $\text{K min}^{-1}$ . After the pretreatment, the reactor was cooled down under the same gas flow. Each kinetic measurement was repeated two or more times for any given catalyst material to establish the uncertainty in the measurements. For the selectivities and Turnover Rate (TOR) comparison measurements a constant flow (at 293 K) of purified liquid reactant was continually injected using a high pressure Teledyne ISCO 500D liquid flow pump. In the preheating zone, the reactant evaporated and mixed with 16 sccm flow of  $\text{H}_2$ , resulting in a two-component gas flow with a reactant: $\text{H}_2$  ratio of 1:5 entering the reactor at near ambient pressure. A Baratron type (890B, MKS Instruments) capacitance pressure manometer was used to monitor the reactor inlet pressure. The reaction products were sampled in the vapor phase at the reactor outlet and analyzed via an in-line gas chromatograph (GC). After



passing through a GC sampling loop, the reactor outlet flow was then directed to a hydrocarbon scrubber which was vented at ambient pressure. All flow lines between the reactor outlet and the scrubber were heated to 433 K to maintain the flow components in the vapor phase. The quantitative analysis of the flow composition was performed using a Hewlett-Packard (5890 Series II) GC which was equipped with a 10 m dimethylpolysiloxane (HP-1, Hewlett-Packard) capillary column and a flame ionization detector (FID). The characteristic retention times and FID response factors for the individual compounds were established via prior calibrations. A PC based GC Chemstation software (Hewlett-Packard) was used for automation of the GC sampling, data collection, and post-run processing.

## 2.5 References

1. Somorjai, G. A.; Li, Y. *Introduction to Surface Chemistry and Catalysis*; Wiley: New York, 2010; .
2. Rioux, R. M.; Song, H.; Hoefelmeyer, J. D.; Yang, P.; Somorjai, G. A. High-Surface-Area Catalyst Design: Synthesis, Characterization, and Reaction Studies of Platinum Nanoparticles in Mesoporous SBA-15 Silica. *J. Phys. Chem. B* **2005**, *109*, 2192-2202.
3. Han, Y.; Lee, S. S.; Ying, J. Y. Spherical Siliceous Mesocellular Foam Particles for High-Speed Size Exclusion Chromatography. *Chem. Mater.* **2007**, *19*, 2292-2298.
4. Schmidt-Winkel, P.; Lukens, W. W.; Yang, P.; Margolese, D. I.; Lettow, J. S.; Ying, J. Y.; Stucky, G. D. Microemulsion Templating of Siliceous Mesostructured Cellular Foams with Well-Defined Ultralarge Mesopores. *Chem. Mater.* **2000**, *12*, 686-696.
5. Ren, Y.; Ma, Z.; Qian, L.; Dai, S.; He, H.; Bruce, P. G. Ordered Crystalline Mesoporous Oxides as Catalysts for CO Oxidation. *Catal. Lett.* **2009**, *131*, 146-154.
6. Bernard, D. B.; Carter, C. B. *Transmission Electron Microscopy: A Textbook for Materials Science*; Plenum Press: New York, 1996; .
7. Grass, M. E.; Karlsson, P. G.; Aksoy, F.; Lundqvist, M.; Wannberg, B.; Mun, B. S.; Hussain, Z.; Liu, Z. New Ambient Pressure Photoemission Endstation at Advanced Light Source Beamline 9.3.2. *Rev. Sci. Instrum.* **2010**, *81*, 053106-1-053106-7.

## Chapter 3

# High Structure Sensitivity of Vapor-phase Furfural Decarbonylation/Hydrogenation Reaction Network as a Function of Size and Shape of Pt Nanoparticles

### Abstract

Vapor-phase transformations of furfural in  $\text{H}_2$  over a series of Pt nanoparticles (NPs) with various uniform particle sizes (1.5–7.1 nm size range) and shapes (rounded, cubes, octahedra) encapsulated in poly(vinylpyrrolidone) (PVP) and dispersed on MCF-17 mesoporous silica were investigated at ambient pressure in the 443–513 K temperature range. Furan and furfuryl alcohol (FFA) were two primary products as a result of furfural decarbonylation and hydrogenation reactions, respectively. Under conditions of the study both reactions exhibited structure sensitivity evidenced by changes in product selectivities, turnover rates (TORs), and apparent activation energies ( $E_A$ 's) with Pt particle size and shape. For instance, upon an increase in Pt particle size from 1.5 to 7.1 nm, the selectivity toward FFA increases from 1% to 66%, the TOR of FFA production increases from  $1 \times 10^{-3} \text{ s}^{-1}$  to  $7.6 \times 10^{-2} \text{ s}^{-1}$ , and  $E_A$  decreases from 104 kJ  $\text{mol}^{-1}$  to 15 kJ  $\text{mol}^{-1}$  (9.3 kPa furfural, 93 kPa  $\text{H}_2$ , 473 K). Conversely, under the same experimental conditions the decarbonylation reaction path is enhanced over smaller nanoparticles. The smallest NPs (1.5 nm) produced the highest selectivity (96%) and highest TOR values ( $8.8 \times 10^{-2} \text{ s}^{-1}$ ) toward furan formation. The  $E_A$  values for decarbonylation ( $\sim 62 \text{ kJ mol}^{-1}$ ) were Pt particle size independent. Furan was further converted to propylene via a decarbonylation reaction, but also to dihydrofuran, tetrahydrofuran, and *n*-butanol in secondary reactions. Furfuryl alcohol was converted mostly to 2-methylfuran.

\* This chapter covers similar material as in Pushkarev, V.V.; Musselwhite, N.; An, K.; Alayoglu, S.; Somorjai, G.A. *Nano Lett.* **2012**, *12*, 5196-5201. — reproduced with permission, copyright 2012 American Chemical Society.

### 3.1 Introduction

Achieving the highest possible performance in catalytic reaction processing only becomes possible when the catalyst structure is tuned to and sustained at its optimal state under reaction conditions. This is especially important for a class of heterogeneous catalytic reactions that are commonly referred to as structure-sensitive; that is, their reaction kinetics are influenced by the active metal's particle size and/or morphology.<sup>1,2</sup> Previous studies have demonstrated that many industrially significant reactions including ammonia synthesis, hydrocarbon reforming, Fischer–Tropsch synthesis, and catalytic combustion are structure sensitive.<sup>2,3</sup> More recently, the advances in the synthetic chemistry of well-defined transition metal nanoparticles have provided the tools to study structure sensitivity, and subsequent structure sensitivity was found for many of the selective hydrogenation reactions of heteroatom containing hydrocarbons.<sup>4–7</sup> In this chapter, the selective chemistry of furfural over a size-dependent series of PVP-capped Pt nanoparticle (NP) catalysts is examined. It was found that Pt NPs of sizes less than 2 nm are highly selective toward decarbonylation of furfural's carbonyl group, while Pt NPs larger than 2 nm predominately produce furfuryl alcohol. Furfural was selected as the reactant because of the recent interest in sustainable production of liquid fuels and fine chemicals from non-petroleum derived feedstock (such as biomass).

Furfural is an aromatic compound produced primarily from the dehydration of C<sub>5</sub> sugars and is a major component of bio-oils.<sup>8</sup> Different transition metals show different catalytic activity with respect to transformations of its highly reactive carbonyl group. For instance, Cu is highly selective for hydrogenation of the furfural to furfuryl alcohol.<sup>9,10</sup> On the other hand, Pd is an efficient catalyst for decarbonylation of furfural to furan.<sup>11–13</sup> Ni and Pt, depending on conditions, can promote both reactions to a different extent.<sup>14,15</sup> At high temperatures (550–600 K), the decarbonylation reaction dominates, while at lower temperatures the hydrogenation activity becomes significant, which leads to the formation of furfuryl alcohol.

### 3.2 Experimental

#### 3.2.1 Materials

Hexachloroplatinic acid, H<sub>2</sub>PtCl<sub>6</sub>·6H<sub>2</sub>O (99.9% pure on metals basis), Pt(acetylacetonate)<sub>2</sub> (97%), polyvinylpyrrolidone (PVP) (*M*<sub>w</sub> = 29,000 g/mol), Pluronic P123 (*M*<sub>n</sub> = 5800, EO<sub>20</sub>PO<sub>70</sub>EO<sub>20</sub>, EO = ethylene oxide, PO = propylene oxide), tetraethoxysilane (TEOS, 98%) and all other chemicals used in material synthesis (all of high purity) were purchased from Sigma-Aldrich. The liquid furfural (ACS purity, 99%, Sigma-Aldrich) was purified by vacuum distillation. The H<sub>2</sub>, N<sub>2</sub>, He, and ethylene gas (all high purity, >99.995%) used in reaction studies were supplied by Praxair. The H<sub>2</sub> and N<sub>2</sub> gases used in furfural reaction kinetic studies were additionally purified by passing through molecular sieve traps (S-trap, Supelco).

#### 3.2.2 Material Synthesis

The PVP-capped Pt NPs in the size range 1.5–7.1 nm were synthesized by alcohol reduction methods. The approach for synthesis of the 1.5, 2.6, 3.6, and 7.1 nm mean particle sizes is described in literature.<sup>16</sup> The methods for preparing 1.9 and 5.0 nm sizes were developed in house. For the 1.5 nm Pt/PVP NPs, NaOH was dissolved in ethylene glycol (12.5 mL, 0.5 M)

and the resulting solution was added to an ethylene glycol solution (12.5 mL) containing (0.25 g, 0.48 mmol) of  $\text{H}_2\text{PtCl}_6 \cdot 6\text{H}_2\text{O}$  in a 50 ml three-necked flask. Under an argon atmosphere the mixture was heated to 433 K and held at that temperature for 3 h. The resulting NPs were precipitated with 0.5 ml of 2.0 M HCl and re-dispersed in a 0.1 mM solution of PVP in ethanol. To synthesize 1.9 nm Pt NPs, 60 mg of  $\text{H}_2\text{PtCl}_6 \cdot 6\text{H}_2\text{O}$  (0.15 mmol) and 0.1 g of PVP were added to 7 ml of water and 14 ml of ethanol in a 100 ml three necked flask installed with a condenser. When the solution was refluxed at 100 °C for 2.5 h, water and ethanol as solvents allow the Pt precursor in the solution to be reduced slowly due to their mild reducing properties. On the contrary, ethylene glycol and diethylene glycol are strong enough to reduce Pt precursors to Pt NPs because the glycols have strong reduction ability and the reaction proceeds at high temperature (above 200 °C). In order to make 2.6 nm Pt/PVP NPs, 60 mg of  $\text{H}_2\text{PtCl}_6 \cdot 6\text{H}_2\text{O}$  (0.15 mmol) and 0.1 g of PVP were added to 7 ml of water and 14 ml of ethanol in a 100 ml three necked flask installed with a condenser. The solution was refluxed at 373 K for 3 h under an argon gas atmosphere; 80 ml of acetone was then added to form a cloudy black suspension after the solution was cooled to room temperature. The black precipitant was separated by centrifugation at 3000 rpm for 10 min and then re-dispersed in 40 mL of ethanol. For 3.6 nm Pt particles, first Pt NPs with 2.9 size were prepared: PVP (133 mg) was dissolved in a mixture of 180 mL of methanol and 20mL of aqueous  $\text{H}_2\text{PtCl}_6 \cdot 6\text{H}_2\text{O}$  (6.0 mM). Then, freshly synthesized colloidal 2.9 nm Pt particle solution (100 mL) was added to 90 ml methanol and 10mL of aqueous  $\text{H}_2\text{PtCl}_6 \cdot 6\text{H}_2\text{O}$  (6.0 mM). The solution was refluxed for 3 h under constant stirring. To synthesize 5.0 nm Pt NPs, PVP (55 mg) and  $\text{H}_2\text{PtCl}_6 \cdot 6\text{H}_2\text{O}$  (26 mg) were dissolved in diethylene glycol (10 mL). The solution was then placed under vacuum at 353 K for 20 min, followed by Argon flow over the solution for 20 min. The solution was then heated to 508 K and held at this temperature for 5 min. Particles were precipitated by adding triple volume of acetone. For 7.1 nm Pt NPs, a 0.375 M PVP solution (3 mL) and a 0.0625 M  $\text{H}_2\text{PtCl}_6 \cdot 6\text{H}_2\text{O}$  (1.5 mL) were alternatively added to 2.5 mL of boiling ethylene glycol every 30 s over 16 min. The solution was then refluxed for an additional 5 min. Particles were precipitated by adding a triple volume of acetone. In a typical synthesis for 6.8 nm cubes, 15.4 mg  $\text{Pt}(\text{acac})_2$  and 28.0 mg PVP55k were dissolved in 10 mL triethylene glycol (TEG) under Ar atmosphere. 100 mL acetylacetone was added to the reaction solution and the reaction flask was placed in an oil bath preheated to 453 K. The solution turned dark at 453 K within 5 hours, and completely black and colloidal in 12 hours. The colloidal suspension was further aged at 453 K for 12 hours. As-synthesized colloids are stable for about 1 year. The synthetic procedure for 6.3 nm octahedra is similar to that of 6.8 nm Pt cubes. Differently, the reaction solution was placed in an oil bath at 160°C, and the reaction was carried out for 96 hours. The final product was dark brown and stable in the colloidal suspension for about 1 year. TEM images are shown in Figure 1. The shape of all Pt NPs used in the study (excluding cubic and octahedral nanoparticles) can be characterized as rounded (polyhedral) based on TEM characterization.

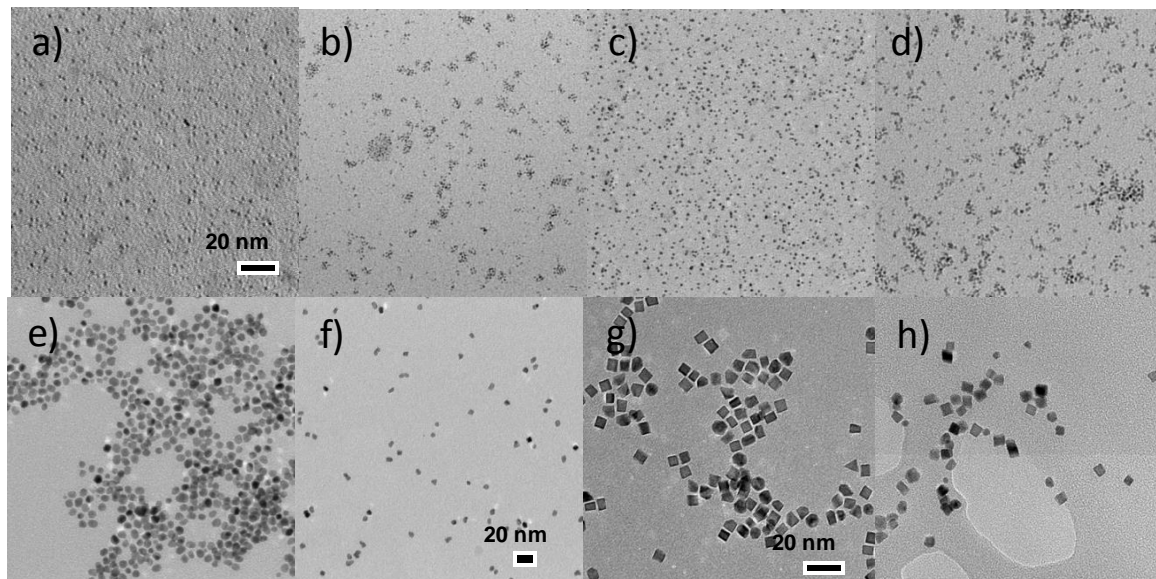


**Figure 1.** TEM Images of Pt NPs with average sizes of a) 1.5 nm b) 1.9 nm c) 2.6 nm d) 2.9 nm e) 5.0 nm f) 7.1 nm (different scale bar) g) 6.8 nm (cubes) h) 6.3 nm (octahedron)

The synthesis of MCF-17 mesoporous silica with 25 nm average pore diameter, 500 m<sup>2</sup>/g BET surface area, and 2.5 cm<sup>3</sup>/g pore volume was accomplished by using common literature methods.<sup>17,18</sup> Triblock copolymer Pluronic P123 (4 g), 1,3,5 trimethylbenzene (4 g), and concentrated HCl (10 mL) were all added to a flask containing deionized water (75 mL). The resulting solution was stirred constantly for 2 h, while being heated at 313 K. Tetraethoxysilane (9.2 mL) was then added, followed by an additional 5 min of stirring. The solution was then aged at 313 K, without stirring, for 20 h, followed by the addition of NH<sub>4</sub>F (46 mg). The solution was then hydrothermally aged in an autoclave for 24 h at 373 K. The precipitate was then filtered, washed with ethanol and water, and calcined at 873 K for 6 hours in air. The powdery white product was kept in a desiccator for further use.

The MCF-17 supported catalysts were prepared by mixing the mesoporous silica powder with colloidal solutions of Pt NPs in ethanol, then subjecting the mixture to sonication for 3 h at room temperature in a commercial ultrasonic cleaner (1510R-MT, 70 W, Branson). After immobilization of the NPs in the support, the resulting precipitate was separated by centrifugation ( $550 \times 9.8 \text{ m/s}^2$ , 20 min). The samples prepared using PVP were thoroughly washed with ethanol to ensure removal of excess polymer at this stage. The resulting catalysts were dried in air at 373 K overnight before use.

### 3.2.3 Material Characterization

The sizes of the Pt NPs were analyzed using a Hitachi H-7650 transmission electron microscope (TEM) operated at 120 kV. High-resolution (HR) and annular dark field (ADF) TEM images were obtained using a JEOL 2100 LaB<sub>6</sub> microscope and a JEOL 2100-F microscope,

both operating at 200 kV. The average TEM-projected Pt particle sizes and the size distribution histograms were determined from TEM images by counting 300 particles. Figure 2 shows the particle size distribution histograms, the mean sizes, and standard deviations of the different sized Pt NPs. TEM and HRTEM pictures (Figures 1 and 2) indicate nanocrystalline Pt nanoparticles with polyhedral shapes (i.e., spherical). The total Pt loadings were determined by inductively coupled plasma atomic emission spectroscopy (ICP-AES) using a Perkin-Elmer optical emission spectrometer (Optima 7000 DV). The instrument was calibrated using a Pt standard (Fluka, TraceCERT 1000 mg L<sup>-1</sup>). The total specific surface area of MCF-17 support was determined via N<sub>2</sub> (UHP grade, 99.999%, PraxAir) physisorption at 77 K using an Autosorb-1 (Quantachrome) analyzer.

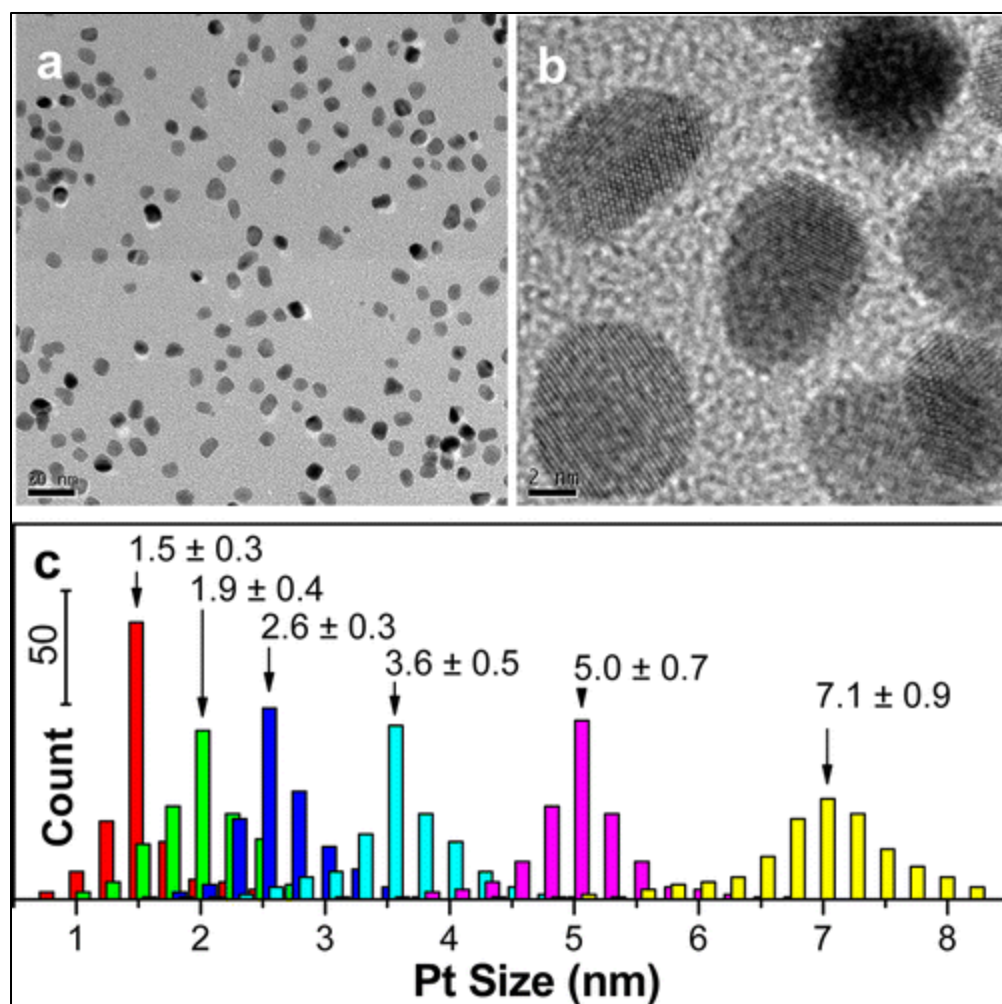


**Figure 2.** (a and b) TEM and HR-TEM images for the 7.1 nm Pt-PVP NPs, respectively. The scale bar is (a) 20 nm and (b) 2 nm. (c) Particle size distribution histograms of the Pt-PVP series catalysts obtained from TEM images. The number inserts indicate the mean particle diameter and standard deviation for each sample.

### 3.2.4 Catalytic Activity Measurements

Activities of the Pt/MCF-17 series catalysts in the vapor-phase furfural/H<sub>2</sub> reaction were evaluated in a tubular fixed catalyst bed reactor at ambient pressure. The 1/4" diameter stainless steel reactor was mounted vertically, which allowed for the downflow operation. A 0.300 g load of catalyst/dilutant mixture, corresponding to a 8.5 cm catalyst bed height, was placed in the middle of the reactor tube, delimited by a layer of purified glass wool and a layer of purified alundum granulate at each end. Prior to mixing, both catalyst sample and diluent (pure MCF-17) were pelletized to obtain 160–250  $\mu\text{m}$  size granules. The amount of catalyst in the catalyst/diluent mixture was varied from 0.050 to 0.300 g to achieve a similar furfural conversion ( $3\% \pm 1\%$  at 473 K, 9.3 kPa furfural, 93 kPa H<sub>2</sub>, 1300 h<sup>-1</sup> GHSV), which is required for selectivity comparisons. The “freshly” loaded catalyst was pre-treated in an ambient pressure flow of a H<sub>2</sub> (10 sccm) and N<sub>2</sub> (10 sccm) gas mixture at 533 K for 2 h. The heating/cooling rate during the pretreatment was limited to 1 K min<sup>-1</sup>. After the pretreatment, the reactor was cooled down to 443 K under the same gas flow. Each kinetic measurement was repeated two or more times for any given catalyst material to establish the uncertainty in the measurements. For the selectivities and TOR comparison measurements a constant 0.4 mL h<sup>-1</sup> flow (at 293 K) of liquid purified furfural was continually injected using a syringe pump (Kent Scientific) equipped with a Hamilton syringe (Gastight) into the preheating reactor head which was maintained at 423 K. In the preheating zone, furfural evaporated and mixed with 20 sccm flow of H<sub>2</sub>, resulting in a two-component gas flow with a furfural:H<sub>2</sub> ratio of 1:10 entering the reactor at near ambient pressure. A Baratron type (890B, MKS Instruments) capacitance pressure manometer was used to monitor the reactor inlet pressure. The reaction products were sampled in the vapor phase at the reactor outlet and analyzed via an in-line gas chromatograph (GC). After passing through a GC sampling loop, the reactor outlet flow was then directed to a hydrocarbon scrubber which was vented at ambient pressure. All flow lines between the reactor outlet and the scrubber were heated to 433 K to maintain the flow components in the vapor phase. The quantitative analysis of the flow composition was performed using a Hewlett-Packard (5890 Series II) GC which was equipped with a 10 m dimethylpolysiloxane (HP-1, Hewlett-Packard) capillary column and a flame ionization detector (FID). The characteristic retention times and FID response factors for the individual compounds were established via prior calibrations. A PC based GC Chemstation software (Hewlett-Packard) was used for automation of the GC sampling, data collection, and post-run processing.

The reaction sequence included conditioning of a “fresh” catalyst sample under reactant stream (9.3 kPa furfural, 93 kPa H<sub>2</sub>, 1300 h<sup>-1</sup> GHSV) at 443 K for 1 h and an Arrhenius dependence measurement, which was performed as an increasing temperature sequence measured in the 443–513 K temperature range with 5 and 10 K temperature increments and a 2 h hold time at each temperature point. Additionally, for the 3.6 nm sample, the partial pressure dependence measurements were performed at 453, 473, and 493 K by varying the furfural flow rate in the 0.2–1.2 mL h<sup>-1</sup> range and H<sub>2</sub> flow rate in the 10–60 sccm range. During the measurements no detectable catalyst deactivation was observed, suggesting that the deactivation rates were very low. The product selectivity was calculated as:

$$\text{selectivity}(\%) = \frac{\text{mol product formed}}{\text{mol furfural consumed}} \times 100\%$$

Ethylene hydrogenation was utilized to determine the number of available Pt surface sites. The number of Pt surface sites per unit weight of catalyst (Pt sites  $\text{mg}^{-1}$ ) was determined using the known TOR of 11 molecules of ethylene (surface Pt site) $^{-1} \text{ s}^{-1}$  at 293 K, 13.3 kPa  $\text{H}_2$ , and 1.33 kPa  $\text{C}_2\text{H}_4$ .<sup>4,5</sup> The data from these ethylene hydrogenation surface area quantification reactions are shown in Table 1. Catalyst powder was first diluted with a low surface area quartz and then loaded into a U-shaped glass reactor. A Watlow temperature controller equipped with a K-type thermocouple was used to control temperature. The flows of ethylene,  $\text{H}_2$  and He were controlled by mass flow controllers. All samples were pretreated in 380 Torr  $\text{H}_2$  with a balance of He (total flow rate of 50 sccm) at 533 K for 2 h. During the ethylene turnover measurements, the temperature of the catalyst bed was maintained at 263 K using a refrigerated bath filled with a water/ethylene glycol slurry. The gas atmosphere was 10 Torr ethylene, 100 Torr  $\text{H}_2$ , and a makeup of He (total flow rate of 80 sccm). Gas composition was analyzed using a HP 5890 Series II gas chromatograph (GC) equipped with a flame ionization detector (FID). The TOR of ethylene hydrogenation at 293 K were calculated using the TOR values of ethylene hydrogenation at 263 K and using the rate equation with  $E_a = 41.9 \text{ kJ/mol}$ , first order dependence on hydrogen partial pressure and zero order dependence on ethylene partial pressure. The TOR values for furan and FFA production were calculated by taking a ratio of the molecular production rate measured per unit weight of catalyst (molecules  $\text{mg}^{-1} \text{ s}^{-1}$ ) for each individual compound and the number of active surface Pt sites per unit mass determined during the ethylene hydrogenation measurements.

**Table 1.** Description, characterization and ethylene hydrogenation data for MCF-17 supported Pt catalysts.

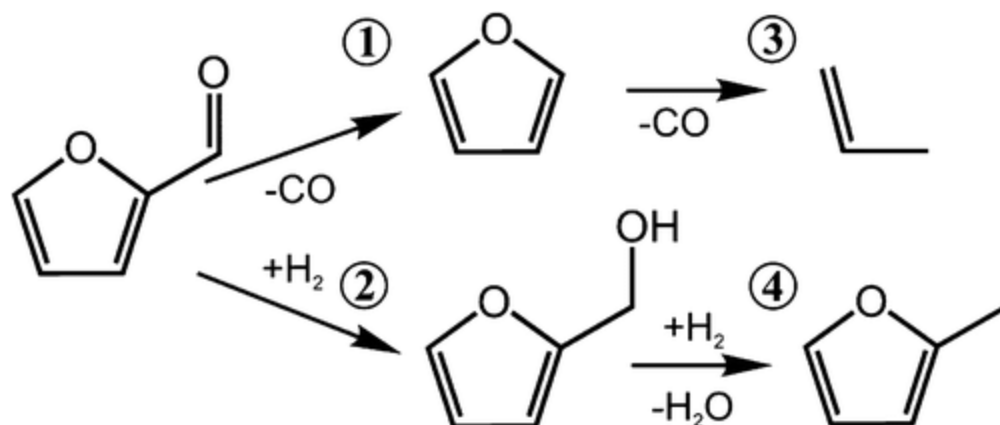
Pt Size (nm) <sup>(a)</sup>	SS/mg ( $\text{mg}^{-1}$ ) <sup>(b)</sup>	% Pt <sup>(c)</sup>	$E_a$ ( $\text{kJ mol}^{-1}$ ) <sup>(d)</sup>
$1.5 \pm 0.3$	$5.0 \pm 1 \times 10^{-9}$	0.49	42.1
$1.9 \pm 0.4$	$4.3 \pm 0.3 \times 10^{-9}$	0.51	41.9
$2.6 \pm 0.3$	$5.2 \pm 0.9 \times 10^{-9}$	0.46	43.2
$3.6 \pm 0.5$	$3.2 \pm 0.6 \times 10^{-9}$	0.49	40.6
$5.0 \pm 0.7$	$1.0 \pm 0.4 \times 10^{-9}$	0.41	43.6
$7.1 \pm 0.9$	$1.0 \pm 0.3 \times 10^{-9}$	0.33	41.9

<sup>(a)</sup> Sizes determined by TEM. <sup>(b)</sup> Surface sites per mg of catalyst determined by ethylene hydrogenation data using a value of -0.17 for  $\text{C}_2\text{H}_4$  order of reaction and a TOF of 11 molecules  $\text{site}^{-1} \text{ s}^{-1}$ .<sup>4,5</sup> <sup>(c)</sup> Pt loading mass determined by ICP-AES. <sup>(d)</sup> Activation energy determined for ethylene hydrogenation.



### 3.3 Results and Discussion

The reaction chemistry of furfural, when catalyzed by supported heterogeneous Pt catalysts, is complex and leads to the formation of multiple primary and secondary reaction products. Nevertheless, during the vapor phase catalysis in the 443–513 K temperature range (the experimental conditions of the study) the four dominant reaction products are: furan, furfuryl alcohol, 2-methylfuran, and propylene, as shown in the reaction Scheme 1. Two primary reactions dominate the reaction network, the carbonyl group decarbonylation and the carbonyl group hydrogenation, which lead to formation of the two primary reaction products: furan and furfuryl alcohol, respectively. Two major secondary reactions are the furan aromatic ring cracking/decarbonylation that leads to formation of propylene and CO, and the hydrogenolysis of the –OH group on furfuryl alcohol, which leads to the formation of 2-methylfuran and water. It is important to note that the aromatic ring hydrogenation reactions for both furfural and furan based compounds do not readily occur on Pt under conditions studied, presumably because the Pt



**Scheme 1.** Essential reactions network in furfural transformations over Pt, including two primary reactions: (1) furfural decarbonylation and (2) carbonyl group hydrogenation, and two secondary reactions: (3) furan ring cracking/decarbonylation, and (4) –OH group hydrogenolysis reaction pathways. The combined selectivity to the products shown exceeds 95% under conditions studied (9.3 kPa furfural and 93 kPa H<sub>2</sub> feed in the 443–513 K temperature range). The remaining volume of reaction products consists of the trace amounts of 2,3-dihydrofuran (DHF), tetrahydrofuran (THF), *n*-butanol, 2-methyltetrahydrofuran, 1-pentanol, 2-pentanol, tetrahydrofurfuryl alcohol, 1,2-pentadiol, 1,5-pentadiol, and furfural aldol condensation products.

surface is poisoned with chemisorbed CO that is produced during furfural decarbonylation (one molecule of CO per molecule of converted furfural is produced during a furfural decarbonylation turnover and the CO coverage of the Pt metal surface is expected to be high under conditions studied). Indeed, only trace amounts of dihydrofuran, tetrahydrofuran, tetrahydrofurfuryl alcohol, 2-methyltetrahydrofuran, and other similar compounds were detected during the measurements. Another possible catalytic route for a secondary reaction—an aldol condensation of furfuryl

alcohol with furfural is also a minor route on the Pt/MCF-17 catalysts, with the measured selectivity to aldol condensation product being less than 1% under conditions studied.

Figure 3 shows steady-state product selectivities of vapor phase furfural transformations to furan, furfuryl alcohol, 2-methylfuran, and propylene (furan ring cracking) measured in the 443–513 K temperature range as a function of Pt NP size. These data are also summarized in Table 2 for the 3.6 nm Pt NPs. Additional data on the product selectivity dependencies on Pt NPs shapes and the Arrhenius plots for different particle sizes are shown in Figures 4 and 5, respectively.

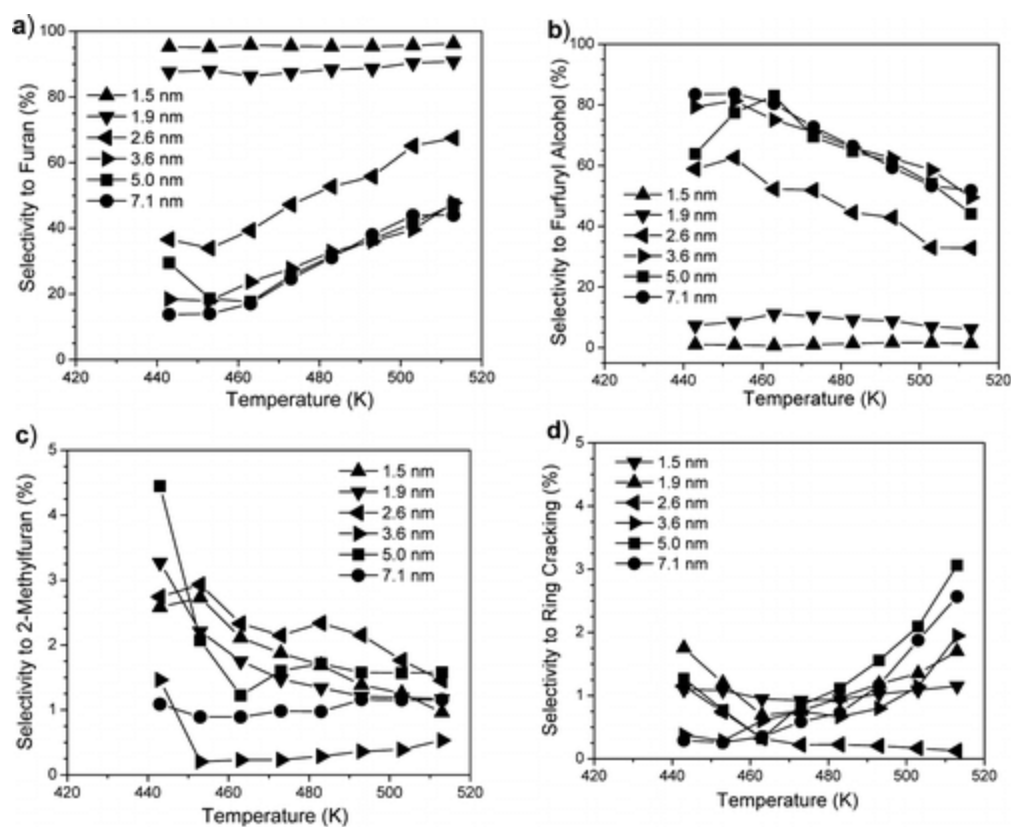


**Figure 3.** Steady-state product selectivities to (a) furan, (b) furfuryl alcohol, (c) 2-methylfuran, and (d) furan ring cracking products measured in the 443–513 K temperature range under  $1300 \text{ h}^{-1}$  of GHSP flow of reactants mixture containing 9.3 kPa furfural and 93 kPa  $\text{H}_2$ .

---

**Table 2.** Conversion and Product Selectivities of the Furfural Reaction over 3.6 nm Pt/MCF-17 Catalyst

Temp. (K)	Conv. (%)	W/F g/(mol/h)	Selectivity (%)				
			Furan	DHF <sup>a</sup>	Pr <sup>b</sup>	FFA <sup>c</sup>	2-MF <sup>d</sup>
453	1.2	41.4	28	0.7	0.6	68	1.5
	0.8	20.7	24	0.7	0.8	72	1.8
	0.5	13.8	22	1.0	0.7	74	1.8
473	1.8	41.4	34	0.7	0.7	63	1.3
	1.1	20.7	31	0.9	0.8	66	1.3
	0.8	13.8	31	1.1	0.8	65	1.7
493	3.1	41.4	30	1.0	0.8	67	1.3
	1.9	20.7	31	0.9	0.7	66	1.3
	1.4	13.8	31	1.1	0.8	65	1.4

<sup>a</sup>2,3-dihydrofuran <sup>b</sup>propylene <sup>c</sup>furfuryl alcohol <sup>d</sup>2-methylfuran

---

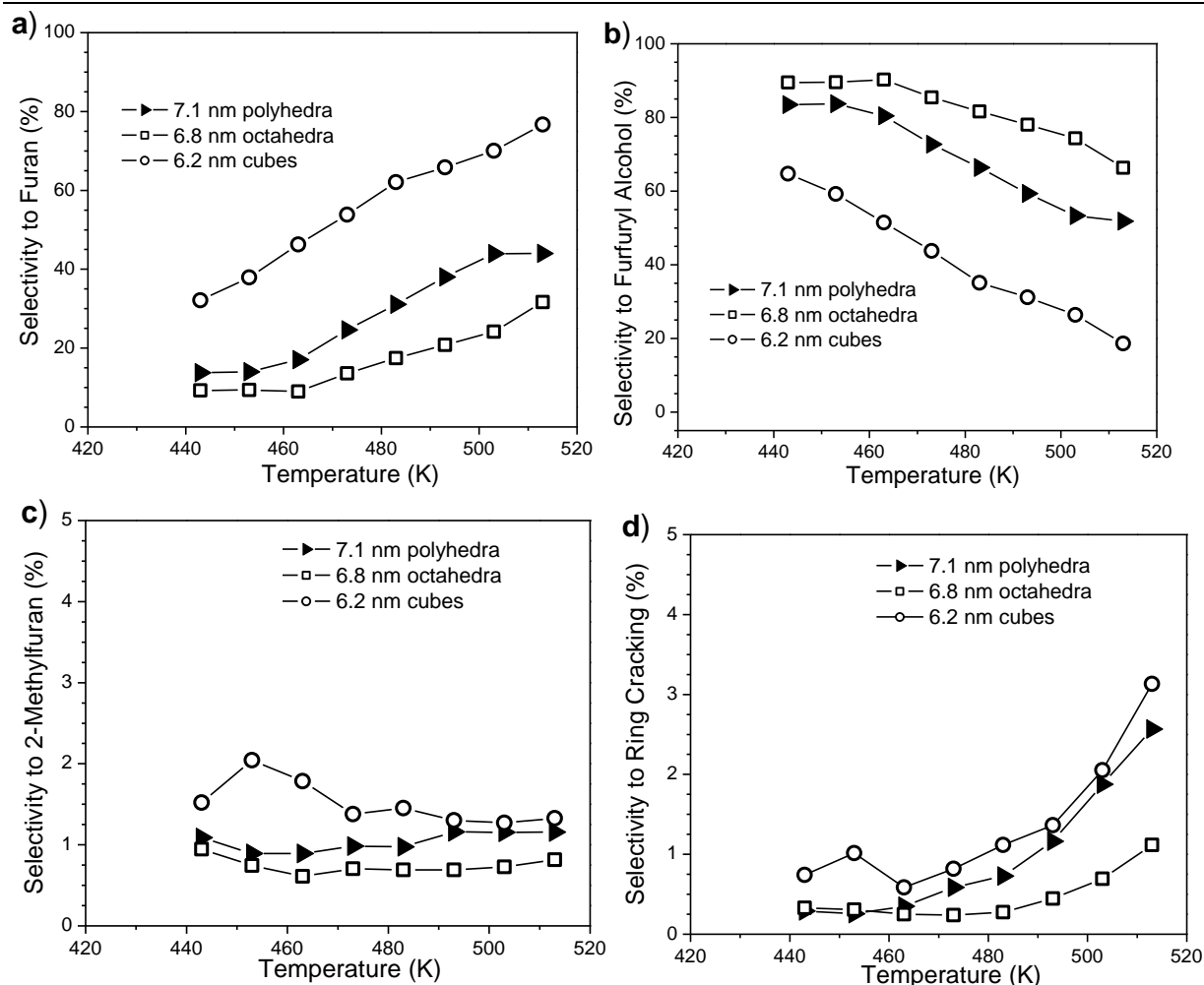


**Figure 4.** Steady-state product selectivities to (a) furan, (b) furfuryl alcohol, (c) 2-methylfuran and (d) furan ring cracking products measured for three different Pt NPs shapes: 7.1 nm polyhedra, 6.8 nm octahedra, and 6.2 nm cubes, in the 443–513 K temperature range under  $1300 \text{ h}^{-1}$  of GHSP flow of reactants mixture containing 9.3 kPa furfural and 93 kPa  $\text{H}_2$ .

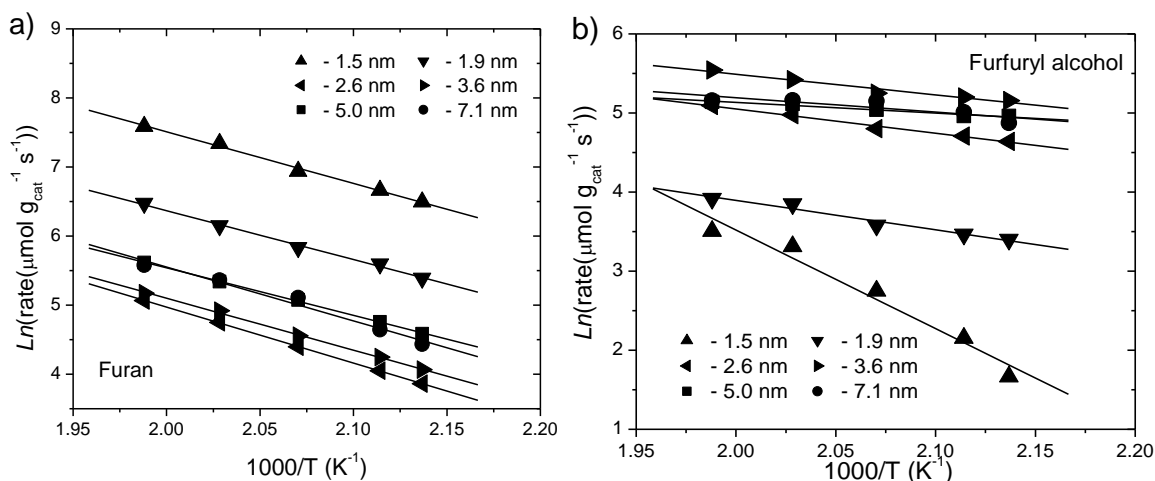


**Figure 5.** Arrhenius plots for (a) furan and (b) furfuryl alcohol production for the 1.5 -7.1 size dependent series of Pt NPs in the 443–513 K temperature range under  $1300 \text{ h}^{-1}$  of GHSP flow of reactants mixture containing 9.3 kPa furfural and 93 kPa  $\text{H}_2$ .

Figure 6 shows steady-state product selectivities to furan and furfuryl alcohol products measured at a single temperature of 473 K multiple times to determine the standard deviation of selectivity value as a function of the Pt NP size. The two primary reactions in the furfural reaction network over Pt NP catalysts are very sensitive to both Pt particle size and shape. The polyhedral Pt particles below 2 nm in size produce predominantly furan, while the polyhedral Pt particles above 3 nm produced predominantly furfuryl alcohol. The highest selectivity to furfuryl alcohol is achieved over 6.2 nm Pt NPs with octahedral morphology, while similarly sized 6.8 nm Pt NPs with cube morphology show a substantially lower selectivity to the product. The product selectivities to formation of 2-methylfuran and propylene appear to be structure-insensitive, as there were no clear correlations between the selectivity values and the Pt NPs size and/or shape.

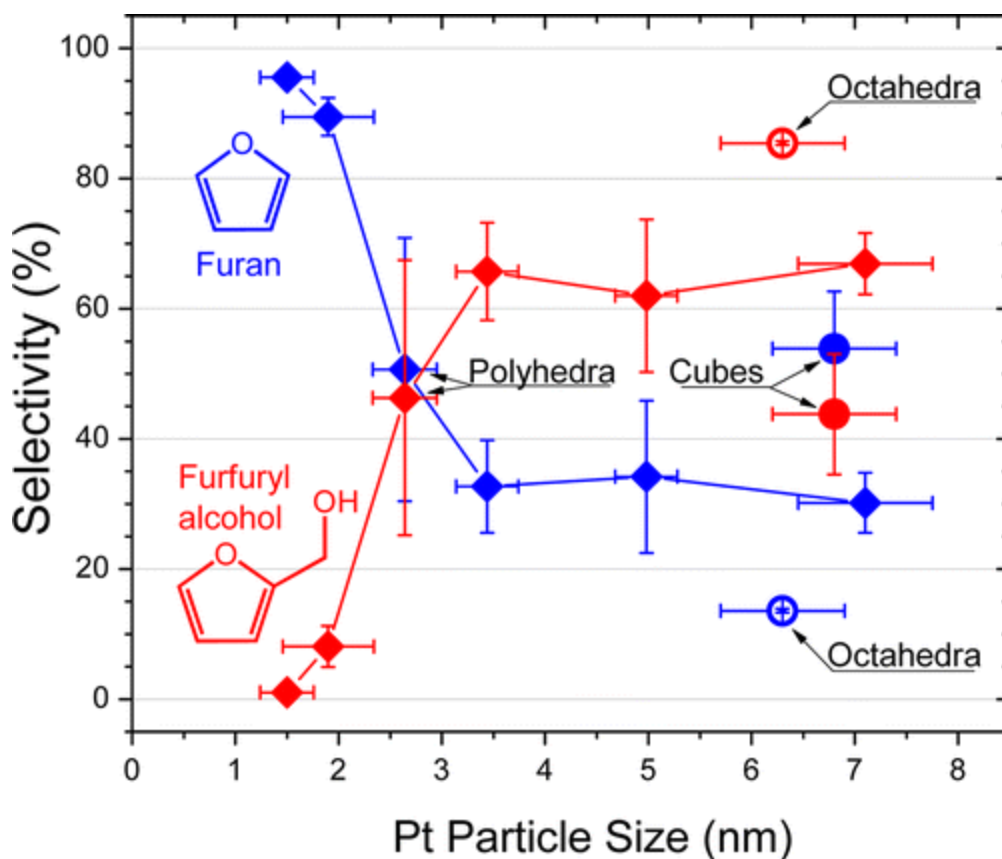


**Figure 6.** Steady-state product selectivities to furan (blue) and furfuryl alcohol (red) versus TEM-projected Pt particle sizes measured at 473 K under 1300 h<sup>-1</sup> of GHSP flow of reactant mixture containing 9.3 kPa furfural and 93 kPa H<sub>2</sub>.

The primary catalytic reactions leading to formation of furan and furfuryl alcohol dominate the reaction network, as combined product selectivities to these two compounds are in excess of 90% in the 443–513 K temperature range. The formation of furfuryl alcohol is favored on the lower side of the temperature range, while the formation of furan becomes dominant on the higher side of the temperature range. This temperature dependence is likely to be due to the thermodynamic limitation of the decarbonylation/hydrogenation reaction network, as the endothermic decarbonylation reaction becomes more favorable at higher temperatures, opposing the exothermic hydrogenation reaction, which becomes more favorable at lower temperatures.

Figure 7 shows the apparent activation energies measured for formation of furan, furfuryl alcohol, and total conversion of furfural as a function of size for polyhedrally shaped Pt NPs. The apparent  $E_A$  for furan formation is on the order of 60 kJ mol<sup>-1</sup> and is Pt NP size independent, while the apparent  $E_A$  of furfuryl alcohol formation is highest (107 kJ mol<sup>-1</sup>) for very small Pt NPs (1.5 nm) but drops rapidly as particle size increases to 1.9 nm (32 kJ mol<sup>-1</sup>) and to 5 nm (12 kJ mol<sup>-1</sup>). The total conversion apparent activation energy (not shown on the plot) also drops

from the value of 60 kJ mol<sup>-1</sup> for the 1.5 nm Pt NPs to 34 kJ mol<sup>-1</sup> for the Pt NP sizes in between 3.6 and 7.1 nm.

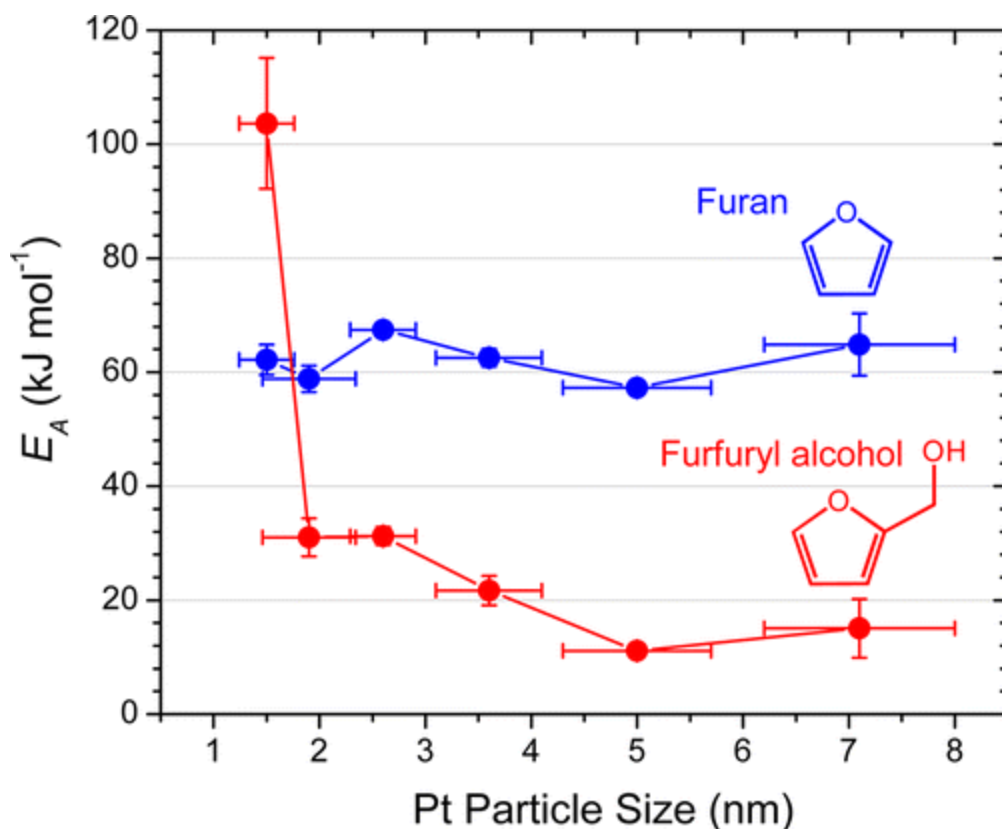


**Figure 7.** Apparent activation energies of furan (blue) and furfuryl alcohol (red) formation versus TEM-projected Pt particle sizes measured in the 468–503 K temperature range under 1300 h<sup>-1</sup> of GHSP flow of reactants mixture containing 9.3 kPa furfural and 93 kPa H<sub>2</sub>.

Figure 8 shows turnover rates determined for the decarbonylation and hydrogenation reaction paths as a function of Pt NPs size. Decarbonylation of furfural to furan is clearly a structure sensitive reaction as the TOR values decrease more than a factor of 12 upon increasing the Pt particle size from 1.5 to 2.6 nm, followed by a moderate increase in the TOR values upon further increase of Pt particle size from 2.6 to 7.1 nm.

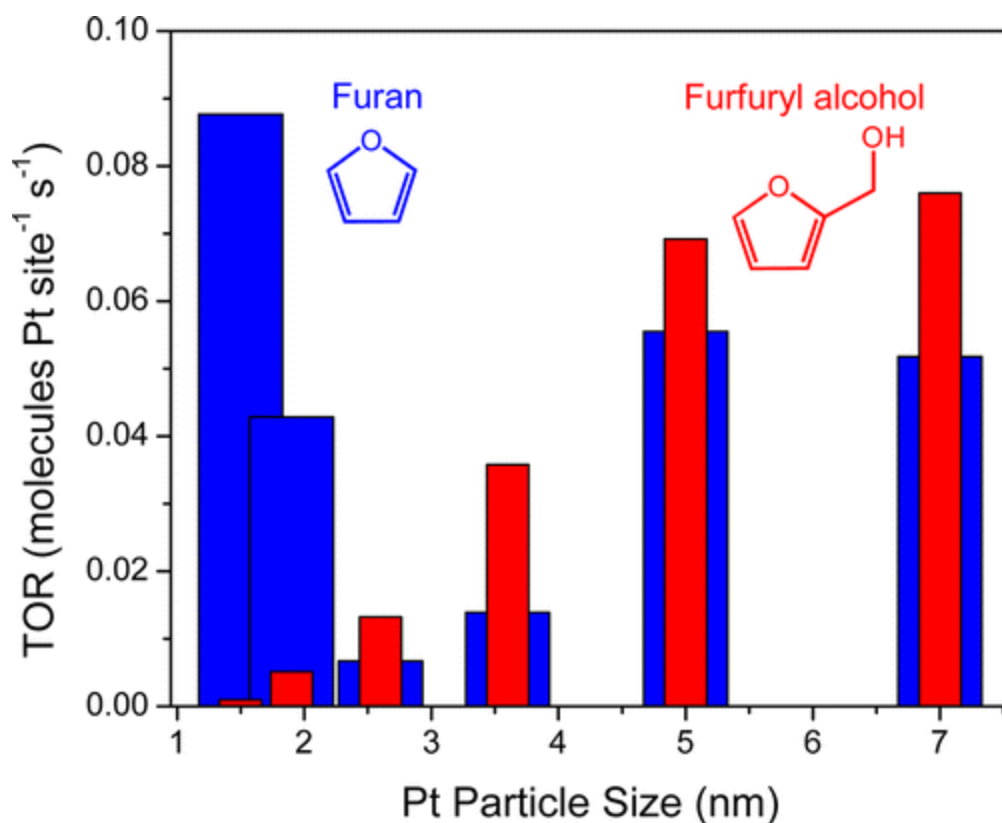


**Figure 8.** TOR values (estimated by using the active site numbers determined from ethylene hydrogenation) plotted against mean Pt particle size measured at 473 K under 1300 h<sup>-1</sup> of GHSV flow of reactants mixture containing 9.3 kPa furfural and 93 kPa H<sub>2</sub>. The C<sub>2</sub>H<sub>4</sub> hydrogenation study was performed at 101.35 kPa of total pressure at 265 K in a 100 cc/min flow containing 1.33 kPa C<sub>2</sub>H<sub>4</sub> and 13.3 kPa H<sub>2</sub> with balance of He.

The “U”-shaped dependence of TOR on Pt NP size can be explained by a presence of two different types of catalytically active surface sites. The first site is highly active and available only on the small particles (below 2 nm), while the second site is less active and becomes available only as a Pt particle size increases above 2.5 nm. Alternatively, this behavior could be related to the electronic effects of a single catalytic site as a function of Pt NPs size. Indeed, the very small Pt NPs could be electron-deficient, and this deficiency could substantially facilitate the rate of catalytic turnover, compared to the activity of the same site on “more” metallic larger size Pt NPs. The furfural’s carbonyl group hydrogenation is, also structure-sensitive, evident by more than 40-fold increase in TOR values upon increasing the Pt particle size from 1.5 to 5 nm and also by the change of the apparent activation energy.

### 3.4 Conclusion

Vapor phase furfural hydrogenation studies were performed on a series of silica supported uniform Pt NP catalysts. It was found that the product selectivity was highly dependent on the size and shape of the NP catalysts. Small particles were found to give predominantly furan as a product, via decarbonylation, while larger sized particles yielded both



furan and furfuryl alcohol, the carbonyl hydrogenation product. Octahedral particles were found to be selective to furfuryl alcohol, while cube shaped particles produced an equal amount of furan and furfuryl alcohol. The differences in selectivity have been attributed to the presence of two different catalytically active sites which change in ratio with NP size and shape.

### 3.5 References

1. Boudart, M. In *Catalysis by Support Metals*; Eley, D. D., Ed.; Advances in Catalysis and Related Subjects; Elsevier: New York, 1969; Vol. 20, pp 153-166.
2. Somorjai, G. A.; Park, J. Y. Molecular Factors of Catalytic Selectivity. *Angew. Chem., Int. Ed* **2008**, *47*, 9212-9228.
3. Zhou, B.; Hermans, S.; Somorjai, G. A., Eds.; In *Nanotechnology in Catalysis*; Kluwer Academic/ Plenum Publishers: New York, 2004; Vol. 1.
4. Kuhn, J. N.; Huang, W.; Tsung, C. K.; Zhang, Y.; Somorjai, G. A. Structure Sensitivity of Carbon-Nitrogen Ring Opening: Impact of Platinum Particle Size From Below 1 to 5 nm Upon Pyrrole Hydrogenation Product Selectivity Over Monodisperse Platinum Nanoparticles Loaded onto Mesoporous Silica. *J. Am. Chem. Soc.* **2008**, *130*, 14026-14027.
5. Tsung, C. K.; Kuhn, J. N.; Huang, W.; Aliaga, C.; Hung, L. I.; Somorjai, G. A.; Yang, P. Sub-10 nm Platinum Nanocrystals with Size and Shape Control: Catalytic Study for Ethylene and Pyrrole Hydrogenation. *J. Am. Chem. Soc.* **2009**, *131*, 5816-5822.
6. Grass, M.; Rioux, R. M.; Somorjai, G. A. Dependence of Gas-Phase Crotonaldehyde Hydrogenation Selectivity and Activity on the Size of Pt Nanoparticles (1.7–7.1 nm) Supported on SBA-15. *Catal. Lett.* **2009**, *128*, 1-8.
7. Aliaga, C.; Tsung, C. K.; Alayoglu, S.; Komvopoulos, K.; Yang, P.; Somorjai, G. A. Sum Frequency Generation Vibrational Spectroscopy and Kinetic Study of 2-Methylfuran and 2,5-Dimethylfuran Hydrogenation over 7 nm Platinum Cubic Nanoparticles. *J. Phys. Chem. C* **2011**, *115*, 8104-8109.
8. Elliott, D. C.; Hart, T. R. Catalytic Hydroprocessing of Chemical Models for Bio-oil. *Energy Fuels* **2009**, *23*, 631-637.
9. Rao, R. S.; Baker, R. T. K.; Vannice, M. A. Furfural Hydrogenation over Carbon-Supported Copper. *Catal. Lett.* **1999**, *60*, 51-57.
10. Sitthisa, S.; Sooknoi, T.; Ma, Y.; Balbuena, P. B.; Resasco, D. E. Kinetics and Mechanism of Hydrogenation of Furfural on Cu/SiO<sub>2</sub> Catalysts. *J. Catal.* **2011**, *277*, 1-13.
11. Lejemble, P.; Gaset, A.; Kalck, P. From Biomass to Furan Through Decarbonylation of Furfural Under Mild Conditions. *Biomass* **1984**, *4*, 263-274.

12. Jung, K. J.; Gaset, A.; Molinier, J. Furfural Decarbonylation Catalyzed by Charcoal Supported Palladium: Part II — A Continuous Process. *Biomass* **1988**, *16*, 89-96.
13. Zhang, W.; Zhu, Y.; Niu, S.; Li, Y. A Study of Furfural Decarbonylation on K-doped Pd/Al<sub>2</sub>O<sub>3</sub> Catalysts. *Biomass* **2011**, *335*, 71-81.
14. Kijenski, J.; Winiarek, P.; Paryjczak, T.; Lewicki, A.; Mikolajska, A. Platinum Deposited on Monolayer Supports in Selective Hydrogenation of Furfural to Furfuryl Alcohol. *Appl. Catal. A* **2002**, *233*, 171-182.
15. Sitthisa, S.; Resasco, D. E. Hydrodeoxygenation of Furfural Over Supported Metal Catalysts: A Comparative Study of Cu, Pd and Ni. *Catal. Lett.* **2011**, *141*, 784-791.
16. Rioux, R. M.; Song, H.; Hoefelmeyer, J. D.; Yang, P.; Somorjai, G. A. High-Surface-Area Catalyst Design: Synthesis, Characterization, and Reaction Studies of Platinum Nanoparticles in Mesoporous SBA-15 Silica. *J. Phys. Chem. B* **2005**, *109*, 2192-2202.
17. Han, Y.; Lee, S. S.; Ying, J. Y. Spherical Siliceous Mesocellular Foam Particles for High-Speed Size Exclusion Chromatography. *Chem. Mater.* **2007**, *19*, 2292-2298.
18. Schmidt-Winkel, P.; Lukens, W. W.; Yang, P.; Margolese, D. I.; Lettow, J. S.; Ying, J. Y.; Stucky, G. D. Microemulsion Templating of Siliceous Mesostructured Cellular Foams with Well-Defined Ultralarge Mesopores. *Chem. Mater.* **2000**, *12*, 686-696.

# Chapter 4

## Reforming of C<sub>6</sub> Hydrocarbons over Model Pt Nanoparticle Catalysts

### Abstract

Size-controlled model Pt nanoparticle catalysts, synthesized by colloidal chemistry, were used to study the hydrogenative reforming of three C<sub>6</sub> hydrocarbons in mixtures with 5:1 molar excess of H<sub>2</sub>: methylcyclopentane, n-hexane and 2-methylpentane. We found a strong particle size dependence on the distribution of different reaction products for the hydrogenolysis of methylcyclopentane. The reactions of 50 Torr methylcyclopentane in 250 Torr H<sub>2</sub> at 320 °C, using 1.5 and 3.0 nm Pt nanoparticles produced predominantly C<sub>6</sub> isomers, especially 2-methylpentane, whereas 5.2 and 11.3 nm Pt nanoparticles were more selective for the formation of benzene. For the hydrogenolysis of n-hexane and 2-methylpentane, strong particle size effects on the turnover rates were observed. Hexane and 2-methylpentane reacted up to an order of magnitude slower over 3.0 nm Pt than over the other particle sizes. At 360 °C the isomerization reactions were more selective than the other reaction pathways over 3.0 nm Pt, which also yielded relatively less benzene.

\* This chapter covers similar material as in Alayoglu, S.; Pushkarev, V.V.; Musselwhite, N.; An, K.; Beaumont, S.K.; Somorjai, G.A. *Nano Lett.* **2012**, *12*, 5196-5201. — reproduced with permission, copyright 2012 Springer Science+Business Media, LLC.

## 4.1 Introduction

Structure-sensitive multi-product reactions, such as the hydrogenation of crotonaldehyde, pyrrole and furan, show strong dependence of reactivity on particle size and/or shape over Pt crystals and nanoparticles.<sup>1-5</sup> Hence, model nanoparticle catalysts with well-defined structural and chemical properties such as particle size, morphology, crystallographic orientation, and redox state offer a unique way of assessing surface reactivity and reaction mechanisms for heterogeneous metal-catalyzed hydrocarbon transformations. The hydrogenative reforming of C<sub>6</sub> hydrocarbons are multi-path and multi-product reactions, which yield C<sub>6</sub> isomers (i.e. hexane and its derivatives) via hydrogenative ring opening/skeletal re-arrangement<sup>6-12</sup>, benzene via ring enlargement/closure and aromatization<sup>11-14</sup>, as well as shorter chain hydrocarbons (i.e. C<sub>1</sub>–C<sub>5</sub> isomers) via hydrogenolysis.<sup>15,16</sup> Pt catalysts have been reported to be selective for the formation of branched hexane derivatives (i.e. 2-methylpentane and 3-methylpentane) during the reforming of methylcyclopentane.<sup>6,7,17-20</sup> Recently, the strong correlation between the Pt particle morphology and catalytic reactivity for reactions of 10 Torr methylcyclopentane and 50 Torr H<sub>2</sub> at 240 °C has been documents.<sup>21</sup> It was found that ~6 nm Pt nanoparticles with spherical, cubo-octahedral, octahedral and cubic morphologies (and the corresponding crystallographic shapes) exhibited distinct surface dependent reactivity during this catalytic reaction.

In this paper, we focus on the hydrogenative reforming reactions of three C<sub>6</sub> hydrocarbons - methylcyclopentane, hexane and 2-methylpentane - over model Pt nanoparticle catalysts with mean Pt particle sizes in the range between 1.5 and 11.3 nm. The catalytic reactivity of well-characterized Pt nanoparticles is evaluated under 50 Torr hydrocarbon and 250 Torr H<sub>2</sub>, and in the temperature range of 280–360 °C. We find a strong correlation between the surface reactivity and the Pt particle size for these C<sub>6</sub> hydrocarbon transformations. For the hydrogenolysis of methylcyclopentane at 320 °C, Pt nanoparticle sizes of 3.0 nm and below lead to the production of C<sub>6</sub> alkanes via isomerization, specifically 2-methylpentane, while nanoparticle sizes of 5.2 nm and above yield the formation of benzene via ring enlargement and aromatization. For the hydrogenative reforming of the acyclic alkanes: hexane and 2-methylpentane, we isolate a rather weak particle size dependence on the product distribution. At 360 °C, 3.0 nm Pt nanoparticles isomerize both hexane and 2-methylpentane to 3-methylpentane more selectively than any other size of Pt nanoparticles. However, 3.0 nm Pt nanoparticles perform poorly for the conversion of C<sub>6</sub> alkanes (4–10 times diminished) as compared to 1.5 and 5.2 nm Pt nanoparticles.

## 4.2 Experimental

### 4.2.1 Material Preparation and Characterization

Polyvinylpyrrolidone (PVP)-capped Pt nanoparticles with average particle sizes of  $1.5 \pm 0.26$ ,  $3.0 \pm 0.45$ ,  $5.2 \pm 0.68$  and  $11.3 \pm 1.10$  nm were synthesized and supported in mesoporous silica (SBA-15 or MCF-17) according to previously reported protocols.<sup>21</sup> Typically, Pt(acac)<sub>2</sub> (acac=acetylacetonate) and/or H<sub>2</sub>PtCl<sub>6</sub> precursor salts were dissolved in alcohols (i.e. methanol or ethylene glycol) in the presence of PVP, and reacted at boiling solvent temperatures. The as-synthesized nanoparticles were washed and redispersed with chloroform. To prepare the supported catalysts, nanoparticle colloids were mixed with mesoporous silica support giving a nominal metal loading of 1 wt.%. The mixtures were sonicated for 1 h, and then supported nanoparticle catalysts were collected by centrifugation. To remove excess PVP, nanoparticle catalysts were washed in 20 vol.% ethanol in acetone 7 times. The 1.5 and 5.2 nm Pt

nanoparticles were supported on SBA-15 (with an average pore size of 9.5 nm), while MCF-17 (with pore sizes in the range of 20–50 nm) was used to support the 11.3 nm Pt nanoparticles. Both SBA-15 and MCF-17 were used separately to support the 3.0 nm Pt nanoparticles and similar catalytic activities and selectivities were obtained for the resulting supported catalysts. As-synthesized nanoparticles were characterized by TEM (JEOL 2100 LaB<sub>6</sub>). The supported catalysts were characterized by inductively coupled plasma atomic emission spectroscopy, (ICP-AES), ethylene hydrogenation, and TEM (JEOL 2100-FE) and reported elsewhere.<sup>21</sup> Turnover rates were calculated from the measured reaction rates and comparison with the number of active surface sites as obtained by using ethylene hydrogenation as a probe reaction to titrate the surface sites.

#### 4.2.2 Catalytic Testing

The catalytic testing was performed using a home-built plug-flow reactor connected to a Hewlett Packard 5890 gas chromatograph. A 10 % SP-2100 on 100/120 Supelcoport packed column in line with a FID detector was used to separate and analyze the C<sub>1</sub>–C<sub>6</sub> hydrocarbons. Mass flow controllers were calibrated using a bubble flow-meter and used to introduce the ultra-high purity (99.9999 % Praxair) H<sub>2</sub> and He gases. Saturated vapor pressure C<sub>6</sub> hydrocarbons (methylcyclopentane, GC grade Aldrich; n-hexane, ReagentPlus® ≥99 % Aldrich; and 2-methylpentane, ≥99 % Aldrich) at room temperature (23 °C) were introduced to the reactor using a bubbler. The reactant flow was carefully calibrated at different temperatures and partial pressures of He carrier. A total flow of 40 ml/min was used. Total pressure under flow conditions, measured by using a Baratron capacitance gauge located above the reactor bed, was 790 Torr. Partial pressure of reactants was calculated by using the known temperature vs. saturated vapor pressure plots and was 50 Torr with 5:1 H<sub>2</sub> excess. 100–250 mg charges of the catalysts were diluted by quartz sand with average granular size of 0.4 mm and loaded in the reactor bed. The actual weight of catalyst used was selected to give similar total conversions in each case. The catalysts were reduced at 260 °C for 2 h under a flow of 210 Torr H<sub>2</sub> in 550 Torr He prior to catalytic testing. The catalytic activity and selectivity were evaluated for total conversions below 5 %.

### 4.3 Results

Size controlled Pt nanoparticles have been evaluated for the hydrogenolysis of three C<sub>6</sub> hydrocarbons to investigate possible reforming reaction pathways. For this, 50 Torr of any C<sub>6</sub> hydrocarbon in a mixture with 250 Torr H<sub>2</sub> was reacted at temperatures between 280 and 360 °C over Pt nanoparticles with the average particle sizes of  $1.5 \pm 0.26$ ,  $3.0 \pm 0.45$ ,  $5.2 \pm 0.68$  and  $11.3 \pm 1.10$  nm. Figure 1 shows representative TEM pictures of the post-reaction Pt nanoparticle catalysts. As-synthesized nanoparticles, and pre- and post-reaction nanoparticle catalysts are polyhedral in shape and nanocrystalline. The selectivities for the different reaction pathways, namely isomerization, cyclization (and/or dehydrogenation to cyclic olefins), aromatization and cracking, are shown at 280 °C (low temperature), 320 °C (intermediate temperature) and 360 °C (high temperature) for methylcyclopentane (MCP), 2-methylpentane (2-MP) and n-hexane (Hex) in Figures 2, 3, and 4 for the different hydrocarbons, respectively. No significant sintering was detected from the post-reaction TEM imaging of the catalysts, as shown in Figure 1.

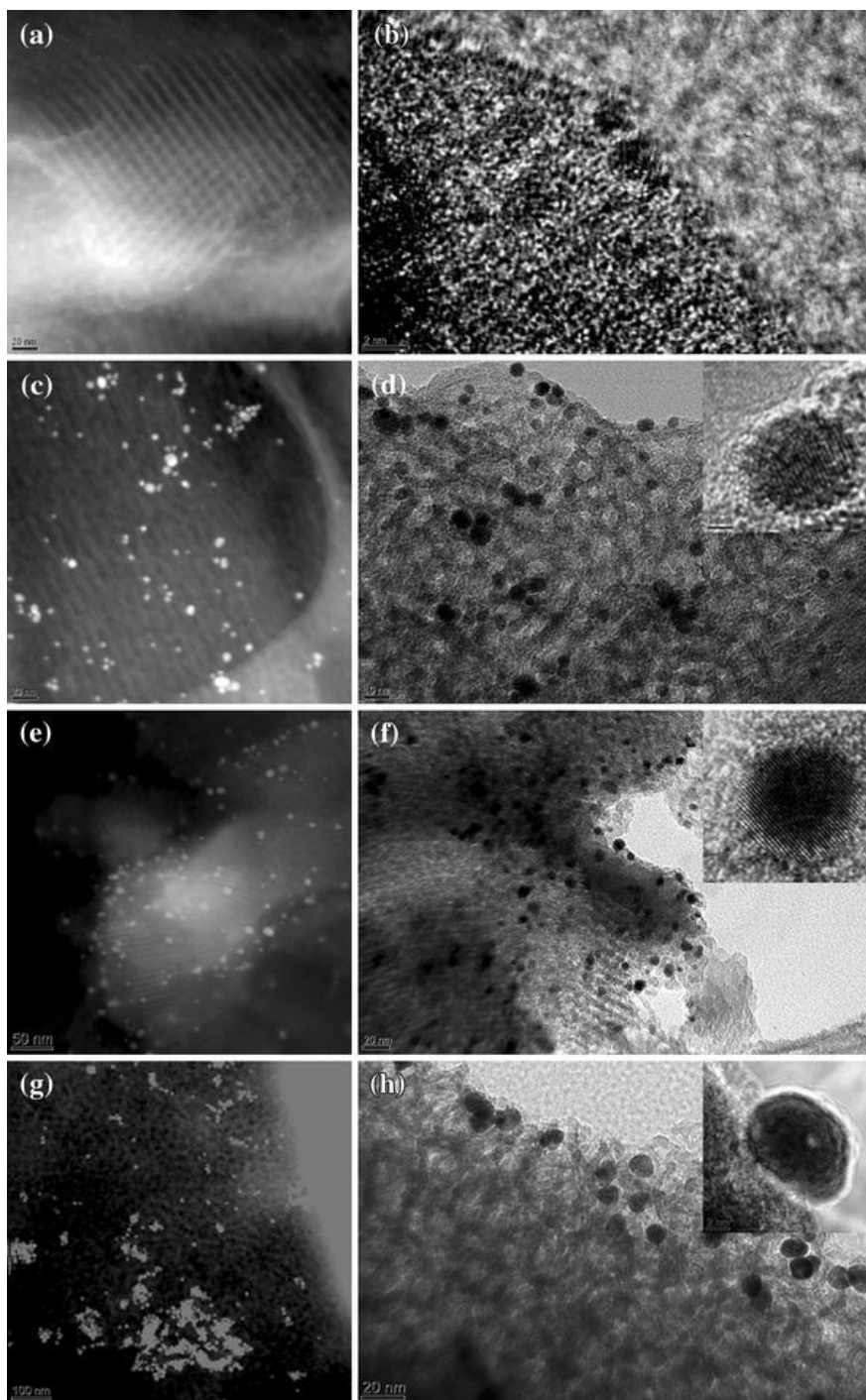


**Figure 1.** Representative dark field and bright field TEM images of the post-MCP/H<sub>2</sub> reaction catalysts: a,b) 1.5 nm Pt in SBA-15 c,d) 3.0 nm Pt in SBA-15 e, f) 5.2 nm Pt in SBA-15 and g,h) 11.3 nm Pt in MCF-17. Insets show the HRTEM pictures.

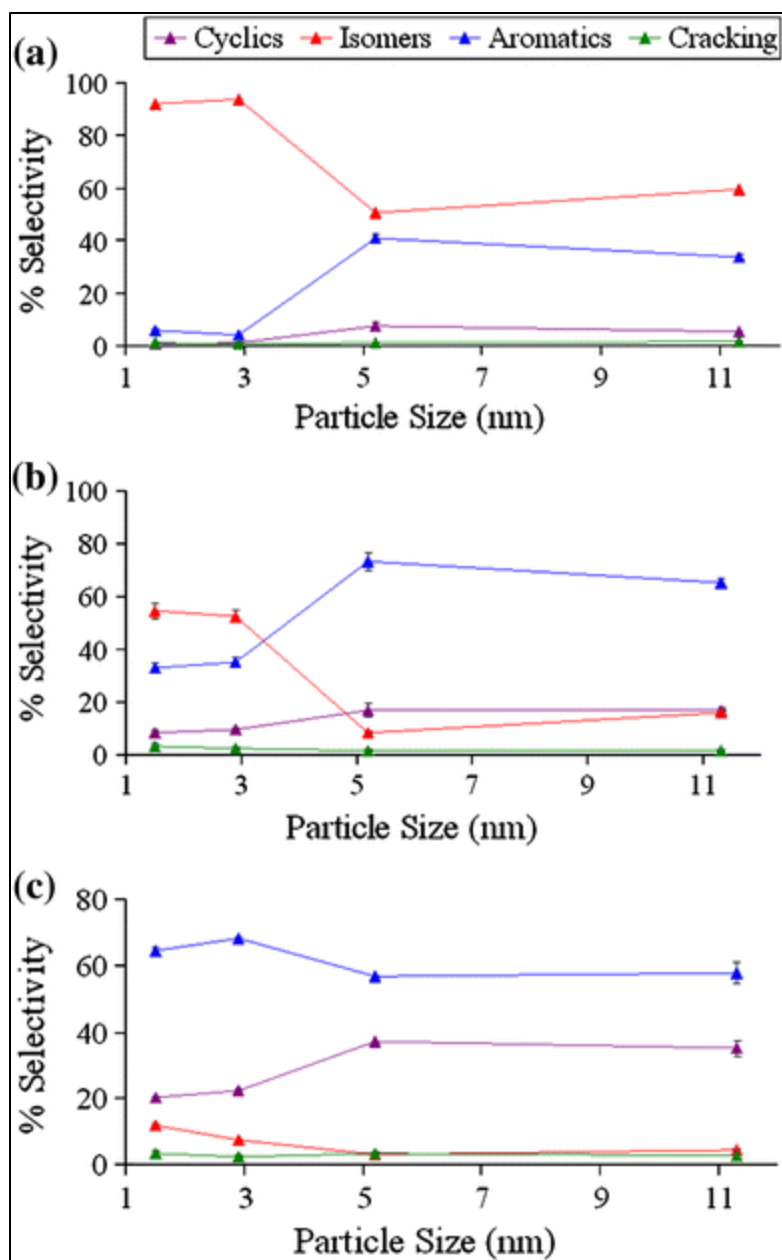


**Figure 2.** Plots of % selectivity versus particle size for 50 Torr methylcyclopentane and 250 Torr H<sub>2</sub> at a 280 °C, b 320 °C and c 360 °C. Different reaction pathways are color-coded: red for isomerization, blue for aromatization, purple for cyclization and green for cracking.

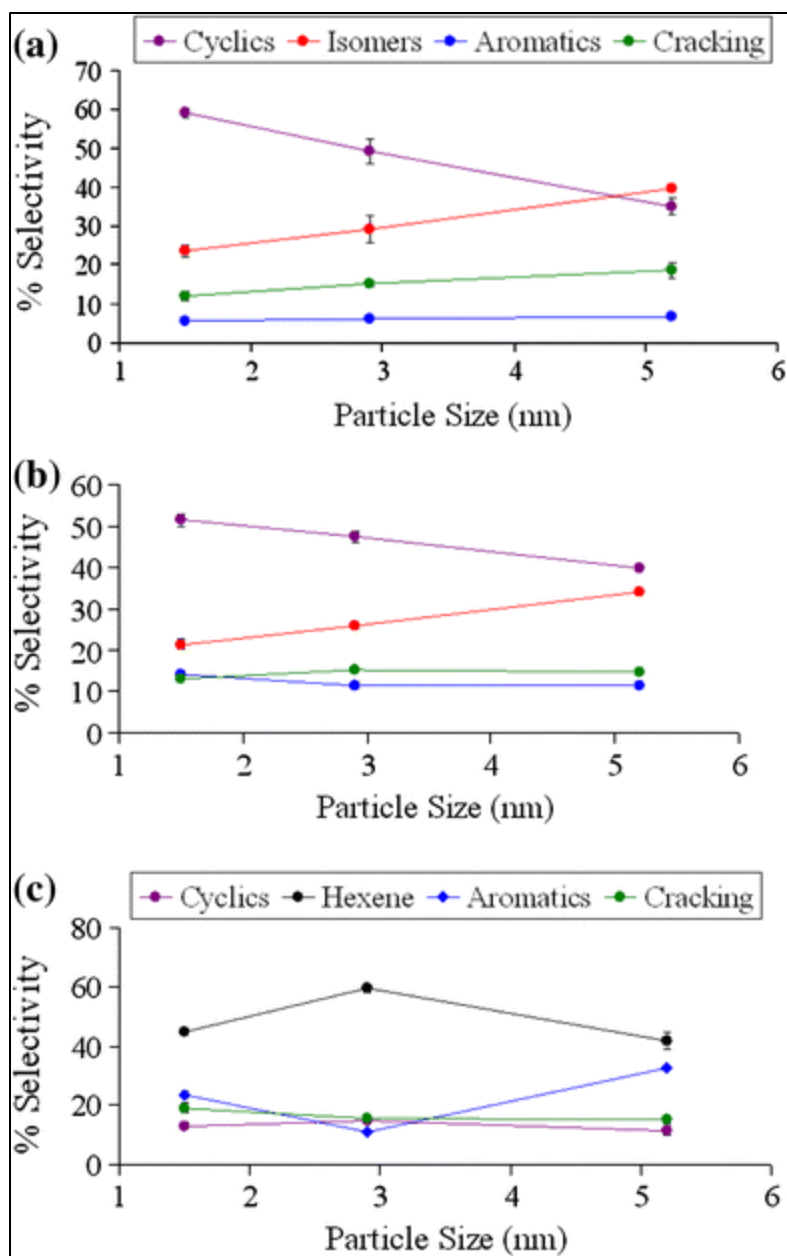


**Figure 3.** Plots of % selectivity versus particle size for 50 Torr n-hexane and 250 Torr H<sub>2</sub> at a 280 °C, b 320 °C and c 360 °C. Different reaction pathways are color-coded as red for isomerization, blue for aromatization, purple for cyclization, green for cracking and black for dehydrogenation (to hexene).



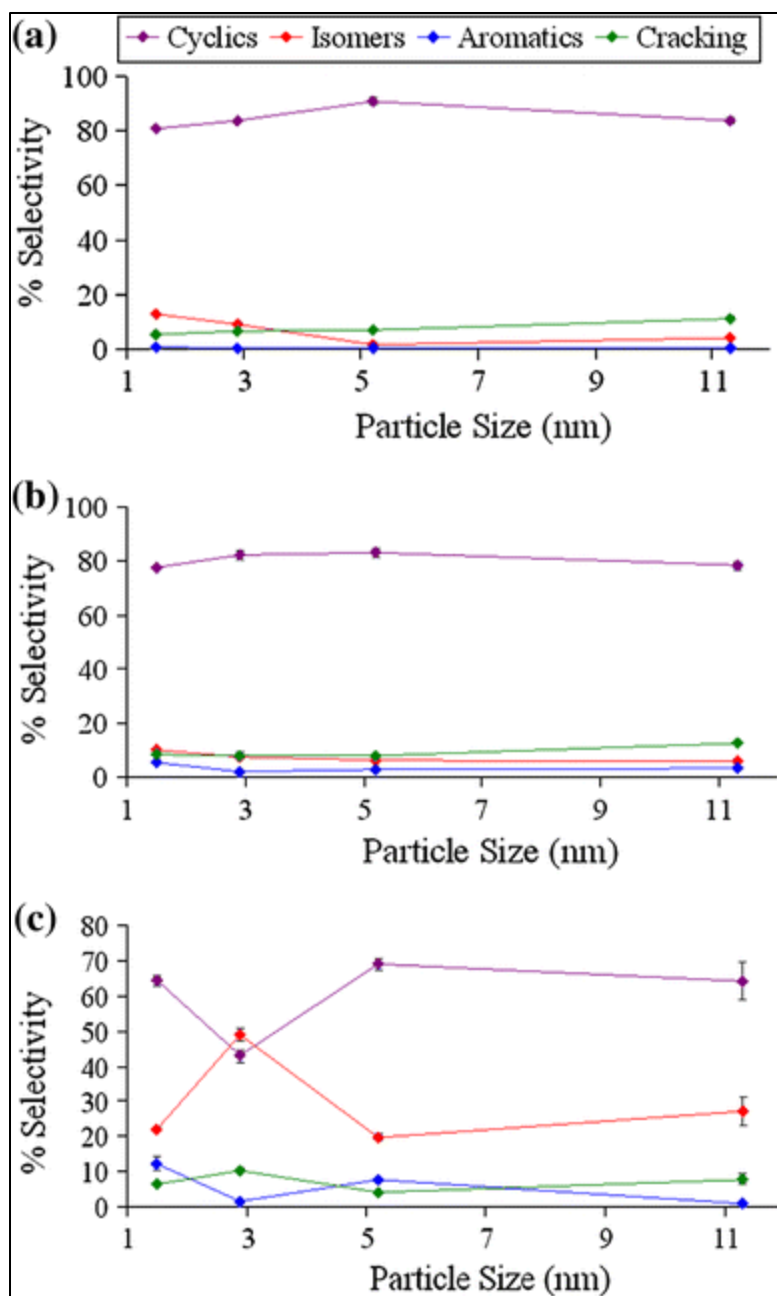


**Figure 4.** Plots of % selectivity versus particle size for reaction of 50 Torr 2-methylpentane and 250 Torr H<sub>2</sub> at a 280 °C, b 320 °C and c 360 °C. Different reaction pathways are color-coded: red for isomerization, blue for aromatization, purple for cyclization and green for cracking.

The selectivity for the MCP/H<sub>2</sub> reaction is shown in Figure 2. Isomerization was the dominant reaction pathway for all Pt particle sizes at 280 °C. Small Pt nanoparticles, with mean size 3.0 nm and below, formed almost exclusively C<sub>6</sub>-isomers under low operating temperature conditions (280 °C). Larger Pt nanoparticles, on the other hand, produced mixtures of C<sub>6</sub>-isomers and benzene in comparable amounts at low temperatures (280 °C, Figure 2a). At 320 °C, small Pt nanoparticles yielded C<sub>6</sub> isomers and benzene, isomerization remaining the dominant reaction pathway. However, for large Pt nanoparticles benzene was the major product at this temperature (Figure 2b). At 360 °C aromatization became the main reaction pathway with a selectivity of greater than 55 % for all Pt particle sizes. Large Pt nanoparticles also led to the formation of methylcyclopentenenes, whereas smaller Pt nanoparticles produced some C<sub>6</sub>-isomers in addition to methylcyclopentenenes (Figure 2c). The selectivity for cracking hydrogenolysis stayed below 10 % for all Pt particle sizes and across all temperatures studied.

Next, we investigated the hydrogenative reforming of acyclic C<sub>6</sub> hydrocarbons to isolate the potential role of ring-opening products on the formation of benzene. It was found that there was only a weak particle size dependence and a minor temperature effect on the product selectivity for the reforming of acyclic C<sub>6</sub> hydrocarbons. Figure 3 shows the selectivity for the observed reaction pathways for the reforming of n-hexane, the linear C<sub>6</sub>-isomer, at different temperatures. At 280 °C, the product distribution showed only a weak particle size dependence. 1.5 nm Pt nanoparticles produced selectively more cyclics (60 % MCP) whereas 5.2 nm Pt nanoparticles more selectively isomerized n-hexane (~40 %) to 2-MP and 3-MP (Figure 3a). Broadly speaking, the isomerization and cyclization pathways diminished upon increasing temperature to 360 °C in favor of dehydrogenation to hexene for all the particle sizes (Figure 3c). Benzene production, on the other hand, slightly increased and hence reached ~30 % over 1.5 and 5.2 nm Pt nanoparticles. 3.0 nm Pt nanoparticles, however, did not produce any significant fractions of benzene in the temperature range studied.

The reforming of 2-MP, a branched C<sub>6</sub> alkane, showed similar product distributions for different particle sizes, but did exhibit a strong particle size dependence on catalytic activity. C<sub>5</sub> cyclization to MCP (and methylcyclopentenenes at 360 °C) was the main reaction pathway with almost invariably ~90 % selectivity at 280 °C and ~60 % selectivity at 360 °C (Figure 4a, c). The 1.5 and 3.0 nm particles exhibited slightly higher selectivity towards C<sub>6</sub> isomerization than the 5.2 and 11.3 nm particles. Specifically, at 280 and 320 °C, n-hexane was the primary C<sub>6</sub> alkane produced, while 3-MP and/or dimethylbutanes were generated in higher yield at 360 °C. Benzene formation was less than 10 % at all temperatures studied.

Having provided a detailed description of the particle size dependent product distributions, we should discuss the relative turnover rates for the reforming of various C<sub>6</sub> hydrocarbons over size-controlled Pt nanoparticles, as this is equally important for a thorough assessment of the structure-sensitive hydrocarbon transformations over Pt. Figure 5 displays the plots of turnover rates versus mean Pt nanoparticle sizes for the hydrogenative reforming of these C<sub>6</sub> hydrocarbons (MCP, 2-MP and n-hexane).

For the hydrogenolysis of MCP at 280 and 320 °C, 5.2 nm Pt nanoparticles exhibited a peak in activity over the other particle sizes by a factor of 3 in turnover rate. However, the turnover rate dropped monotonically from 0.05 s<sup>-1</sup> for 1.5 nm Pt nanoparticles to 0.0013 s<sup>-1</sup> for 11.3 nm Pt nanoparticles at 360 °C (Figure 5a). It is important to note that the product distributions at 360 °C were significantly different from those at lower temperatures.

For the hydrogenative reforming of C<sub>6</sub> alkanes, 3.0 nm Pt nanoparticles performed poorly compared with the other particle sizes over the whole range of temperatures studied. The activity drop over 3.0 nm Pt nanoparticles was more pronounced for the hydrogenolysis of 2-MP, about an order of magnitude decrease compared to the 1.5 nm Pt nanoparticles at 360 °C (Figure 5b). Similarly, the hydrogenolysis rate of n-hexane at 360 °C was lower over 3.0 nm Pt nanoparticles by a factor of 7 compared to 5.2 nm Pt nanoparticles and a factor of 4 compared to 1.5 nm Pt nanoparticles. Interestingly, 3.0 nm Pt nanoparticles were more selective for the isomerization of C<sub>6</sub> alkanes at 360 °C whereas the other particle sizes selectively led to cyclization and aromatization reactions under identical conditions.

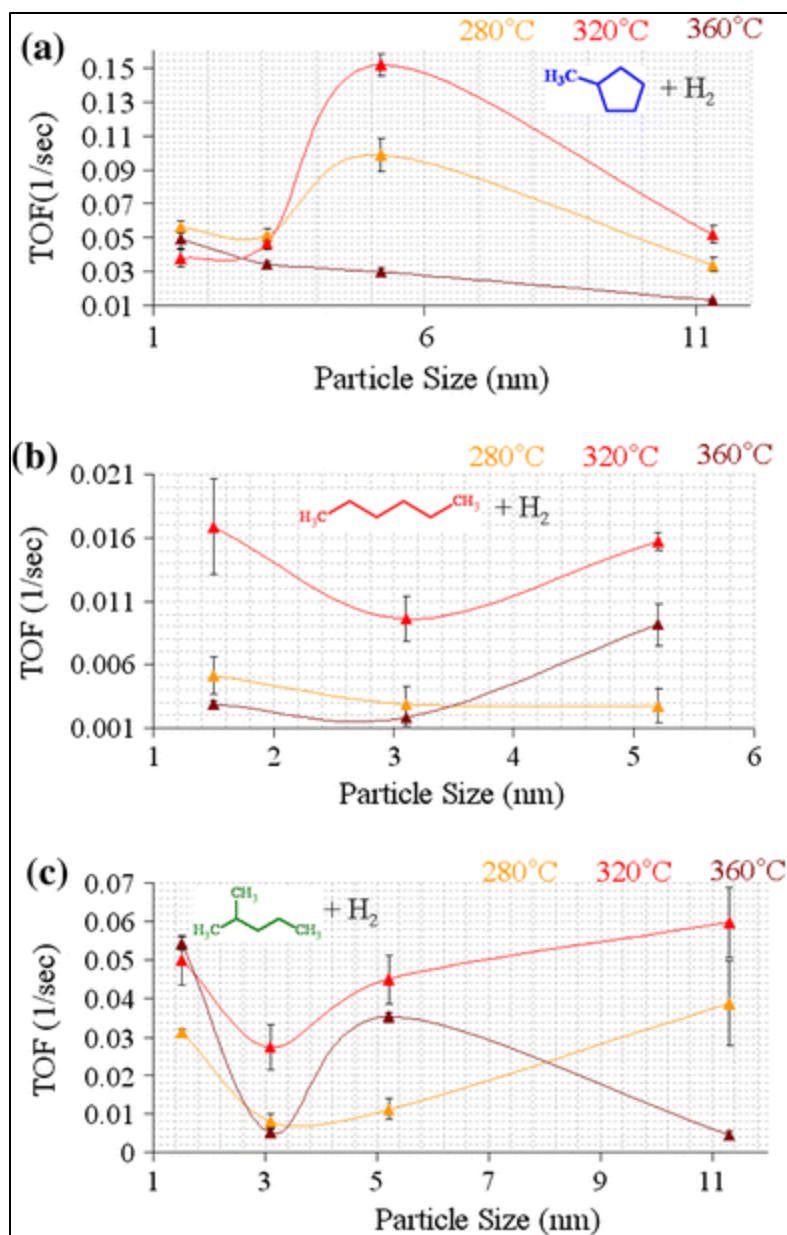


**Figure 5.** Plots of turnover frequency versus size for the hydrogenolysis of a methylcyclopentane, b n-hexane and c 2-methylpentane. Temperatures are color-coded as orange for 280 °C, red for 320 °C and brown for 360 °C.

## 4.4 Discussion

The results for the hydrogenative reforming of various C<sub>6</sub> hydrocarbons over size-controlled Pt nanoparticles reveal measurable particle size effects. We have isolated a strong particle size dependence of the product distribution for the hydrogenolysis of MCP. Specifically, Pt nanoparticles size 3.0 nm and below selectively favored the hydrogenative ring opening and produced C<sub>6</sub> alkanes whereas large Pt nanoparticles size 5.2 nm and above yielded benzene via ring enlargement and aromatization. Furthermore, we have shown the impact of Pt particle sizes on the turnover rates along with selectivity for the reforming of C<sub>6</sub> alkanes, where 3.0 nm Pt nanoparticles were distinctly less active and yet more selective for the skeletal rearrangement to other C<sub>6</sub> isomers.

The findings concerning the catalytic reactivity over uniform Pt nanoparticles in the 1.5–11.3 nm range are partly consistent with those that are reported in the literature. Paál and co-workers studied the n-hexane/H<sub>2</sub> reaction over regenerated 1.8 nm Pt/SiO<sub>2</sub> (EUROPT) and found that cyclization was the dominant reaction pathway (~43 %) followed by isomerization (~23 %) at 330 °C and 10 Torr hexane, 120 Torr H<sub>2</sub>.<sup>22</sup> They also detected some hydrogenolysis cracking products (~13 %) and benzene (~12 %) in agreement with our results for 50 Torr n-hexane and at 5:1 H<sub>2</sub> excess and 320 °C. Likewise, Chandler et al. documented the selective formation of cyclic hydrocarbons over 3.0 nm Pt/SiO<sub>2</sub> for 49 Torr n-hexane and 200 Torr H<sub>2</sub> at 400 °C.<sup>23</sup> These studies were carried out with Pt/SiO<sub>2</sub> catalysts that were not uniform in size. In these studies, using uniform catalysts, we have shown a marked difference between 1.5 and 5.2 nm Pt nanoparticles concerning the preferred reaction pathways under similar conditions (Figure 3c).

The hydrogenolysis of 2-MP over unsupported Pt crystals and 3.0 nm Pt supported on alumina was reported by Garin et al. at 350 °C and at very high H<sub>2</sub> excess (151:1).<sup>24</sup> They found that cyclization was the main reaction pathway with selectivities in the range of 40–50 %. This is in good accord with the findings over 3.0 nm Pt nanoparticles at 360 °C and at 5:1 H<sub>2</sub> excess. However, a deviation from this observation was detected for the other uniform Pt nanoparticles as shown in Figure 4c. Gault and co-workers also reported the formation of 2,3-dimethylbutane during the hydrogenative reforming of 2-methylpentane over Pt films, which they attributed to a mechanism that involved a  $\alpha$ ,  $\gamma$  di-sigma adsorbed intermediate.<sup>11</sup> In studies for the reforming of 2-methylpentane, the selectivity for the formation of dimethylbutanes was only moderate (~10 %) even at elevated temperature, except the 11.3 nm Pt catalyst (i.e. large enough to be compared to bulk particle/film) which produced dimethylbutanes in significant fractions (~30 %) at 360 °C.

The hydrogenative reforming of C<sub>6</sub> hydrocarbons indicated a subtle dependence of catalytic reactivity on Pt nanoparticle sizes. To help in assessing the reforming mechanism over Pt and to isolate the most likely reaction sites, we looked into a provisional correlation between the observed reactivity and size dependent surface coordination site distributions. For this purpose, we employed the methodology originally developed by Van Hardeveld and Hartog.<sup>25</sup> We used a modified cube-octahedron model, also described by Van Hardeveld and Hartog, for which (111) and (100) planes were covered by an extra layer of atoms, giving additional (110) and (311) planes. This way, we obtained model polyhedral clusters that mimic the as-synthesized nanoparticles as well as the post-reaction supported catalysts shown in Figure 1. Then, coordination numbers (CNs) of surface atoms were calculated by using the magic number algorithms given in by Van Hardeveld and Hartog.<sup>25</sup> Corner sites were defined as surface atoms

with CNs of 5 and 6, edge sites as those of 7 and 8, and terraces a coordination number of 9. The distributions of different surface sites for cluster sizes from 1.6 to 11.5 nm are depicted in Figure 6. Based on this model, the spherical particles in the size range of 1.5–11.3 nm exhibit a constant fraction of edge sites ( $\sim 0.3$ ). More specifically, 1.5 nm particles possess the highest fraction of corner atoms, 3.0 nm particles have more edge atoms than corner and terrace atoms, while 5.2 nm particles possess the comparable fractions of edge and terrace atoms and 11.3 nm particles have terrace atoms maximized.

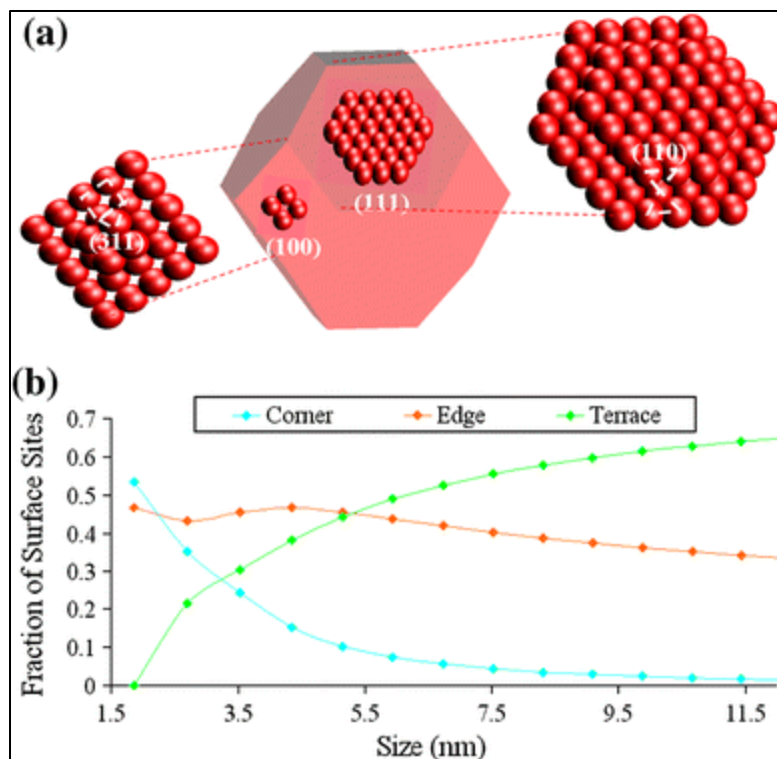


**Figure 6.** a) A modified cubo-octahedron cluster model showing the crystal faces with the extra atom planes superimposed in the [111] and [100] directions. b) A plot of fraction of surface sites versus size for the modified cubo-octahedron cluster model.

A tentative comparison between the observed catalytic reactivity and the calculated distribution of surface coordination sites shows similarities. First, small Pt nanoparticles size 3.0 nm and below would have higher fractions of corner and edge atoms and were catalytically more selective for the hydrogenative ring opening and isomerization reactions of MCP. Moreover, 3.0 nm Pt nanoparticles led to the isomerization of 2-MP and n-hexane more selectively than 1.5 nm Pt nanoparticles, yet they were the least active of all the particle sizes studied. Since the fraction of edge sites is broadly constant with varying particle size, the corner atoms are more likely to be the active catalytic sites for the isomerization of C<sub>6</sub> alkanes. Consistent with this hypothesis and our observations, Paal and co-workers<sup>22,26</sup>, with the aid of a

morphological model proposed by Gnutzman and Vogel<sup>27</sup>, attributed the isomerization of C<sub>6</sub> hydrocarbons to the presence of corner and edge sites. A sextet mechanism was proposed by Balandin, who predicted 6-atom (111) planes as the active sites for aromatization.<sup>28</sup> Consistent with this, we found Pt nanoparticles with large fractions of terrace atoms provided active catalytic sites for the ring enlargement and dehydrogenolysis of MCP. However, 1.5 nm Pt nanoparticles led to the ring closure and dehydrogenation of 2-MP and n-hexane in fractions comparable to that over the 5.2 nm Pt nanoparticles. This suggests a different reaction mechanism operative for the aromatization of C<sub>6</sub> hydrocarbons over the 1.5 nm Pt.

Finally, the peculiar deactivation of these size-controlled Pt nanoparticles for the hydrogenolysis of C<sub>6</sub> hydrocarbons at high temperatures can tentatively be attributed to the deposition of carbonaceous species from hydrocarbons during reaction. This is supported by the absence of particle sintering after reaction (Figure 1) and the known effects of temperature and hydrogen partial pressure on the loss of Pt surface area during catalytic hydrocarbon transformations.<sup>29</sup> We previously documented that the regeneration of the size-controlled Pt nanoparticles by redox cycles at 150 °C could restore about 70 % of the initial catalytic activity for the hydrogenolysis of MCP (1:5 MCP:H<sub>2</sub>) at 340 °C. This suggests that the deactivation is at least in part due to surface accumulation of hydrocarbon deposits. It was proposed that the deactivation was correlated with an increase in the production of C<sub>5</sub>-cycloalkenes. For the MCP/H<sub>2</sub> reaction, we found correlations with Pt nanoparticle size both for the formation of C<sub>5</sub>-cycloalkenes and for the deactivation rates.

## 4.5 Conclusion

Systematic studies for the hydrogenative reforming of various C<sub>6</sub> hydrocarbons over the model Pt nanoparticle catalysts have isolated particle sizes around 3.0 nm as the most active for the formation of C<sub>6</sub> isomers. 3.0 nm Pt nanoparticles yielded C<sub>6</sub> isomers more selectively than any other particle size (50 % vs. a maximum of 20 %) for the 2-methylpentane/H<sub>2</sub> reaction at 360 °C. Yet the turnover rates for the reforming of C<sub>6</sub> alkanes over 3.0 nm Pt nanoparticles were an order of magnitude slower than those over 1.5 and 5.2 nm Pt. Similarly, for the hydrogenolysis of MCP at 320 °C, Pt particle sizes of 3.0 nm and below produced C<sub>6</sub> isomers more selectively than benzene whereas the larger Pt nanoparticles were more selective for the formation of benzene.

## 4.6 References

1. Kuhn, J. N.; Tsung, C. K.; Huang, W.; Somorjai, G. A. Effect of Organic Capping Layers over Monodisperse Platinum Nanoparticles upon Activity for Ethylene Hydrogenation and Carbon Monoxide Oxidation. *J. Catal.* **2009**, *265*, 209-215.
2. Tsung, C. K.; Kuhn, J. N.; Huang, W.; Aliaga, C.; Hung, L. I.; Somorjai, G. A.; Yang, P. Sub-10 nm Platinum Nanocrystals with Size and Shape Control: Catalytic Study for Ethylene and Pyrrole Hydrogenation. *J. Am. Chem. Soc.* **2009**, *131*, 5816-5822.
3. Kuhn, J. N.; Huang, W.; Tsung, C. K.; Zhang, Y.; Somorjai, G. A. Structure Sensitivity of Carbon-Nitrogen Ring Opening: Impact of Platinum Particle Size From Below 1 to 5 nm Upon Pyrrole Hydrogenation Product Selectivity Over Monodisperse Platinum Nanoparticles Loaded onto Mesoporous Silica. *J. Am. Chem. Soc.* **2008**, *130*, 14026-14027.

4. Kliewer, C. J.; Aliaga, C.; Bieri, M.; Huang, W.; Tsung, C. K.; Wood, J. B.; Komvopoulos, K.; Somorjai, G. A. Furan Hydrogenation over Pt(111) and Pt(100) Single-Crystal Surfaces and Pt Nanoparticles from 1 to 7 nm: A Kinetic and Sum Frequency Generation Vibrational Spectroscopy Study. *J. Am. Chem. Soc.* **2010**, *132*, 13088-13095.
5. Narayanan, R.; El-Sayed, M. A. Shape-Dependent Catalytic Activity of Platinum Nanoparticles in Colloidal Solution. *Nano Lett.* **2004**, *4*, 1343-1348.
6. Zaera, F.; Godbey, D.; Somorjai, G. A. Methylcyclopentane Conversion over Platinum Single Crystal Surfaces: Evidence for the Cyclic Mechanism of n-Hexane Isomerization. *J. Catal.* **1986**, *101*, 73-80.
7. Garin, F.; Aeiyaeh, S.; Legare, P.; Maire, G. Isomerization and Hydrogenolysis of C<sub>6</sub> Alkanes on Pt/Al<sub>2</sub>O<sub>3</sub> Catalysts and Pt Single-Crystal Faces. *J. Catal.* **1982**, *77*, 323-337.
8. Brandenberger, S. G.; Callender, W. L.; Meerbott, W. K. Mechanisms of Methylcyclopentane Ring Opening over Platinum-Alumina Catalysts. *J. Catal.* **1976**, *42*, 282-287.
9. Zhuang, Y.; Frennet, A. Kinetic Studies of Methylcyclopentane Ring Opening on EuroPt-1 (Pt/SiO<sub>2</sub>). *Appl. Catal. A* **1999**, *177*, 205-217.
10. Galperin, L. B.; Bricker, J. C.; Holmgren, J. R. Effect of Support Acid-Base Properties on Activity and Selectivity of Pt Catalysts in Reaction of Methylcyclopentane Ring Opening. *Appl. Catal. A* **2003**, *239*, 297-304.
11. Barron, Y.; Maire, G.; Muller, J. M.; Gault, F. G. The Mechanisms of Hydrogenolysis and Isomerization of Hydrocarbons on Metals: II. Mechanisms of Isomerization of Hexanes on Platinum Catalysts. *J. Catal.* **1966**, *5*, 428-445.
12. Dautzenberg, F. M.; Platteeuw, J. C. Isomerization and Dehydrocyclization of Hexanes over Monofunctional Supported Platinum Catalysts. *J. Catal.* **1970**, *19*, 41-48.
13. Bai, X.; Sachtler, M. H. Methylcyclopentane Conversion Catalysis by Zeolite Encaged Palladium Clusters and Palladium-Proton Adducts. *J. Catal.* **1991**, *129*, 121-129.
14. Davis, B. H. Alkane Dehydrocyclization Mechanism. *Catal. Today* **1999**, *53*, 443-516.
15. Teschner, D.; Paal, Z.; Duprez, D. The Effects of Hydrogen Pressure and Temperature on the Methylcyclopentane Conversion on Rh Catalysts. *Catal. Today* **2001**, *65*, 185-190.
16. Samoila, P.; Boutzeloit, M.; Especel, C.; Epron, F.; Marecot, P. Selective Ring-Opening of Methylcyclopentane on Platinum-Based Bimetallic Catalysts. *Appl. Catal. A* **2009**, *369*, 104-112.



17. Poupin, C.; Pirault-Roy, L.; La Fontaine, C.; Toth, L.; Chamam, M.; Wootsch, A.; Paal, Z. Promising PtIr, Catalysts for the Hydrocarbon Transformation: Comparison of Different Preparation Methods. *J. Catal.* **2010**, *272*, 315-319.
18. Vaarkamp, M.; Dijkstra, P.; Vangrondelle, J.; Miller, J. T.; Modica, F. S.; Koningsberger, D. C.; Vansanten, R. A. The Effect of Hydrogen Partial-Pressure on Methylcyclopentane Ring-Opening. *J. Catal.* **1995**, *151*, 330-337.
19. Kramer, R.; Fischbacher, M. Hydrogen Pretreatment Effects on the Hydrogenolysis of Methylcyclopentane on Pt/SiO<sub>2</sub> and Pt/Al<sub>2</sub>O<sub>3</sub> Catalysts. *J. Mol. Catal.* **1989**, *51*, 247-259.
20. Anderson, J. B. F.; Burch, R.; Cairns, J. A. The Influence of Metal-Support Interactions on the Reaction of Methylcyclopentane over Supported Pt Catalysts. *J. Catal.* **1987**, *107*, 351-363.
21. Alayoglu, S.; Aliaga, C.; Sprung, C.; Somorjai, G. A. Size and Shape Dependence on Pt Nanoparticles for the Methylcyclopentane/Hydrogen Ring Opening/Ring Enlargement Reaction. *Catal. Lett.* **2011**, *141*, 914-924.
22. Bond, G. C.; Paal, Z. Recently Published Work on EUROPT-1 a 6% Pt/SiO<sub>2</sub> Reference Catalyst. *Appl. Catal. A* **1992**, *86*, 1-35.
23. Chandler, B. D.; Rubinstein, L. I.; Pignolet, L. H. Alkane Dehydrogenation With Silica Supported Platinum and Platinum-Gold Catalysts Derived From Phosphine Ligated Precursors. *J. Mol. Catal. A: Chem* **1998**, *133*, 267-282.
24. Garin, F.; Girard, P.; Maire, G.; Lu, G.; Guzzi, L. Isomerization of 2-methylpentane and Ring Opening of Methylcyclopentane over Pt-Co/NaY Catalysts. *Appl. Catal. A* **1997**, *152*, 237-247.
25. Van Hardeveld, R.; Hartog, F. The Statistics of Surface Atoms and Surface Sites on Metal Crystals. *Surf. Sci.* **1969**, *15*, 189-230.
26. Paal, Z. The Influence of Hydrogen on Active Centres for Hydrocarbon Reactions over Pt. *Catal. Today* **1992**, *12*, 297-318.
27. Gnutzmann, V.; Vogel, W. Structural Sensitivity of the Standard Platinum/Silica Catalyst EuroPt-1 to Hydrogen and Oxygen Exposure by in situ X-ray Diffraction. *J. Phys. Chem.* **1990**, *94*, 4991-4997.
28. Balandin, A. A. Modern State of the Multiplet Theory of Heterogeneous Catalysis. *Adv. Catal.* **1969**, *19*, 1-210.
29. Bond, G. C.; Lin, X. Alkane Transformation on Supported Platinum Catalysts: 5. Effects of Formation and Removal of Carbon Deposits on Alkane Hydrogenolysis Using EUROPT-1 (6.3% Platinum/Silica). *J. Catal.* **1997**, *168*, 207-216.

## Chapter 5

# Isomerization of *n*-Hexane Catalyzed by Supported Monodisperse PtRh Bimetallic Nanoparticles

### Abstract

Composition and size of Pt<sub>x</sub>Rh<sub>1-x</sub> bimetallic nanoparticles were varied in order to study the effects in the catalytic reforming of *n*-hexane. Hexane isomerization, an analogue to the important industrial process of hydrocarbon reforming is a reaction in which we aim to investigate the molecular level details of catalysis. It is known, that in hydrocarbon isomerization, Pt atoms act to isomerize the reactants, while small amounts of “promoter metal” atoms (such as Rh, Ir, Re and Sn) provide C–C and C–H bond breaking activity. Herein, we report on the effect of composition and size in model bimetallic Pt<sub>x</sub>Rh<sub>1-x</sub> nanoparticle catalysts utilized in *n*-hexane reforming. Both nanoparticle composition and size were shown to influence catalytic turnover frequency and product selectivity. It was found, through ambient pressure X-ray photoelectron spectroscopy, that the surface of these nanoparticles is both dynamic, and Rh rich under relevant reaction conditions. The findings suggest that an ensemble effect exists, in which the highest isomer production occurs when Rh atoms are surrounded by Pt atoms on the metal surface.

\* This chapter covers similar material as in Musselwhite, N.; Alayoglu, S.; Melaet, G.; Pushkarev, V.V.; Lindeman, A.E.; An, K.; Somorjai, G.A. *Catal. Lett.* **2013**, *143*, 907-911.  
— reproduced with permission, copyright 2013 Springer Science+Business Media, LLC.

## 5.1 Introduction

The catalytic reforming of n-hexane, a model reaction for naphtha reforming, is an industrially important multi-product reaction. The goal of studying this reaction, along with any heterogeneous catalysis reaction is to simultaneously optimize catalytic activity and selectivity to desired products.<sup>1-3</sup> Hydrocarbon reforming is normally accomplished through the use of a platinum catalyst, alloyed with small amounts of other “promoter” metals and supported on an acidic support.<sup>4</sup> The promoter metals in this catalyst, which are typically middle transition metals with high C–C bond breaking activity, act to increase the overall activity of the reaction. Through the use of colloidal synthesis, uniformly sized and composition controlled nanoparticles can be synthesized, characterized, and evaluated catalytically at industrially relevant conditions, which can help elucidate the important molecular level information of this reaction.

## 5.2 Experimental

### 5.2.1 Material Synthesis

Platinum nanoparticles alloyed with rhodium were synthesized in various metal compositions through colloidal techniques. Briefly,  $\text{H}_2\text{PtCl}_6 \cdot 6\text{H}_2\text{O}$  (Sigma-Aldrich, 37.50 % Pt basis),  $\text{Pt}(\text{acac})_2$  (Aldrich, 97 %), and  $\text{Rh}(\text{acac})_3$  (Aldrich, 97 %) were used as metal sources in 6.5 nm particle synthesis. The ratio of Pt to Rh metals was varied, but the overall metal amount was kept at a constant  $1.0 \times 10^{-4}$  mol. The mole ratio of  $\text{H}_2\text{PtCl}_6 \cdot 6\text{H}_2\text{O}$  to  $\text{Pt}(\text{acac})_2$  was also kept at a constant 4:1 for 6.5 nm. In a typical synthesis the metal salts were added to a round bottom flask, triethylene glycol (10 mL) and polyvinylpyrrolidone (28 mg, 55,000 g/mol) were added, and the solution was sonicated for 30 min to ensure dissolving of the solids. The flask was then placed under vacuum for 20 min and then repeatedly purged with argon and vacuum pumped before finally being filled with argon, to ensure an oxygen free environment. The flask was then placed in a molten salt bath held at a constant 503 K for 1 h. During this time the solution changed to dark black in color as nanoparticles were formed. Smaller sized bimetallic nanoparticles were synthesized by addition of  $\text{NaNO}_3$  ( $7 \times 10^{-5}$  mol) to a solution containing triethylene glycol, PVP and  $\text{Pt}(\text{acac})_2$  and  $\text{Rh}(\text{acac})_3$  ( $1.0 \times 10^{-4}$  mol total metal) and following a similar reduction procedure as reported above. After synthesis, the nanoparticles were precipitated from solution by addition of acetone and subsequent centrifugation ( $550 \times 9.8 \text{ m/s}^2$ , 20 min). Nanoparticles were then supported on MCF-17 type mesoporous silica, which was synthesized by previously reported methods.<sup>5</sup>

### 5.2.1 Catalytic Measurements

Catalytic measurements were made utilizing a tubular fixed catalyst bed reactor at ambient pressure. A 1/4" diameter stainless steel reactor was mounted vertically, which allowed for a downflow operation. A 0.5 g sample of catalyst was loaded, which corresponded to a 10–12 cm bed height. The catalyst was placed in the center of the reactor tube, capped on each end with purified thermal silica filter. The remaining space in the reactor tube was filled with purified fused aluminum granulate and capped with glass wool. Prior to loading, the catalyst was pelletized and sieved to obtain 60–100  $\mu\text{m}$  size granulates. To allow for selectivity comparison, the catalysis was kept in a kinetic region by holding the total hexane conversion below 10 %.

The catalysts were first pretreated at 633 K under a gas mixture of  $\text{N}_2$  (Praxair, 5.0 UHP, 10 sccm) and  $\text{H}_2$  (Praxair, 5.0 UHP, 10 sccm) for 2 h. The heating rate of the pretreatment was limited to  $2 \text{ K min}^{-1}$ . After the pretreatment, the reactor system was cooled to 513 K under the

same gas flow. The gas flow was then changed to 16 sccm H<sub>2</sub> and n-hexane (Fluka,  $\geq 99.0\%$ ) was introduced using a Teledyne ISCO 500D liquid flow pump at a rate of 1.2 mL h<sup>-1</sup> into the preheating reactor head which was maintained at 423 K. In the preheating zone, hexane evaporated and mixed with H<sub>2</sub>, resulting in a two-component gas flow with a hexane:H<sub>2</sub> molar ratio of 1:5 entering the reactor at near ambient pressure. A Baratron type (890B, MKS Instruments) manometer was used to monitor the reactor inlet pressure. The reaction products were sampled in the vapor phase at the reactor outlet and analyzed via an in-line gas chromatograph (GC). All flow lines were heated to 433 K. Quantitative analysis of flow composition was accomplished with a Hewlett-Packard (5890 Series II) GC which was equipped with an Aldrich HP-1 capillary column and a flame ionization detector (FID). A PC based GC Chemstation software (Hewlett-Packard) was utilized for automatic GC sampling, data collection and post-run processing.

### 5.3 Results and Discussion

Nanoparticles were characterized using a JEOL JEM-2100F scanning transmission electron microscope (STEM) equipped with an INCA electron dispersive spectrometer (EDS) was used in scanning mode to obtain information about the size and composition of the particles. Briefly, Pt and Rh L lines were simultaneously probed by EDS using a point-to-point e-beam size of 1.5 nm, and then overlapped on the respective high angle annular dark field (HAADF) image. STEM-EDS images are shown in Figure 1.

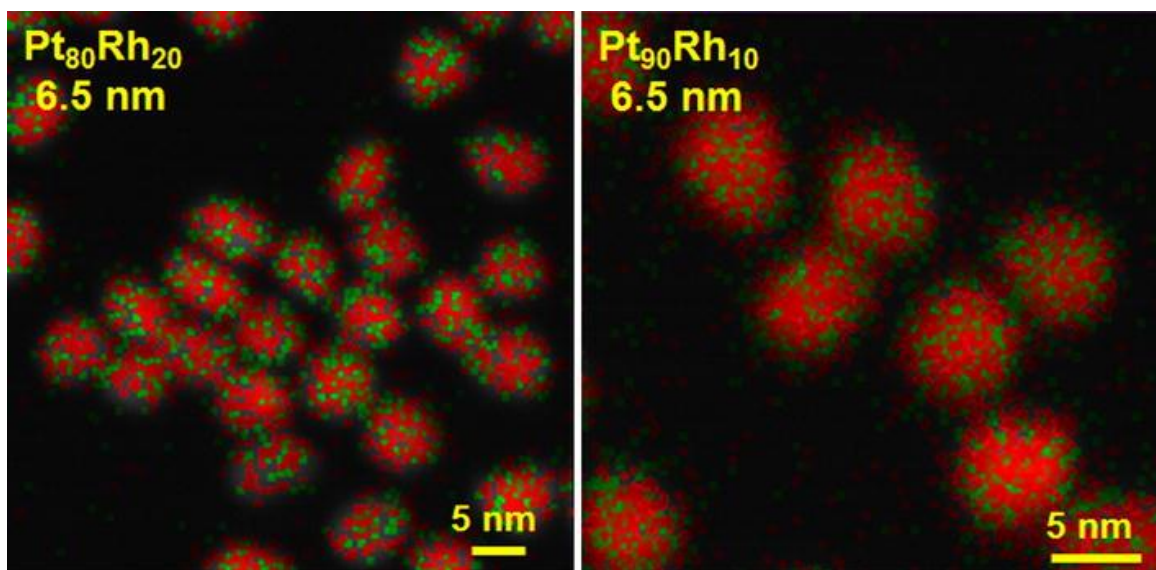


**Figure 1.** Scanning transmission electron microscopy/electron-dispersive spectrometry (STEM-EDS) images of bimetallic nanoparticles. The red points represent the Pt L-line and the green points represent Rh L-line.

The larger sized bimetallic particles were found to be  $6.4 \pm 0.5$  nm with mean Pt/Rh atom ratios of 80/20 and 93/7. Smaller sized Pt<sub>80</sub>Rh<sub>20</sub> were also synthesized and characterized. They were found to have an atomic composition of 80/20 Pt/Rh and a size distribution of  $2.5 \pm 0.3$  nm. No stray monometallic nanoparticles were observed. Nanoparticles were also characterized utilizing synchrotron based ambient pressure X-ray photoelectron spectroscopy (AP-XPS), as a means to ascertain the surface composition of the nanocatalysts under relevant reaction conditions.<sup>6</sup> AP-XPS samples were prepared by deposition of the particles onto a silica wafer by Langmuir–Blodgett techniques. The wafer was then loaded into the instrument for characterization. The particle surface composition was determined by investigating the Pt 4f and the Rh 3d spectra, utilizing both 380 and 650 eV excitation energies, respectively, both with probing depths of 0.8 nm. The partial pressures of the system were 100 mTorr of H<sub>2</sub> and 20 mTorr of hexane for the experiments. The characterization data for the nanoparticles is summarized in Table 1.

**Table 1.** Characterization data of Pt<sub>x</sub>Rh<sub>1-x</sub> nanoparticles

Nanoparticle (size in nm)	Pt/Rh bulk ratio <sup>a</sup>	Pt/Rh surface ratio <sup>b</sup>	Cracking selectivity (%)	Isomer selectivity (%)	Aromatic selectivity (%)	Overall TOF	Isomer TOF
Rh (6.5)	0/100	0/100	90	5	5	0.034	0.0018
Pt (6.5)	100/0	100/0	15	78	7	0.0064	0.0050
Pt <sub>80</sub> Rh <sub>20</sub> (6.5)	80/20	70/30	48	44	8	0.013	0.0059
Pt <sub>90</sub> Rh <sub>10</sub> (6.5)	93/7	80/20	36	55	9	0.012	0.0065
Pt <sub>80</sub> Rh <sub>20</sub> (2.5)	80/20	70/30	57	34	8	0.019	0.0065

<sup>a</sup>Ratio evaluated from EDS analysis

<sup>b</sup>Ratio obtained in in situ condition using AP-XPS

By integration of the AP-XPS spectral data, it was possible to determine the near surface composition of the bimetallic nanoparticles. The percentage of platinum atoms is plotted in Figure 2a as a function of reaction conditions. Notably, the near surface ratio was found to always be rich in rhodium with respect to the bulk nanoparticles. Also, it was determined that the surface composition is dynamic and varies under different conditions. It was also found that nanoparticle size had little influence on the surface composition of nanoparticles, as shown in Figure 2b, c. The final important conclusion is that under reaction conditions (5:1 H<sub>2</sub>:hex 360 °C) the near surface was found to have an excess of rhodium. This result was also found with the Pt<sub>90</sub>Rh<sub>10</sub> nanoparticles.

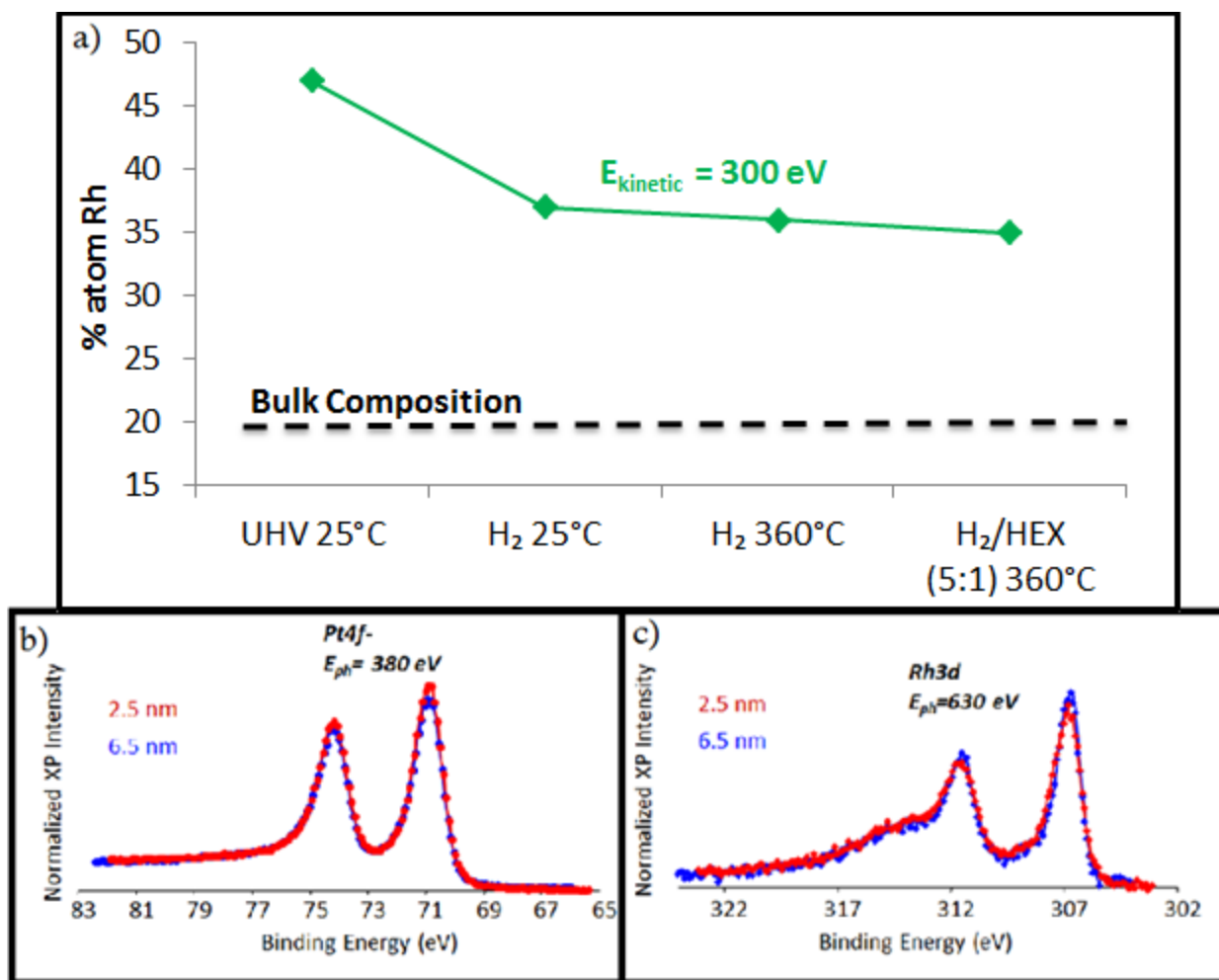


**Figure 2.** a) Composition of near surface atoms in bimetallic 6.5 nm Pt<sub>80</sub>Rh<sub>20</sub> nanoparticles. The green line represents the near surface composition of the nanoparticles as obtained via integration and normalization of the 380 and 630 eV AP-XPS spectra. The dashed line represents the bulk composition of the nanoparticles. b) The Pt 4f and c) Rh 3d spectra (380 and 630 eV, respectively) shown for the 2.5 nm Pt<sub>80</sub>Rh<sub>20</sub> nanoparticles in red and the 6.5 nm Pt<sub>80</sub>Rh<sub>20</sub> in blue. The spectra show there is no difference in surface composition between the two different sized particles.

These nanoparticles, once supported on MCF-17, were then utilized in the hydrogenative reforming of n-hexane. The reforming of n-hexane is a model reaction for the catalytic reforming of naphtha feedstock, an important reaction in oil refining. The scheme for this reaction is shown in Figure 3. The desired pathways in this reaction are towards isomerization and cyclization products, while the cracking and aromatization product pathways are undesired.

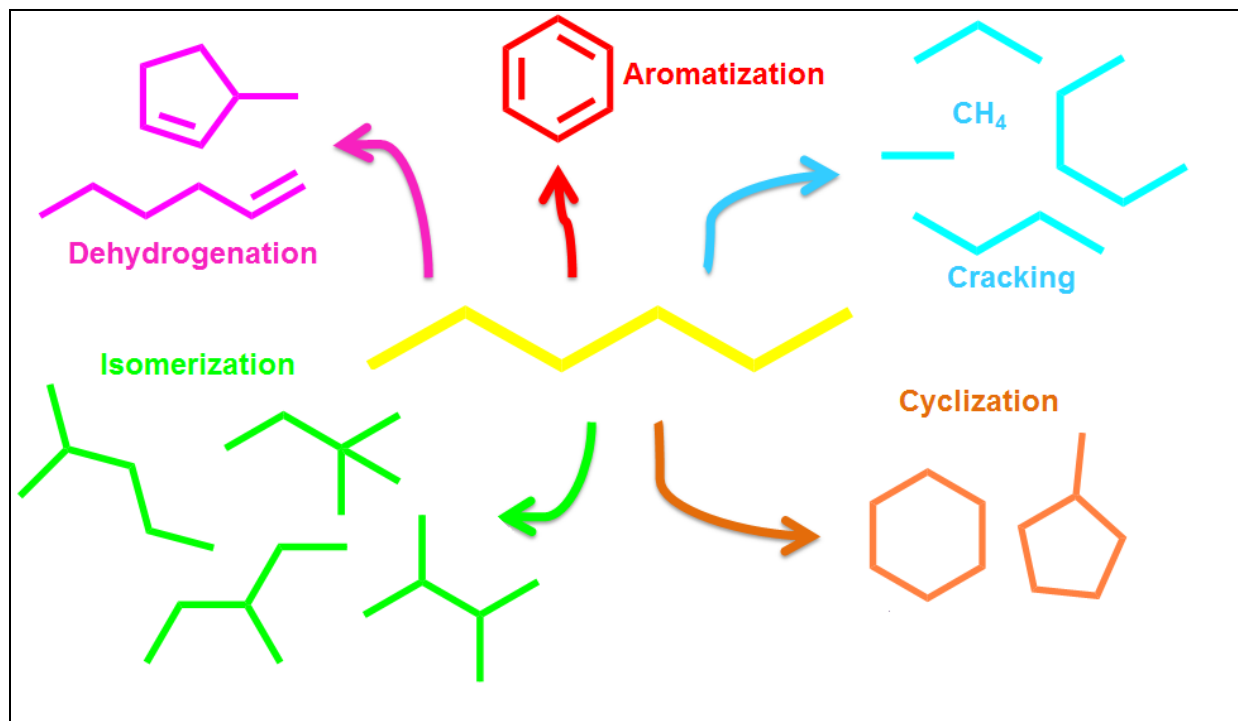


**Figure 3.** Reaction scheme for n-hexane reforming. Desired products are isomerization and cyclization products shown in green and orange, respectively. Undesired products are cracking and aromatization products, shown in blue and red, respectively.

The total n-hexane turnover frequency (TOF) of all tested catalysts is shown in Figure 4. It can be seen that the monometallic rhodium catalyst had the highest activity in hexane reforming ( $0.034 \text{ s}^{-1}$ ), and the monometallic platinum nanoparticles had the lowest of the evaluated catalysts ( $0.0060 \text{ s}^{-1}$ ). The activity of the bimetallic catalysts appear to be approximately linear with respect to the monometallic particles, with the  $\text{Pt}_{80}\text{Rh}_{20}$  having an overall TOF of  $0.013 \text{ s}^{-1}$  and the  $\text{Pt}_{90}\text{Rh}_{10}$  having an overall TOF of  $0.011 \text{ s}^{-1}$ . The selectivity of the catalysts is shown in Figure 5. It can be seen that monometallic rhodium nanoparticles show very low selectivity for the desired isomer products. Monometallic Pt nanoparticles were found to be about 78 % selective for desired products (cyclics and isomers). This result demonstrates that Rh, which forms a stronger metal carbon bond and subsequently has a higher C–C bond breaking ability than Pt, prefers to follow a cracking pathway, whereas Pt allows for the isomerization of hexane. The bimetallic  $\text{Pt}_{80}\text{Rh}_{20}$  and  $\text{Pt}_{90}\text{Rh}_{10}$  nanoparticles were found to be about 44 and 55 % selective to desired products, respectively.

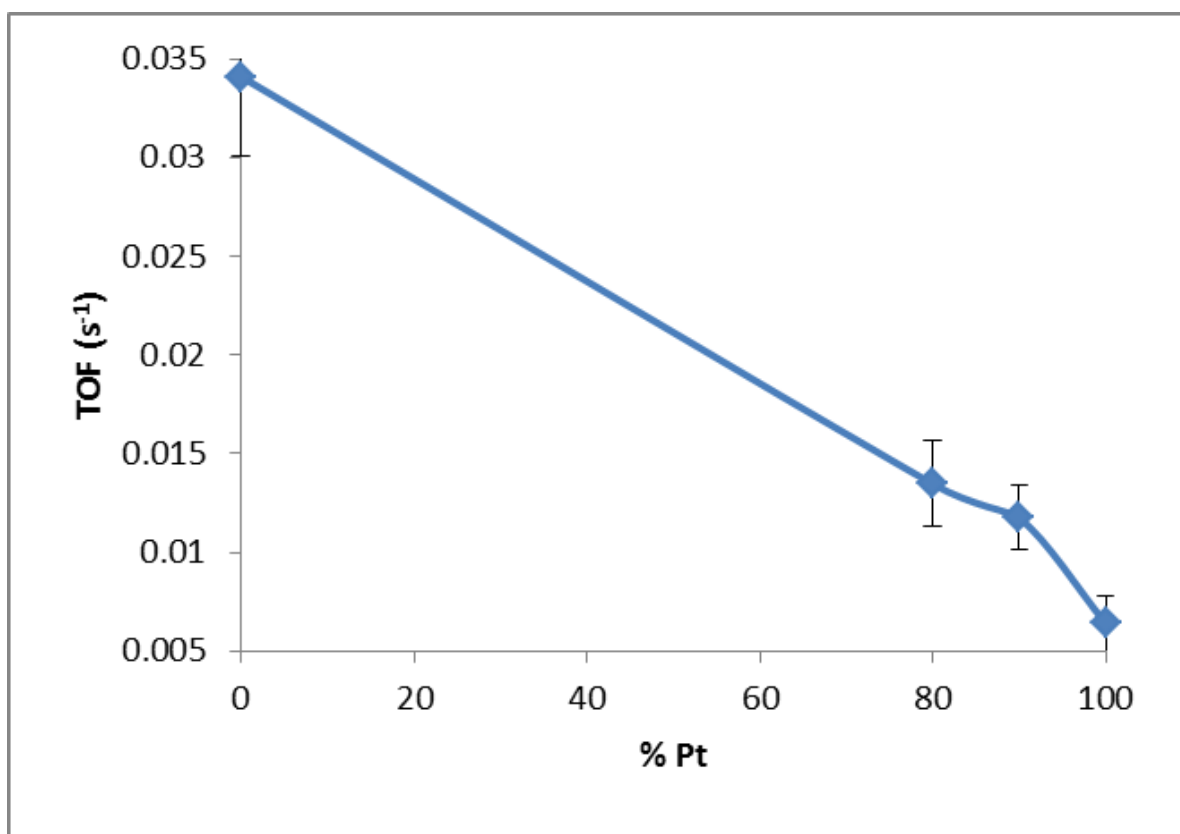


**Figure 4.** Total turnover-frequency (TOF) of evaluated 6.5 nm Pt<sub>x</sub>Rh<sub>1-x</sub> catalysts. It can be seen that activity drops nearly linearly as a function of concentration, with the monometallic Rh particles (x=0) being most active and the monometallic Pt particles (x=1) being least active.

---



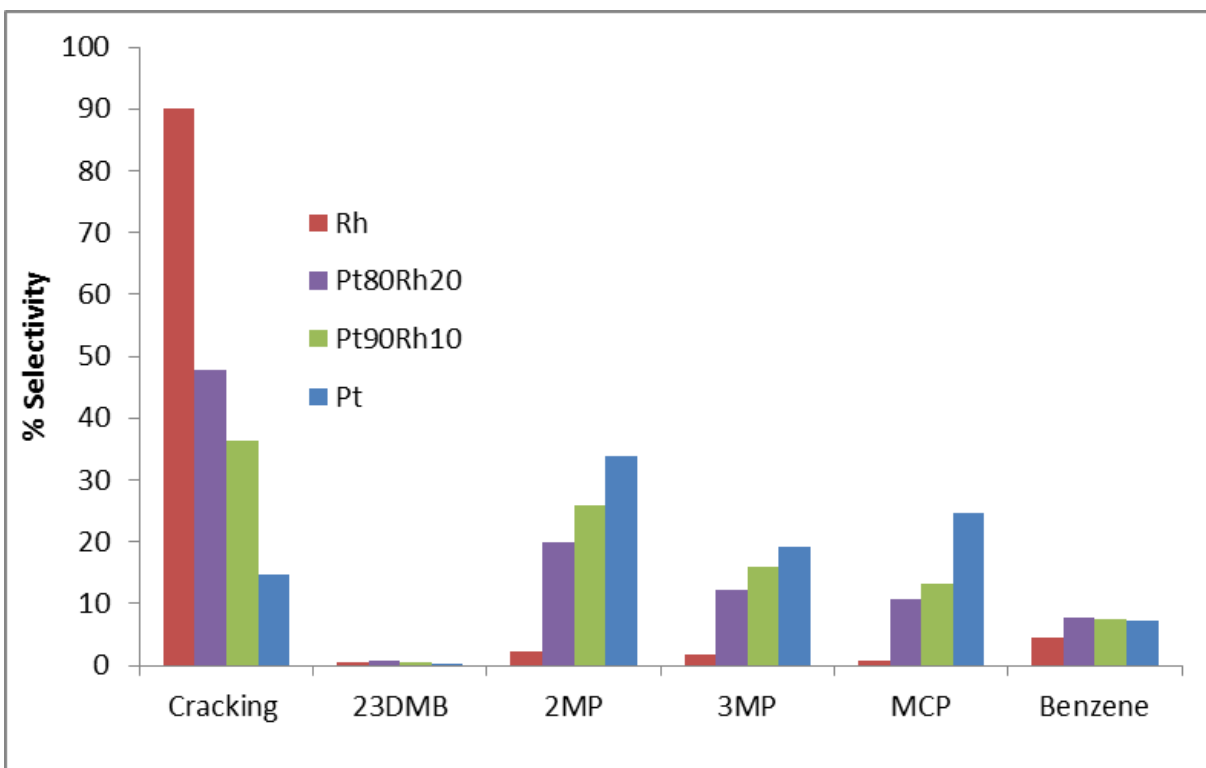


**Figure 5.** Plot displaying the selectivity of different compositions of 6.5 nm  $Pt_xRh_{1-x}$  nanoparticles. It can be seen that monometallic Rh nanoparticles ( $x=0$ ) preferentially crack hexane, while monometallic Pt nanoparticles ( $x=1$ ) produce isomers in abundance. The selectivity for the bimetallic catalysts fall in between that of the two monometallic catalysts. (23DMB = 2,3 dimethylbutane; 2MP = 2-methylpentane; 3MP = 3-methylpentane; MCP = methylcyclopentane).

---

By taking the product of the overall TOF and the percent selectivity of the desired isomer products it is possible to determine the turnover frequency for the isomers, or the overall yield of desired products. This data is shown in Figure 6, plotted against the AP-XPS determined near surface composition of the different catalysts. Shown in Figure 7 is a similar plot for the TOF of the cracking product. It can be seen from the isomer plot that the TOF of desired products exhibits a volcano type behavior in which the maximum occurs not on the monometallic nanoparticles, but on the  $Pt_{90}Rh_{10}$  bimetallic catalyst. By utilizing the AP-XPS measured near surface compositions for these particles, the ratio of Pt to Rh atoms in an ideal FCC (111) face is 1:5, which corresponds to one Rh atom surrounded by five Pt atoms. Which means the maximum isomer production occurs when one Rh atom is encircled by Pt atoms.

---

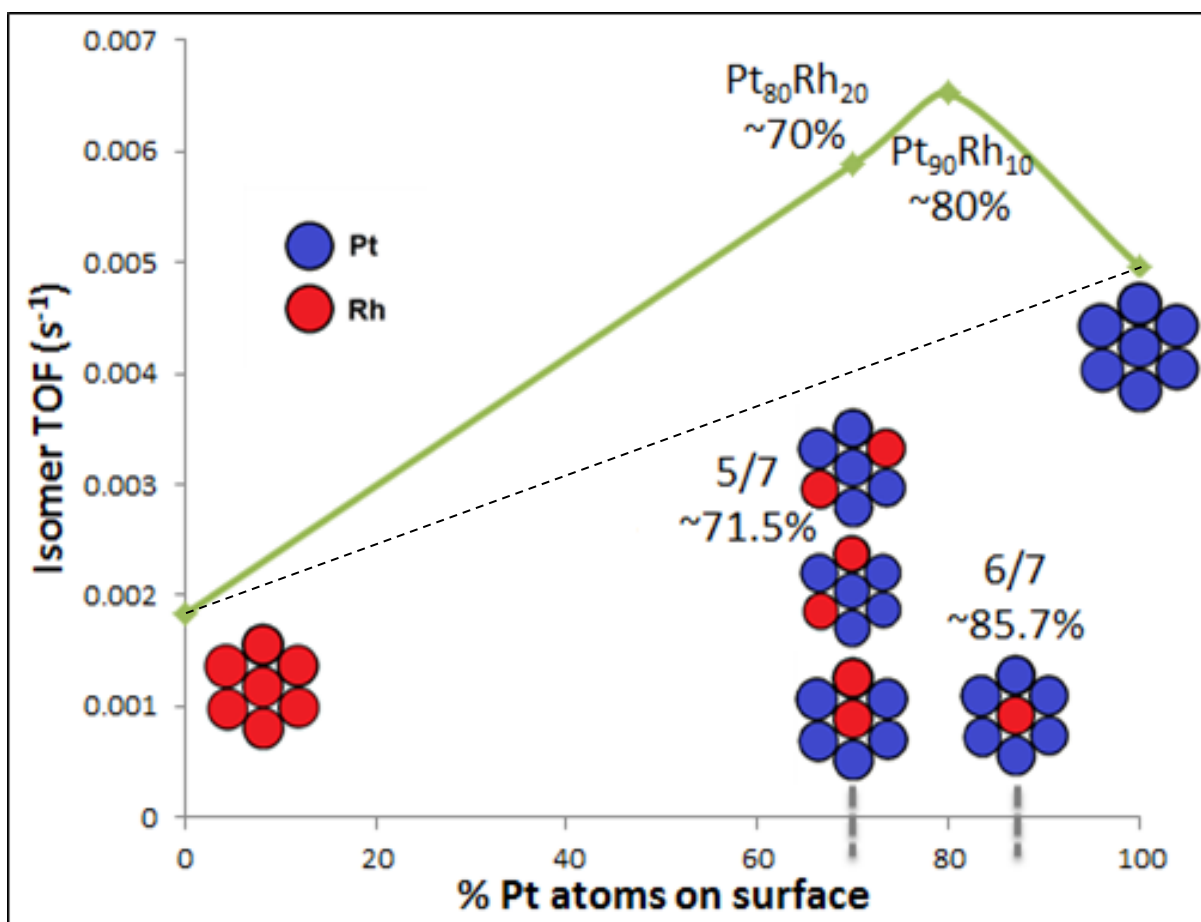


**Figure 6.** Isomer TOF plotted against the near surface composition of the 6.5 nm NPs using AP-XPS. The maximum rate occurs on the bimetallic nanoparticles, where the surface ratio is 80:20 Pt:Rh. The dotted line represents what would be expected if a linear relationship existed with atomic composition. The actual data exhibits about a 60 % increase in isomer TOF. This type of behavior can be attributed to an ensemble effect between the surface Pt and Rh atoms. The images shown are models for 111 fcc crystal faces.

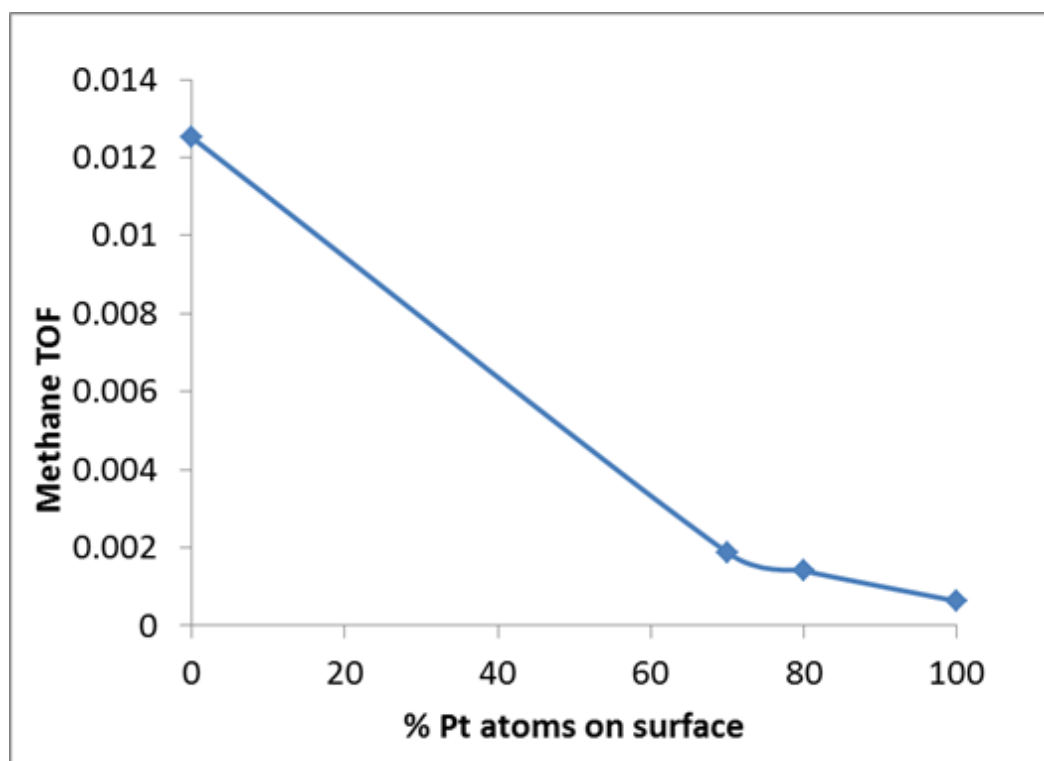


**Figure 7.** Plot of the methane TOF vs. surface platinum atoms on 6.5 nm nanoparticles (as determined by AP-XPS). It can be seen that the change in TOF is not linear with increasing Pt atom concentration.

---

This type of behavior can be attributed to the ensemble effect, a well-known phenomenon in surface science. In the ensemble effect a different catalytic turnover can occur due to the surface ensemble of bimetallic catalysts. This effect has previously been shown to be present in n-hexane reforming catalyzed by Pt–Au alloys.<sup>7,8</sup> It has found that when catalytically inert Au is diluted on a Pt (111) single crystal it acts to block high coordination threefold sites. This acts to decrease aromatization chemistry, thus promoting isomerization. In this work the Pt surface is diluted with a more active Rh atom, this Rh atom acts to promote C–H bond activation, and when surrounded by Pt atoms allows for higher isomer formation.

The size effect of the particles is shown in Figure 8. It can be seen that on the 2.5 nm Pt<sub>80</sub>Rh<sub>20</sub> particles the cracking and aromatization products increased at the expense of the desired isomer products. It should also be noted the activity of the smaller sized catalysts is higher than the larger catalysts. It was found, via APXPS, that the surface compositions of these two catalysts is similar (around 70/30 Pt/Rh), so therefore the differences in selectivity and activity are purely due to particle size and the corresponding position of surface atoms, i.e. corner, terrace, and edge

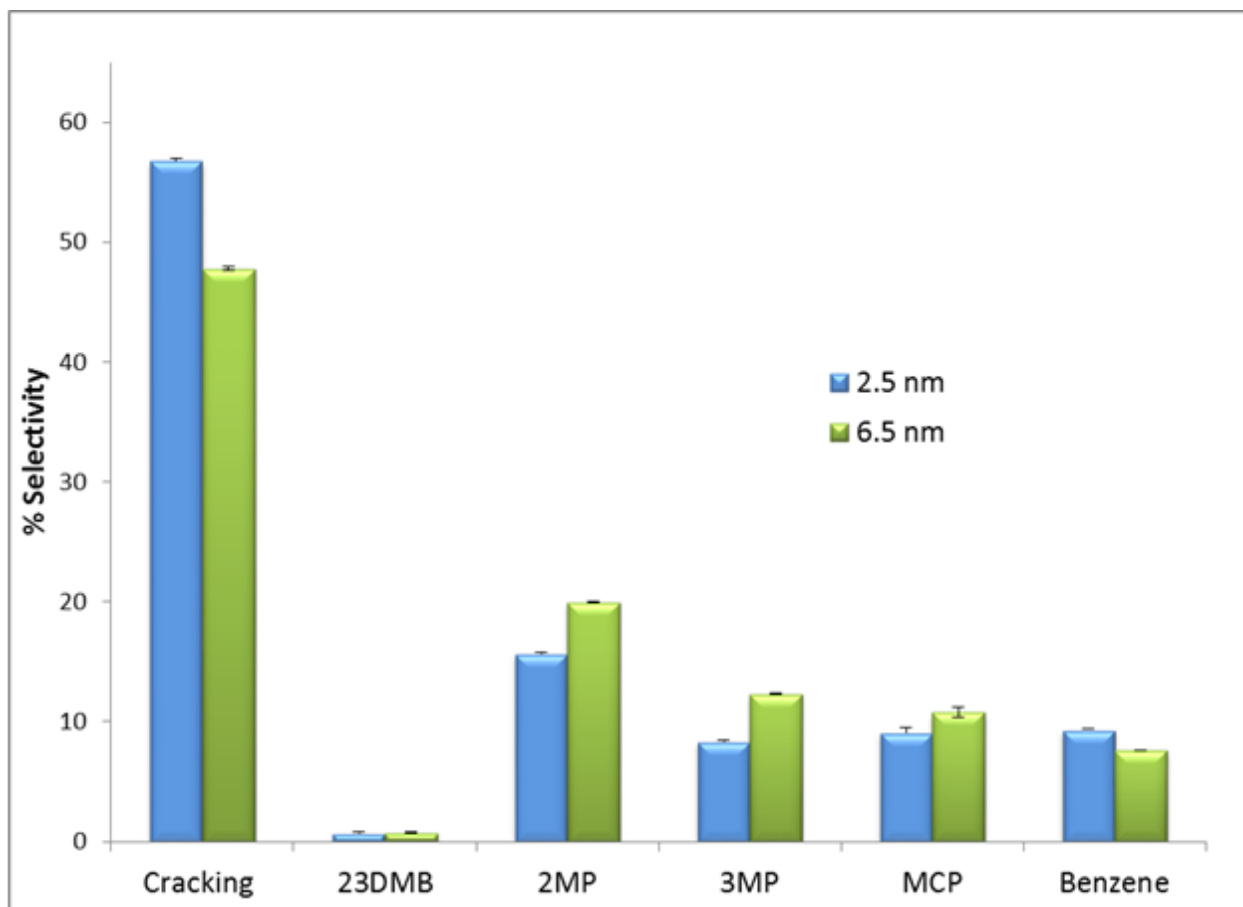


**Figure 8.** Impact of size on the selectivity of n-hexane hydrogenation for  $\text{Pt}_{80}\text{Rh}_{20}$  catalysts: smaller sizes show more selective towards the cracking product, while larger sized nanoparticles produce more isomers (23DMB 2,3-dimethylbutane, 2MP 2-methylpentane, 3MP 3-methylpentane, MCP methylcyclopentane).

sites. It may be possible that Rh atoms preferentially occupy corner and edge sites, which would have high catalytic activity, while Pt rich terraces would have intrinsically lower activity. In the smaller sized particles the ratio of corner and edge sites is much higher, so therefore it would follow that the cracking activity would be higher in these particles.

## 5.4 Conclusions

In summary, on monometallic surfaces, Rh acts to activate the hexane, and then cracks the molecule with high TOF. On monometallic Pt surfaces, selectivity toward desired products is much higher, but activity is very low due to the inability of Pt to activate the C–H bond as well as Rh. However, when Rh is diluted on a surface of Pt, the Rh acts to activate the C–H bond, and the surrounding Pt atoms allow for the formation of desired isomer products. The bimetallic nanoparticles were shown to be rhodium rich under reaction conditions, with the optimum

surface composition for isomer production occurring on the Pt<sub>90</sub>Rh<sub>10</sub> nanoparticles (93/7 Pt/Rh surface composition). The size of the bimetallic nanoparticles was shown to affect product selectivity by increasing isomer production at the expense of cracking on larger sized particles.

## 5.5 References

1. Somorjai, G. A.; Li, Y. *Introduction to Surface Chemistry and Catalysis*; Wiley: New York, 2010.
2. Somorjai, G. A.; Park, J. Y. Molecular Factors of Catalytic Selectivity. *Angew. Chem., Int. Ed* **2008**, *47*, 9212-9228.
3. Clark, J. H. Green chemistry: challenges and opportunities. *Green Chem.* **1999**, *1*, 1-8.
4. Sinfelt, J. H. Catalytic Hydrogenolysis on Metals. *Catal. Lett.* **1991**, *9*, 159-171.
5. Han, Y.; Lee, S. S.; Ying, J. Y. Spherical Siliceous Mesocellular Foam Particles for High-Speed Size Exclusion Chromatography. *Chem. Mater.* **2007**, *19*, 2292-2298.
6. Tao, F.; Grass, M. E.; Zhang, Y.; Butcher, D. R.; Renzas, J. R.; Liu, Z.; Chung, J. Y.; Mun, B. S.; Salmeron, M.; Somorjai, G. A. Reaction-Driven Restructuring of Rh-Pd and Pt-Pd Core-Shell Nanoparticles. *Science* **2008**, *322*, 932-934.
7. Sachtler, J. W. A.; Somorjai, G. A. Influence of Ensemble Size on CO Chemisorption and Catalytic n-Hexane Conversion by Au-Pt (111) Bimetallic Single-Crystal Faces. *J. Catal.* **1983**, *81*, 77-94.
8. Somorjai, G. A.; Carrazza, J. Structure Sensitivity of Catalytic Reactions. *Ind. Eng. Chem. Fundamen.* **1986**, *25*, 63-69.

## Chapter 6

# Enhanced CO Oxidation Rate at the Interface of Mesoporous Oxides and Pt Nanoparticles

### Abstract

The interaction of the metal and support in oxide-supported transition-metal catalysts has been proven to have extremely favorable effects on catalytic performance. Herein, mesoporous  $\text{Co}_3\text{O}_4$ ,  $\text{NiO}$ ,  $\text{MnO}_2$ ,  $\text{Fe}_2\text{O}_3$ , and  $\text{CeO}_2$  were synthesized and utilized in CO oxidation reactions to compare the catalytic activities before and after loading of 2.5 nm Pt nanoparticles. Turnover frequencies (TOFs) of pure mesoporous oxides were  $0.0002\text{--}0.015\text{ s}^{-1}$ , while mesoporous silica was catalytically inactive in CO oxidation. When Pt nanoparticles were loaded onto the oxides, the TOFs of the Pt/metal oxide systems ( $0.1\text{--}500\text{ s}^{-1}$ ) were orders of magnitude greater than those of the pure oxides or the silica-supported Pt nanoparticles. The catalytic activities of various Pt/oxide systems were further influenced by varying the ratio of CO and  $\text{O}_2$  in the reactant gas feed, which provided insight into the mechanism of the observed support effect. In situ characterization using near-edge X-ray absorption fine structure (NEXAFS) and ambient-pressure X-ray photoelectron spectroscopy (AP-XPS) under catalytically relevant reaction conditions demonstrated a strong correlation between the oxidation state of the oxide support and the catalytic activity at the oxide–metal interface. Through catalytic activity measurements and in situ X-ray spectroscopic probes,  $\text{CoO}$ ,  $\text{Mn}_3\text{O}_4$ , and  $\text{CeO}_2$  have been identified as the active surface phases of the oxide at the interface with Pt nanoparticles.

\* This chapter covers similar material as in An, K.<sup>‡</sup>; Alayoglu, S.<sup>‡</sup>; Musselwhite, N.; Plamthottam, S.; Melaet, G.; Lindeman, A.E.; Somorjai, G.A. *J. Am. Chem. Soc.* **2013**, *135*, 16689-16696. — reproduced with permission, copyright 2013 American Chemical Society.

<sup>‡</sup>Contributed Equally

## 6.1 Introduction

The chemistry of heterogeneous catalysis on transition-metal surfaces involves the covalent bonding of neutral molecules, which leads to dissociation and rearrangements to produce other neutral atoms and molecules.<sup>1,2</sup> Many previous studies have demonstrated large enhancements of catalytic behavior due to the role of the oxide–metal interface, wherein charge plays a crucial role in the catalytic chemistry.<sup>3–13</sup> Examples include the hydrogenation of CO<sub>2</sub> on rhodium by many different transition-metal oxides, the use of titanium oxide as a catalyst support for CO hydrogenation (Fischer–Tropsch) reactions, and even tandem catalysis.<sup>5–13</sup> Despite the large amounts of research on oxide–metal interfaces, the mechanism that causes the enhanced catalytic properties is not fully understood. This is mainly due to a limitation of insight of the interfaces under catalytic reaction conditions, as opposed to pre- and post-catalysis characterizations. Through the use of synchrotron-based characterization techniques, it is possible to study the surface chemistry of many catalytic systems on the molecular level in order to find vital mechanistic insights under the catalytic working conditions.<sup>14</sup>

Herein, several novel mesoporous oxides (Co<sub>3</sub>O<sub>4</sub>, NiO, MnO<sub>2</sub>, Fe<sub>2</sub>O<sub>3</sub>, and CeO<sub>2</sub>) were synthesized and loaded with size-controlled Pt nanoparticles to investigate the oxide–metal interface effects on catalytic CO oxidation reactions in both excess O<sub>2</sub> and excess CO. While pure mesoporous oxides are poor catalysts compared with pure Pt nanoparticles, all of the mesoporous oxide/Pt catalysts exhibit large enhancements of the CO oxidation rate beyond the turnover rates of pure Pt nanoparticles and pure mesoporous oxides. These systems were extensively characterized, both ex situ and in situ, in order to provide insight into the working conditions of the catalyst systems. In situ studies showed that the redox behavior of the oxides provides the charge that changes the mechanism of CO oxidation from covalent-bond chemistry to so-called acid–base or charge-transfer chemistry. This change of mechanism was found to be a general phenomenon for all the oxide–metal interfaces studied. Through the utilization of near-edge X-ray absorption fine structure (NEXAFS) and ambient-pressure X-ray photoelectron spectroscopy (AP-XPS) under catalytically relevant reaction conditions, we were able to demonstrate a strong correlation between the oxidation state of the oxide support and the catalytic activity at the oxide–metal interface.

## 6.2 Experimental Section

### 6.2.1 Synthesis of Mesoporous Co<sub>3</sub>O<sub>4</sub>, NiO, MnO<sub>2</sub>, Fe<sub>2</sub>O<sub>3</sub>, and CeO<sub>2</sub>

Mesoporous silica KIT-6 with a bi-continuous pore structure was used as a hard template.<sup>15</sup> For the synthesis of KIT-6, 27 g of P123 and 43.5 mL of concentrated HCl were dissolved with 980 mL of water in a polypropylene bottle, and 33.3 mL of *n*-butanol was added to the solution at 308 K with vigorous stirring. After 1 h, 58 g of TEOS was added to the solution followed by stirring at this temperature for 24 h. The capped bottle was stored at 313 K for another 24 h in an oven. The solid was filtered, dried at 363 K overnight, and calcined at 823 K for 6 h.

Mesoporous oxides were prepared through the hard-templating approach using KIT-6, which was developed by Schüth and co-workers.<sup>16–18</sup> Co(NO<sub>3</sub>)<sub>2</sub>·6H<sub>2</sub>O, Ni(NO<sub>3</sub>)<sub>2</sub>·6H<sub>2</sub>O, Mn(NO<sub>3</sub>)<sub>2</sub>·xH<sub>2</sub>O, Fe(NO<sub>3</sub>)<sub>3</sub>·9H<sub>2</sub>O, and Ce(NO<sub>3</sub>)<sub>3</sub>·6H<sub>2</sub>O (Sigma-Aldrich) were used to synthesize mesoporous Co<sub>3</sub>O<sub>4</sub>, NiO, MnO<sub>2</sub>, Fe<sub>2</sub>O<sub>3</sub>, and CeO<sub>2</sub>, respectively.<sup>16–18</sup> In a typical synthesis, 16 mmol of metal nitrate dissolved in 8 mL of water was added to 4 g of KIT-6 in 50 mL of toluene

at 338 K with stirring. After evaporation of toluene, the precipitated sol was collected and dried at 333 K overnight, followed by calcination at 573 K for 6 h. The silica template was removed completely using 2 M aqueous NaOH solution heated to 333 K followed by several washing steps with water and a final drying step at 323 K.

#### 6.2.2 Preparation of Oxide-Supported Pt Nanoparticle Catalysts

Poly(vinylpyrrolidone) (PVP)-capped Pt nanoparticles with an average diameter of 2.5 nm were synthesized by following the reported methods.<sup>19</sup> For the preparation of oxide-supported nanoparticle catalysts, colloidal solutions of Pt nanoparticles ( $1 \text{ mg mL}^{-1}$ ) were diluted in ethanol. The desired amounts of solution (0.3–0.5 wt. % Pt) were added to the mesoporous oxides, and the mixtures were sonicated for 3 h at room temperature using a commercial ultrasonic cleaner (Branson, 1510R-MT, 70 W, 42 kHz). The brown precipitates were separated by centrifugation (3000 rpm, 20 min), thoroughly washed with acetone and ethanol four times, and dried in an oven at 353 K overnight.

#### 6.2.3 Characterization

Structural characterizations of Pt nanoparticles were performed using a Hitachi H-7650 transmission electron microscope operated at 120 kV. X-ray diffraction (XRD) patterns were measured on a Bruker D8 GADDS diffractometer using Co  $K\alpha$  radiation ( $1.79 \text{ \AA}$ ). Nitrogen physisorption data were obtained on a Quantachrome Autosorb-1 analyzer. Elemental analyses by inductively coupled plasma atomic emission spectroscopy (ICP-OES) were conducted using a PerkinElmer optical emission spectrometer (Optima 7000 DV). Before an ICP-OES measurement, calibration was conducted using a platinum standard (Fluka, TraceCERT,  $1000 \text{ mg L}^{-1}$ ) as a certified reference material (CRM). Catalysts dissolved in aqua regia were diluted with DI water and filtered for the measurement.

#### 6.2.4 Catalytic CO Oxidation

CO oxidation was performed in a laboratory-scale flow reactor operated at atmospheric pressure over the temperature range between 373 and 573 K. Gas flows (Praxair, UHP) were regulated using calibrated mass-flow controllers. Temperature was controlled using a type-K thermocouple and a PID controller (Watlow 96). Catalyst (0.01–0.1 g) was diluted with low-surface-area quartz sand (washed with acid, rinsed with DI water, and calcined before use) and loaded into quartz reactors. Two different CO oxidation rates were measured, in 100 Torr CO and 40 Torr O<sub>2</sub> with a balance of He for net reducing conditions or in 40 Torr CO and 100 Torr O<sub>2</sub> with a balance of He for net oxidizing conditions. Gas compositions were analyzed with a thermal conductivity detector (TCD) on an HP 5890 Series II gas chromatograph (GC). For comparison, mesoporous silica SBA-15 was used with and without loading of Pt nanoparticles for this reaction.<sup>19</sup> When the SBA-15 was used solely for CO oxidation, no activity was obtained up to a temperature of 673 K. Turnover frequencies (TOFs) were calculated by normalizing the conversion to the number of available surface Pt atoms as measured by ethylene hydrogenation and calculated on the basis of size arguments. Ethylene hydrogenation activities were used to determine the number of Pt surface sites per unit mass of catalyst by using the known TOF of 11 molecules of ethylene per surface Pt per second at 293 K with 100 Torr H<sub>2</sub> and 10 Torr C<sub>2</sub>H<sub>4</sub>.<sup>20</sup> The TOF values of the mesoporous oxides were determined by taking the molecular production rates measured per unit surface site of the oxides based on their BET surface areas ( $\text{m}^2 \text{ g}^{-1}$ ) and crystalline structures. The TOFs of the Pt–oxide interfaces (i.e., after subtraction of the contributions from pure Pt and metal oxide) were calculated from the number of surface Pt sites.



### 6.2.5 In Situ Characterization

AP-XPS and NEXAFS experiments were performed at beamlines 9.3.2 and 7.0.1 of the Advanced Light Source (ALS) at Lawrence Berkeley National Laboratory. NEXAFS studies were carried out in our purpose-built flow cell. Supported catalysts were exposed to pure CO or O<sub>2</sub> or a CO/O<sub>2</sub> mixture (either 39 Torr O<sub>2</sub> and 15 Torr CO or 39 Torr CO and 15 Torr O<sub>2</sub>) at 473 or 523 K. The NEXAFS total electron yield (TEY) spectra with 0.3 eV resolution at the metal L (Co and Mn) or M (Ce) edge were monitored via a current amplifier by detecting compensating electrons from ground to the sample.<sup>21</sup> The oxidation states of the metal oxides in the near-surface regions were determined by a linear-combination fitting of the reference compounds.<sup>21</sup> AP-XPS at beamline 9.3.2 of the ALS was conducted because it overcomes the limitations of short mean free paths of emitted photoelectrons by bringing a small aperture cone, which is differentially pumped, very close to the sample surface, which is in the reaction gas mixture.<sup>22</sup>

## 6.3 Results and Discussion

### 6.3.1 Preparation of Mesoporous Oxides of Co<sub>3</sub>O<sub>4</sub>, $\beta$ -MnO<sub>2</sub>, NiO, $\alpha$ -Fe<sub>2</sub>O<sub>3</sub>, and CeO<sub>2</sub> and Pt-Loaded Oxide Catalysts

Mesoporous Co<sub>3</sub>O<sub>4</sub>, NiO, MnO<sub>2</sub>, Fe<sub>2</sub>O<sub>3</sub>, and CeO<sub>2</sub> were prepared through the hard-templating (nanocasting) approach using mesoporous silica templates.<sup>16-18</sup> The hard template determines the final structure of the oxide and provides stability during high-temperature crystallization.<sup>17,23,24</sup> In the present study, KIT-6 mesoporous silica was used as a hard template with an ordered bi-continuous mesostructure with cubic *Ia3d* symmetry.<sup>15</sup> When metal nitrates as metal oxide precursors were combined with KIT-6 in solution, they were completely impregnated into the silica templates and readily converted to the desired crystalline oxides after calcination at 573 K. The KIT-6 was removed completely by washing with aqueous NaOH solution, leaving mesoporous Co<sub>3</sub>O<sub>4</sub>,  $\beta$ -MnO<sub>2</sub>, NiO,  $\alpha$ -Fe<sub>2</sub>O<sub>3</sub>, and CeO<sub>2</sub> replicas. Figure 1 shows a general nanocasting approach for the preparation of ordered mesoporous oxides and representative transmission electron microscopy (TEM) images of the KIT-6 silica template, mesoporous Co<sub>3</sub>O<sub>4</sub>, and Pt-nanoparticle-loaded Co<sub>3</sub>O<sub>4</sub> catalysts. TEM images of the mesoporous oxides demonstrate that the well-ordered structures and the wall thicknesses (ca. 3 nm) of the oxides were in accordance with the replicated KIT-6 (see Figure 2 and Table 1).

PVP-capped Pt nanoparticles with an average diameter of 2.5 nm were incorporated into the mesoporous oxides for the preparation of Pt nanoparticle-loaded mesoporous oxide catalysts. Sonication induced efficient dispersion of the Pt nanoparticles over the inner pores of the mesoporous oxides.<sup>19</sup> The TEM image in Figure 1c clearly shows that the Pt nanoparticles were deposited and well-dispersed on mesoporous Co<sub>3</sub>O<sub>4</sub> homogeneously. Elemental analyses by energy-dispersive spectroscopy (EDS) phase mappings on Pt/Co<sub>3</sub>O<sub>4</sub> (Figure 1d) were in agreement with the values obtained by ICP-OES (i.e., 0.38 wt. % Pt).

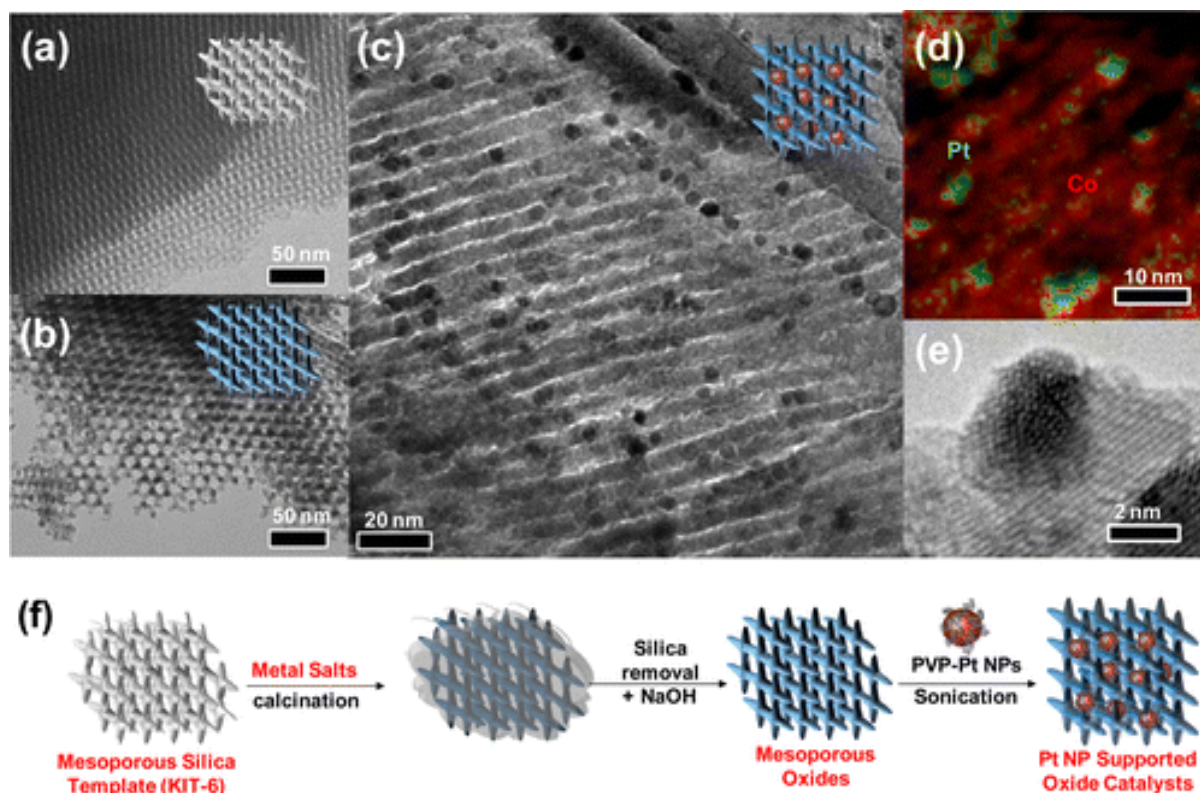


**Figure 1.** Preparation of Pt-nanoparticle-loaded  $\text{Co}_3\text{O}_4$  catalysts. a, b) TEM images of a) the mesoporous silica template and b) the resulting  $\text{Co}_3\text{O}_4$  replica. c) TEM image of Pt/ $\text{Co}_3\text{O}_4$  catalysts and d) their corresponding energy-dispersive spectroscopy (EDS) phase mapping, showing the merged image of the Co K (red) and Pt L (green) lines. e) High-resolution TEM image of Pt/ $\text{Co}_3\text{O}_4$  catalysts. f) Illustration of the hard-templating (nanocasting) approach for the preparation of mesoporous-oxide-supported Pt nanoparticle catalysts.

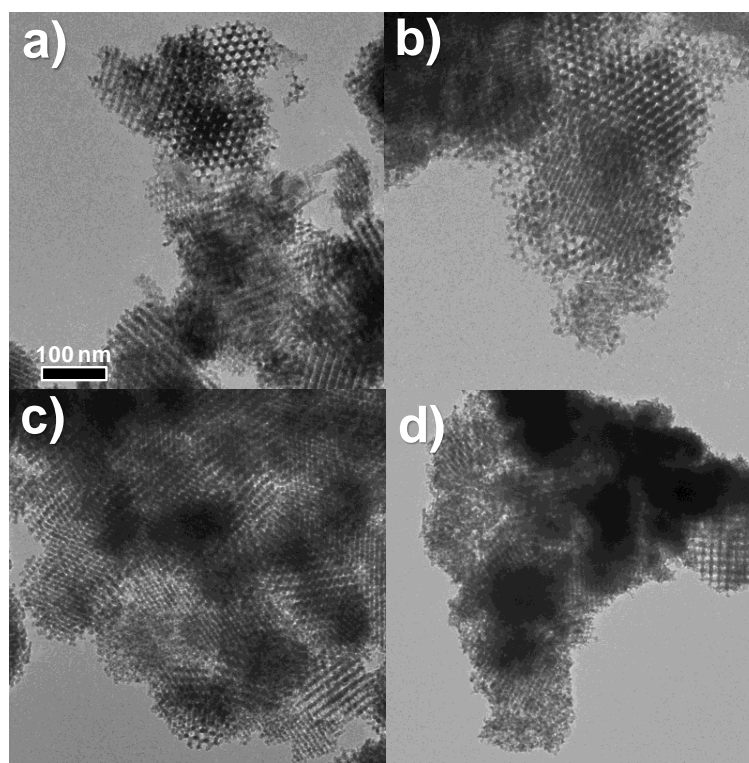


**Figure 2.** TEM images of mesoporous a) NiO, b) MnO<sub>2</sub>, c) Fe<sub>2</sub>O<sub>3</sub>, and d) CeO<sub>2</sub>.

**Table 1:** BET surface areas, average pore sizes, and pore volumes of mesoporous oxides.

Mesoporous Materials	Surface Area (m <sup>2</sup> /g)	Pore Size (nm)	Pore Volume (cc/g)
Co <sub>3</sub> O <sub>4</sub>	80	7.2	0.14
NiO	98	11.9	0.29
MnO <sub>2</sub>	56	9.4	0.13
Fe <sub>2</sub> O <sub>3</sub>	128	12.8	0.41
CeO <sub>2</sub>	107	7.9	0.21
KIT-6 (template)	654	3.2	0.52

### 3.2 CO Oxidation on Pure Mesoporous Oxides

Mesoporous oxides have shown notable catalytic activity as heterogeneous catalysts even in the absence of noble metals.<sup>16,25-31</sup> Ren et al. studied ordered mesoporous oxides of  $\text{Co}_3\text{O}_4$ ,  $\text{Cr}_2\text{O}_3$ ,  $\text{CuO}$ ,  $\text{Fe}_2\text{O}_3$ ,  $\text{MnO}_2$ ,  $\text{Mn}_2\text{O}_3$ ,  $\text{NiO}$ , and  $\text{CeO}_2$  as catalysts for CO oxidation.<sup>18</sup> In their study,  $\text{Co}_3\text{O}_4$ ,  $\beta\text{-MnO}_2$ , and  $\text{NiO}$  exhibited high CO oxidation activities, which were determined by measuring the temperatures required for 50% CO conversion ( $T_{50}$ ). In order to study the catalytic activity of the metal-support interaction and the effect of gas feed composition, CO oxidation was carried out under two different sets of conditions, with either reducing (100 Torr CO and 40 Torr  $\text{O}_2$  with a balance of He) or oxidizing (40 Torr CO and 100 Torr  $\text{O}_2$  with a balance of He) gas feeds. The reaction was performed in a laboratory-scale flow reactor operated at atmospheric pressure over the temperature range between 373 and 573 K. It has been reported that  $\text{Co}_3\text{O}_4$  shows extraordinarily high low-temperature activity, and  $\text{Co}^{3+}$  is believed to be an active site in CO oxidation.<sup>29-31</sup> Jansson et al. proposed that CO oxidation over  $\text{Co}_3\text{O}_4$  proceeds through a redox cycle in which gas-phase CO adsorbs on a cobalt site and subsequently reacts with a lattice oxygen atom.<sup>29</sup> This then forms  $\text{CO}_2(\text{g})$  and an oxygen vacancy, thus reducing the oxidation state of the cobalt site to  $\text{Co}^{2+}$ . Reoxidation of the cobalt site occurs with gas-phase oxygen.

As shown in Figure 3a, pure  $\text{Co}_3\text{O}_4$  and  $\text{NiO}$  showed higher TOFs (normalized to surface area) than  $\text{MnO}_2$ ,  $\text{Fe}_2\text{O}_3$ , and  $\text{CeO}_2$  under both reducing and oxidizing conditions. The TOFs of  $\text{MnO}_2$ ,  $\text{Fe}_2\text{O}_3$ , and  $\text{CeO}_2$  under the net reducing reaction conditions were much higher than those under the net oxidizing reaction conditions. On the contrary, the catalytic activity of  $\text{NiO}$  was found to be higher under  $\text{O}_2$ -rich conditions than under CO-rich conditions. Intrinsic properties of the oxides seem to determine the catalytic behavior under these oxidizing or reducing reaction conditions.

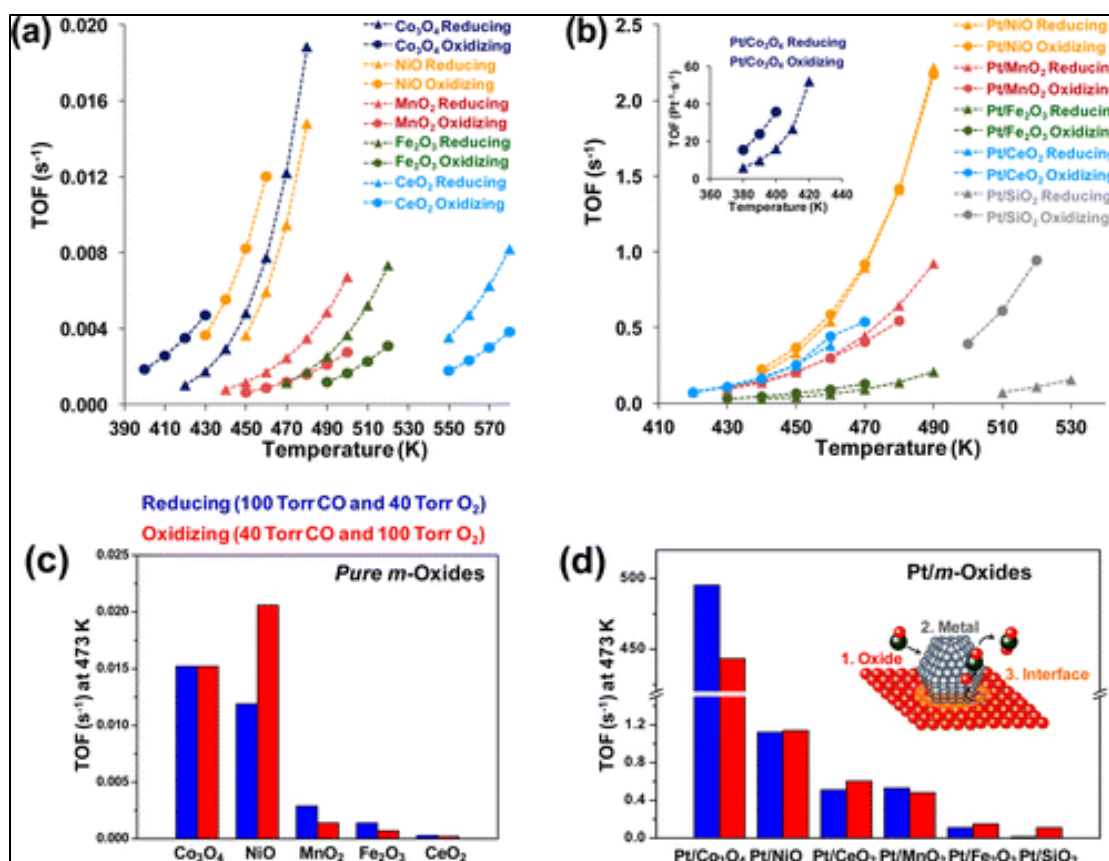


**Figure 3.** CO oxidation over (a, c) pure mesoporous oxides and (b, d) Pt-nanoparticle-loaded oxide catalysts. (a, b) Temperature-dependent turnover frequencies (TOFs) under either net reducing (100 Torr CO and 40 Torr O<sub>2</sub>) or net oxidizing (40 Torr CO and 100 Torr O<sub>2</sub>) conditions. (c, d) Comparison of TOFs at 473 K. The inset in (d) is an illustration showing the potential reaction sites of Pt-nanoparticle-loaded oxide catalysts during CO oxidation.

### 6.3.3 CO Oxidation Studies on a Pt-Nanoparticle-Loaded Silica Support

In order to find the contribution to the catalytic activity of only Pt nanoparticles, mesoporous silica was used as an inert support. It has been shown that mesoporous silica, such as SBA-15 or MCF-17, does not contribute to the catalytic activity of Pt for many reactions.<sup>18</sup> When pure SBA-15 was solely used for CO oxidation in the current study, no conversion was found up to 673 K. In Figure 3a, the TOF for the Pt/SiO<sub>2</sub> catalyst was substantially higher under the O<sub>2</sub>-rich reaction conditions than under the CO-rich reaction conditions across the temperature range studied. The TOFs for CO oxidation over Pt/SiO<sub>2</sub> were 0.014 and 0.11 s<sup>-1</sup> at 473 K under CO- and O<sub>2</sub>-rich reaction conditions, respectively. Goodman and co-workers reported TOF values of 0.01–0.1 s<sup>-1</sup> at 473 K and an activation energy of ca. 26 kcal/mol over Pt/SiO<sub>2</sub> catalysts

and Pt(100) single crystals under CO-rich reaction conditions, which are in agreement with the values for the Pt/SiO<sub>2</sub> catalyst from this work (0.014–0.11 s<sup>-1</sup> and 23 kcal/mol).<sup>32</sup>

CO oxidation on Pt-group metal surfaces has been shown to be structure-insensitive under CO-dominant conditions, under which the reaction rate is limited by CO adsorption because CO blocks the active sites for O<sub>2</sub> adsorption and dissociation.<sup>32–35</sup> This agrees with our findings on CO oxidation over Pt nanoparticles supported on SiO<sub>2</sub>, which exhibited no size dependence of the TOFs over the size range from 1.5 to 5 nm under both CO- and O<sub>2</sub>-rich reaction conditions.

### 3.4 CO Oxidation Studies of Pt-Nanoparticle-Loaded Mesoporous Oxide Systems

When Pt nanoparticles were loaded into the mesoporous oxides, the observed catalytic TOFs were significantly higher than those expected simply by summing the contributions from the oxide support and the pure Pt nanoparticles. This enhancement can be attributed to activity at the oxide–metal interface coupled with the activities of the oxide and Pt (Figure 3b). The TOFs over the Pt-loaded oxide catalysts were 495.27, 1.12, 0.57, 0.53, and 0.11 Pt<sup>-1</sup> s<sup>-1</sup> at 473 K under CO-rich reaction conditions and 443.31, 1.14, 0.60, 0.48, and 0.15 Pt<sup>-1</sup> s<sup>-1</sup> at 473 K under O<sub>2</sub>-rich reaction conditions for Pt/Co<sub>3</sub>O<sub>4</sub>, Pt/NiO, Pt/CeO<sub>2</sub>, Pt/MnO<sub>2</sub>, and Pt/Fe<sub>3</sub>O<sub>4</sub>, respectively. The contributions of the oxide–metal interfaces were found to be orders of magnitude greater than those of Pt and the oxides regardless of the gas composition (Figure 3c,d). When Pt nanoparticles were loaded on the mesoporous oxides, the reaction rates were further altered by the redox behaviors of the oxide supports. Since the 3d-block metal oxides are subject to alternation of their oxidation states under redox gas atmospheres, synergistic acid–base and/or redox sites are regarded as the key for the catalytic oxidation reaction.<sup>36–38</sup> The fact that the TOFs over the Pt/NiO, Pt/MnO<sub>2</sub>, Pt/Fe<sub>2</sub>O<sub>3</sub>, and Pt/CeO<sub>2</sub> catalysts were identical under the net reducing and net oxidizing reaction atmospheres strongly suggests the existence of a catalytic reaction pathway at the interface between the CO-covered Pt and metal oxide surfaces. We observed that the Pt/SiO<sub>2</sub> catalyst showed less activity in the CO-rich environment than under the O<sub>2</sub>-rich reaction conditions. This is in line with the CO/O<sub>2</sub> reaction rate being inversely proportional to the CO partial pressure over the Pt catalyst because of the surface poisoning effect of CO.<sup>39,40</sup> The extraordinarily large enhancements of the reaction rates over the Pt-loaded oxide catalysts and the changes in their TOFs under the net reducing reaction conditions can be explained by the following pathway: (1) chemisorption of CO on the Pt surface; (2) migration of the CO adsorbate to the interface between Pt and the oxide; (3) formation of active oxygen in the oxide lattice of the metal interface; (4) reaction between the chemisorbed CO and the activated oxygen at the interface; and (5) refill of oxygen vacancies in the oxide by gaseous O<sub>2</sub>.<sup>10,41,42</sup>

### 3.5 In Situ Characterization of Oxide Catalysts during CO Oxidation

In order to understand the observed behavior of activity enhancement, in situ characterizations using NEXAFS and AP-XPS were conducted under catalytically relevant reaction conditions.<sup>43</sup> Briefly, supported Pt/Co<sub>3</sub>O<sub>4</sub>, Pt/MnO<sub>2</sub>, and Pt/CeO<sub>2</sub> catalysts were exposed to pure CO or O<sub>2</sub> or a CO/O<sub>2</sub> mixture [–39 Torr O<sub>2</sub> and 15 Torr CO (denoted as O<sub>2</sub>-rich) or 39 Torr CO and 15 Torr O<sub>2</sub> (denoted as CO-rich)] at 473 or 523 K. Figure 4a shows NEXAFS TEY spectra of the Pt/MnO<sub>2</sub> catalyst at 523 K under the O<sub>2</sub>-rich and CO-rich reaction conditions. A linear-combination fitting of the reference compounds indicated that an excess of the MnO<sub>2</sub> phase (a fraction of 0.8) was present in equilibrium with the spinel Mn<sub>3</sub>O<sub>4</sub> phase under the O<sub>2</sub>-rich conditions. Under the CO-rich reaction conditions, however, the surface regions were

further reduced, resulting in a 50:50 mixture of the  $\text{MnO}_2$  and  $\text{Mn}_3\text{O}_4$  phases (Figure 4). Figure 4b shows the proportions of  $\text{MnO}_2$  on the surface and TOFs that have been decomposed into metal–oxide interface and Pt metal contributions during the  $\text{CO}/\text{O}_2$  reactions at 473 and 523 K. We found a strong correlation between the oxidation state of Mn and the normalized catalytic activity at the metal–oxide interface. In the  $\text{O}_2$ -rich reaction, the fraction of  $\text{MnO}_2$  was changed

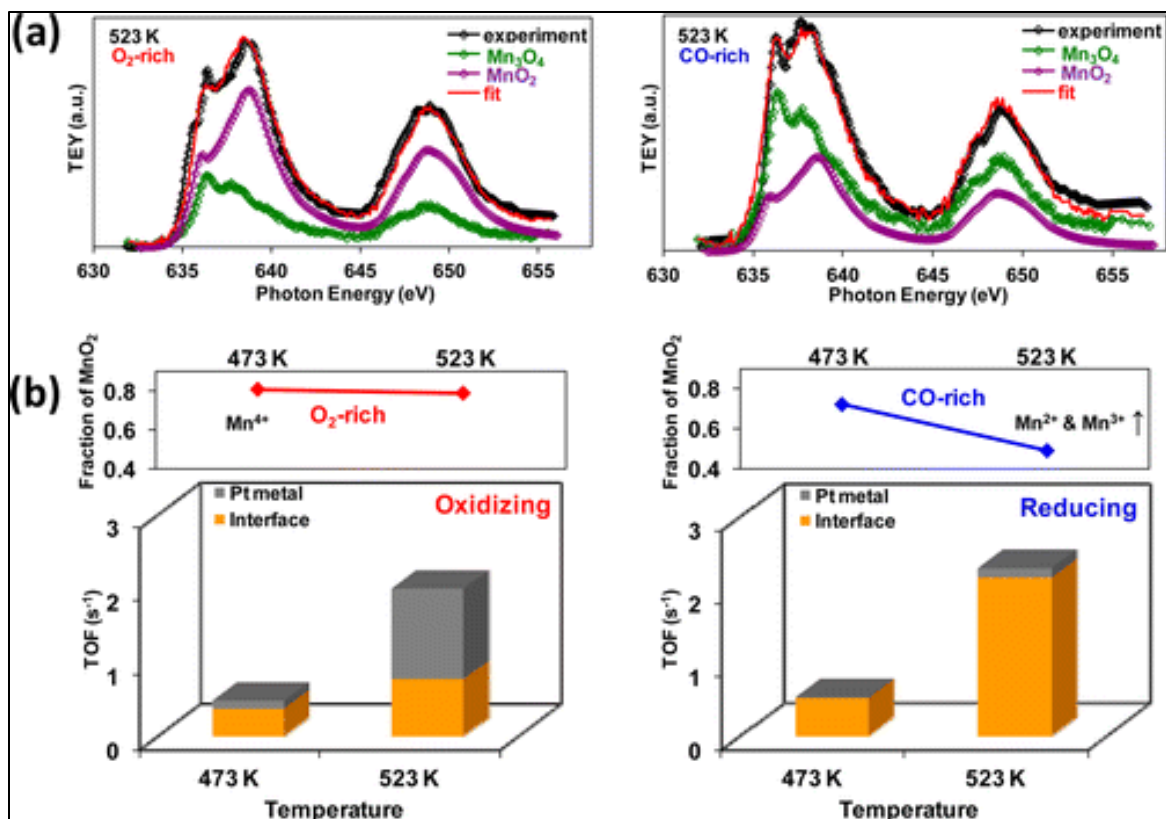


**Figure 4.** a) Near-edge X-ray absorption fine structure (NEXAFS) total electron yield (TEY) spectra at the Mn L edges for the Pt/ $\text{MnO}_2$  catalyst and b) graphs correlating the catalytic activity (TOF) and oxidation state of Mn in  $\text{CO}$  oxidation. Shown in a) are representative linear-combination fittings obtained at 523 K under (left) 15 Torr  $\text{CO}$  and 39 Torr  $\text{O}_2$  ( $\text{O}_2$ -rich) and (right) 39 Torr  $\text{CO}$  and 15 Torr  $\text{O}_2$  ( $\text{CO}$ -rich) conditions. The top panels in b) show the proportions of  $\text{MnO}_2$  obtained by linear-combination fitting of the reference compounds to the NEXAFS spectra, and the corresponding TOF plots at both 473 and 523 K under different reaction conditions are given in the bottom panels. The bar graphs showing the total TOFs of the Pt/ $\text{MnO}_2$  catalyst have been decomposed into the contributions of pure Pt (in gray) and the Pt– $\text{MnO}_2$  interface (in orange). The TOFs exhibited by pure mesoporous  $\text{MnO}_2$  were too small to be represented.



very little (from 0.81 at 473 K to 0.79 at 523 K). In parallel with this, the turnover rate at the metal–oxide interface (color-coded in orange) was slightly increased from 0.37 to 0.77 s<sup>-1</sup>, exhibiting a 2-fold change in CO oxidation rate at the interface compared with pure Pt (color-coded in gray) (Figure 4b, left). However, in the CO-rich reaction, both the extent of the reduction of Mn and the relative change in turnover rates at the metal–oxide interface were substantial. The fraction of MnO<sub>2</sub> phase decreased from 0.72 to 0.49, while the turnover rate at the interface jumped from 0.51 to 2.16 s<sup>-1</sup>, which was an order of magnitude change with respect to pure Pt. On the basis of the observed trend, spinel Mn<sub>3</sub>O<sub>4</sub> was identified as the dominant phase at the metal–support interface and thus the species responsible for the orders of magnitude enhancement in the CO oxidation rate.

Both a bifunctional mechanism<sup>44</sup> and a Mars–van Krevelen mechanism<sup>36-38</sup> could potentially explain the catalytic activity enhancement by the support in this case; however, neither could give insight into the detailed reaction scheme of the CO-rich or CO-deficit atmospheres. The O 1s AP-XPS spectra of the Pt/MnO<sub>2</sub> catalyst were obtained under CO-rich and O<sub>2</sub>-rich CO/O<sub>2</sub> reaction conditions at 473 K. In these spectra, the peak at 529 eV was assigned to the lattice oxygen of MnO<sub>2</sub><sup>45,46</sup> and the higher binding energy peak at 531 eV is due to OH species or adsorbed H<sub>2</sub>O<sup>46</sup> (Figure 5). The normalized XPS intensities indicate that the lattice oxygen was more abundant under the O<sub>2</sub>-rich reaction conditions than under the CO-rich conditions, although the CO/O<sub>2</sub> reaction was more favorable under the CO-rich conditions. From these results, we concluded that the interfacial reaction is governed by the oxidation state of MnO<sub>2</sub>.

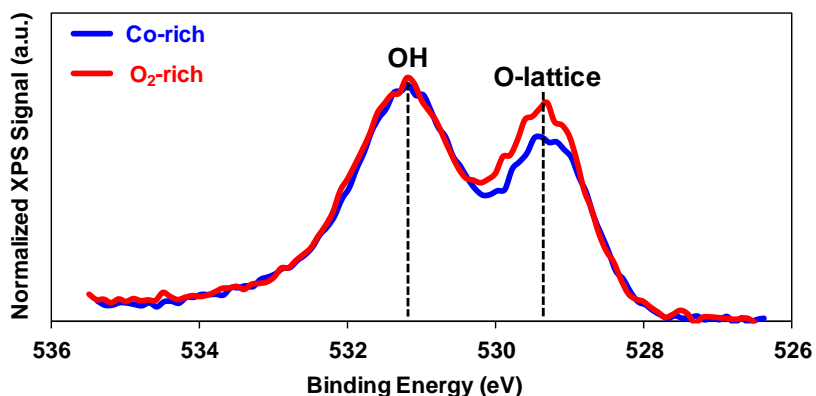


**Figure 5.** Ambient pressure X-ray photoelectron spectroscopy (APXPS) spectra of Pt/MnO<sub>2</sub> catalyst. Normalized O1s APXPS spectra of the Pt/MnO<sub>2</sub> catalyst obtained under the CO-rich (100 mTorr CO and 40 mTorr O<sub>2</sub>) and O<sub>2</sub>-rich (40 mTorr CO and 100 mTorr O<sub>2</sub>) reaction conditions at 473 K (Dashed lines indicate the positions of OH and lattice oxygen).

This phenomenon was not limited to the case of the Pt/MnO<sub>2</sub> catalyst but could be generalized to the other Pt/metal oxide systems. The Pt/CeO<sub>2</sub> catalyst exhibited greater overall



interfacial enhancement under the O<sub>2</sub>-rich conditions, while the enhancement was more dramatic relative to pure Pt under the CO-rich reaction condition. AP-XPS and NEXAFS independently revealed that the near-surface region (ca. 2 nm) of the Pt/CeO<sub>2</sub> catalyst mainly was composed of Ce<sup>4+</sup> during the CO/O<sub>2</sub> reaction at 523 K. On the other hand, the Ce<sup>3+</sup> concentration was appreciable (ca. 15%) under CO-rich conditions but was negligibly small (less than 5%) under O<sub>2</sub>-rich conditions at 523 K, suggesting that CO reduces CeO<sub>2</sub> without apparent reaction turnovers (Figure 6). The O 1s AP-XPS spectra also indicated no correlation between lattice oxygen (or OH) and the reaction rate. The overlapping conclusion was that Ce<sup>4+</sup> sites give rise to the interfacial enhancement over the Pt/CeO<sub>2</sub> catalyst during the CO/O<sub>2</sub> reaction: Ce<sup>3+</sup> sites formed upon reduction of CeO<sub>2</sub> under the CO-rich conditions, rendering the overall enhancement (i.e., higher turnover rates under O<sub>2</sub>-rich vs CO-rich conditions) without significantly impacting the enhancement factor (i.e., similar orders of magnitude enhancement at the interface relative to pure Pt).

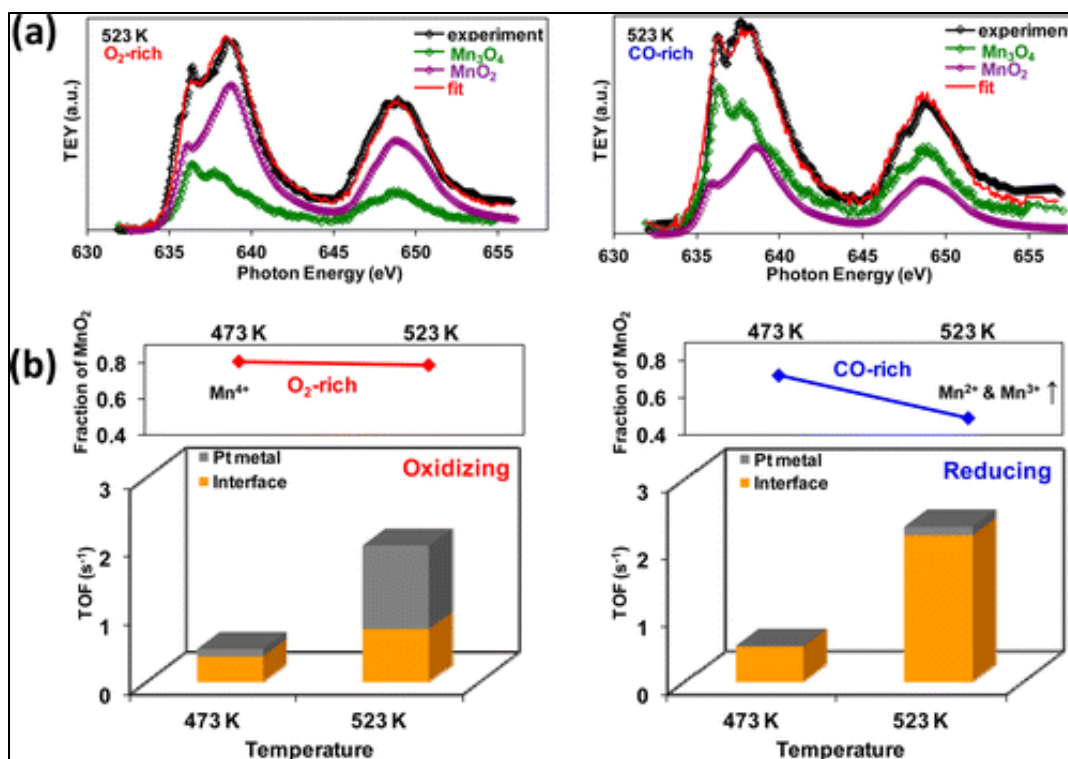


**Figure 6.** a) NEXAFS TEY spectra at the Ce M edges for the Pt/CeO<sub>2</sub> catalyst and b) graphs correlating the catalytic activity (TOF) and oxidation state of Ce in CO oxidation. Shown in a) are representative linear-combination fittings obtained at 523 K under (left) 15 Torr CO and 39 Torr O<sub>2</sub> (O<sub>2</sub>-rich) and (right) 39 Torr CO and 15 Torr O<sub>2</sub> (CO-rich) conditions. The top panels in b) show the proportions of Ce<sup>4+</sup> obtained by linear-combination fitting of the reference compounds to the NEXAFS spectra and analysis of Ce 4d XPS spectra, and the corresponding TOF plots at both 473 and 523 K under different reaction conditions are given in the bottom panels. The bar graphs showing the total TOFs of the Pt/CeO<sub>2</sub> catalyst have been decomposed into the contributions of pure Pt (in gray) and the Pt–CeO<sub>2</sub> interface (in orange). The contribution of pure mesoporous CeO<sub>2</sub> was too small to be represented. It should be noted that both the line plots and bar graphs are given to the same scale.

For the Pt/Co<sub>3</sub>O<sub>4</sub> catalyst, the characteristic NEXAFS spectra of spinel Co<sub>3</sub>O<sub>4</sub> at the Co L edge were mainly maintained under CO-rich reaction conditions at and below 473 K, whereas CoO formed as the dominant phase at the expense of the spinel Co<sub>3</sub>O<sub>4</sub> phase above 523 K under the CO-rich conditions (Figure 7). Our linear-combination fitting indicated the simultaneous formation of two CoO phases: one with Co(II) in octahedral sites and another with Co(II) in tetrahedral sites.<sup>20</sup> For the reaction in the O<sub>2</sub>-rich environment, the spinel Co<sub>3</sub>O<sub>4</sub> phase remained dominant over the whole temperature range studied, in agreement with the findings of Oku and

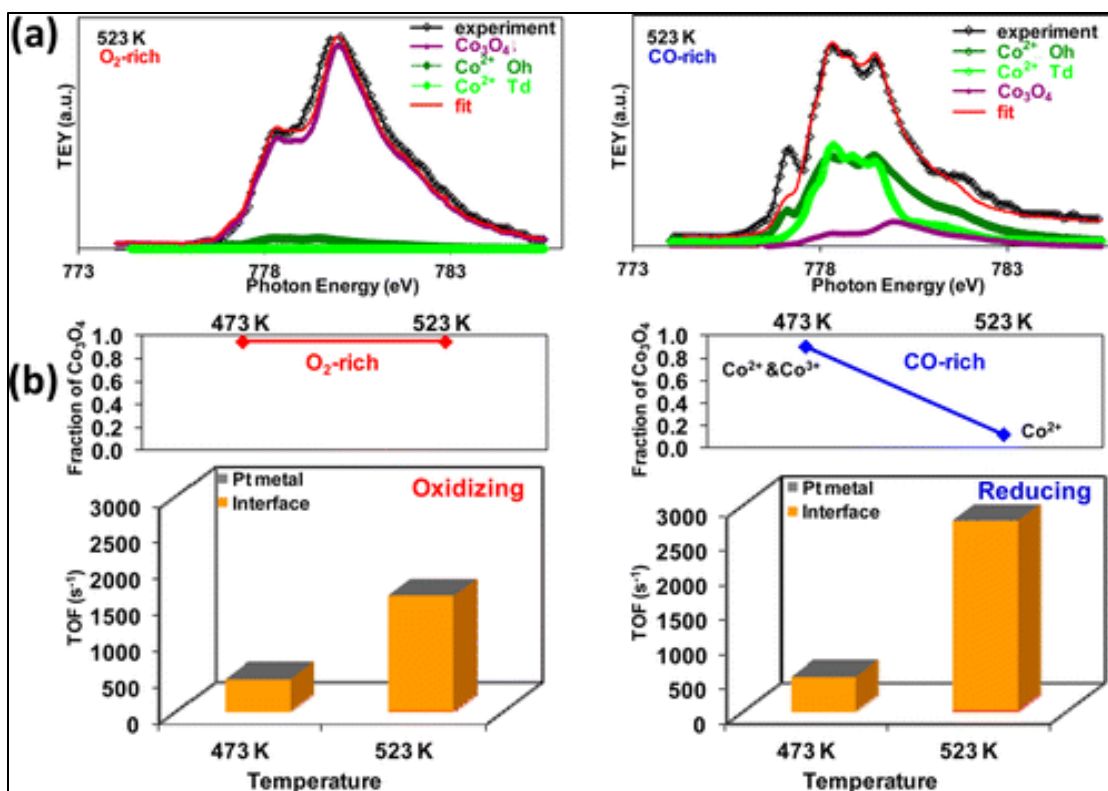


**Figure 6.** a) NEXAFS TEY spectra at the Co L edges for the Pt/Co<sub>3</sub>O<sub>4</sub> catalyst and b) graphs correlating the catalytic activity (TOF) and oxidation state of Co in CO oxidation. Shown in a) are representative linear-combination fittings obtained at 523 K under (left) 15 Torr CO and 39 Torr O<sub>2</sub> (O<sub>2</sub>-rich) and (right) 39 Torr CO and 15 Torr O<sub>2</sub> (CO-rich) conditions. The top panels in b) show the proportions of Co<sub>3</sub>O<sub>4</sub> obtained by linear-combination fitting of the reference compounds to the NEXAFS spectra, and the corresponding TOF plots at both 473 and 523 K under different reaction conditions are given in the bottom panels. The bar graphs showing the total TOFs of the Pt/Co<sub>3</sub>O<sub>4</sub> catalyst have been decomposed into the contributions of pure Pt (in gray) and the Pt–Co<sub>3</sub>O<sub>4</sub> interface (in orange). The contribution of pure mesoporous Co<sub>3</sub>O<sub>4</sub> was too small to be represented.

Sato.<sup>47</sup> From the viewpoint of catalysis, the CO oxidation rates were enhanced by 4 orders of magnitude at the metal–oxide interface under both the CO- and O<sub>2</sub>-rich conditions; however, the enhancement factor was greater in the case of the CO-rich reactions, where CoO phases were dominant at the near-surface regions (Figure 7). While Co(III) sites were usually attributed to the CO/O<sub>2</sub> reaction turnovers on pure Co<sub>3</sub>O<sub>4</sub>,<sup>48</sup> we found that Co(II) sites are responsible for the orders of magnitude enhancement in the reaction kinetics at the metal–oxide interface.

Through catalytic activity measurements and in situ surface probe experiments, we identified that Mn<sup>2+</sup> and Mn<sup>3+</sup> in spinel Mn<sub>3</sub>O<sub>4</sub>, Ce<sup>4+</sup> in CeO<sub>2</sub>, and Co<sup>2+</sup> in Co<sub>3</sub>O<sub>4</sub> are the active surface phases of the oxides in contact with Pt nanoparticles. The mesoporous oxides of 3d transition metals (Co and Mn) appeared to be more active in CO oxidation at a reduced form of

the oxide in contact with Pt, while CeO<sub>2</sub> exhibited the opposite behavior, as Ce<sup>4+</sup> was catalytically more active than Ce<sup>3+</sup> when interfaced with Pt. This reflects on the fact that the catalytic TOF on the Pt/CeO<sub>2</sub> catalyst under the O<sub>2</sub>-rich reaction conditions was significantly larger than that under the CO-rich reaction conditions.

On the basis of our measurements of oxidation state and catalytic activities, we propose the existence of a charge-flow channel for the catalytic oxidation of CO. The role of Pt is to provide metal sites for charge to flow at Schottky interfaces, which in return create a new reaction pathway for CO to be oxidized at such high rates.<sup>49-52</sup> This explanation is based on previous studies that measured the flow of hot electrons simultaneously with turnover rates for the CO/O<sub>2</sub> and H<sub>2</sub>/O<sub>2</sub> reactions using catalytic nanodiodes constructed from ca. 4 nm thick Pt films deposited on titanium oxide to form Schottky barriers.<sup>49</sup> The current flow across the rectifying barrier was linearly correlated with the reaction turnover rate, indicating the major role of electron flow at the Pt-TiO<sub>2</sub> interface in the catalytic reactions. However, the turnover rates were 10<sup>4</sup> times greater than the electron flow rates measured at steady state, indicating that the electrons have several competing reaction paths (such as absorption at defect sites, heating by the thermoelectric effect, etc.) in addition to becoming part of the transition state (such as CO<sub>2</sub><sup>-</sup> or H<sub>2</sub>O<sup>-</sup>) that controls their influence on the catalytic reaction.<sup>52</sup> We believe that cobalt oxide has a higher concentration of electrons choosing the reaction path that enhances the catalytic turnover for some reason that is yet to be determined. It should be mentioned that cobalt oxide is an active material in studies of water splitting using solar energy, probably for similar reasons of efficient charge transfer during the chemical process.

## 6.4 Conclusions

At the interface of Pt nanoparticles and mesoporous oxides, we have observed great enhancements of catalytic activity in CO oxidation, which has rendered the “structure-insensitive” reaction on pure Pt surfaces very much “structure-sensitive” at oxide metal interfaces. Compared with pure Pt nanoparticles and pure mesoporous oxides, the turnover rates were increased by orders of magnitude with catalysis by the Pt-oxide interface. The reaction rates over Pt-nanoparticle-loaded oxide catalysts were further controlled by the redox properties of the oxides at the oxide-metal interface under reducing reaction conditions. Even under O<sub>2</sub>-deficient reaction conditions, active oxygen could be provided from the oxide lattice. The redox chemistry in the near-surface regions of the oxide catalysts was dynamic, depending on the temperature and whether CO- or O<sub>2</sub>-rich atmospheres were utilized during the reaction. It appears that the redox behaviors of the oxides provide the charges that participate at the oxide-metal interface, which act to amplify the CO oxidation. Through in situ characterizations using NEXAFS and AP-XPS under alternating redox conditions combined with catalytic activity measurements, we found that CoO, Mn<sub>3</sub>O<sub>4</sub>, and CeO<sub>2</sub> are responsible for the orders of magnitude enhancement in CO oxidation rate as the active surface phases of the oxide at the interface with Pt nanoparticles. This discovery of the relationship between surface redox chemistry and catalytic activity offers great advancements in the knowledge of how the oxide-metal interface functions during catalytic reactions. The in-depth understanding of these phenomena will have wide implications in understanding catalytic selectivity on charged and polar oxide surfaces for a number of heterogeneous transformations.

## 6.5 References

1. Geus, J. W.; van Ween, J. A. R. In Mouljin, J. A., van Leeuwen, P. W. N. M. and van Santen, R. A., Eds.; *Catalysis: An Integrated Approach to Homogeneous, Heterogeneous and Industrial Catalysis*; Elsevier: Amsterdam, 1993; .
2. Somorjai, G. A.; Li, Y. *Introduction to Surface Chemistry and Catalysis*; Wiley: New York, 2010; .
3. Schwab, G. M.; Koller, K. Combined Action of Metal and Semiconductor Catalysts. *J. Am. Chem. Soc.* **1968**, *90*, 3078-3080.
4. Somorjai, G. A.; Park, J. Y. Molecular Factors of Catalytic Selectivity. *Angew. Chem. , Int. Ed* **2008**, *47*, 9212-9228.
5. Boffa, A. B.; Lin, C.; Bell, A. T.; Somorjai, G. A. Lewis Acidity as an Explanation for Oxide Promotion of Metals: Implications of its Importance and Limits for Catalytic Reactions. *Catal. Lett.* **1994**, *27*, 243-249.
6. Tauster, S. J.; Fung, S. C.; Garten, R. L. Strong Metal-Support Interactions. Group 8 Noble Metals Supported on Titanium Dioxide. *J. Am. Chem. Soc.* **1978**, *100*, 170-175.
7. Wang, S. J.; Moon, S. H.; Vannice, M. A. The Effect of SMSI (Strong Metal Support Interaction) Behavior on CO Adsorption and Hydrogenation on Pd Catalysts: II. Kinetic Behavior in the Methanation Reaction. *J. Catal.* **1981**, *71*, 167-174.
8. Liu, X.; Liu, M. H.; Luo, Y. C.; Mou, C.,Y.; Lin, S. D.; Cheng, H.; Chen, J. M.; Lee, J. F.; Lin, T. S. Strong Metal-Support Interactions Between Gold Nanoparticles and ZnO Nanorods in CO Oxidation. *J. Am. Chem. Soc.* **2012**, *134*, 10251-10258.
9. Yoon, K.; Yang, Y.; Lu, P.; Wan, D.; Peng, H. C.; Stamm Masias, K.; Fanson, P. T.; Campbell, C. T.; Xia, Y. A Highly Reactive and Sinter-Resistant Catalytic System Based on Platinum Nanoparticles Embedded in the Inner Surfaces of CeO<sub>2</sub> Hollow Fibers. *Angew. Chem. , Int. Ed* **2012**, *51*, 9543-9546.
10. Jia, A. P.; Jiang, S. Y.; Lu, J. Q.; Luo, M. F. Study of Catalytic Activity at the CuO-CeO<sub>2</sub> Interface for CO Oxidation. *J. Phys. Chem. C* **2010**, *114*, 21605-21610.
11. Widman, D.; Behm, R. J. Active Oxidation on a Au/TiO<sub>2</sub> Catalyst: Formation, Stability, and CO Oxidation Activity. *Angew. Chem. , Int. Ed* **2011**, *50*, 10241-10245.
12. Baker, L. R.; Kennedy, G.; Van Spronsen, M.; Hervier, A.; Cai, X.; Chen, S.; Wang, L. W.; Somorjai, G. A. Furfuraldehyde Hydrogenation on Titanium Oxide-Supported Platinum Nanoparticles Studied by Sum Frequency Generation Vibrational Spectroscopy: Acid-Base Catalysis Explains the Molecular Origin of Strong Metal -Support Interactions. *J. Am. Chem. Soc.* **2012**, *134*, 14208-14216.

13. Yamada, Y.; Tsung, C. K.; Huang, W.; Huo, Z.; Habas, S. E.; Soejima, T.; Aliaga, C. E.; Somorjai, G. A.; Yang, P. Nanocrystal Bilayer for Tandem Catalysis. *Nature Chem.* **2011**, *3*, 372-376.
14. Somorjai, G. A.; Beaumont, S. K.; Alayoglu, S. Determination of Molecular Surface Structure, Composition, and Dynamics under Reaction Conditions at High Pressures and at the Solid-Liquid Interface. *Angew. Chem., Int. Ed* **2011**, *50*, 10116-10129.
15. Kleitz, F.; Choi, S. H.; Ryoo, R. Cubic *Ia3d* Large Mesoporous Silica: Synthesis and Replication to Platinum Nanowires, Carbon Nanorods and Carbon Nanotubes. *Chem. Commun.* **2003**, 2136-2137.
16. Taguchi, A.; Schuth, F. Ordered Mesoporous Materials in Catalysis. *Micropor. Mesopor. Mat.* **2005**, *77*, 1-45.
17. Lu, A. H.; Schuth, F. Nanocasting: A Versatile Strategy for Creating Nanostructured Porous Materials. *Adv. Mater.* **2006**, *18*, 1793-1805.
18. Ren, Y.; Ma, Z.; Qian, L.; Dai, S.; He, H.; Bruce, P. G. Ordered Crystalline Mesoporous Oxides as Catalysts for CO Oxidation. *Catal. Lett.* **2009**, *131*, 146-154.
19. Rioux, R. M.; Song, H.; Hoefelmeyer, J. D.; Yang, P.; Somorjai, G. A. High-Surface-Area Catalyst Design: Synthesis, Characterization, and Reaction Studies of Platinum Nanoparticles in Mesoporous SBA-15 Silica. *J. Phys. Chem. B* **2005**, *109*, 2192-2202.
20. Pushkarev, V. V.; An, K.; Alayoglu, S.; Beaumont, S. K.; Somorjai, G. A. Hydrogenation of Benzene and Toluene over Size Controlled Pt/SBA-15 Catalysts: Elucidation of the Pt Particle Size Effect on Reaction Kinetics. *J. Catal.* **2012**, *292*, 64-72.
21. Zheng, F.; Alayoglu, S.; Guo, J.; Pushkarev, V. V.; Li, Y.; Glans, P. A.; Chen, J. L.; Somorjai, G. In-situ X-ray Absorption Study of Evolution of Oxidation States and Structure of Cobalt in Co and CoPt Bimetallic Nanoparticles (4 nm) under Reducing (H<sub>2</sub>) and Oxidizing (O<sub>2</sub>) Environments. *Nano Lett.* **2011**, *11*, 847-853.
22. Grass, M. E.; Karlsson, P. G.; Aksoy, F.; Lundqvist, M.; Wannberg, B.; Mun, B. S.; Hussain, Z.; Liu, Z. New Ambient Pressure Photoemission Endstation at Advanced Light Source Beamline 9.3.2. *Rev. Sci. Instrum.* **2010**, *81*, 053106-1-053106-7.
23. Yue, W.; Zhou, W. Crystalline Mesoporous Metal Oxide. *Prog. Nat. Sci.* **2008**, *18*, 1329-1338.
24. Sun, X.; Shi, Y.; Zhang, P.; Zheng, C.; Zheng, X.; Zhang, F.; Zhang, Y.; Guan, N.; Zhao, D.; Stucky, G. Container Effect in Nanocasting Synthesis of Mesoporous Metal Oxides. *J. Am. Chem. Soc.* **2011**, *133*, 14542-14545.

25. Rao, Y.; Antonelli, D. Mesoporous Transition Metal Oxides: Characterization and Applications in Heterogeneous Catalysis. *J. Mater. Chem.* **2009**, *19*, 1937-1944.
26. Liang, Y.; Li, Y.; Wang, H.; Zhou, J.; Wang, J.; Regier, T.; Dai, H. Co<sub>3</sub>O<sub>4</sub> Nanocrystals on Graphene as a Synergistic Catalyst for Oxygen Reduction Reaction. *Nature Mater.* **2011**, *10*, 780-786.
27. Tuysuz, H.; Schuth, F. Chapter Two - Ordered Mesoporous Materials as Catalysts. *Adv. Catal.* **2012**, *55*, 127-239.
28. Jia, C. J.; Schwickardi, M.; Weidenthaler, C.; Schmidt, W.; Korhonen, S.; Weckhuysen, B. M.; Schuth, F. Co<sub>3</sub>O<sub>4</sub>-SiO<sub>2</sub> Nanocomposite: A Very Active Catalyst for CO Oxidation with Unusual Catalytic Behavior. *J. Am. Chem. Soc.* **2011**, *133*, 11279-11288.
29. Jansson, J.; Palmqvist, A. E. C.; Fridell, E.; Skoglundh, M.; Osterlund, L.; Thormahlen, P.; Langer, V. On the Catalytic Activity of Co<sub>3</sub>O<sub>4</sub> in Low-Temperature CO Oxidation. *J. Catal.* **2002**, *211*, 387-397.
30. Thormahlen, P.; Skoglundh, M.; Fridell, E.; Andersson, B. Low-Temperature CO Oxidation over Platinum and Cobalt Oxide Catalysts. *J. Catal.* **1999**, *188*, 300-310.
31. Jansson, J.; Skoglundh, M.; Fridell, E.; Thormahlen, P. A Mechanistic Study of Low Temperature CO Oxidation over Cobalt Oxide. *Top. Catal.* **2001**, *16-17*, 385-389.
32. McClure, S. M.; Lundwall, M.; Zhou, Z.; Yang, F.; Goodman, D. W. Characterization of Pt/SiO<sub>2</sub> Model Catalysts at UHV and Near Atmospheric Pressures. *Catal. Lett.* **2009**, *133*, 298-306.
33. Cant, N. W.; Hicks, P. C.; Lennon, B. S. Steady-State Oxidation of Carbon Monoxide over Supported Noble Metals with Particular Reference to Platinum. *J. Catal.* **1978**, *54*, 372-383.
34. Berlowitz, P. J.; Peden, C. H. F.; Goodman, D. W. Kinetics of Carbon Monoxide Oxidation on Single-Crystal Palladium, Platinum, and Iridium. *J. Phys. Chem.* **1988**, *92*, 5213-5221.
35. Allian, A. D.; Takanabe, K.; Fajdala, K. L.; Hao, X.; Truex, T. J.; Cai, J.; Buda, C.; Neurock, M.; Iglesia, E. Chemisorption of CO and Mechanism of CO Oxidation on Supported Platinum Nanoclusters. *J. Am. Chem. Soc.* **2011**, *133*, 4498-4517.
36. Doornkamp, C.; Ponc, V. The Universal Character of the Mars and Van Krevelan Mechanism. *J. Mol. Catal. A: Chem* **2000**, *162*, 19-32.
37. Mars, P.; van Krevelen, D. W. Oxidations Carried Out by Means of Vanadium Oxide Catalysts. *Chem. Eng. Sci.* **1954**, *3*, 41-59.
38. Mars, P.; Maessen, J. G. H. In Proceedings of the Third ICC, Amsterdam; North-Holland: Amsterdam, 1964; Vol. 1, pp 266.

39. McCrea, K. R.; Parker, J. S.; Somorjai, G. A. The Role of Carbon Deposition from CO Dissociation on Pt Crystal Surface during CO Oxidation: Effects on Turnover Rate, Ignition Temperature, and Vibrational Spectra. *J. Phys. Chem. B* **2002**, *106*, 10854-10863.
40. Li, Q.; He, R.; Gao, J. A.; Jenson, J. O.; Bjerrum, N. J. The CO Poisoning Effect in PEMFCs Operational at Temperatures up to 200° C. *J. Electrochem. Soc.* **2003**, *150*, A1599-A1605.
41. Weisz, P. B. Polyfunctional Heterogeneous Catalysis. *Adv. Catal.* **1962**, *13*, 137-190.
42. Coonradt, H. L.; Garwood, W. E. Mechanism of Hydrocracking. Reactions of Paraffins and Olefins. *Ind. Eng. Chem. Process Des. Dev.* **1964**, *3*, 38-45.
43. Alayoglu, S.; Krier, J. M.; Michalak, W. D.; Zhu, Z.; Gross, E.; Somorjai, G. A. In Situ Surface Reaction Probe Studies with Model Nanoparticle Catalysts. *ACS Catal.* **2012**, *2*, 2250-2258.
44. Bunluesin, T.; Gorte, R. J.; Graham, G. W. Studies of the Water-Gas-Shift Reaction on Ceria-Supported Pt, Pd, and Rh: Implications for Oxygen-Storage Properties. *Appl. Catal. B* **1998**, *15*, 107-114.
45. Oku, M.; Hirokawa, K. X-ray Photoelectron Spectroscopy of Manganese-Oxygen Systems. *J. Electron Spectrosc.* **1975**, *7*, 465-473.
46. Stranick, M. A. MnO<sub>2</sub> by XPS. *Surf. Sci. Spectra* **1999**, *6*, 31-38.
47. Oku, M.; Sato, Y. In-situ X-ray Photoelectron Spectroscopic Study of the Reversible Phase Transition between CoO and Co<sub>3</sub>O<sub>4</sub> in Oxygen of 10<sup>-3</sup> Pa. *App. Surf. Sci.* **1992**, *55*, 37-41.
48. Xie, X.; Li, Y.; Liu, Z. Q.; Haruta, M.; Shen, W. Low-Temperature Oxidation of CO Catalysed by Co<sub>3</sub>O<sub>4</sub> Nanorods. *Nature* **2009**, *458*, 746-749.
49. Park, J. Y.; Renzas, J. R.; Hsu, B. B.; Somorjai, G. A. Interfacial and Chemical Properties of Pt/TiO<sub>2</sub>, Pd/TiO<sub>2</sub>, and Pt/GaN Catalytic Nanodiodes Influencing Hot Electron Flow. *J. Phys. Chem. C* **2007**, *111*, 15331-15336.
50. Baker, L. R.; Hervier, A.; Seo, H.; Kennedy, G.; Komvopoulos, K.; Somorjai, G. A. Highly n-Type Titanium Oxide as an Electronically Active Support for Platinum in the Catalytic Oxidation of Carbon Monoxide. *J. Phys. Chem. C* **2011**, *115*, 16006-16011.
51. Hervier, A.; Renzas, J. R.; Park, J. Y.; Somorjai, G. A. Hydrogen Oxidation-Driven Hot Electron Flow Detected by Catalytic Nanodiodes. *Nano Lett.* **2009**, *9*, 3930-3933.
52. Maximoff, S. N.; Head-Gordon, M. P. Chemistry of Fast Electrons. *Proc. Natl. Acad. Sci. U. S. A.* **2009**, *106*, 11460-11465.



## Chapter 7

# Designed Catalysts from Pt Nanoparticles Supported on Macroporous Oxides for Selective Isomerization of *n*-Hexane

### Abstract

Selective isomerization toward branched hydrocarbons is an important catalytic process in oil refining to obtain high-octane gasoline with minimal content of aromatic compounds. Colloidal Pt nanoparticles with controlled sizes of 1.7, 2.7, and 5.5 nm were deposited onto ordered macroporous oxides of SiO<sub>2</sub>, Al<sub>2</sub>O<sub>3</sub>, TiO<sub>2</sub>, Nb<sub>2</sub>O<sub>5</sub>, Ta<sub>2</sub>O<sub>5</sub>, and ZrO<sub>2</sub> to investigate Pt size- and support-dependent catalytic selectivity in *n*-hexane isomerization. Among the macroporous oxides, Nb<sub>2</sub>O<sub>5</sub> and Ta<sub>2</sub>O<sub>5</sub> exhibited the highest product selectivity, yielding predominantly branched C<sub>6</sub> isomers, including 2- or 3-methylpentane, as desired products of *n*-hexane isomerization (140 Torr *n*-hexane and 620 Torr H<sub>2</sub> at 360 °C). *In situ* characterizations including X-ray diffraction and ambient-pressure X-ray photoelectron spectroscopy showed that the crystal structures of the oxides in Pt/oxide catalysts were not changed during the reaction and oxidation states of Nb<sub>2</sub>O<sub>5</sub> were maintained under both H<sub>2</sub> and O<sub>2</sub> conditions. Fourier transform infrared spectra of pyridine adsorbed on the oxides showed that Lewis sites were the dominant acidic site of the oxides. Macroporous Nb<sub>2</sub>O<sub>5</sub> and Ta<sub>2</sub>O<sub>5</sub> were identified to play key roles in the selective isomerization by charge transfer at Pt–oxide interfaces. The selectivity was revealed to be Pt size-dependent, with improved isomer production as Pt sizes increased from 1.7 to 5.5 nm. When 5.5 nm Pt nanoparticles were supported on Nb<sub>2</sub>O<sub>5</sub> or Ta<sub>2</sub>O<sub>5</sub>, the selectivity toward branched C<sub>6</sub> isomers was further increased, reaching ca. 97% with a minimum content of benzene, due to the combined effects of the Pt size and the strong metal–support interaction.

\* This chapter covers similar material as in An, K.; Alayoglu, S.; Musselwhite, N.; Na, K.; Somorjai, G.A. *J. Am. Chem. Soc.* **2014**, *136*, 6830-6833. — reproduced with permission, copyright 2014 American Chemical Society.

## 7.1 Introduction

In the 21st century, catalysis aims for 100% selectivity, in order to realize “green chemistry”, or the production of only one desired product at a high turnover rate without byproducts in multipath reactions.<sup>1-3</sup> Recent advances in colloidal chemistry provide a novel method to generate metal nanoparticles with precisely controlled size and shape, as well as porous materials used as supports with a high surface area and an ordered pore structure.<sup>4</sup> Since heterogeneous catalysts are prepared mainly by deposition of nanoparticles on oxide supports, oxide–metal interfaces have attracted much attention as important catalytic sites, along with the morphologies of metal nanoparticles and oxide supports.<sup>5,6</sup> Recent studies demonstrate that oxide–metal interfaces are responsible for changes in the catalytic activity and selectivity due to charge transfer between the metal and the oxide support.<sup>7</sup>

Catalytic reforming of hydrocarbons is of key importance for the production of high-octane gasoline in petroleum chemistry.<sup>8-10</sup> Since environmental regulations limit aromatic compounds in gasoline due to their carcinogenic nature, selective production of branched hydrocarbons with high octane number is highly desirable. *n*-Hexane reforming is an excellent model reaction to study structure- and support-dependent catalytic selectivity, because it has four distinct reaction pathways: isomerization, cyclization, aromatization, and cracking. Previous studies revealed the possibility of changing catalytic selectivity by introducing different oxide supports to the transition metal catalyst as well as by manipulating the size and shape of metal nanoparticles.<sup>7,11,12</sup> Recently, several mesoporous oxides were used for the preparation of Pt nanoparticle-supported catalysts to study the effect of the support in catalytic hydrogenation reactions.<sup>13,14</sup> However, the small pore sizes (less than 3 nm) of several oxides limited their incorporation of metal nanoparticles with various sizes (1.5–5.0 nm), resulting in metal loading less than 0.1 wt%.<sup>13</sup>

Herein, macroporous oxides were synthesized by using polymer microspheres as a hard template, generating highly crystalline Al<sub>2</sub>O<sub>3</sub>, TiO<sub>2</sub>, Nb<sub>2</sub>O<sub>5</sub>, Ta<sub>2</sub>O<sub>5</sub>, and ZrO<sub>2</sub> with an average pore size of ~300 nm. Colloidal Pt nanoparticles with sizes of 1.7, 2.7, and 5.5 nm were deposited onto them to investigate the Pt size- and support-dependent catalytic selectivity and their reaction mechanism in *n*-hexane isomerization. By utilizing Pt nanoparticles with controlled sizes onto different types of supports, reaction pathways could be changed by combining the effects of the Pt metal and the metal–support interaction. From this study, the best catalyst could be designed for the selective production of branched isomers with high octane numbers and the minimal concentration of benzene.

## 7.2 Experimental

### 7.2.1 Synthesis of Macroporous Al<sub>2</sub>O<sub>3</sub>, TiO<sub>2</sub>, Nb<sub>2</sub>O<sub>5</sub>, Ta<sub>2</sub>O<sub>5</sub>, and ZrO<sub>2</sub>

Macroporous oxides were prepared by using polystyrene beads. The polystyrene beads were synthesized through emulsifier-free emulsion polymerization.<sup>15</sup> Briefly, 14 g of styrene monomer and 0.7 g of divinylbenzene as a cross-linker were washed with 0.1 M NaOH solution and then with DI water to remove inhibitors, in which each washing was repeated for 4 times, respectively. The mixture of styrene and divinylbenzene was stirred in 140 mL of DI water at 70 °C and purged by flowing Ar for 1 h then potassium persulfate (0.03 g dissolved in water) as an initiator was added for the polymerization. After reacting at 70 °C for 12 h, the polystyrene beads

with an average diameter of 500 nm were collected by washing with methanol and water and following centrifugation.

For the preparation of macroporous aluminas 4.0 g of Pluronic P123 ((EO)<sub>20</sub>(PO)<sub>70</sub>(EO)<sub>20</sub> triblock copolymer, EO = ethylene oxide, PO = propylene oxide,  $M_w = \sim 5,800$ ) was dissolved in 40 mL of anhydrous ethanol for 4 h. Separately, 8.16 g of aluminum isopropoxide (40 mmol, Sigma-Aldrich, >98%) was dissolved in 6.4 mL of 68-70 wt.% nitric acid and 20 mL of anhydrous ethanol under vigorous stirring.<sup>16</sup> After the solid was completely dissolved, the precursor solution was added dropwise into the P123 solution. For macroporous Nb<sub>2</sub>O<sub>5</sub> and Ta<sub>2</sub>O<sub>5</sub>, 30 mmol of niobium chloride (Sigma-Aldrich, 99%) or tantalum chloride (Sigma-Aldrich, >99%) in 30 ml ethanol was added to 3 g of P123 and 30 ml of ethanol. For macroporous TiO<sub>2</sub> and ZrO<sub>2</sub>, 20 mmol of titanium isopropoxide (Sigma-Aldrich, 97%) or zirconium isopropoxide (in 70 wt.% in 1-propanol, Sigma-Aldrich) was added to P123 dissolved in ethanol and HCl. The combined solution was stirred for 5 h and 4 g of the dried polystyrene beads was added. The solvent of the mixture was evaporated at 60 °C for 48 h. The resulting flakes were calcined in a furnace at 700 °C for 6 h (for Al<sub>2</sub>O<sub>3</sub>, 900 °C for 10 h) in air. After calcinations, highly crystalline macroporous Al<sub>2</sub>O<sub>3</sub>, TiO<sub>2</sub>, Nb<sub>2</sub>O<sub>5</sub>, Ta<sub>2</sub>O<sub>5</sub>, and ZrO<sub>2</sub> with an average pore size of 300 nm were obtained. The supports also contained intrinsic mesoporous channels (ca. 10 nm) within the macroporous structure. When the oxides were prepared with the same recipe described above without the polystyrene beads, mesoporous oxides with an average pore size of ca.10 nm were synthesized as well.

#### 7.2.2 Synthesis of 1.7, 2.7, and 5.5 nm Pt Nanoparticles.

The synthesis of poly(vinylpyrrolidone) (PVP)-capped spherical Pt nanoparticles with the size of 1.5 – 6 nm was carried out by following reported literature methods with modifications.<sup>17,18</sup> For 1.7 nm Pt nanoparticles, 0.1 g of NaOH was dissolved in ethylene glycol (5 mL, 0.5 M) and the solution was added to an ethylene glycol solution (5 mL) containing H<sub>2</sub>PtCl<sub>6</sub>·xH<sub>2</sub>O (0.08 g, 0.2 mmol, Sigma-Aldrich, >99.9%). The mixture was heated to 160 °C and held at that temperature for 2 h under a N<sub>2</sub> atmosphere. The resulting nanoparticles were precipitated with 2 ml of 2 M HCl and re-dispersed in ethanol with 0.1 g of PVP (Sigma-Aldrich,  $M_w = 55,000$ ). In order to synthesize 2.7 nm Pt nanoparticles, mixed precursors of 4 mg of H<sub>2</sub>PtCl<sub>6</sub>·xH<sub>2</sub>O (0.01 mmol) and 0.016 g of Pt(acac)<sub>2</sub> (0.04 mmol, Sigma-Aldrich, 97%), and 0.1 g of PVP were added to 10 ml of ethylene glycol in a 50 ml three-necked flask. The solution was heated to 50 °C and evacuated at this temperature for 20 min to remove water and oxygen under vigorous magnetic stirring. The flask was then heated to 200 °C and maintained at this temperature for 10 min under Ar atmosphere. The solution was then cooled to room temperature and an excess of acetone was poured into the solution to form a cloudy black suspension. The Pt nanoparticles were precipitated by centrifugation and re-dispersed in ethanol. 5.5 nm Pt nanoparticles were synthesized by using 0.02 g of Pt(acac)<sub>2</sub>, 0.1 g of PVP, and 10 ml of diethyleneglycol (Aldrich, >99%) at 245°C for 1 h.

#### 7.2.3 Preparation of Pt Nanoparticle Catalysts Supported onto Macroporous Oxides

The desired amount of a macroporous oxide was added to the Pt nanoparticle dispersion and sonicated for 2 h at room temperature. The brown precipitates were collected by centrifugation. In order to remove PVP surfactants, the catalysts were washed with acetone and ethanol, and then calcined at 360 °C for 6 h in air.

#### 7.2.4 Characterization

Structural characterizations of Pt nanoparticles were analyzed using a Hitachi H-7650 transmission electron microscope (TEM) operated at 120 kV. Pt particle sizes were measured by TEM and the average particle sizes and their histograms were determined by counting 300 particles on TEM images. XRD patterns were measured on a Bruker D8 GADDS diffractometer using Co K $\alpha$  radiation (1.79 Å). Nitrogen physisorption data was obtained on a Micromeritics ASAP 2020. Elemental analyses by inductively coupled plasma atomic emission spectroscopy (ICP-OES) were conducted using a Perkin Elmer optical emission spectrometer, Optima 7000 DV. Before a measurement of ICP-OES, calibration was conducted by using platinum standard (Fluka, TraceCERT 1000 mg L<sup>-1</sup>) as a certified reference material (CRM).

#### 7.2.5 Catalytic Reaction Studies

n-hexane isomerization was conducted over supported Pt nanoparticle catalysts in a stainless steel tubular plug-flow reactor. Reaction products were analyzed using an HP 5890 Series II GC equipped with a 10 m dimethylpolysiloxane (HP-1) capillary column in line with a flame ionization detector (FID). 0.5 – 0.7 g of catalysts were diluted by quartz and loaded in the reactor bed. The catalyst pre-treatment consisted of a reduction in a flow of 50 vol.% mixture of H<sub>2</sub> (Praxair 5.0 Ultra-high Purity) and N<sub>2</sub> (Praxair 5.0 Ultra-high Purity) at 20 sccm total flow rate. The reduction treatment was performed under ambient pressure at 260 °C for 2 h. The heating/cooling rate during catalyst reduction treatment was kept at 1 °C/min. *N*-hexane isomerization was conducted with 140 Torr *n*-hexane and 620 Torr H<sub>2</sub> in the temperature range of 240 – 360 °C. *n*-hexane ( $\geq$  99%, Aldrich) vapor was carried to the reactor using a syringe pump. Each temperature was maintained for 1 h in the reactor for steady-state environment. The catalytic measurements were taken in the steady state under isothermal conditions. The reaction was kept in a kinetic region by having the total conversion below 10 % to allow for selectivity comparisons. Furthermore, the catalysts checked positive for the Madon-Boudart criterion, indicating no mass or heat transfer limitations.

#### 7.2.6 AP-XPS and XRD Measurements

All synchrotron-based X-ray studies were conducted in the Advanced Light Source (ALS) at the Lawrence Berkeley National Laboratory. For AP-XPS<sup>19</sup> and XRD<sup>20</sup> under catalytically relevant reaction conditions, Pt/oxide catalysts were pressed into a thin pellet (ca. 200  $\mu$ m) and heated to 150 °C under He for XRD or in vacuum for AP-XPS. AP-XPS measurement was carried out by dosing 100 mTorr (0.13 mbar) H<sub>2</sub> or O<sub>2</sub> at 360 °C in beamline 9.3.2 and XPS data were analyzed using CasaXPS software. *In situ* XRD study was conducted in the purpose-built flow cell, described elsewhere,<sup>21</sup> under 50 sccm flow of 20 vol. % (150 Torr) H<sub>2</sub> in Ar at 360 °C in beamline 12.2.2. The diffraction experiment was carried out in the transmission geometry using 25 keV photons. Sample-to-detector distance was calibrated by using LaB<sub>6</sub> standard.

#### 7.2.7 FT-IR Measurement of Oxides Adsorbed by Pyridine

For FT-IR measurement, all the macroporous oxides were pressed into a thin wafer after grinding with KBr (25.5 mg cm<sup>-2</sup>, 25 wt.% of oxides in KBr). Each thin wafer was placed in glass IR-cell equipped with CaF<sub>2</sub> windows. Before the measurement, each sample was degassed at 500 °C for 2 h in a vacuum and cooled to room temperature in an IR-cell. Then, the degassed macroporous oxides were oxidized at 350 °C for 1 h in O<sub>2</sub>. For the measurement of acidity,

pyridine was used as an organic base probe molecule.<sup>22</sup> Pyridine was adsorbed on the degassed samples at room temperature, and the weakly physisorbed pyridine was desorbed at 150°C for 1 h in a vacuum. After cooling to room temperature, IR spectra were collected using an FT-IR spectrometer (Thermo electron corporation Nicolet 6700) with 160 scans and 2 cm<sup>-1</sup> resolution in the 4000 – 400 cm<sup>-1</sup> range.<sup>22</sup>

### 7.3 Results and Discussion

While synthetic methods for mesoporous silicas such as MCM-41, SBA-15, and MCF-17 are well-established to manipulate their pore structures,<sup>23</sup> preparation of non-siliceous oxides with large pore sizes (>20 nm) has remained challenging for effective loading of nanoparticles with various sizes. The hard-templating approach using polystyrene beads was chosen to synthesize highly crystalline macroporous oxides of Al<sub>2</sub>O<sub>3</sub>, TiO<sub>2</sub>, Nb<sub>2</sub>O<sub>5</sub>, Ta<sub>2</sub>O<sub>5</sub>, and ZrO<sub>2</sub> with a pore size greater than 300 nm.<sup>16,24,25</sup> Figure 1a shows a general procedure for the preparation of macroporous oxides and their supported Pt nanoparticle catalysts.

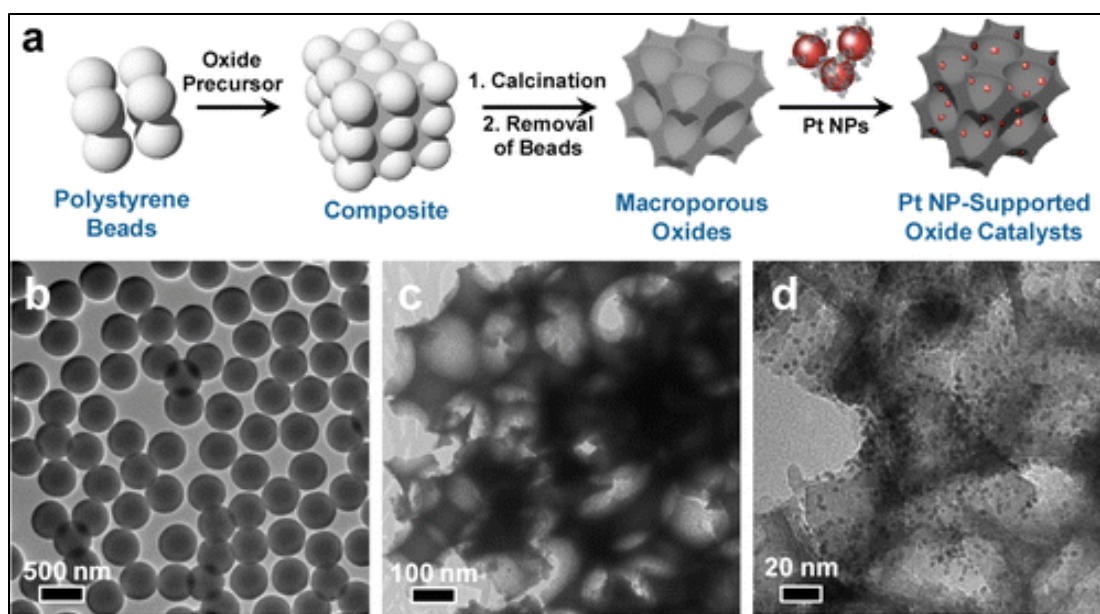


**Figure 1.** a) Illustration of the preparation of macroporous oxides using the polymer template and their supported Pt nanoparticle catalysts. b) TEM images of polystyrene beads as a template, c) the resulting Al<sub>2</sub>O<sub>3</sub> replicas with macropores d), and 2.7 nm Pt nanoparticle-supported macroporous Al<sub>2</sub>O<sub>3</sub> catalysts.

Transmission electron microscopy (TEM) images of macroporous oxides demonstrate that macropores and mesopores of the oxide replicas resulted from the polystyrene beads and P123 surfactants,<sup>16</sup> respectively (Figure 1b,c). During the calcinations at 700 °C, polystyrene beads with a diameter of 500 nm were shrunk and removed completely to generate 300 nm macropores, and the creation of crystalline walls was confirmed by X-ray diffraction (XRD) shown in Figure 2. The sizes of mesopores generated by P123 were 3–11 nm, obtained from the adsorption branch using the BJH algorithm. The BET surface areas of the resulting oxides were ca. 100 m<sup>2</sup>/g for Al<sub>2</sub>O<sub>3</sub>, Nb<sub>2</sub>O<sub>5</sub>, and Ta<sub>2</sub>O<sub>5</sub>, while TiO<sub>2</sub> and ZrO<sub>2</sub> had relatively small areas (Table 1) due to their large grain sizes. The dual pores of the oxides enabled effective loading of poly(vinylpyrrolidone) (PVP)-capped Pt nanoparticles, as shown in Figure 1d. In our previous study, mesoporous Ta<sub>2</sub>O<sub>5</sub> could not be loaded with 1.9 nm Pt nanoparticles homogeneously (less than 0.05 wt.% Pt) due to its small pores (ca. 2.7 nm).<sup>13</sup> The polymer templating strategy enabled us to incorporate PVP-capped Pt nanoparticles into macroporous oxides up to 1 wt.%, regardless of the nanoparticle size.

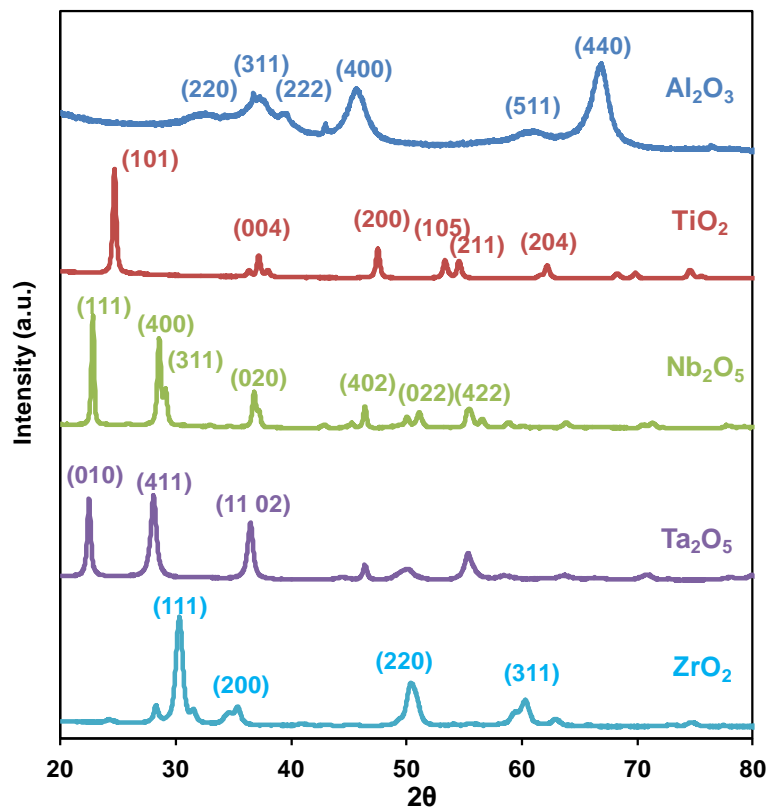


**Figure 2.** XRD Pattern of macroporous oxides of Al<sub>2</sub>O<sub>3</sub>, TiO<sub>2</sub>, Nb<sub>2</sub>O<sub>5</sub>, Ta<sub>2</sub>O<sub>5</sub>, and ZrO<sub>2</sub>.

**Table 1.** BET surface areas, pore volumes, and average pore sizes of macroporous oxides.

Macroporous Materials	Surface Area (m <sup>2</sup> /g)	Pore Volume (cc/g)	Mesopore Size (nm)
Al <sub>2</sub> O <sub>3</sub>	117.8	0.263	8.9
TiO <sub>2</sub>	13.3	0.041	11.8
Nb <sub>2</sub> O <sub>5</sub>	102.9	0.098	3.8
Ta <sub>2</sub> O <sub>5</sub>	96.7	0.068	2.8
ZrO <sub>2</sub>	19.2	0.047	9.7

*n*-Hexane reforming as a multipath reaction was carried out over 2.7 nm Pt nanoparticles on different kinds of oxide supports over the temperature range of 240–360 °C in 140 Torr *n*-hexane and 620 Torr H<sub>2</sub>. Under these reaction conditions, multiple products were generated through four distinct reaction pathways: branched isomers via isomerization, methylcyclopentane and cyclohexane via cyclization, benzene via dehydrogenation (aromatization), and cracked hydrocarbons with short chains (C<sub>1</sub>–C<sub>5</sub> paraffin) via hydrogenolysis (Figure 4a). As shown in Figure 4b, branched C<sub>6</sub> isomers including 2- or 3-methylpentane and 2,2- or 2,3-dimethylbutane, which are desirable for the production of high-octane gasoline, were generated as major products with greater than 45% selectivity over Pt/SiO<sub>2</sub> and Pt/Al<sub>2</sub>O<sub>3</sub> catalysts. Methylcyclopentane, C<sub>1</sub>–C<sub>5</sub> alkanes, and benzene were produced in with progressively lower selectivities. While the silica support does not contribute to the catalytic activity of Pt,<sup>26</sup> it is noteworthy that the macroporous alumina with an acidic site showed a negligible effect of the support in this study. When macroporous TiO<sub>2</sub>, Nb<sub>2</sub>O<sub>5</sub>, Ta<sub>2</sub>O<sub>5</sub>, and ZrO<sub>2</sub> were used as oxide supports, the product selectivity was significantly changed (Figure 4b). When 2.7 nm Pt nanoparticles were supported on TiO<sub>2</sub>, Nb<sub>2</sub>O<sub>5</sub>, and Ta<sub>2</sub>O<sub>5</sub>, the amount of C<sub>6</sub> isomers formed was increased at the expense of other products at 360 °C.

When the reaction was conducted over macroporous oxides without Pt loading (Figure 4c), pure macroporous Nb<sub>2</sub>O<sub>5</sub> and Ta<sub>2</sub>O<sub>5</sub> yielded cracking products predominantly, but the conversion was 10-fold lower compared to those obtained on Pt-supported catalysts. In the case of pure SiO<sub>2</sub> and Al<sub>2</sub>O<sub>3</sub>, no catalytic activity was found in the current reaction at 360 °C, while the other oxides were catalytically active. It is noteworthy that Rh and Ir, which are used as promoters in the industrial catalyst, exhibited the same results with Nb<sub>2</sub>O<sub>5</sub> and Ta<sub>2</sub>O<sub>5</sub>, yielding cracking products dominantly in the reaction. When the reaction was carried out over monometallic Rh (6.5 nm) and Ir (1.5 nm) nanoparticles under identical reaction condition, Rh and Ir nanoparticles favored the cracking pathway with 90% selectivity.<sup>27</sup> Oxides of group V metals such as Nb and Ta have been investigated for their catalytic properties, because they possess variable oxidation states, an acidic surface, and an empty d-orbital which allow electron transfer between the reactants and surface active site during the reaction.<sup>28-31</sup>

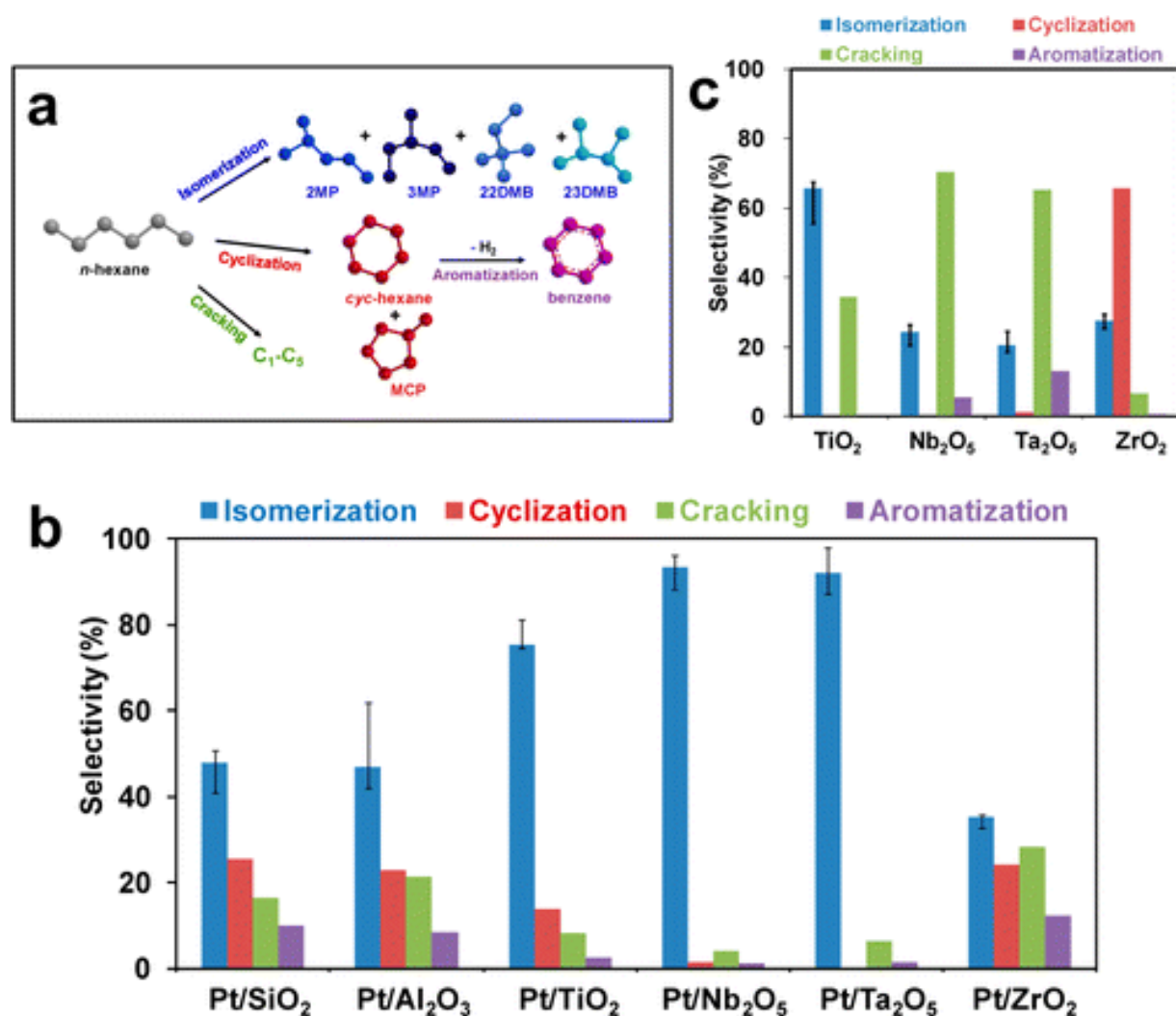


**Figure 3.** a) Reaction pathways and possible products of *n*-hexane isomerization. b) Product selectivity at 633 K over pure mesoporous oxides c) and 2.7 nm Pt nanoparticle catalysts supported on mesoporous oxides. The reaction was conducted with a hexane:H<sub>2</sub> ratio of 1:4.3 at ambient pressure.

We characterized Pt/oxide catalysts using XRD and ambient-pressure X-ray photoelectron spectroscopy (AP-XPS) under catalytically relevant reaction conditions. *In situ* XRD study of Pt/Ta<sub>2</sub>O<sub>5</sub> and Pt/ZrO<sub>2</sub> in 150 Torr H<sub>2</sub> at 360 °C confirmed no structural changes under the reaction conditions. AP-XPS identified the presence of various oxidation states in oxides under H<sub>2</sub> or O<sub>2</sub> at 360 °C. While Pt/TiO<sub>2</sub> showed a reduced charge state of TiO<sub>2</sub> under H<sub>2</sub> atmosphere, Pt/Nb<sub>2</sub>O<sub>5</sub> had identical XP spectra in both H<sub>2</sub> and O<sub>2</sub> environments. Furthermore,



there is no measurable XPS signature of charge transfer between metallic Pt and the metal oxides. Therefore, the stable charge state was responsible for the enhanced isomerization selectivity of the Nb<sub>2</sub>O<sub>5</sub> support beyond the TiO<sub>2</sub> support. This means that such a charge transfer is fast, and the reduced charge centers are short-lived in the time scale of our XPS measurements. TiO<sub>2</sub>, Nb<sub>2</sub>O<sub>5</sub>, and Ta<sub>2</sub>O<sub>5</sub> are known as acidic oxides exhibiting a strong metal–support interaction (SMSI) effect. Boffa et al. reported that TiO<sub>2</sub>, Nb<sub>2</sub>O<sub>5</sub>, and Ta<sub>2</sub>O<sub>5</sub> showed the greatest promotional effect in CO and CO<sub>2</sub> hydrogenation by SMSI at the interfaces of the oxides and Rh foils.<sup>11</sup> They found that oxides with higher oxidation states increased the reaction rate by changing Lewis acidity. We also carried out Fourier transform infrared (FT-IR) spectroscopy to identify surface acidic sites on the oxides. FT-IR spectra of pyridine adsorbed on the oxides show that Al<sub>2</sub>O<sub>3</sub>, TiO<sub>2</sub>, Nb<sub>2</sub>O<sub>5</sub>, Ta<sub>2</sub>O<sub>5</sub>, and ZrO<sub>2</sub> have characteristic peaks typical of Lewis and Brönsted acidic sites and H-bonded pyridine, and their acidic properties mostly come from Lewis acidic sites. From these results, we concluded that Nb<sub>2</sub>O<sub>5</sub> and Ta<sub>2</sub>O<sub>5</sub>, with stable oxidation states of 5+, promoted the highest selectivity for isomerization. TiO<sub>2</sub> was the next due to its oxidation state less than 4+.

With a typical bifunctional reforming catalyst, dehydrogenation/hydrogenation occurs on the Pt metal, while isomerization is determined by the oxide support.<sup>8-10,32</sup> Schmal and co-workers also reported the promoting effect of Nb<sub>2</sub>O<sub>5</sub>-supported Pt catalysts, resulting in the selectivity change in hydrocarbon dehydrogenation.<sup>33,34</sup> They found that the production of light hydrocarbons was decreased at the expense of C7 isomers and alkenes over Pt/Nb<sub>2</sub>O<sub>5</sub> in *n*-heptane dehydrogenation by the SMSI effect, when compared to the reaction on Pt/Al<sub>2</sub>O<sub>3</sub>.<sup>33</sup> The selectivity change on Pt/Nb<sub>2</sub>O<sub>5</sub> due to SMSI was also confirmed in 1,3-butadiene hydrogenation.<sup>34</sup> In those reports, the increase in the electron density of Pt on Pt/Nb<sub>2</sub>O<sub>5</sub> was responsible for the SMSI effect and the subsequent selectivity change. Therefore, we concluded that the acidic Nb<sub>2</sub>O<sub>5</sub> and Ta<sub>2</sub>O<sub>5</sub> facilitated electron transfer to Pt nanoparticles with the formation of higher electron density, leading to selective isomerization.

PVP organic capping molecules protect the surface of Pt nanoparticles during the reaction. When the PVP was substantially removed following calcination at 360 °C in air, it enabled a direct contact between the Pt and the oxide during the reaction. To study the role of the oxide–metal interface, we conducted the reaction over Pt/Nb<sub>2</sub>O<sub>5</sub> and Pt/Ta<sub>2</sub>O<sub>5</sub>, where the catalysts were prepared separately before and after removal of the PVP. Without calcination, Pt/Nb<sub>2</sub>O<sub>5</sub> and Pt/Ta<sub>2</sub>O<sub>5</sub> catalysts, with a poor contact between the Pt and the oxide, exhibited selectivity trends similar to those of Pt/SiO<sub>2</sub> or Pt/Al<sub>2</sub>O<sub>3</sub> in the reaction. However, over Pt/Nb<sub>2</sub>O<sub>5</sub> and Pt/Ta<sub>2</sub>O<sub>5</sub> catalysts from which the PVP was removed by calcination, the catalytic selectivity toward isomers was enhanced, as discussed above. It is concluded that the oxide–metal interface acts to change catalytic selectivity, promoting selective isomerization.

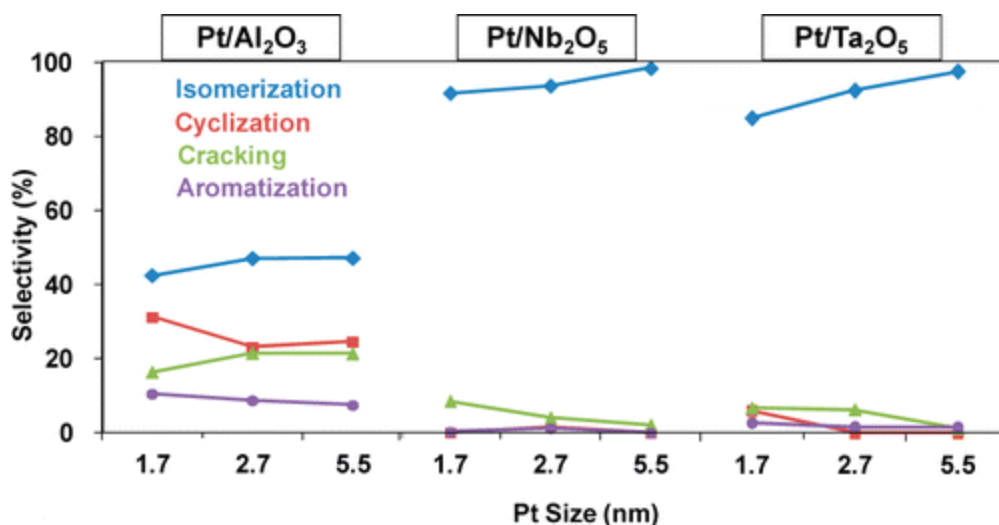


**Figure 4.** Pt size- and support-dependent catalytic selectivity in *n*-hexane isomerization at 360 °C. Pt nanoparticles of 1.7, 2.7, and 5.5 nm were supported on macroporous Al<sub>2</sub>O<sub>3</sub>, Nb<sub>2</sub>O<sub>5</sub>, and Ta<sub>2</sub>O<sub>5</sub>, respectively.

Previous studies on reforming of C<sub>6</sub> hydrocarbons over supported Pt nanoparticle catalysts have shown that isomerization was enhanced at increased Pt sizes.<sup>35-38</sup> In the current study, uniformly synthesized Pt nanoparticles with sizes ranging from 1.7 to 5.5 nm were supported on macroporous aluminas and utilized in *n*-hexane isomerization. As shown in Figure 4, as the size of Pt was increased, the selectivity toward isomers was also increased, in agreement with the observations with Pt-supported mesoporous silicas in the previous studies.<sup>35-38</sup> It is known that large Pt nanoparticles (at and above 5 nm) have a larger concentration of terrace sites than smaller sizes (1.5–3 nm), which predominantly contain corner or edge sites.<sup>35</sup> In reaction studies on *n*-hexane isomerization over Pt single crystals, Pt (100) or (111) surfaces were shown to yield increased isomer products due to their well-defined terrace sites.<sup>9</sup>

Activation energies measured from this reaction over different Pt particle sizes, oxide support catalysts, and even single-crystal Pt catalysts have similar values (26–28 kcal/mol),<sup>9</sup> demonstrating that the isomerization of *n*-hexane follows the same mechanism regardless of carbon poisoning from capping agents or other sources.

XPS studies of Pt-supported oxide catalysts in 100 mTorr H<sub>2</sub> at 360 °C revealed a Pt:C ratio of 1:3, exhibiting the presence of carbons related or unrelated to PVP on the Pt surface. Although the wispy PVP caused inevitable sintering during the calcination and catalytic reaction, the current reaction conditions (up to 360 °C) seemed to be sufficient to conclude that there exist

Pt size-dependent catalytic properties, because the initial order of size distributions was maintained after the reaction. With the knowledge that large Pt nanoparticles yielded higher selectivity toward isomerization due to their abundant terrace sites, we loaded Pt nanoparticles of three different sizes onto macroporous Nb<sub>2</sub>O<sub>5</sub> and Ta<sub>2</sub>O<sub>5</sub> in order to determine the best catalyst for the isomerization reaction. In terms of turnover frequencies (TOFs), the smaller Pt nanoparticles had higher TOFs. Nevertheless, it was concluded that 5.5 nm Pt nanoparticles supported on Nb<sub>2</sub>O<sub>5</sub> or Ta<sub>2</sub>O<sub>5</sub> yielded the best catalysis, giving ca. 97% selectivity toward the desired isomer products, as shown in Figure 4.

## 7.4 Conclusions

In summary, rational combination of metal nanoparticles and oxide supports can increase catalytic selectivity to obtain only desirable products, because metal, oxide support, and the oxide–metal interface simultaneously influence the catalytic performance. In the isomerization of *n*-hexane over Pt nanoparticle-supported catalysts, when macroporous Nb<sub>2</sub>O<sub>5</sub> and Ta<sub>2</sub>O<sub>5</sub> were used as supports, the production of C<sub>6</sub> isomers as the most desired products was increased selectively, due to the effect of SMSI. The Nb<sub>2</sub>O<sub>5</sub> and Ta<sub>2</sub>O<sub>5</sub> allowed charge transfer at the Pt–oxide interfaces and thus high electron density of the Pt during the reaction. While Pt nanoparticles showed size-dependent selectivity, large-sized Pt nanoparticles (5.5 nm) supported on Nb<sub>2</sub>O<sub>5</sub> or Ta<sub>2</sub>O<sub>5</sub> produced branched hydrocarbons with ca. 97% selectivity. By utilizing colloidal synthetic chemistry, a selective catalyst composed of well-defined metal nanoparticles and oxide supports can be designed appositely to realize 100% selectivity without any undesired byproducts.

## 7.5 References

1. Geus, J. W.; van Ween, J. A. R. In Mouljin, J. A., van Leeuwen, P. W. N. M. and van Santen, R. A., Eds.; *Catalysis: An Integrated Approach to Homogeneous, Heterogeneous and Industrial Catalysis*; Elsevier: Amsterdam, 1993; .
2. Somorjai, G. A.; Li, Y. *Introduction to Surface Chemistry and Catalysis*; Wiley: New York, 2010; .
3. Somorjai, G. A.; Park, J. Y. Molecular Factors of Catalytic Selectivity. *Angew. Chem., Int. Ed* **2008**, *47*, 9212-9228.
4. An, K.; Somorjai, G. A. Size and Shape Control of Metal Nanoparticles for Reaction Selectivity in Catalysis. *Chemcatchem* **2012**, *4*, 1512.
5. Tauster, S. J.; Fung, S. C.; Garten, R. L. Strong Metal-Support Interactions. Group 8 Noble Metals Supported on Titanium Dioxide. *J. Am. Chem. Soc.* **1978**, *100*, 170-175.
6. Wang, S. J.; Moon, S. H.; Vannice, M. A. The Effect of SMSI (Strong Metal Support Interaction) Behavior on CO Adsorption and Hydrogenation on Pd Catalysts: II. Kinetic Behavior in the Methanation Reaction. *J. Catal.* **1981**, *71*, 167-174.

7. Gross, E.; Somorjai, G. A. The Impact of Electronic Charge on Catalytic Reactivity and Selectivity of Metal-Oxide Supported Metallic Nanoparticles. *Top. Catal.* **2013**, *56*, 1049-1058.
8. Hagen, J. *Industrial Catalysis: A Practical Approach*; Wiley-VCH: Weinheim, 2006; Vol. 2.
9. Davis, S. M.; Zaera, F.; Somorjai, G. A. Surface Structure and Temperature Dependence of n-Hexane Skeletal Rearrangement Reactions Catalyzed over Pt Single Crystal Surfaces: Marked Structure Sensitivity of Aromatization. *J. Catal.* **1984**, *85*, 206-223.
10. Ciapetta, F. G.; Hunter, J. Isomerization of Saturated Hydrocarbons in Presence of Hydrogenation-Cracking Catalysts: Normal Hexane. *Ind. Eng. Chem.* **1953**, *45*, 147-155.
11. Boffa, A. B.; Lin, C.; Bell, A. T.; Somorjai, G. A. Lewis Acidity as an Explanation for Oxide Promotion of Metals: Implications of its Importance and Limits for Catalytic Reactions. *Catal. Lett.* **1994**, *27*, 243-249.
12. Baker, L. R.; Kennedy, G.; Van Spronsen, M.; Hervier, A.; Cai, X.; Chen, S.; Wang, L. W.; Somorjai, G. A. Furfuraldehyde Hydrogenation on Titanium Oxide-Supported Platinum Nanoparticles Studied by Sum Frequency Generation Vibrational Spectroscopy: Acid-Base Catalysis Explains the Molecular Origin of Strong Metal-Support Interactions. *J. Am. Chem. Soc.* **2012**, *134*, 14208-14216.
13. An, K.; Musselwhite, N.; Kennedy, G.; Pushkarev, V. V.; Baker, L. R.; Somorjai, G. A. Preparation of Mesoporous Oxides and Their Support Effect on Pt Nanoparticle Catalysts in Catalytic Hydrogenation of Furfural. *J. Colloid Interface Sci.* **2013**, *392*, 122-128.
14. Rao, Y.; Antonelli, D. Mesoporous Transition Metal Oxides: Characterization and Applications in Heterogeneous Catalysis. *J. Mater. Chem.* **2009**, *19*, 1937-1944.
15. Park, M.; Gandhi, K.; Sun, L.; Salovey, R.; Aklonis, J. J. Model-Filled Polymers. III. Rheological Behavior of Polystyrene Containing Cross-linked Polystyrene Beads. *Polym. Eng. Sci.* **1990**, *1990*, 1158-1164.
16. Dacquin, J. P.; Dhainaut, J.; Duprez, D.; Royer, S.; Lee, A. F.; Wilson, K. An Efficient Route to Highly Organized, Tunable Macroporous-Mesoporous Alumina. *J. Am. Chem. Soc.* **2009**, *131*, 12896-12897.
17. Teranishi, T.; Hosoe, M.; Tanaka, T.; Miyake, M. Size Control of Monodispersed Pt Nanoparticles and Their 2D Organization by Electrophoretic Deposition. *J. Phys. Chem. B* **1999**, *103*, 3818-3827.
18. Pushkarev, V. V.; An, K.; Alayoglu, S.; Beaumont, S. K.; Somorjai, G. A. Hydrogenation of Benzene and Toluene over Size Controlled Pt/SBA-15 Catalysts: Elucidation of the Pt Particle Size Effect on Reaction Kinetics. *J. Catal.* **2012**, *292*, 64-72.

19. Grass, M. E.; Karlsson, P. G.; Aksoy, F.; Lundqvist, M.; Wannberg, B.; Mun, B. S.; Hussain, Z.; Liu, Z. New Ambient Pressure Photoemission Endstation at Advanced Light Source Beamline 9.3.2. *Rev. Sci. Instrum.* **2010**, *81*, 053106-1-053106-7.
20. Kunz, M.; MacDowell, A. A.; Caldwell, W. A.; Cambie, D.; Celestre, R. S.; Domning, E. E.; Duarte, R. M.; Gleason, A. E.; Glossinger, J. M.; Kelez, N.; Plate, D. W.; Yu, T.; Zaug, J. M.; Padmore, H. A.; Jeanloz, R.; Alivisatos, A. P.; Clark, S. M. A Beamline for High-Pressure Studies at the Advanced Light Source With a Superconducting Bending Magnet as the Source. *J. Synchrotron Rad.* **2005**, *12*, 650-658.
21. Alayoglu, S.; An, K.; Melaet, G.; Chen, S.; Bernardi, F.; Wang, L. W.; Lindeman, A. E.; Musselwhite, N.; Guo, J.; Liu, Z.; Marcus, M. A.; Somorjai, G. A. Pt-Mediated Reversible Reduction and Expansion of CeO<sub>2</sub> in Pt Nanoparticle/Mesoporous CeO<sub>2</sub> Catalyst: In Situ X-ray Spectroscopy and Diffraction Studies under Redox (H<sub>2</sub> and O<sub>2</sub>) Atmospheres. *J. Phys. Chem. C* **2013**, *117*, 26608-26616.
22. Zaki, M. I.; Hasan, M. A.; Al-Sagheer, F. A.; Pasupulety, L. In-situ FTIR Spectra of Pyridine Adsorbed on SiO<sub>2</sub>-Al<sub>2</sub>O<sub>3</sub>, TiO<sub>2</sub>, ZrO<sub>2</sub>, and CeO<sub>2</sub>: General Considerations for the Identification of Acid Sites on Surfaces of Finely Divided Metal Oxides. *Colloids Surf. A* **2001**, *190*, 261-274.
23. Wan, Y.; Zhao, D. On the Controllable Soft-Templating Approach to Mesoporous Silicates. *Chem. Rev.* **2007**, *107*, 2821-2860.
24. Holland, B. T.; Blanford, C. F.; Stein, A. Synthesis of Macroporous Minerals with Highly Ordered Three-Dimensional Arrays of Spheroidal Voids. *Science* **1998**, *281*, 538-540.
25. Stein, A. Sphere Templating Methods for Periodic Porous Solids. *Micropor. Mesopor. Mat.* **2001**, *44-45*, 227-239.
26. An, K.; Alayoglu, S.; Musselwhite, N.; Plamthottam, S.; Melaet, G.; Lindeman, A. E.; Somorjai, G. A. Enhanced CO Oxidation Rates at the Interface of Mesoporous Oxides and Pt Nanoparticles. *J. Am. Chem. Soc.* **2013**, *135*, 16689-16696.
27. Musselwhite, N.; Alayoglu, S.; Melaet, G.; Pushkarev, V. V.; Lindeman, A. E.; An, K.; Somorjai, G. A. Isomerization of *n*-Hexane Catalyzed by Supported Monodisperse PtRh Bimetallic Nanoparticles. *Catal. Lett.* **2013**, *143*, 907-911.
28. Rao, Y.; Kang, J.; Trudeau, M.; Antonelli, D. Investigation of the Catalytic Activities of Sulfated Mesoporous Ti, Nb, and Ta Oxides in 1-Hexene Isomerization. *J. Catal.* **2009**, *266*, 1-8.
29. Yue, C.; Trudeau, M.; Antonelli, D. Electroactive Mesoporous Tantalum Oxide Catalysts for Nitrogen Activation and Ammonia Synthesis. *Chem. Commun.* **2006**, *18*, 1918-1920.

30. Rao, Y.; Kang, J.; Antonelli, D. 1-Hexene Isomerization over Sulfated Mesoporous Ta Oxide: The Effects of Active Site Confinement. *J. Am. Chem. Soc.* **2008**, *130*, 394-395.
31. Borgschulte, A.; Rector, J. H.; Dam, B.; Griessen, R.; Zuttel, A. The Role of Niobium Oxide as a Surface Catalyst for Hydrogen Absorption. *J. Catal.* **2005**, *235*, 353-358.
32. Davis, R.J.; Derouane, E. G. A Non-Porous Supported-Platinum Catalyst for Aromatization of n-Hexane. *Nature* **1991**, *349*, 313-315.
33. Schmal, M.; Aranda, D. A. G.; Soares, R. R.; Noronha, F. B.; Frydman, A. A Study of the Promoting Effect of Noble Metal Addition on Niobia and Niobia Alumina Catalysts. *Catal. Today* **2000**, *57*, 169-176.
34. Aranda, D. A. G.; Schmal, M. Ligand and Geometric Effects of Pt/Nb<sub>2</sub>O<sub>5</sub> and Pt-Sn/Nb<sub>2</sub>O<sub>5</sub> Catalysts. *J. Catal.* **1997**, *171*, 398-405.
35. Alayoglu, S.; Pushkarev, V. V.; Musselwhite, N.; An, K.; Beaumont, S. K.; Somorjai, G. A. Reforming of C-6 Hydrocarbons Over Model Pt Nanoparticle Catalysts. *Top. Catal.* **2012**, *55*, 723-730.
36. Boudart, M.; Aldag, A. W.; Ptak, L. D.; Benson, J. E. On the Selectivity of Platinum Catalysts. *J. Catal.* **1968**, *11*, 35-45.
37. Botman, M. J. P.; de Vreugd, K.; Zandbergen, H. W.; de Block, R.; Ponc, V. The Effect of Alloying Pt with Re on the Intermediates in Hydrocarbon Reactions: Reactions of 2,2-Dimethylbutane. *J. Catal.* **1989**, *116*, 467-479.
38. Fogar, K.; Anderson, J. R. Reactions of Neopentane and Neohexane on Platinum/Y-Zeolite and Platinum/Silica Catalysts. *J. Catal.* **1978**, *54*, 318-335.

## Chapter 8

# The Pathway to Total Isomer Selectivity: *n*-Hexane Conversion (Reforming) on Platinum Nanoparticles Supported on Aluminum Modified Mesoporous Silica (MCF-17)

### Abstract

When pure mesoporous silica (MCF-17) was modified with aluminum (Al modified MCF-17), Lewis acid sites were created, but this material was inactive for the catalytic conversion (reforming) of *n*-hexane to isomers. When colloidally synthesized platinum nanoparticles were loaded onto traditional MCF-17, the catalyst showed very low activity toward isomer production. However, when Pt nanoparticles were loaded onto Al modified MCF-17, isomerization became the dominant catalytic pathway, with extremely high activity and selectivity (>90%), even at high temperatures (240–360 °C). This highly efficient catalytic chemistry was credited to the tandem effect between the acidic Al modified MCF-17 and the Pt metal.

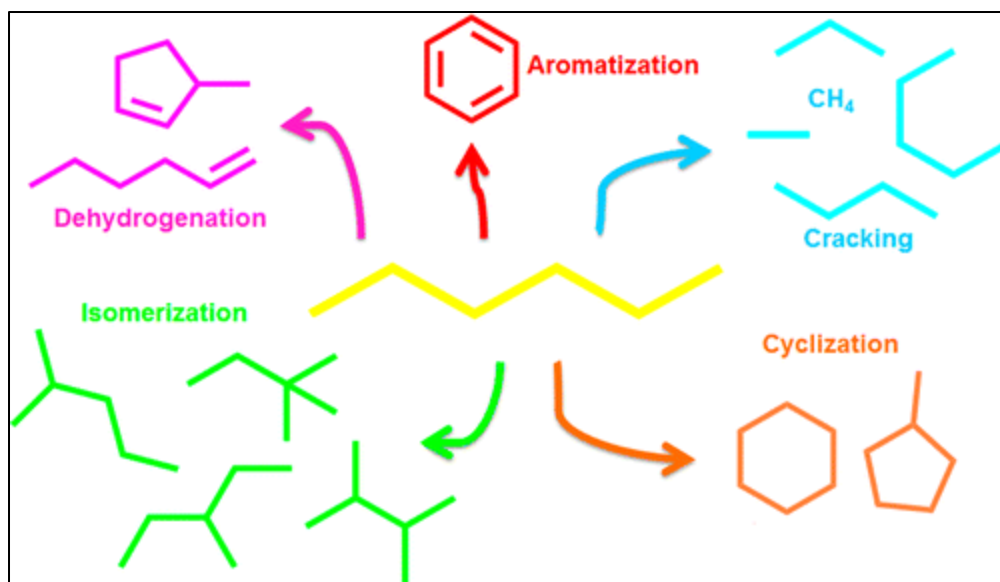
\* This chapter covers similar material as in Musselwhite, N.; Na, K.; Alayoglu, S.; Somorjai, G.A. *J. Am. Chem. Soc.* **2014**, *136*, 16661-16665. — reproduced with permission, copyright 2014 American Chemical Society.

## 8.1 Introduction

The catalytic conversion (reforming) of linear hydrocarbons to their corresponding branched isomers is a vital reaction in the production of high octane gasoline from the naphtha feedstock of crude oil.<sup>1</sup> The target, like all catalytic reactions, is to optimize both the overall activity and product selectivity, simultaneously.<sup>1-3</sup> In naphtha reforming, branched isomers are the desired product, while cracking the hydrocarbon creates the unwanted byproducts. This chemistry is normally accomplished through the use of a platinum catalyst, alloyed with small amounts of other transition metals, and loaded onto an acidic support, such as a zeolite.<sup>4-7</sup> It is believed that the platinum catalyzes the dehydrogenation and hydrogenation of the hydrocarbons (promoted by the alloying of additional metals), while the isomerization occurs on the acidic support via carbocation transition species.<sup>8,9</sup>

The reforming of *n*-hexane provides a good model reaction in order to scientifically study the complex process of naphtha refining. Hexane can react via five major pathways: (1) cracking to shorter chain hydrocarbons; (2) isomerization to 2-methylpentane, 3-methylpentane, or multi-branched isomers; (3) cyclization to methylcyclopentane or cyclohexane; (4) aromatization to benzene; (5) dehydrogenation to hexene or other unsaturated compounds. The possible reaction products for *n*-hexane reforming are displayed in Scheme 1.

In the present chapter, we report on the evaluation of several catalysts in the vapor phase hydrogenation of *n*-hexane. When Al modified mesoporous silica MCF-17 loaded with Pt nanoparticles (Al modified MCF-17/Pt) was evaluated, it was found to be highly active and selective (>90%) toward isomer production, even at high temperatures. When either the Al modified MCF-17 or Pt nanoparticles loaded onto unmodified MCF-17 were tested separately, it was found that both catalysts were relatively inactive. This behavior was attributed to metal-oxide interface formed between the Al modified MCF-17 and the Pt nanoparticles.



**Scheme 1.** Possible reaction products for *n*-hexane reforming.



## 8.2 Experimental

### 8.2.1 Synthesis of MCF-17 Mesoporous Silica

MCF-17 type mesoporous silica was synthesized by previously reported literature methods.<sup>5</sup> Briefly, 1,3,5-trimethylbenzene (TMB), which was utilized as a pore swelling agent, was added to an aqueous solution of triblock copolymer Pluronic P123 and HCl. After stirring of this solution for 2 h at 40 °C, Tetraethylorthosilicate (TEOS) was then added and the solution was stirred for an additional 20 h. NH<sub>4</sub>F was then added, and the solution was allowed to hydrothermally react at 100 °C for 24 h. The product was then calcined for 6 h at 550 °C. The pore size of the material is 30–50 nm and the surface area is ~1000 m<sup>2</sup>/g.

### 8.2.2 Aluminum Modification of MCF-17

The mesopore surface of pure silica MCF-17 was aluminated through utilization of the grafting method.<sup>10</sup> The as-synthesized MCF-17 was calcined at 550 °C for 4 h in air to remove organic molecules. Then, the calcined sample was grafted with aluminum by slurring with anhydrous AlCl<sub>3</sub> in absolute ethanol, in order to give a Si/Al ratio of 10:1. The slurring solution was stirred overnight at room temperature, and then the ethanol was removed by rotary-evaporation. The precipitated Al-modified MCF-17 was dried at 130 °C for 1 h, and subsequently calcined at 550 °C for 4 h in air. For the introduction of acidic sites, the calcined Al-modified MCF-17 was slurred in 1 M of NH<sub>4</sub>NO<sub>3</sub> aqueous solution for 4 h at room temperature.<sup>11</sup> The sample was then filtered, washed with distilled water, and dried at 130 °C for 1 h. This process was repeated three times and the final sample was calcined at 550 °C for 4 h in air to give H<sup>+</sup>-Al-modified MCF-17.

### 8.2.3 Synthesis and Supporting of Pt Nanoparticles

Polyvinylpyrrolidone (PVP) capped Pt nanoparticles with an average particle size of 2.5 nm were synthesized and supported on mesoporous silica (MCF-17), Al modified MCF-17, and mesoporous zeolite (MFI) according to previously reported methods.<sup>12</sup> Briefly, H<sub>2</sub>PtCl<sub>6</sub> precursor salt was dissolved in ethylene glycol in the presence of PVP, then was allowed to react at 470 K, until particles were formed and stable. The as-synthesized nanoparticles were then washed and redispersed in ethanol. To load the nanoparticles on the various support materials, a colloidal solution of PVP-capped Pt nanoparticles in ethanol was mixed with the desired support material to give a nominal metal loading of 0.5 wt. %. The mixtures were then sonicated for 3 h, and the supported catalysts were then collected by centrifugation and washed with 20% ethanol in acetone.

### 8.2.4 Catalytic Testing

After synthesis, the catalytic behavior of the materials was investigated in the reforming of *n*-hexane. Catalytic measurements were made utilizing a tubular fixed catalyst bed reactor at ambient pressure, which has been described in previous publications.<sup>13-15</sup> Briefly, a 1/4 in. diameter stainless steel reactor was loaded with 0.02–0.5 g catalyst (which was pelletized and sieved to yield 60–100 µm size granulates), then capped on each end with a purified thermal silica filter. The remaining space in the reactor tube was filled with purified fused aluminum granulate and capped with glass wool. To keep the catalysis in a kinetic region and allow for selectivity comparisons, the total hexane conversion was held between 1% and 5%.

After loading, the catalysts were first pretreated at 633 K under a gas mixture of N<sub>2</sub> (Praxair, 5.0 UHP, 10 sccm) and H<sub>2</sub> (Praxair, 5.0 UHP, 10 sccm) for 2 h, with a heating rate of 2

K min<sup>-1</sup>. After pretreatment, the reactor system was cooled to 513 K, under the same gas flow. The gas flow was then changed to 16 sccm H<sub>2</sub>, and *n*-hexane (Fluka, ≥ 99.0%) was introduced using a Teledyne ISCO 500D liquid flow pump at a rate of 1.2 mL h<sup>-1</sup> into the heated reactor head which was maintained at 423 K. In the reactor head, hexane was evaporated and mixed with H<sub>2</sub>, resulting in a two-component gas flow with a hexane:H<sub>2</sub> ratio of 1:5 entering the reactor at near ambient pressure. A Baratron type (890B, MKS Instruments) manometer was used to monitor the reactor inlet pressure. The reaction products were sampled in the vapor phase at the reactor outlet and analyzed via an in-line gas chromatograph (GC), with all flow lines heated to 433 K. Quantitative analysis of product composition was accomplished with a Hewlett-Packard (5890 Series II) GC which was equipped with an Aldrich HP-1 capillary column and a flame ionization detector (FID). A PC based GC Chemstation software (Hewlett-Packard) was utilized for automatic GC sampling, data collection and post-run processing. Postreaction characterization of the Al modified MCF-17/Pt catalyst using scanning transmission electron microscopy (STEM)/energy dispersive spectroscopy (EDS) was conducted using a JEOL 2100F TEM. Point-to-point spatial resolution of the electron probe was 1.5 nm.

### 8.3 Results and Discussion

The overall activity of all tested catalysts is shown in Figure 1. The activity is displayed as a turnover frequency, which is based on the total surface area of platinum, which is calculated based on geometrical methods and TEM analysis of average nanoparticle size (2.5 nm). The reference catalyst of Pt nanoparticles loaded on mesoporous silica MCF-17 (red) displayed very low activity, and had to be scaled by a factor of 10 in order to be plotted on the same graph. The Al modified MCF-17 is not shown in the plot because it was found to be catalytically inactive at all temperatures studied. The Al modified MCF-17/Pt, which is shown in blue, displayed high activity compared to the metal free support and the unmodified MCF-17/Pt catalyst.

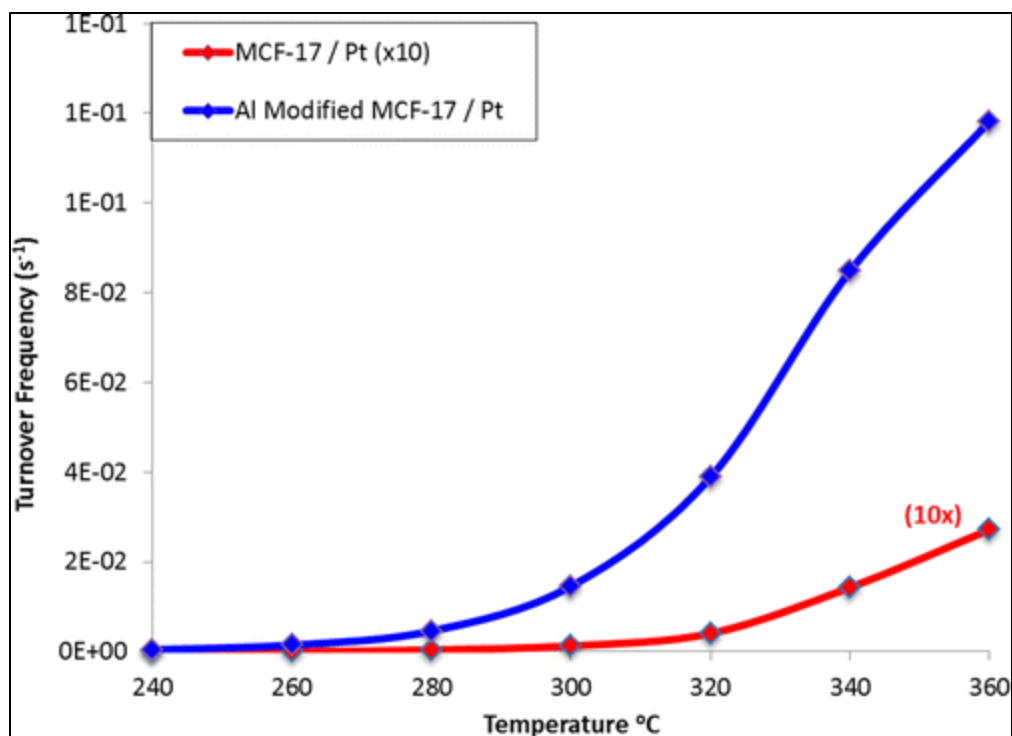


**Figure 1.** Overall turnover frequency (moles hexane converted mole Pt site per second) plotted against temperature for evaluated catalysts. Pt loaded on MCF-17 is shown in red for reference and is scaled by a factor of 10 to allow it to be plotted on the graph. Al modified MCF-17 is catalytically inactive, so is not plotted. Al modified MCF-17 loaded with Pt is shown in blue. The TOF for the Al modified catalyst is about 43.5× greater at the highest temperature studied (360 °C).

The overall isomer activity of the hexane reforming reaction for each catalysts is shown in Figure 2; this data is recorded at the highest temperature studied (360 °C). This data was obtained by taking the product of the overall isomer selectivity and the overall turnover frequency, in order to obtain the isomer turnover frequency (moles isomer produced per mole Pt site per second). The MCF-17/Pt catalyst (red) shows very low isomer activity ( $9.66 \times 10^{-4} \text{ s}^{-1}$ ), due to the lack of acidity. The Al Modified MCF-17 (orange “x”) catalyst shows no activity when Pt is not present. However, when Pt is loaded into the Al modified MCF-17 catalyst (blue), the isomer production is highly increased to  $1.18 \times 10^{-1} \text{ s}^{-1}$ , which is about 120 times the isomer activity of the MCF-17/Pt catalyst and the Al modified MCF-17 support separately.

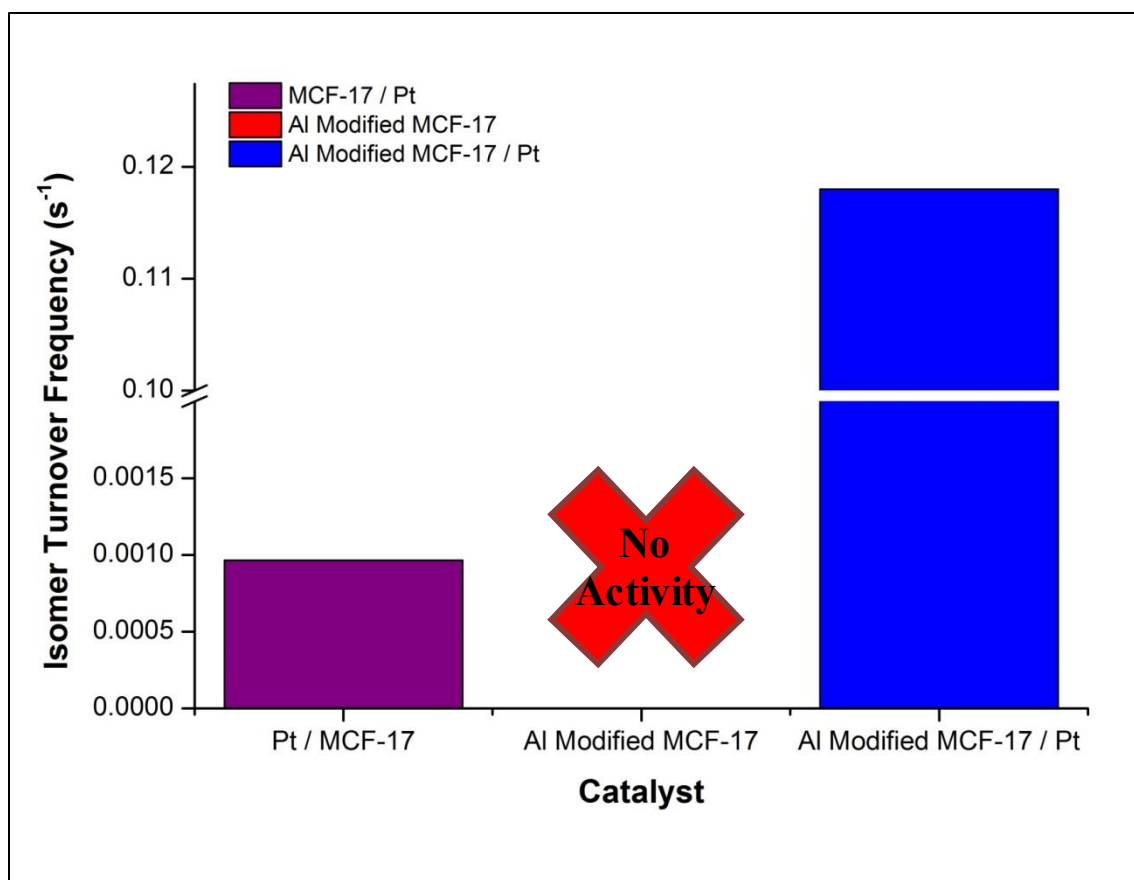


**Figure 2.** The product of the overall catalytic turnover and the isomer selectivity at 360 °C reaction in order to show the enhancement of adding acidity to catalysis. The MCF-17/Pt catalyst (red) shows very low activity ( $9.66 \times 10^{-4} \text{ s}^{-1}$ ) without the presence of acidity. The Al Modified MCF-17 catalyst shows no activity when Pt is not present. However, when Pt is loaded into the Al modified MCF-17 catalyst (blue) the isomer production is highly increased to  $1.18 \times 10^{-1} \text{ s}^{-1}$ , which is about 120 times the activity of the catalyst and support separately.

The specific product selectivity of the reaction is shown in Figure 3; this data is recorded at the highest temperature reactions (360 °C). The data shown is at approximately 5% total hexane conversion. Al modified MCF-17 without Pt loading showed no activity at this temperature. Isomerization is the dominant pathway on the Al modified MCF-17/Pt catalyst, with high selectivity (>90%) toward 2-methylpentane (2MP) and 3-methylpentane (3MP). The MCF-17/Pt (red) shows ~20% selectivity toward C1–C5 cracking products, and ~7% selectivity to olefins (the major product being hexene); the remaining products are isomerization products. It can be seen that when the same support is previously modified with Al, the selectivity is altered to very little of these products, but greater than 90% selectivity toward the 2MP and 3MP isomers. It can be clearly ascertained that the selectivity is vastly superior after Al modification and subsequent Pt loading of the MCF-17 support.

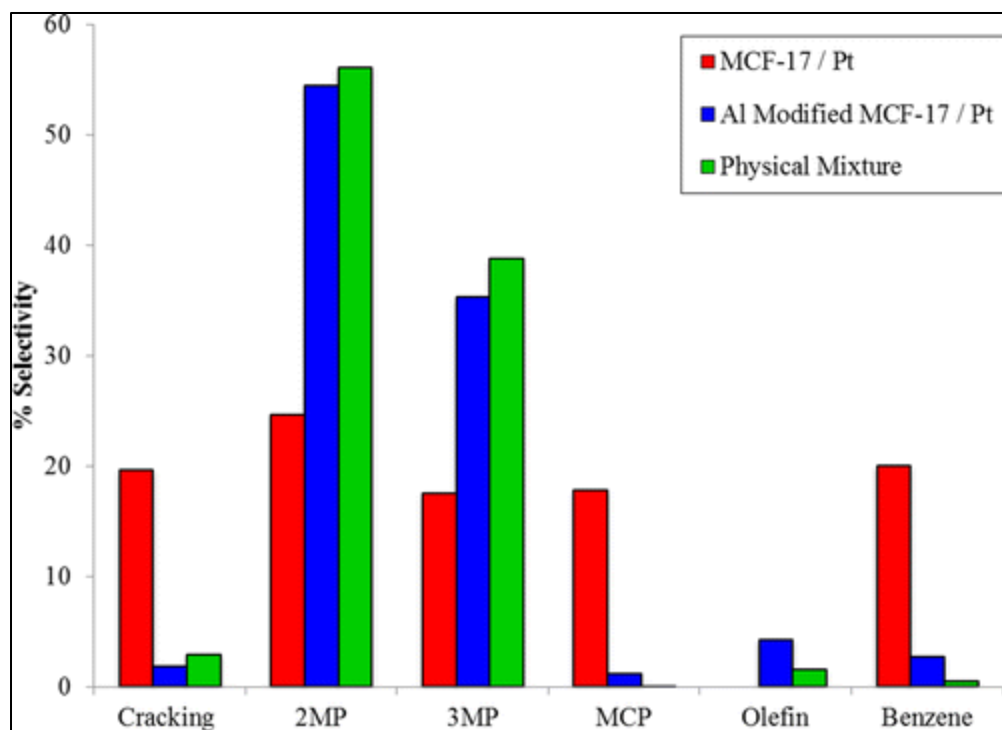


**Figure 3.** Product selectivity at high temperature reaction (360 °C). Al modified MCF-17 without Pt loading showed no activity at this temperature. Isomerization is the dominant pathway on the Al modified MCF-17/Pt catalyst, with high selectivity (>90%) to 2-methylpentane (2MP) and 3-methylpentane (3MP). The MCF-17/Pt (red) shows relatively higher (~20%) selectivity toward C1–C5 cracking products, and ~7% selectivity to olefins (the major product being hexene); the remaining products are isomerization products. A physical mixture of the MCF-17/Pt and the Al modified MCF-17 (green) showed nearly identical selectivity to the Al modified MCF-17/Pt catalyst, indicating a bifunctional mechanism may be present. However, the activity for the physically mixed catalyst was an order of magnitude lower, indicating that the close proximity of the Pt and acidic catalytic sites is necessary for the high isomer production in the Al Modified MCF-17/Pt catalyst. All data shown are at similar conversion.

The STEM, TEM, and HR-TEM images of the postreaction Al modified MCF-17/Pt catalyst are shown in Figure 4, in parts a, b, and c, respectively. It can be seen from the STEM and TEM images that the particles are well dispersed throughout the catalyst, with little agglomeration of the metal. The representative STEM images and corresponding color-coded EDS spectral maps at Si K (green), Al K (blue), and Pt M (red) lines are shown in Figure 4d. It can be seen that the Al is well dispersed among the catalyst, and segregated Al domains do not exist on either the silica support or around the Pt nanoparticles. It is also important to note that no evidence of chlorine was observed in the EDS analysis, as residual Cl<sup>-</sup> from the AlCl<sub>3</sub> used for support modification could have an effect on the Brønsted acidity of the catalyst.

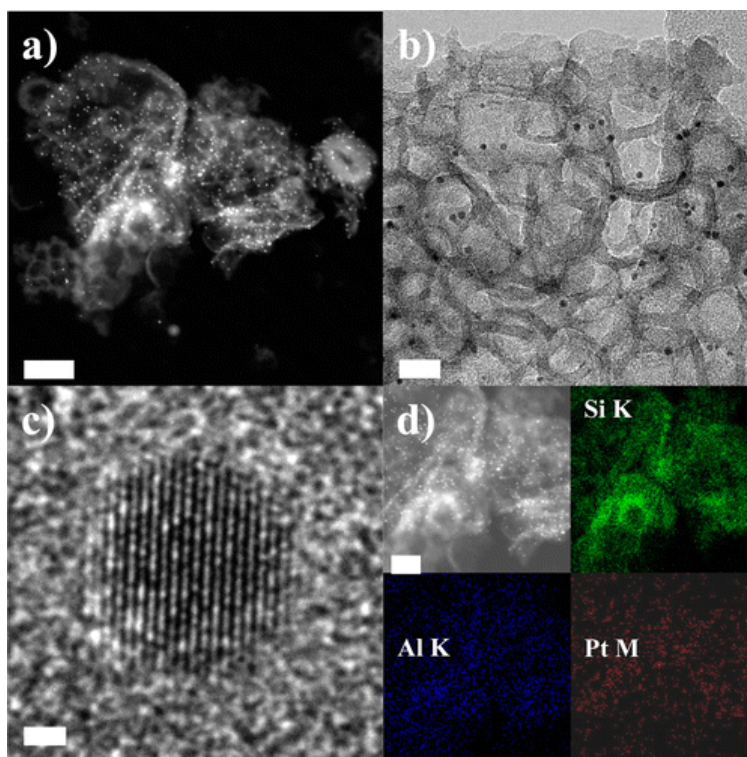


**Figure 4.** a) STEM, b) TEM, and c) HR-TEM images of the post-reaction 2.5 nm Pt NPs supported on Al-modified MCF-17. d) Representative STEM image and corresponding color-coded EDS spectral maps at Si K (green), Al K (blue), and Pt M (red) lines. The scale bars in the images correspond to a) 50, b) 20, c) 1, and d) 50 nm.

The high temperature isomer selectivity of the Al modified MCF-17 catalyst is a remarkable finding, and most likely a direct effect of the interface between the oxide support and the Pt nanoparticles. Zeolites contain catalytically active micropores with both Lewis and Brønsted acid sites.<sup>16</sup> These acidic micropores are capable of catalyzing the *n*-hexane reaction without the use of any metal catalyst. Zeolite catalysis favors isomerization at low temperature, but at high temperature, cracking is the dominant pathway, even when Pt is loaded onto the zeolite.<sup>17</sup> The high temperature catalytic behavior of the Al modified MCF-17/Pt catalyst is strikingly different from the zeolite catalysts. From Figures 2 and 3, it can be seen that the Al modified MCF-17/Pt catalyst is highly selective for isomerization, at a temperature at which traditional zeolite catalysts perform predominantly cracking reactions. This favorable selectivity is attributed to the Al modified MCF-17 support providing acidity, without catalyzing the reaction by itself. It is well-known that aluminum modification of silica provides strong Lewis acid sites which are not present in normal silica.<sup>18-20</sup> These Lewis acid sites are known to stabilize carbocation transition state species, which in turn with the dehydrogenation/hydrogenation chemistry of the Pt metal, act to promote the production of isomers through a bifunctional mechanism on a traditional reforming catalyst.<sup>21-25</sup>

To determine the type of mechanism present in this system, a catalytic experiment using a physical mixture of Pt supported on unmodified MCF-17 and Pt free Al modified MCF-17 was run. If a bifunctional promotion of isomerization between the Pt nanoparticles and the Al modified MCF-17 support exists, the catalytic results should be identical to the results obtained from the Al modified MCF-17/Pt catalyst. It was found that the selectivity for this reaction is similar to that for the Al modified MCF-17 with Pt loaded (selectivity data shown in Figure 3). However, the activity of the mixed catalysts was an order of magnitude lower than that of the Al modified MCF-17 catalyst ( $1.08 \times 10^{-2} \text{ s}^{-1}$ ). This could be explained by the fact that a bifunctional mechanism may be occurring; however, it appears that a majority of isomer products formed from the Al modified MCF-17/Pt catalyst require the direct contact of the Al modified support and the Pt metal. This result suggests that the primary active sites in this reaction, the Pt metal surface and the acidic Al sites, must be in a very close proximity to each other (nanometers not microns) in order to produce the high isomerization activity.

Infrared spectroscopy was utilized to investigate the amount of acid sites in the Al modified MCF-17 support, and the resulting spectrum is shown in Figure 5. When we utilize the adsorption coefficients for both Lewis and Brønsted acid sites (1.13 and 1.28  $\text{cm}/\mu\text{mol}$ , respectively),<sup>26</sup> it is possible to quantify the amount of each type of acid site in the support to 0.4 and 1.3 mmol/g, respectively. To put this into relation with the amount of metal sites, the number of surface Pt atoms was calculated based on spherical TEM projected surface areas and metal loading (as determined by elemental analysis). The concentration of surface Pt atoms per gram catalyst was found to be 0.011 mmol/g, giving an acid site to metal site ratio of about 40:1 for Brønsted sites and about 120:1 for Lewis sites. It appears that when Pt nanoparticles are added to the catalytically inactive modified silica support, the Pt metal accomplishes the necessary dehydrogenation/hydrogenation reactions to the hydrocarbon, while the Lewis acidity of the support promotes isomerization through an enhanced formation of carbocation intermediates.

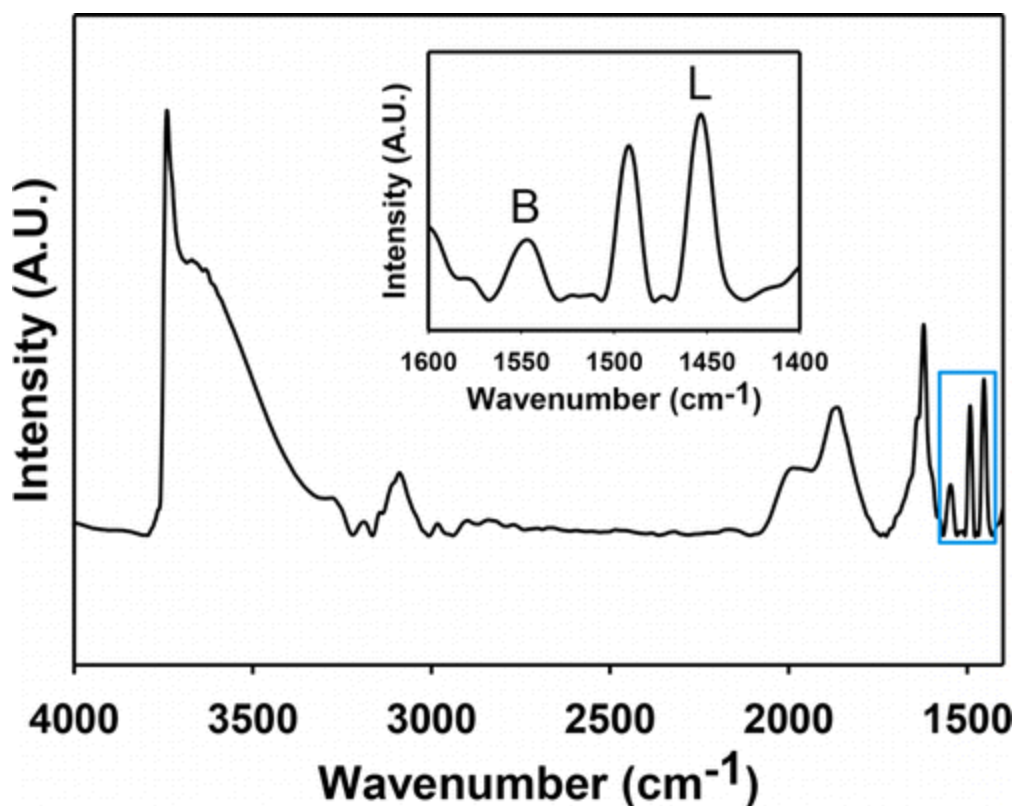


**Figure 4.** FT-IR spectrum of Al-modified MCF-17. Due to the large density of silanol on the mesopore wall, an intense peak is observed at  $3720\text{ cm}^{-1}$ , which indicates a stretching band of the Si-OH bond. After pyridine adsorption, both Brønsted and Lewis acid sites are distinguishable at  $1550$  and  $1450\text{ cm}^{-1}$ , respectively (see inset spectrum for magnification). When we utilize the adsorption coefficients of Brønsted and Lewis acid sites ( $1.13$  and  $1.28\text{ cm}^3/\mu\text{mol}$ , respectively),<sup>26</sup> the amount of Brønsted and Lewis acid sites can be quantified to  $0.4$  and  $1.3\text{ mmol/g}$ , respectively.

It was found that neither the Pt nanoparticle size nor the concentration of Al added to the mesoporous silica altered either the catalytic activity or selectivity. No changes in Pt nanoparticle stability were found between the modified and unmodified MCF-17 catalysts (based on catalytic deactivation rates and post reaction TEM images). The Al modified MCF-17/Pt catalyst also shows only a 20% deactivation after a second cycle. It is well-known that Pt dissociates molecular hydrogen, which can spill over onto the support and prevent coke formation, which is the primary reason for catalytic deactivation in zeolites.<sup>27,28</sup> The catalyst studied in this work is less susceptible to this type of catalytic deactivation.



## 8.4 Conclusions

In summary, three model catalysts were studied for the isomerization of *n*-hexane. The catalysts were colloiddally synthesized Pt nanoparticles (2.5 nm) loaded onto mesoporous silica (MCF-17), MCF-17 which had been modified with Al, and the third catalyst was Al modified MCF-17 mesoporous silica loaded with Pt nanoparticles (2.5 nm). It was found that the unmodified MCF-17/Pt catalyst was selective toward the undesired cracking products, and showed low overall activity for *n*-hexane reforming, indicating that the Pt metal alone was not a major contributor to the chemistry. The Al modified MCF-17 catalyst without Pt was found to be catalytically inactive at all studied temperatures, indicating the acidity alone could not accomplish the isomerization chemistry. However, when Pt nanoparticles were loaded onto this Al modified MCF-17 support, the catalyst was found to be remarkably active and selective for the isomerization of *n*-hexane. This remarkable selectivity was attributed to the close proximity between the acidic sites in the catalytically inactive oxide support and the Pt metal, which act in tandem to significantly promote the isomerization of the hydrocarbon.

## 8.5 References

1. Somorjai, G. A.; Li, Y. *Introduction to Surface Chemistry and Catalysis*; Wiley: New York, 2010; .
2. Somorjai, G. A.; Park, J. Y. Molecular Factors of Catalytic Selectivity. *Angew. Chem. , Int. Ed* **2008**, *47*, 9212-9228.
3. Clark, J. H. Green Chemistry: Challenges and Opportunities. *Green Chem.* **1999**, *1*, 1-8.
4. Sinfelt, J. H. Catalytic Hydrogenolysis on Metals. *Catal. Lett.* **1991**, *9*, 159-171.
5. Han, Y.; Lee, S. S.; Ying, J. Y. Spherical Siliceous Mesocellular Foam Particles for High-Speed Size Exclusion Chromatography. *Chem. Mater.* **2007**, *19*, 2292-2298.
6. Yang, M.; Somorjai, G. A. Adsorption and Reactions of C<sub>6</sub> Hydrocarbons at High Pressures on Pt(111) Single-Crystal Surfaces Studied by Sum Frequency Generation Vibrational Spectroscopy: Mechanisms of Isomerization and Dehydrocyclization of *n*-Hexane. *J. Am. Chem. Soc.* **2004**, *126*, 7698-7708.
7. Davis, S. M.; Zaera, F.; Somorjai, G. A. Surface Structure and Temperature Dependence of Light-Alkane Skeletal Rearrangement Reactions Catalyzed over Platinum Single-Crystal Surfaces. *J. Am. Chem. Soc.* **1982**, *104*, 7453-7461.
8. Iglesia, E.; Soled, S. L.; Kramer, G. M. Isomerization of Alkanes on Sulfated Zirconia: Promotion by Pt and by Adamantyl Hydride Transfer Species. *J. Catal.* **1993**, *144*, 238-253.
9. Antos, G. J.; Aitani, A. M., Eds.; In *Catalytic Naphtha Reforming*; CRC Press: New York, 2004; .

10. Jun, S.; Ryoo, R. Aluminum Impregnation into Mesoporous Silica Molecular Sieves for Catalytic Application to Friedel-Crafts Alkylation. *J. Catal.* **2000**, *195*, 237-243.
11. Na, K.; Jo, C.; Kim, J.; Cho, K.; Jung, J.; Seo, Y.; Messinger, R. J.; Chmelka, B. F.; Ryoo, R. Directing Zeolite Structures into Hierarchically Nanoporous Architectures. *Science* **2011**, *333*, 328-332.
12. Alayoglu, S.; Aliaga, C.; Sprung, C.; Somorjai, G. A. Size and Shape Dependence on Pt Nanoparticles for the Methylcyclopentane/Hydrogen Ring Opening/Ring Enlargement Reaction. *Catal. Lett.* **2011**, *141*, 914-924.
13. Pushkarev, V. V.; An, K.; Alayoglu, S.; Beaumont, S. K.; Somorjai, G. A. Hydrogenation of Benzene and Toluene over Size Controlled Pt/SBA-15 Catalysts: Elucidation of the Pt Particle Size Effect on Reaction Kinetics. *J. Catal.* **2012**, *292*, 64-72.
14. Pushkarev, V. V.; Musselwhite, N.; An, K.; Alayoglu, S.; Somorjai, G. A. High Structure Sensitivity of Vapor-Phase Furfural Decarbonylation/Hydrogenation Reaction Network as a Function of Size and Shape of Pt Nanoparticles. *Nano Lett.* **2012**, *12*, 5196-5201.
15. Musselwhite, N.; Alayoglu, S.; Melaet, G.; Pushkarev, V. V.; Lindeman, A. E.; An, K.; Somorjai, G. A. Isomerization of *n*-Hexane Catalyzed by Supported Monodisperse PtRh Bimetallic Nanoparticles. *Catal. Lett.* **2013**, *143*, 907-911.
16. Bhatia, S. *Zeolite Catalysis: Principles and Applications*; CRC Press: Boca Raton, 1990; .
17. Corma, A.; Planelles, J.; Sanchez-Marin, J.; Tomas, F. The Role of Different Types of Acid Site in the Cracking of Alkanes on Zeolite Catalysts. *J. Catal.* **1985**, *93*, 30-37.
18. Fraile, J. M.; Garcia, J. I.; Mayoral, J. A.; Pires, E.; Salvatella, L.; Ten, M. On the Nature of the Lewis Acid Sites of Aluminum-Modified Silica. A Theoretical and Experimental Study. *J. Phys. Chem. B* **1999**, *103*, 1664-1670.
19. Fraile, J. M.; Garcia, J. I.; Mayoral, J. A.; Pires, E. Structure and Relative Lewis Acidity of the Catalytic Sites of an Aluminum-Modified Silica Gel A Theoretical Study. *J. Mol. Catal. A: Chem* **1997**, *119*, 95-103.
20. Xu, M.; Arnold, A.; Buchholz, A.; Wang, W.; Hunger, M. Low-Temperature Modification of Mesoporous MCM-41 Material with Sublimated Aluminum Chloride in Vacuum. *J. Phys. Chem. B* **2002**, *106*, 12140-12143.
21. Fung, J.; Wang, I. The Reaction Mechanism of C<sub>6</sub> Hydrocarbons over Acid-Base Bifunctional Catalysts TiO<sub>2</sub>-ZrO<sub>2</sub>. *J. Catal.* **1996**, *164*, 166-172.
22. Triwahyono, S.; Jalil, A. A.; Ruslan, N. N.; Kamarudin, N. H. N. C<sub>5</sub>-C<sub>7</sub> Linear Alkane Hydroisomerization over MoO<sub>3</sub>-ZrO<sub>2</sub> and Pt/MoO<sub>3</sub>-ZrO<sub>2</sub> Catalysts. *J. Catal.* **2013**, *303*, 50-59.

23. Ramirez, S.; Viniegra, M.; Dominguez, J. M.; Schacht, P.; De Menorval, L. C. n-Heptane Reforming over Pt Supported on Beta Zeolite Exchanged with Cs and Li Cations. *Catal. Lett.* **2000**, *66*, 25-32.
24. Pajonk, G. M. Contribution of Spillover Effects to Heterogeneous Catalysis. *Appl. Catal. A* **2000**, *202*, 157-169.
25. Roessner, F.; Roland, U. Hydrogen Spillover in Bifunctional Catalysis. *J. Mol. Catal. A: Chem* **1996**, *112*, 401-412.
26. Ayrault, P.; Datka, J.; Laforge, S.; Martin, D.; Guisnet, M. Characterization of the Internal and External Acidity of H-MCM-22 Zeolites. *J. Phys. Chem. B* **2004**, *108*, 13755-13763.
27. Srinivas, S. T.; Rao, P. K. Direct Observation of Hydrogen Spillover on Carbon-Supported Platinum and Its Influence on the Hydrogenation of Benzene. *J. Catal.* **1994**, *148*, 470-477.
28. Guisnet, M.; Magnoux, P. Deactivation by Coking of Zeolite Catalysts. Prevention of Deactivation. Optimal Conditions for Regeneration. *Catal. Today* **1997**, *36*, 477-483.

# **Chapter 9**

## **Summary and Outlook**

### **Abstract**

This chapter will begin with a brief summary of the research and discoveries of this thesis. Conclusions will then be drawn from the body of work. These conclusions, as always in science should draw more questions. Therefore this dissertation will close with future research ideas and scientific inquiries.

## 9.1 Summary of Dissertation

This work has exemplified how small changes in catalyst variables can make large changes in reaction activity and selectivity. Chapters 3, 4 and 5 focus on the variables associated with the active metal catalysts. In Chapter 3, the Pt catalyzed furfural chemistry is studied, and Pt nanoparticle size is shown to have an enormous effect on product selectivity.<sup>1</sup> Small nanoparticles predominantly produce furan via a decarbonylation. Larger sized nanoparticles favor hydrogenation to furfuryl alcohol. In Chapter 4, the size effect of Pt nanoparticles is studied on various C<sub>6</sub> hydrocarbons including: hexane, methylcyclopentane, 2-methylpentane, and 3-methylpentane.<sup>2</sup> The trends in this chapter provide reference material for future studies on hydrocarbons, especially n-hexane. It was learned that nanoparticle size shows a relatively weak effect on selectivity in n-hexane reforming, and also that activity on pure Pt nanoparticles is extremely low.

In Chapter 5 the effect of Rh composition in Pt<sub>x</sub>Rh<sub>1-x</sub> bimetallic nanoparticles is studied.<sup>3</sup> Through investigation with Ambient Pressure X-ray Photoelectron Spectroscopy (AP-XPS), the actual Pt and Rh compositions on the surface of the nanoparticles under reaction conditions was determined. It was deduced, based on the surface compositions and statistical analysis, that the reaction proceeded most efficiently through isomer production when the surface consisted of the correct atomic ensemble.

After studying the catalytic effects from changing variables in the metal nanoparticles, the effect of the catalytic support on reaction activity and selectivity was studied in Chapters 6, 7 and 8. In this portion of the research, nanoparticle size, shape and composition are held constant in order to study the effect of the mesoporous support material on the reaction. In Chapter 6, Pt nanoparticles are loaded onto mesoporous supports made of Co<sub>3</sub>O<sub>4</sub>, NiO, MnO<sub>2</sub>, Fe<sub>2</sub>O<sub>3</sub>, and CeO<sub>2</sub>.<sup>4</sup> It was found that their activity for carbon monoxide oxidation was greatly enhanced relative to the support alone or Pt loaded onto inert mesoporous silica. This enhancement was attributed to the strong metal-support interaction (SMSI) generated from the interface of the Pt nanoparticles and the mesoporous oxide support. To further exploit the SMSI chemistry of this interface, macroporous oxides made of Al<sub>2</sub>O<sub>3</sub>, TiO<sub>2</sub>, Nb<sub>2</sub>O<sub>5</sub>, Ta<sub>2</sub>O<sub>5</sub>, and ZrO<sub>2</sub> were synthesized, loaded with Pt nanoparticles, and evaluated in n-hexane isomerization reactions in Chapter 7.<sup>5</sup> The selectivity for isomers was greatly enhanced when Nb<sub>2</sub>O<sub>5</sub> and Ta<sub>2</sub>O<sub>5</sub>, the supports with highest Lewis acidity, were used.

Chapter 8 discusses hexane reforming over an aluminum modified mesoporous silica catalyst.<sup>6</sup> This aluminum modification greatly increases the Lewis acidity of the mesoporous silica. However, the support itself performs no catalysis, unlike the standard aluminosilicate zeolites used in industrial reforming. When Pt nanoparticles are loaded onto the aluminum modified support, the isomer production of the catalyst is greatly enhanced. This enhancement comes through an order of magnitude increase in activity and a complete shift in selectivity to nearly 100% isomer production.

## 9.2 Future Research Directions

The research described in this dissertation involves careful synthesis of model catalysts with controlled variables, in-depth characterization, and kinetic evaluation under industry relevant reaction conditions. It is my belief that this research method is the reason for the

multitude of scientific discoveries in not only this work, but the entire Somorjai research group. Therefore, my outlook for future research is to stay true to this three-pronged approach involving synthesis, characterization, and catalysis.

Each of the three areas can (and should) be scientifically furthered on their own. New synthetic techniques would greatly enhance the variables which could be studied. The idea of catalytic architecture in nanomaterial synthesis is also an extremely promising pathway for future research.<sup>7</sup> The premise of catalytic architecture is using material complexity to perform complicated (often multi-step) chemical reactions. This would be the heterogeneous analogue to homogenous tandem catalysis in which one catalytic reaction cascades into another catalytic reaction, often with two separate active sites.<sup>8</sup> This concept in surface catalyzed reactions could allow for one intermediate to be formed at one active site, then while in an energetically favorable state, diffuse to a new active site to perform a different reaction. This could allow for complex chemical transformations to occur over a single catalyst bed.

Catalyst characterization improvements require the need for more in situ techniques. Studying the materials under reaction conditions is the only method to learn the actual structure and behavior of the active catalytic species. AP-XPS is becoming ever more advanced, as spatial resolution of the beam on the sample narrows and the working pressure of the sample chamber grows.<sup>9</sup> To be able to focus a beam on a particular nanoparticle or interface, while operating at the actual industrial catalytic pressures is the ultimate goal. The utilization of electron microscopy under in situ conditions is also an important technique known as environmental TEM.<sup>10,11</sup> The use of this technique to study nanoparticles during catalytic reactions is still in its infancy, but provides a much promise and a plethora of future research opportunities.

For the advancement of the catalytic portion of this research, we plan to investigate the isomerization of hexadecane (C<sub>16</sub>), which is a model reaction for the isodewaxing process in crude oil refining.<sup>12</sup> With this aim in mind, the high pressure – high temperature catalytic reactor described in this thesis has been converted into a reactor capable of performing hexadecane isomerization reactions. To accomplish this all lines have been modified to be heated above the boiling point of hexadecane and a GC/MS instrument was installed and will be utilized for product detection in order to elucidate mechanistic information about the isodewaxing process. By utilizing the same scientific approach, with more complex catalytic materials, improved characterization tools, and new and interesting chemical reactions, I am confident that this research will continue to provide new and interesting insight to the workings of a heterogeneous catalyst.

### 9.3 References

1. Pushkarev, V. V.; Musselwhite, N.; An, K.; Alayoglu, S.; Somorjai, G. A. High Structure Sensitivity of Vapor-Phase Furfural Decarbonylation/Hydrogenation Reaction Network as a Function of Size and Shape of Pt Nanoparticles. *Nano Lett.* **2012**, *12*, 5196-5201.
2. Alayoglu, S.; Pushkarev, V. V.; Musselwhite, N.; An, K.; Beaumont, S. K.; Somorjai, G. A. Reforming of C-6 Hydrocarbons Over Model Pt Nanoparticle Catalysts. *Top. Catal.* **2012**, *55*, 723-730.

3. Musselwhite, N.; Alayoglu, S.; Melaet, G.; Pushkarev, V. V.; Lindeman, A. E.; An, K.; Somorjai, G. A. Isomerization of *n*-Hexane Catalyzed by Supported Monodisperse PtRh Bimetallic Nanoparticles. *Catal. Lett.* **2013**, *143*, 907-911.
4. An, K.; Alayoglu, S.; Musselwhite, N.; Plamthottam, S.; Melaet, G.; Lindeman, A. E.; Somorjai, G. A. Enhanced CO Oxidation Rates at the Interface of Mesoporous Oxides and Pt Nanoparticles. *J. Am. Chem. Soc.* **2013**, *135*, 16689-16696.
5. An, K.; Alayoglu, S.; Musselwhite, N.; Na, K.; Somorjai, G. A. Designed Catalysts from Pt Nanoparticles Supported on Macroporous Oxides for Selective Isomerization of *n*-Hexane. *J. Am. Chem. Soc.* **2014**, *136*, 6830.
6. Musselwhite, N.; Na, K.; Alayoglu, S.; Somorjai, G. A. The Pathway to Total Isomer Selectivity: *n*-Hexane Conversion (Reforming) on Platinum Nanoparticles Supported on Aluminum Modified Mesoporous Silica (MCF-17). *J. Am. Chem. Soc.* **2014**, *136*, 16661-16665.
7. Mori, K.; Yamashita, H. Progress in Design and Architecture of Metal Nanoparticles for Catalytic Applications. *Phys. Chem. Chem. Phys.* **2010**, *12*, 14410-14432.
8. Breit, B.; Zahn, S. K. Stereoselective Hydroformylation, Cuprate Addition and Domino Reactions with the Aid of a Catalyst Directing Group. *Polyhedron* **2000**, *19*, 513-515.
9. Schnadt, J.; Knudsen, J.; Andersen, J. N.; Siegbahn, H.; Pietzsch, A.; Hennies, F.; Johansson, N.; Martensson, N.; Ohrwall, G.; Bahr, S.; Mahl, S.; Schaff, O. The New Ambient-Pressure X-ray Photoelectron Spectroscopy Instrument at MAX-Lab. *J. Synchrotron Rad.* **2012**, *19*, 701-704.
10. Xin, H. L.; Niu, K.; Alsem, D. H.; Zheng, H. In situ TEM Study of Catalytic Nanoparticle Reactions in Atmospheric Pressure Gas Environment. *Microsc. Microanal.* **2013**, *19*, 1558-1568.
11. Xin, H. L.; Alayoglu, S.; Tao, R.; Genc, A.; Wang, C. M.; Kovarik, L.; Stach, E. A.; Wang, L. W.; Salmeron, M.; Somorjai, G. A.; Zheng, H. Revealing the Atomic Restructuring of Pt-Co Nanoparticles. *Nano Lett.* **2014**, *14*, 3203-3207.
12. Thormann, J.; Maier, L.; Pfeifer, P.; Kunz, U.; Deutschmann, O.; Schubert, K. Steam Refroming of Hexadecane over a Rh/CeO<sub>2</sub> Catalyst in Microchannels: Experimental and Numerical Investigation. *Int. J. Hydrogen Energ.* **2009**, *34*, 5108-5120.